University of California
Los Angeles

Study of Flow, Turbulence and Transport on the Large Plasma Device

A dissertation submitted in partial satisfaction
of the requirements for the degree
Doctor of Philosophy in Physics

by

David Andrew Schaffner

2013

Abstract of the Dissertation

Study of Flow, Turbulence and Transport on the Large Plasma Device

by

David Andrew Schaffner

Doctor of Philosophy in Physics

University of California, Los Angeles, 2013

Professor Troy A. Carter, Chair

The relationships amongst azimuthal flow, radial particle transport and turbulence on the Large Plasma Device (LAPD) are explored through the use of biasable limiters which continuously modify the rotation of the plasma column. Four quarter annulus plates serve as an iris-like boundary between the cathode source and the main plasma chamber. Application of a voltage to the plates using a capacitor bank drives cross-field current which rotates the plasma azimuthally in the electron diamagnetic direction (EDD). With the limiters inserted, a spontaneous rotation in the ion diamagnetic direction is observed; thus, increasing biasing tends to first slow rotation, null it out, then reverse it. This experiment builds on previous LAPD biasing experiments which used the chamber wall as the biasing electrode rather than inserted limiter plates. The use of inserted limiter biasing rather than chamber wall biasing allows for better cross-field current penetration between the plasma source and the electrodes which in turn allow for a finer variation of applied torque on the plasma.

The modification of plasma parameter profiles, turbulent characteristics, and radial transport are tracked through these varying flow states. Azimuthal flow radial profiles are peaked at the limiter edge. Consequently, the variation in flow states also results in variation of sheared flow. Improved radial particle confinement is observed in states with sheared flow regardless of the direction of rotation. This improvement is indicated by both steepened density profiles and decreased radial particle flux. Conversely, a confinement degradation is seen

in the minimum sheared flow state. Comparison of density fluctuation power and crossphase between density and radial velocity fluctuations show that both quantities are suppressed by sheared flow, but that the density fluctuation suppression is dominant and contributes most to the decrease in radial particle flux. Also, some observed changes to density and flux profiles suggest disagreement with a purely local model of transport including the formation of a hollow density profile at state of high flow (high bias) and regions where the direction of measured flux is opposite to that predicted by the direction of density gradient. Changes in flux and density gradient with bias are correlated but in a way that is inconsistent with a Fick's Law like model.

Changes in turbulent spectra and features are observed with modification of the rotation state. Log-linear spectra with rotation in either azimuthal direction tends to exhibit a linear slope for power versus frequency and versus wavenumber, while spectra curves in the null flow case have an upward concave shape. Time traces corresponding to these spectra indicate a clear presence of Lorentzian structures in flow states but not in the null flow state. Spectral density histograms, showing the distribution of density fluctuation power in both frequency and wavenumber space, indicate that the modes tend to propagate azimuthally in the same direction as the flow. This suggests a large contribution of rotational interchange instability to the plasma turbulence. Regions with significant flow exhibit spectral density distributions which follow narrow curves in frequency and wavenumber space, much like a dispersion relation line. Regions without flow (either the null flow state or the plasma core) have broader, more diffuse distributions.

A pair of coherent modes develop with rotation in the EDD direction. The mode fluctuation power peaks at the limiter edge; since maximum flow is observed at the limiter edge, the modes are most likely flow driven. Comparison with a linear Braginskii-fluid model eigenfunction solver supports this conclusion. The lower frequency mode—first observed at about 1-2kHz—is identified as a pure interchange mode while the higher frequency mode—first observed at about 5-6kHz—is determined to be a coupled drift-wave interchange mode. The frequency of these modes increases with flow velocity; the appearance of sideband modes in

the frequency spectra also suggests that these mode begin to interact.

The dissertation of David Andrew Schaffner is approved.

Jon Aurnou

George Morales

Walter Gekelman

Troy A. Carter, Committee Chair

University of California, Los Angeles

2013

To Erin, of course. And to my parents for setting me down this path.

Table of Contents

List of Figures

List of Tables

Acknowledgments

I have learned through my graduate school experience that being a good scientist means being a member of an interactive community and that is nowhere more true than working in the BAPSF at UCLA. First of, I would like to thank my advisor, Dr. Troy Carter, for giving me the opportunity to join this community and for simultaneously providing me the guidelines and the freedom to be successful. Troy has not only been a wonderful mentor for my research, but also, a role model for how I can in turn be an active participant in the plasma physics community as well as a mentor myself to my younger colleagues. I would also like to thank Dr. George Morales for his many contributions to my physics education including teaching me the basics of plasma physics in the classroom as well as the realities of physics research through his help in forming my dissertation. Dr. Jim Maggs and Dr. Walter Gekelman deserve my appreciation for their many helpful comments and recommendations regarding my work. Moreover, I want to especially thank Walter for being the reliable steward of our BAPSF community here at UCLA. Thank you to Dr. Jon Aurnou for serving on my committee and showing such enthusiasm for the research I was conducting.

I also want to thank my first advisor, Dr. Rainer Wallny, for introducing me to real physics research both in my last year of undergraduate and my first two years of graduate school.

I want to thank the many, many members of this plasma research group who have made my graduate experience not only successful, but extremely fulfillling and fun. Thank you to Dr. Steve Vincena for always being available—and willing—to help solve any problem that might arise in the course of my work. He is definitely LAPD's caped crusader. Thanks also, to Dr. Shreekrishna Tripathi and Dr. Bart Von Compernolle for there willingness to provide help and useful feedback on my research as well as to Dr. Pat Pribyl for his electronics help and tips in the lab and down in the LAPD machine room.

Thank you to Zoltan Lucky and Marvin Drandell, without whom the lab would likely grind to a screeching halt. I could not have done my research, literally, without your help in

building probes and the limiter biasing plates for my experiment.

A big, big thank you and a hug to Meg Murphy for providing a respite spot for me to commiserate and decompress. I'm sorry for making travel difficult sometimes, though.

Thank you to my fellow graduate students, Dr. David Auerbach, Dr. Chris Cooper, Dr. Jon Hillesheim, Brett Friedman, Jie Zhang, Yuhou Wang, Mike Martin, Nathaniel Moore, Jeffery Bonde, Derek Schaeffer and Anton Bondarenko for making daily life, and especially conference trips, that much more fun as well as being a sounding board for science-y problems and discussions.

Thank you to Giovanni Rossi, Danny Guice, and Eli Haims for bearing with my nascent attempts at being a physics mentor. I hope I have served you well. I certainly appreciate all of the help you have given me.

Thank you to my scientific partner-in-crime, Erik Everson. Whether its hosting pirate parties or debating physics topics (sometimes) over a cup of coffee at Starbuck's, my sanity throughout grad school could not have been maintained.

Thank you to my parents, Jane and Jim Schaffner, for creating and maintaining the foundation that has allowed me to develop into the person I am. Thank you for not pushing me to be a great anything-in-particular, but just to be a good person. You understood that love and compassion was all I needed to be able to take flight.

Thank you to my wife, Erin Englert, without whom I would not be a complete person. I would likely have finished my degree without you, but it would have been as an empty, burned-out shell of a person. You breathed life into me when the world would have squished it out. I am forever grateful to your love and support. Now that I am done, I'm excited to see where our adventure will take us next.

Vita

2006	B.S. Physics
	University of California, Los Angeles, USA
2007	M.S. Physics
	University of California, Los Angeles, USA

Publications and Presentations

R.I. Pinsker, M. Porkolab, W.W. Heidbrink, Y.Luo, C.C. Petty, R. Prater, M. Choi, D.A. Schaffner, F.W. Baity, E. Fredd, J.C. Hosea, R.W. Harvey, A.P. Smirnov, M. Murakami and M.A. Van Zeeland, *Absorption of fast waves at moderate to high ion cyclotron harmonics on DIII-D*, Nuclear Fusion **46**, S416-S424 (2006).

Turbulence and Flow in the Large Plasma Device, D.A. Schaffner, T.A. Carter, P.Popovich, B. Friedman, Talk, Gyrokinetics in Laboratory and Astrophysical Plasmas Conference, Isaac Newton Institude of Mathematical Sciences, UK, June 2010.

D. Asner et al, The RD42 Collaboration, *Diamond pixel modules*, Nuclear Instruments and Methods in Physics Research A: Accelerators, Spectrometers, Detectors and Associated Equipment **636**, Issue 1, Supplement 21, S125-S129 (2011).

Shu Zhou, W.W. Heidbrink, H. Boehmer, R. McWilliams, T.A. Carter, S. Vincena, B. Friedman, D. Schaffner, *Sheared-Flow Induced Confinement Transition in a Linear Magnetized Plasma*, Physics of Plasmas **19**, 012116 (2012).

D.A. Schaffner, T.A. Carter, G.D. Rossi, D.S. Guice, J.E. Maggs, S. Vincena and B. Friedman, *Modification of Turbulent Transport with Continuous Variatio of Flow Shear in the Large Plasma Device*, Physical Review Letters **109**, 135002 (2012).

B. Friedman, T.A. Carter, M.V. Umansky, D. Schaffner and B. Dudson, *Energy Dynamics in a simulation of LAPD turbulence*, Physics of Plasmas **19**, 102307, (2012).

D.A. Schaffner, T.A. Carter, G.D. Rossi, D.S. Guice, J.E. Maggs, S. Vincena, and B. Friedman, *Turbulence and transport suppression scaling with flow shear on the Large Plasma Device*, Physics of Plasmas (accepted March 2013).

Observation of improved and degraded confinement through driven flow on the LAPD, D.A. Schaffner, T.A. Carter, G.D. Rossi, D.S. Guice, Plenary Talk, U.S. Transport Task Force Meeting, Annapolis, MD, US, April 2012

Observation of improved and degraded confinement through driven flow on the LAPD, D.A. Schaffner, T.A. Carter, G.D. Rossi, D.S. Guice, Invited Talk, International Workshop for Open Systems-International Work Shop on Plasma Material Interaction Facilities for Fusion Joint Conference, Tsukuba, Japan, July 2012

Observation of improved and degraded confinement through driven flow on the LAPD, D.A. Schaffner, T.A. Carter, G.D. Rossi, D.S. Guice, Contributed Oral Presentation, EU-US Joint Transport Task Force Meeting, Padua, Italy, August 2012

Modification of Turbulent Transport with Continuous Variation of Flow Shear in the Large Plasma Device, D.A. Schaffner, T.A. Carter, G.D. Rossi, D.S. Guice, Invited Talk, American Physical Society Division of Plasma Physics Meeting, Providence, RI, US, November 2012

CHAPTER 1

Overview of the Study of Flow, Turbulence, and Transport on the Large Plasma Device

This opening chapter provides summaries for the main topics and results presented in this dissertation and a brief overview of the chapter contents.

1.1 Control of Plasma Rotation on LAPD

The rotation of the LAPD plasma column can be continuously modified and finely tuned using a biasable annular limiter between the cathode source and the main vacuum chamber. A triggered capacitor bank bias circuit drives cross-field current between anode/cathode connected field lines and limiter connected field lines generating a radial electric field in the plasma column which rotates due to $E \times B$ drift. Figure 1.1 shows an overview of the range of rotation profiles that can be achieved through limiter biasing. With limiters inserted to produce an aperture radius of 26cm, the unbiased LAPD plasma column exhibits spontaneous rotation in the ion diamagnetic drift (IDD) direction for radii larger than 22cm. The flow peaks around 28cm. The capacitor banks supply a triggered bias to the limiter plates in a range from 0 to 230V above the cathode potential. Applied bias tends to drive flow in the electron diamagnetic drift direction. Thus, as bias is increased, the rotation of the plasma within about 31cm is first slowed, nulled, and then reversed. The biasing can drive stronger plasma flow than is observed spontaneously and this driven flow in the EDD direction peaks at the limiter edge.

In addition to flow modification and control, the different flow states exhibit continuously

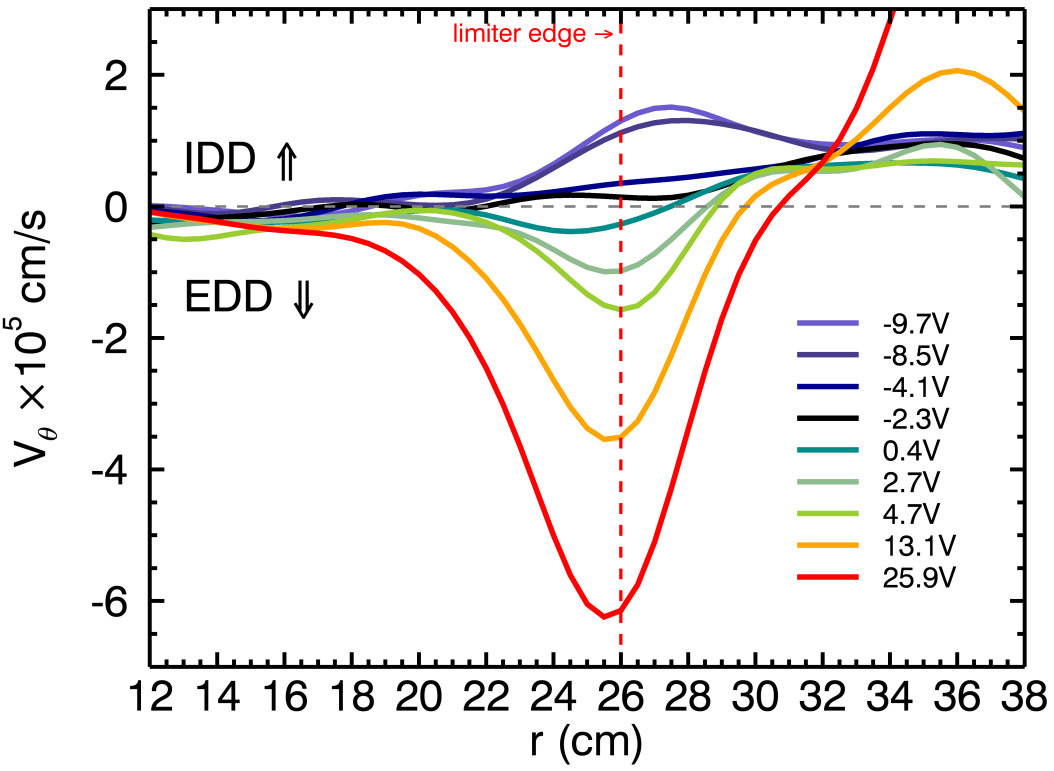

Figure 1.1: Azimuthal velocity profiles for various bias states labeled by the measured voltage difference between the limiters and the anode. The dark blue curves show spontaneous (unbiased) flow in the ion diamagnetic drift direction (IDD). The black curve shows the velocity of the minimum flow state. Lighter color curves show driven flow in the electron diamagnetic drift direction (EDD).

varying sheared flow in the radial regions surrounding the flow peak. In the radial region of 27 to 31cm, just beyond the limiter edge, the shearing rate ranges from 0 to $\sim$ 120kHz. When normalized to the unsheared inverse autocorrelation time, τ_{ac}^{-1}—a quantity reflecting how quickly in time density fluctuations decorrelate—the shearing rate ranges from zero to five times τ_{ac}^{-1}. Thus, this data set has points both in the weak shear regime, defined as $\gamma_s \tau_{ac} < 1$, and the strong shear regime, $\gamma_s \tau_{ac} > 1$.

A detailed description of the limiters is provided in Chapter 4.

1.2 Modification of Density Profile and Radial Particle Confinement

A major consequence of setting the flow and flow shear states through limiter biasing is an accompanying change in the density profile, which can be indicative of a change in radial particle transport. Figure 1.2 shows the range of density profiles that are observed with varying bias states. Each colored line indicates a different bias state labeled as to the voltage difference measured between the anode potential and the limiter potential ($V_{\text{lim}} - V_{\text{ano}}$). The scan shows that the density gradient is initially relaxed (black curve to dashed blue) when the flow and flow shear are nulled out indicating a degradation in radial confinement. Increasing the bias and rotation into the EDD direction causes a steepening of the density gradient. This change occurs because of improved radial confinement in sheared flow region. Additionally, changes in the density and flux profiles with increasing bias are observed that could be indicative of a modification of the plasma source and of non-local transport. These include the observation of a hollowing of the density profile in the core at high bias—red curve of Figure 1.2—and regions of inward pointing measured flux. Chapters 5 and 6 covers details of the changes in density profile and radial confinement.

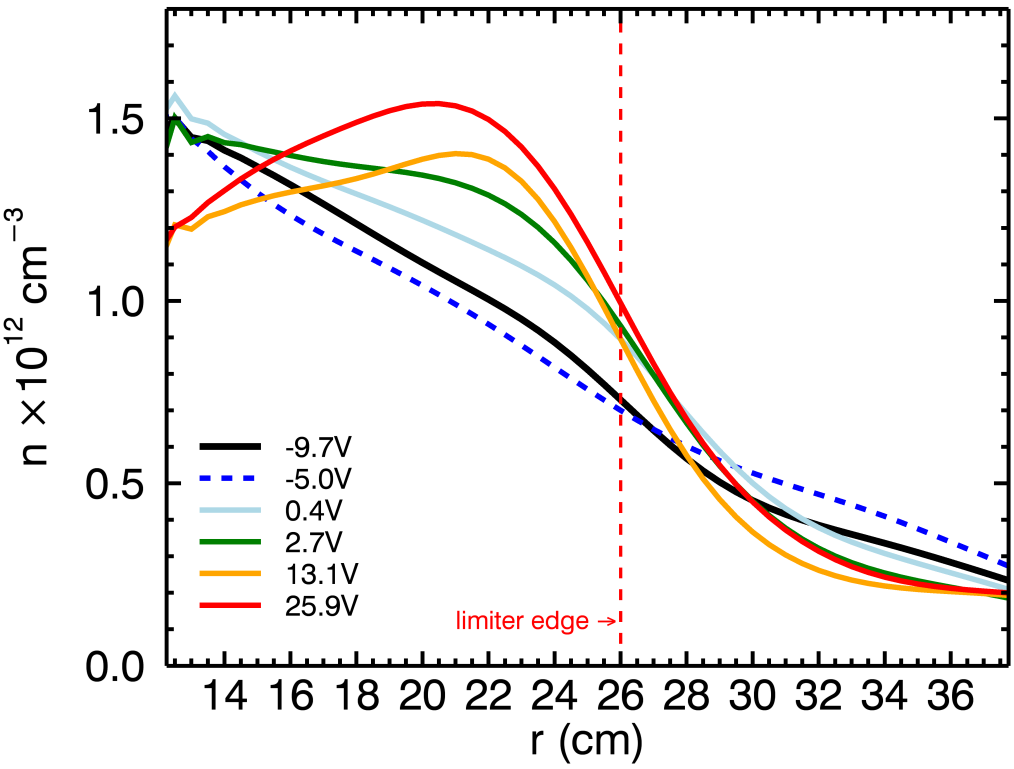

Figure 1.2: Density profiles for various biases labeled by the voltage difference between limiters and anode. The black curve here is the unbiased density profile and the dashed blue line the profile for the minimum sheared flow state. The remaining four curves show increasingly steepened curves for higher biases.

1.3 Modification of Turbulence

Another consequence of modifying the flow profile is a change in the features of the plasma turbulence. Both frequency and wavenumber spectra are affected by the changes in flow state. Figure 1.3 shows that the frequency spectra curves of the density undergo a change

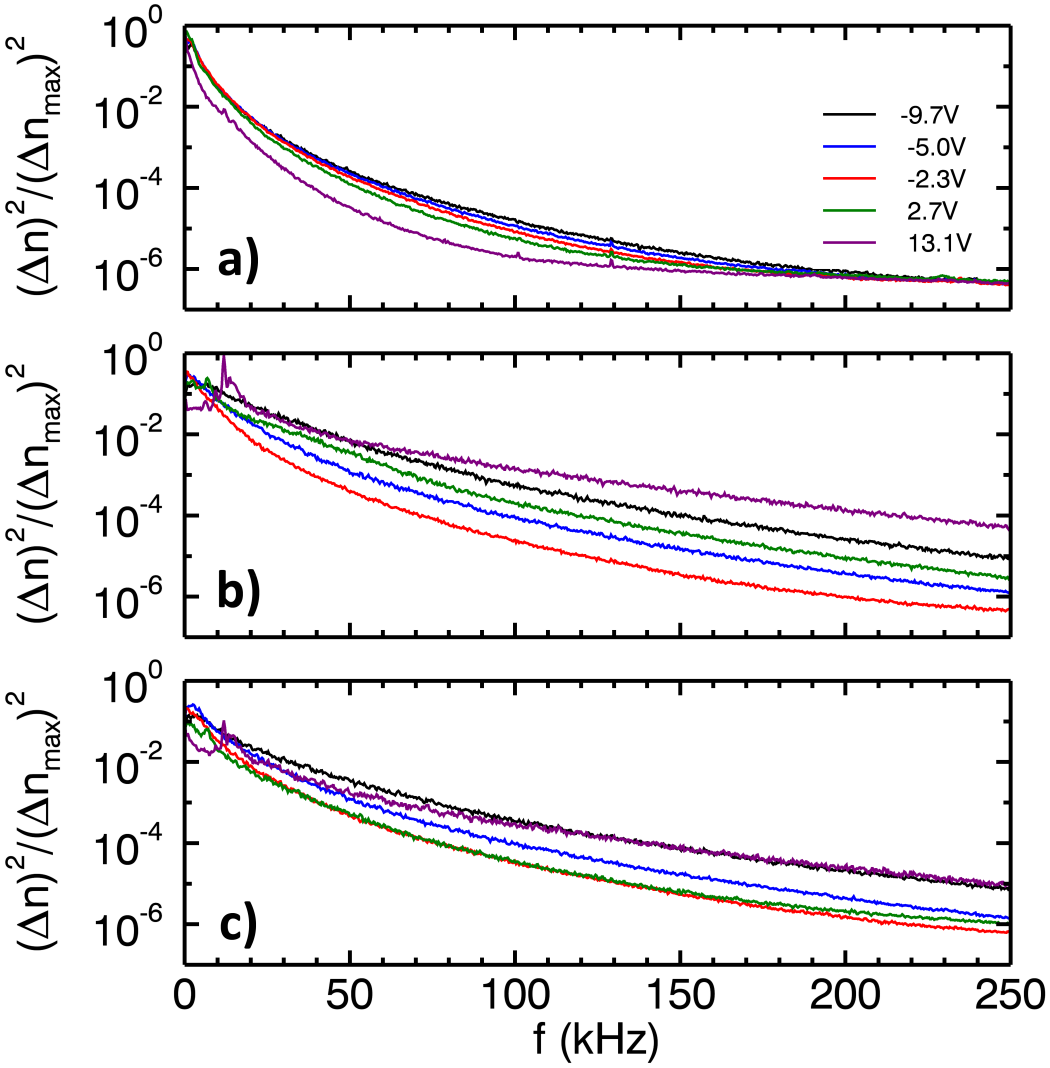

Figure 1.3: Density fluctuation power as a function of frequency plotted in Log-Linear format averaged over various radial regions: (a) Core region (12-22cm), (b)Limiter Edge region (24-27cm) and (c) Outer edge region (27-31cm). Each curve in each section is for a different bias state indicated by the limiter-anode voltage difference.

in shape as a function of both location and bias. The top plot (a) shows spectra for the core region 12 to 22cm. The curves are all concave regardless of bias state. Compared to the core, the spectra curves for the (b) limiter edge region, 24 to 27cm, and the (c) outer edge region, 27 to 31 cm, are more linear and gently sloped. Linear curves in a log-linear plot are indicative of an exponential spectrum. In the edge regions only (b) and (c), the bias state also affects the shape. Regions with significant flow (black and purple curves) tend to be much more linear than the minimum flow and flow shear states (red and blue curves). These contrasts suggest changes in the nature of the turbulent fluctuations between flow and non-flow states. Further discussion regarding turbulence features and modifications are made in Chapter 5.

1.4 Emergence of a Coherent Mode

A pair of coherent modes is shown to grow when flow is driven in the EDD direction; comparison of the measured frequencies of these modes to the fastest growing modes predicted by a linear Braginskii-fluid calculation show excellent correspondence. These modes are identified as a pure rotational interchange (n=0) and a drift-interchange mode (n=0.5) where n is the axial mode number(i.e. n=0 refers to an infinite wavelength and n=0.5 is a wavelength half the size of the cylindrical chamber). The n=0 mode emerges at a low frequency, around 1-2kHz while the n=0.5 mode emerges at slightly higher frequency, around 5-6kHz. The frequency and power of these modes increases with increasing plasma rotation with the n=0.5 mode reaching its peak power at a frequency of about 12kHz. The appearance of sidebands at higher biases suggests these modes begin to interact and beat with one another. Figure 1.4 shows the limiter edge region (24-27cm) density spectra zoomed into a band of 0.3-50kHz with dashed vertical lines tracing the peak of the n=0.5 mode. The details of this mode analysis are given in Chapter 5.

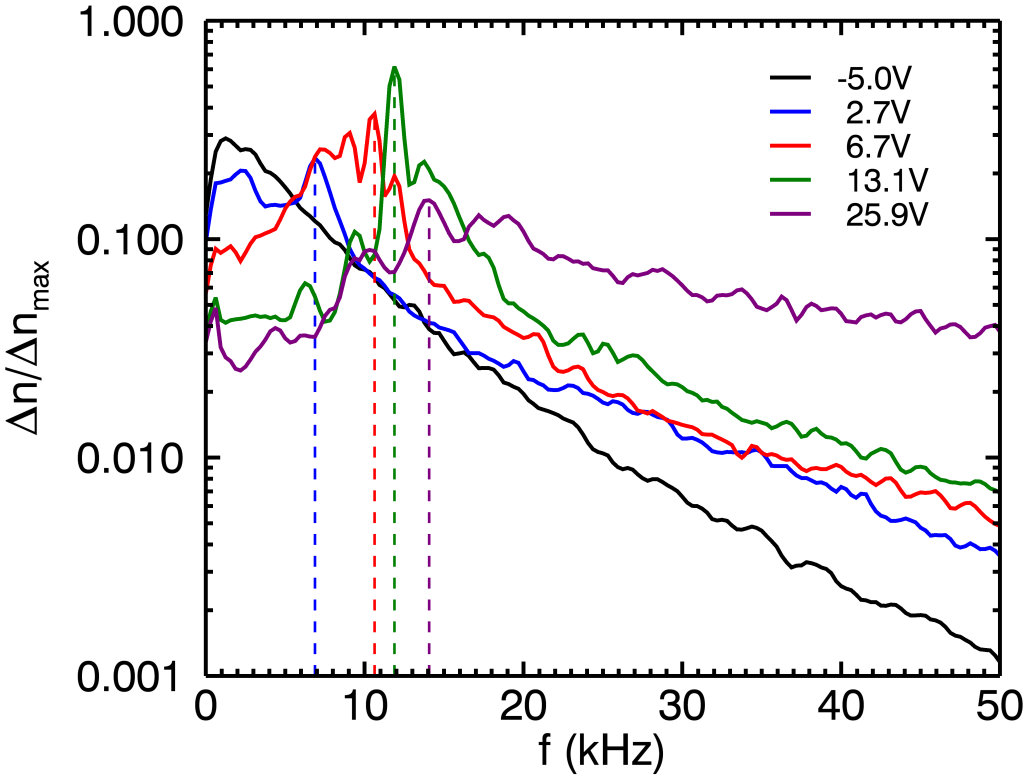

Figure 1.4: Density fluctuation power spectra averaged over a small spatial region just around the limiter as a function of frequency zoomed into a range between 0 and 50kHz in order to emphasize the peaks of the coherent modes. Two modes can be observed in the spectra at 2.7V which represents a state with small EDD direction flow. The power in the coherent modes increases with higher biases. The frequency of the modes also increase as indicated by the dashed vertical lines which show the progression in frequency of the n=0.5 drift-interchange mode.

1.5 Local Analysis of Turbulence and Transport variation with shearing rate

Decreases in density fluctuation power and particle flux—averaged over a radial region just beyond the limiter edge—correspond to increases in a the radially averaged shearing rate as shown in Figure 1.5. An increase in fluctuations and flux is also observed when the shearing rate is minimized.

Comparison between density fluctuation amplitude and the crossphase between density fluctuations and radial velocity fluctuations show that while both decrease with increasing shearing rate, density fluctuation reduction is the quantity that contributes most to suppression of particle flux. Furthermore, the analysis shows that the direction of flux is unimportant in turbulent fluctuation or flux suppression as a decrease in these quantities is observed for sheared flow that is in either azimuthal direction. Moreover, it is shown that suppression of fluctuations can occur for shearing rates less than the inverse autocorrelation time of the density fluctuations. The details of the shear suppression scaling are provided in Chapters 6 and 7.

1.6 Summary of Dissertation Chapters

Chapter 2 introduces the experimental background to the study of flow and turbulence in plasma physics providing motivation for biased rotation research on the LAPD. It also summaries the important physics background covered in this thesis.

Chapter 3 provides a detailed overview of the Large Plasma Device as well as the primary diagnostics used for the experiment.

Chapter 4 covers the limiters, the biasing circuit and the direct effects of biasing with respect to plasma potential, flow, shear and current.

Chapter 5 surveys the global variations that are observed in the plasma in differing steady-state flow states. The changes in turbulent spectra, both frequency and wavenumber,

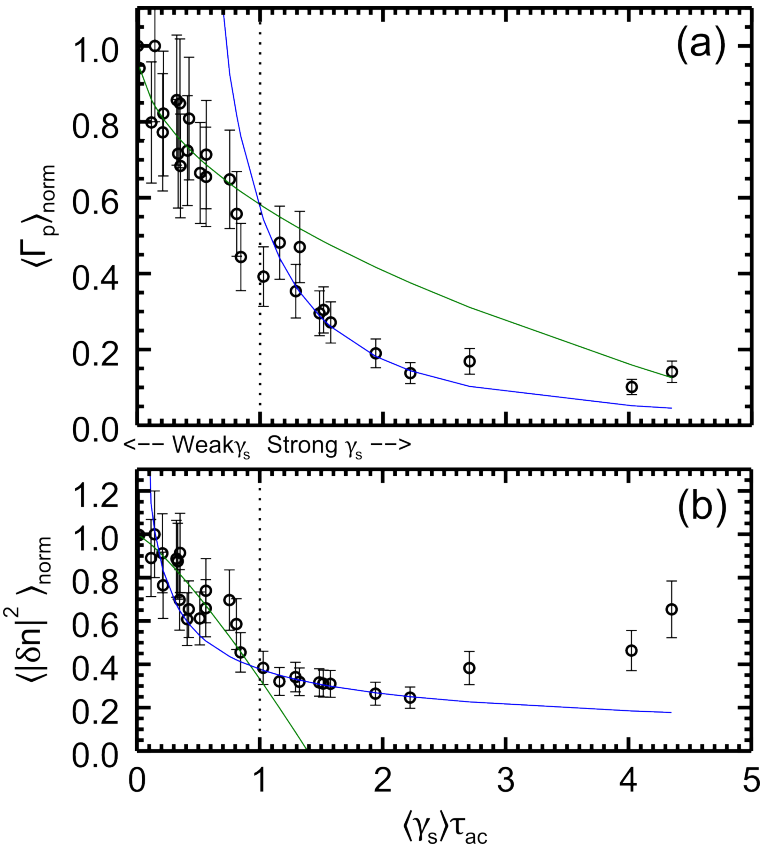

Figure 1.5: (a) Particle flux and (b) density fluctuation power normalized to their respective values at minimum shear averaged over the region 27-31cm. Each quantity is shown as a function of shearing rate normalized to the inverse autocorrelation time measured at the minimum shear state. The error bars represent a statistical error from averaging over multiple shots. The blue and green curves are fits to shear suppression models: the blue is a fit to a γ_s^ν model for strong shearing rate points and the green is a fit to $1 - \gamma_s^\nu$ for weak shearing rate points.

are covered as well as modification of density, temperature and fluctuation profiles. The modification of turbulent structures is also discussed. A detailed mode analysis is given showing how biasing changes the sources of free energy for resistive drift wave, rotational interchange and Kelvin-Helmholtz modes. Detailed comparison of experimental data to linear growth rates calculated from a Braginskii fluid model eigenfunction solver are made in order to differentiate the contributions made by each mode type to the overall turbulence.

Chapter 6 focuses on the scaling of various quantities as a function of shearing rate—including density fluctuations, radial velocity fluctuations, crossphase, particle flux, and radial correlation length.

Chapter 7 shows computed quantitative fits for the shear scalings of Chapter 6 and compares these fit results to the predictions made by shear decorrelation models.

Chapter 8 analyzes the effect of biasing as a function of time showing the dynamics of flow, density and current. The relaxation of flow after bias turn-off is also tracked.

The appendix includes details on the transport models used, the two-point correlation method, comparison of Mach probe flow measurements versus swept Langmuir probe flow measurements, details on the circuitry used for probe measurements, and lastly a brief ode to all that is plasma.

CHAPTER 2

Introduction and Motivation

The study of plasma confinement at its core is an attempt to fix a leaky bucket. Unfortunately, while a few cracks or holes in a bucket can be easily sealed with a judicious application of epoxy or duct tape, successful confinement of plasma has proved more elusive and has incorporated within its study, significant research into instabilities and turbulence, diffusion and transport, flow and shear, particles and fields. While the results contained in this dissertation cannot claim any ultimate solution to the leaky bucket problem, it can contribute to the growing and evolving continuum of knowledge in just why that bucket leaks, and perhaps make progress on to how to minimize the leak or fix it once and for all.

While the study of plasma is extremely fruitful and worthy in its own right, the focus on plasma confinement and transport finds its motivations, as so many subjects do in this field, in the goal of nuclear fusion. The achievement of fusion—more specifically, magnetic confinement fusion— though much more complicated and difficult, is, also at its core, an attempt to fix a leaky bucket. Given enough heat density and particle density, the confined particles of plasma—typically heavy ion isotopes of hydrogen called deuterium and tritium—will fuse into helium and in the process release relatively massive amounts of kinetic energy. Such a reaction, if sustained, could be tapped as an power source, either to produce electrical energy or propulsion. A major reason why controlled nuclear fusion is not yet a power source today is due to our leaky bucket. While this fusion reaction itself has already been achieved, it has only really been used to blow the bucket to smithereens. The science, and art, of nuclear fusion is to come up with a method of keeping the leaky bucket filled with just enough heat and energy that a continued and controlled fusion reaction can occur without

it running away in a mushroom cloud of glory.

Thus the study of plasma confinement. The story of plasma confinement should really begin with the study of charged particles in magnetic fields, and how a charged particle will, due to the Lorentz force $F = e(E \times B)$, travel freely parallel to a magnetic field line, but be restricted in its motion perpendicular to the field such that it will gyrate around the field line in simple harmonic motion. However, since the nature of this dissertation lies not just with plasma confinement in general, but instead narrows its focus to the study of how flow, flow shear, and turbulence influence and modify the transport of these particles perpendicularly across the magnetic field, it is worthwhile to motivate why the study of turbulence and transport is useful from a nuclear fusion point of view. Before delving into an overview of the basic transport and flow related topics, I will go a history of research on this topic starting with the first observation of the H-mode in a fusion plasma device.

2.1 From H-Mode to Biasing Experiments

A new operational regime was discovered on the original ASDEX tokamak (shown in Figure 2.1) in 1982 during neutral beam injection experiments and was characterized by increased particle and energy confinement times. This new regime was dubbed H-mode for the high values of $\beta = nk_BT/(B^2/\mu_0)$—ratio of particle pressure to magnetic pressure—that were observed during the discharge—in contrast to the low β discharges dubbed L-modes [1]. While there appeared to be some correlation to the amount of energy supplied to the tokamak by the neutral beam, it was unclear what mechanisms were involved in this spontaneous confinement improvement.

Following the initial identification of the H-mode [2, 3], many other plasma devices—stellarators [4], mirror machines [5] and other tokamaks—observed a similar improved confinement state initiated through a multitude of heating methods including neutral beam injection as on the first ASDEX H-mode experiments, ion [6] and electron [7, 8] cyclotron heating, and Ohmic heating [9]. As pointed out in a review article by Burrell [10], a common

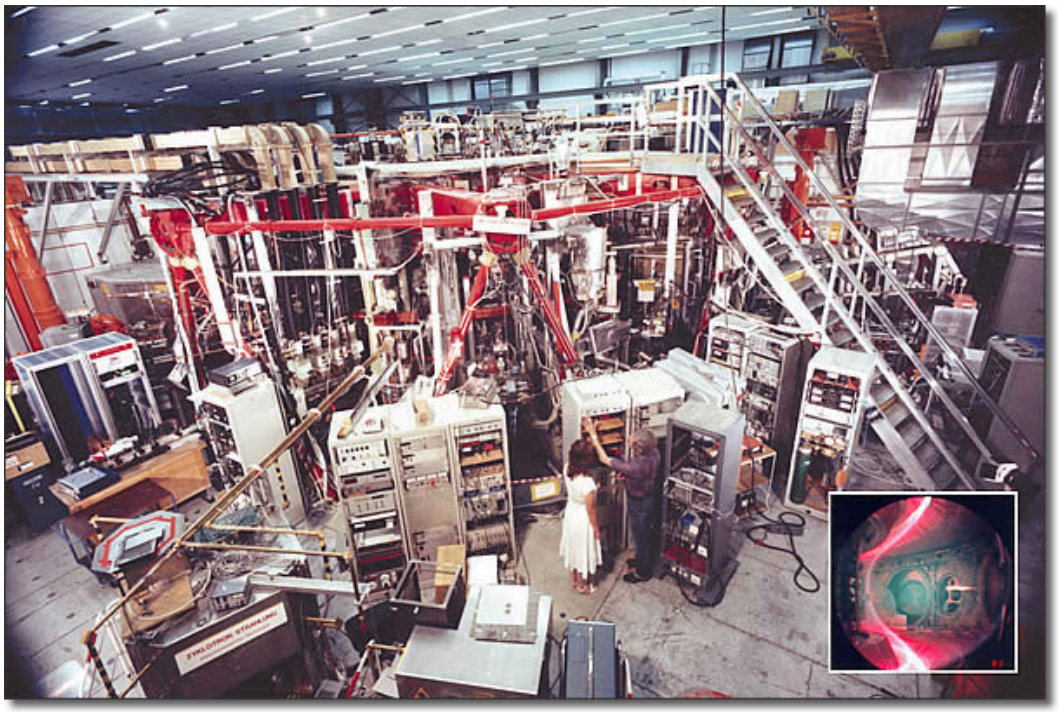

Figure 2.1: Outside of the original ASDEX tokamak where H-mode was first observed—photo from www.tokamak.info

theme amongst all of these examples was the development of an edge radial electric field and thus an edge flow and flow shear [11, 12].

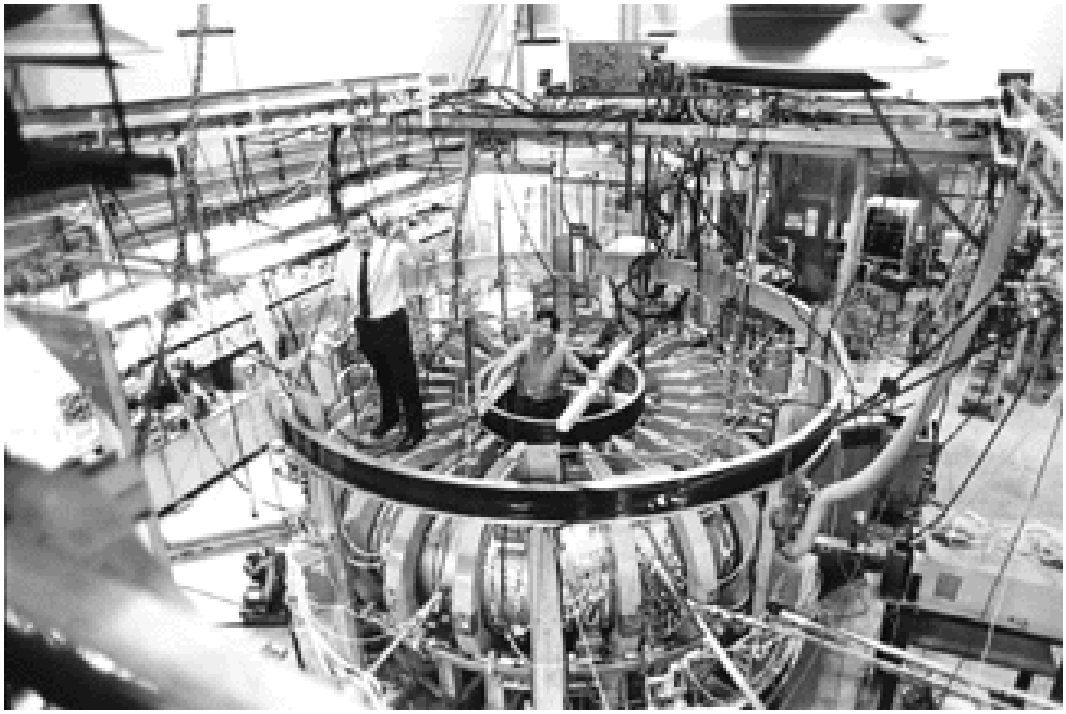

Figure 2.2: Outside of the Continuous Current Tokamak (CCT) built at UCLA in 1986—photo from www.seas.ucla.edu/hsseas/history/

Concurrently with the H-mode studies, other experiments began to show a connection between edge radial electric field and the confinement state of the plasma such as on the Macrotor at UCLA in 1982 [13] and the Russian tokamak TV-1 in 1985 [14]. In fact experiments predating the H-mode discovery—such as by Taylor and Oren in 1979 on the Macrotor tokamak [15], which showed changes in impurity flux modified electric field—anticipated the role electric field played in the newly discovered confinement phenomenon. Detailed limiter biasing experiments on TEXT [16] showed increased density confinement for voltages at least 50V away from ground (either positive or negative) and decreased turbulent particle flux for negative biases (though not for positive). Experiments on the Continuous Current Tokamak at UCLA [17] showed a similar response of confinement with biasing, but moreover noted that the electric fields observed are associated with poloidal rotation and that this rotation

is driven by the torque due to radial currents (that is, the measured electric fields are due to cross-field currents rather than cross-field current due to an induced electric field). Distinct from the so-called spontaneous H-mode observed through heat injection, these driven H-mode biasing experiments sought to understand the mechanisms behind the L-H transition through controlled manipulation of the plasma flow and flow shear. Since flow and flow shear appeared to be fundamental to improved confinement, these experiments also represented a push to understand just how this flow and/or flow shear contributed to reduced transport [18].

As research into the connections among flow, flow shear and confinement states were being made, focus on the nature of turbulence and transport was also being investigated experimentally in fusion devices [19–23]. These works, and many other showed that particle transport was caused by fluctuations, often called anomalous transport, and that transport was dominated by this type of particle loss rather than a collision form called classical transport. Both models are discussed later in this chapter.

Biasing experiments also began to explore not just how flow and shear affected global confinement but how the plasma turbulence itself was modified and suppressed and how, in turn, this suppression resulted in reduction of particle and heat flux. Biasing experiments on CCT showed a reduction in convection and turbulent particle flux in the device edge region [24]. Biasing experiments on the Tokamak Experiment for Technically Oriented Research or TEXTOR has shown improved confinement for states with both inward and outward pointing electric fields [25, 26], that there was a connection between $E \times B$ flow shear and confinement improvement [27, 28], and that changes occur in density, electric field and temperature fluctuations and crossphase with sheared flow [29–31]. Turbulence suppression with biasing have also been investigated on CASTOR [32], ISSTOK [33, 34], MST RFP [35], RFX RFP [36] and T10 [37]. Turbulence suppression biasing studies have also been attempted on linear plasma devices such as the HIEI Tandem Mirror [5] and most recently before the research presented in this dissertation, on the LAPD [38, 39].

2.2 Turbulence, Transport and Shear

Though there has been ample evidence demonstrating a correlation between increased flow, flow shear and turbulence/transport reduction, the precise physical mechanism governing this process has not been definitively determined. Various theoretical models have been proposed to explain the apparent connection between flow and transport. One of the most common is the so-called "decorrelation" model of shear suppression which suggests that the sheared flow tends to break up turbulent eddies in the plasma and consequently reduce the amplitude of fluctuations. A more in-depth review of various decorrelation models is made in Chapter 7. However, many other proposed mechanisms for this damping of turbulence and transport exist including coupling to fluctuating flows called zonal flows [40], coupling to damped eigenmodes [41], a shear-induced shift in wavenumber spectra [42], and changes in deterministic chaos [43–45].

The issue remains that though observation of suppression of turbulence and transport has been made on a myriad of plasma devices, the level of detail in these measurements has not been particularly high and there is much need for continued rotation experimentation especially for validation of the various suppression models.

2.2.1 The Role of Rotation Experiments on LAPD

The LAPD provides a useful testbed for the continuation of research into the role of flow and flow shear in turbulence and transport modification. As a linear device with a fairly low-temperature plasma, it offers high diagnostic accessibility over fusion devices but its size facilitates the development of broadband turbulence more typical of fusion tokamaks or stellerators. With the installation of biasable limiters, the ability to very carefully control the level of flow and flow shear has been achieved including the ability to reduce and nearly null out flow entirely. This dissertation presents the results of these initial limiter biasing experiments and attempts to track the changes in turbulence and transport on the device that occur with fine changes in flow and flow shear.

The next section of this chapter will review the basic concepts involved in the study of flows, turbulence and transport focusing mainly on aspects of these concepts relevant to a linear plasma device (i.e. how transport works in a solenoid rather than toroidal field), though some discussion will involve fairly general topics.

2.3 Plasma Flows

Since plasma flows form a fundamental underpinning of these dissertation, it is worthwhile to look at the origin of basic flows in a linear, magnetized environment such as that found in LAPD. A charged particle in a magnetic field will move freely (or ballistically) in directions parallel to the magnetic field line, while be restricted to circular gyration motion around a guiding center in the perpendicular plane. Thus, any fluid flows in the parallel direction would be due to overall force balance of parallel electric fields and frictional type forces. For LAPD, bulk plasma flows in the parallel direction do not play a significant role though parallel electron flows are important in the development of drift instabilities. In the perpendicular plane, there are three types of flows that can develop in a system with constant and straight magnetic field lines (that is, no magnetic curvature): $E \times B$ drift, diamagnetic drift, and polarization drift. In the context of this disseration, the $E \times B$ drift is the most important and is discussed in more detail.

2.3.1 ExB Drift

From a single particle point of view, $E \times B$ drift arises due to the interplay of the linear acceleration due to an electric field, and the centripetal acceleration due to the magnetic field. A charged particle gyrating in a constant magnetic field will have a Larmor radius, $r_L = mv_\perp/|q|B$. If a constant electric field is applied perpendicular to the magnetic field, the particle will initially be accelerated in one direction along the electric field, causing its velocity to increase. This in turn will result in a slightly larger Larmor radius which means the particle will traverse a slightly larger distance in the $E \times B$ direction then it would have

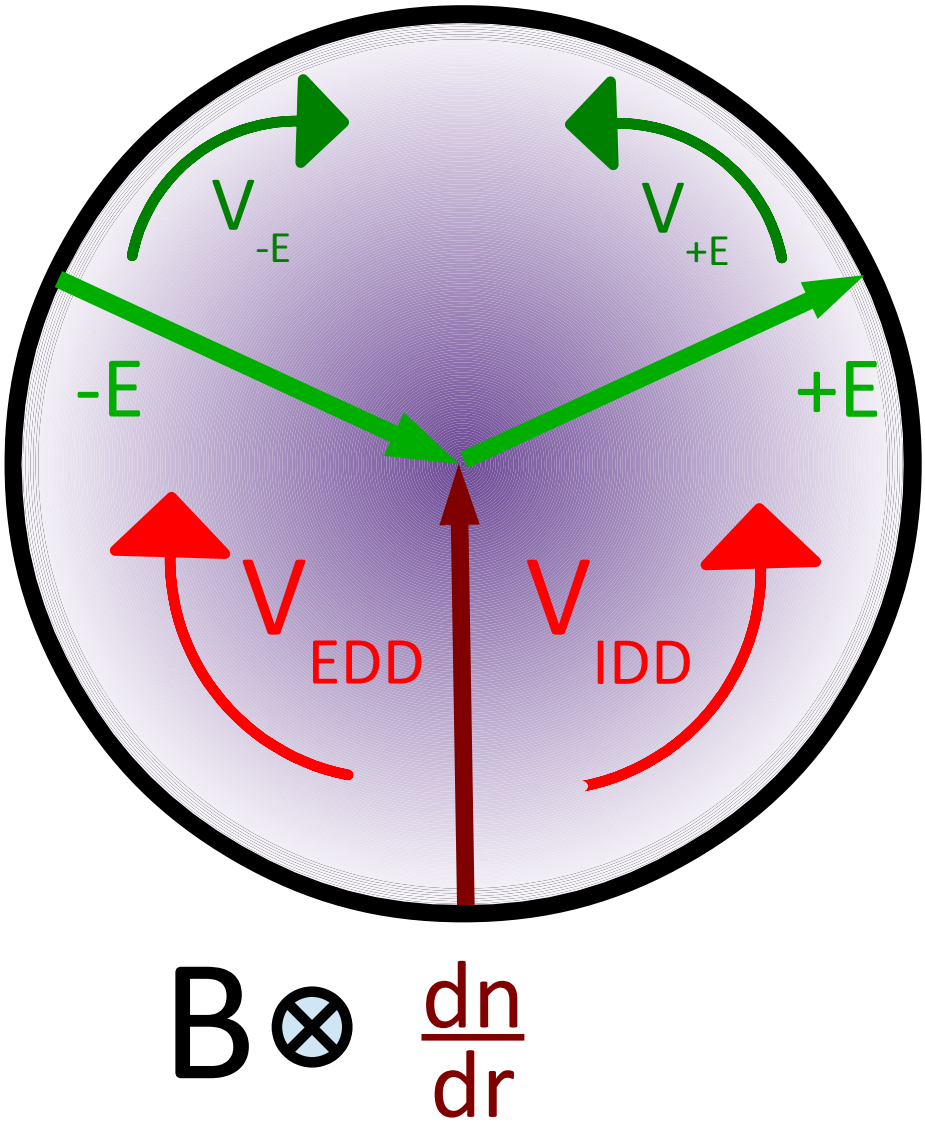

Figure 2.3: Summary of drift directions for LAPD

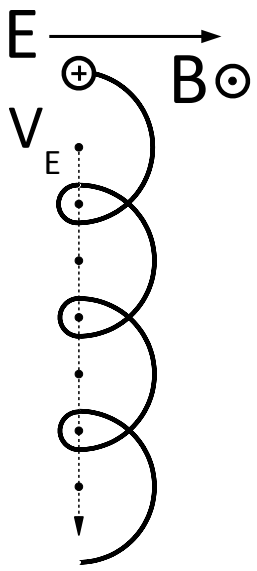

Figure 2.4: Summary of drift directions for LAPD

without the added electric field acceleration. As the particle returns in its orbit to motion along the the electric field, it is now decelerated and consequently has a smaller Larmor radius than its initial radius for the second half of the cycle. The particle moves only a slight distance in the -$E \times B$ direction, whereas without the electric field, it would have returned to its starting position. The cycle repeats itself, but now with the initial point moved a distance $v_E \tau_c$ where τ_c is the gyroperiod and v_E is defined as the $E \times B$ drift velocity of the the guiding center. An expression for v_E can be derived by taking the equation of motion

$$\frac{m}{q}\frac{d\mathbf{v}}{dt} = \mathbf{E} + \mathbf{v} \times \mathbf{B} \tag{2.1}$$

and assuming that the entire left side can be zero as this part is what determines the gyro motion of the particle. Then, taking the cross-product of the remaining part with B and assuming that any remaining velocity is v_E yields

$$\mathbf{B} \times (\mathbf{E} + \mathbf{v}_E \times \mathbf{B}) = \mathbf{E} \times \mathbf{B} + v_E B^2 - \mathbf{B}(\mathbf{v}_E \cdot \mathbf{B}) = 0 \tag{2.2}$$

which, since v_E is assumed perpendicular to B finally gives for v_E

$$\mathbf{v}_E = \frac{\mathbf{E} \times \mathbf{B}}{B^2} \tag{2.3}$$

For LAPD, where the applied electric field will be exactly perpendicular to the magnetic field, $\mathbf{v}_E = c\mathbf{E}/B$ in cm/s for CGS units. Though the above derivation was applied to a single charged particle, it can easily be extended to a full plasmas by noting that the expression does not include the sign of the charge, the mass of the particles or the kinetic energy of the particles in question. Charge is unimportant since the sign will only flip which half of a period the particle is being accelerated or decelerated. It can be shown that particles of different mass will still drift in the same direction at the same rate because while a larger particle will tend to have a larger Larmor radius and cover a larger displacement for each gyroperiod, a smaller particle will gyrate at a higher frequency and the two effects cancel out. Similarly, for particles of different energy, the larger fractional change in Larmor radius for slower particles will be canceled out by a smaller change in the already larger Larmor radius of the faster particles.

Ultimately then, the $E \times B$ bulk flow for a plasma will depend only on the direction of the electric field (and technically magnetic field as well, though on LAPD this direction is constant.)

2.3.2 General Force Drift and Diamagnetic Drift

The $E \times B$ drift equation can be generalized for any force, F as

$$v_D = \frac{-F \times B}{qB^2} \tag{2.4}$$

where q charge. $E \times B$ is found by setting $F = qE$, which cancels out the sign of the charge recovering a drift that is in the same direction for both electrons and ions. The force, F, could really be any external force including gravity or the centrifugal force (which will be important for consideration of the rotational interchange mode). These forces, though, do not depend on charge so electrons and ions will drift in opposite directions. These drifts can be considered in both a single particle point of view or in a fluid point of view since all these forces considered can be seen in both ways as well. However, a force need not be valid on a single particle scale to produce a drift. The force defined as the gradient in pressure,

$F = \nabla p$, where $= nT$, is a purely fluid force, yet a drift based on this force, called the diamagnetic drift, can be defined as,

$$v_{dia} = \frac{-\nabla p \times B}{qnB^2} \tag{2.5}$$

In a magnetized plasma, from a single particle point of view, the drift is not a real drift in the sense that particles are moving from one location to another. However, from a fluid point of view, the drift is real as a fluid element would be technically exhibit motion in a certain direction. This is illustrated by Figure 2.5 which shows gyrating particles in a density gradient. A fluid element is represented by the dashed box; its overall motion would be the average motion of the particles inside it. Since the particles are gyrating about a center, the fluid element contains some particles moving upward and some moving downward. If the density were constant, the average motion of the fluid element would be zero. However, because of the density decrease across the fluid element, there are on average more particles moving downward than upward. The diamagnetic drift is not nearly as important as $E \times B$ drifts, which is actual particle motion, but does play a role in drift wave physics and in measurements of flow using a Mach probe which will be discussed in Chapter 3. Diamagnetic drifts in this experiment are about an order of magnitude less than those $E \times B$ flows observed ($\sim 10^5 vs. 10^4$ cm/s).

2.4 Diffusion: Classical and Bohm

In the most general sense, transport is the movement of plasma from one region to another; from a fluid point of view, the processes involved can be divided into two main avenues: plasm flow and plasma diffusion. Though both avenues ultimately involve the motion of particles, they differ in that one—flow—is a direct motion while the other—diffusion—is motion in a statistically averaged sense. The flows discussed in the previous section, namely $E \times B$ flow and free-streaming flow along magnetic field lines—constitute a type of transport; however, this transport is generally not of interest in the fusion related problem of plasma confinement. (Granted parallel flows on LAPD are an avenue for loss of plasma out of the

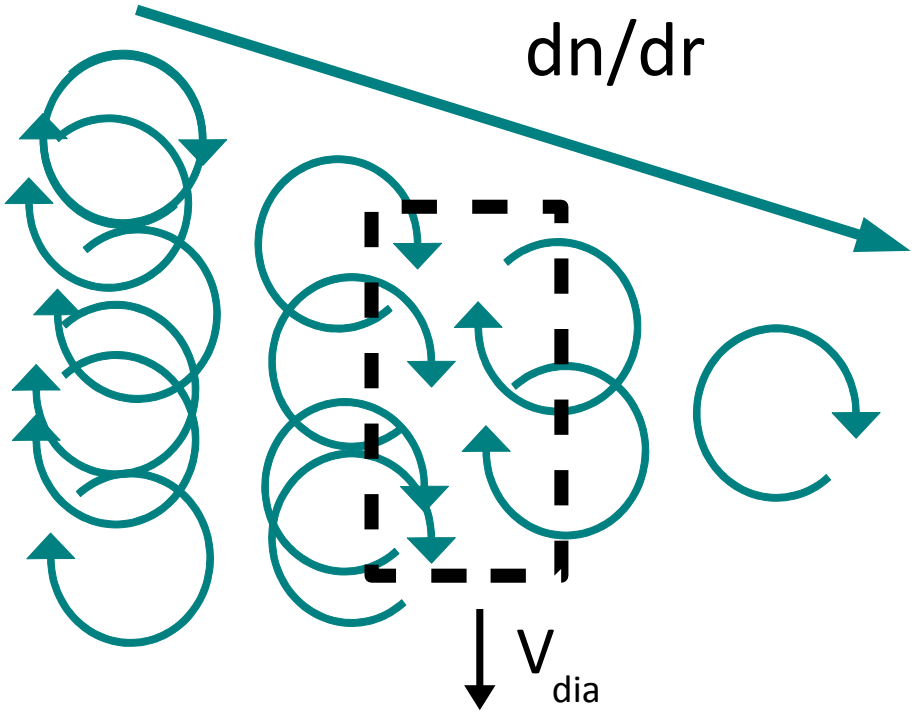

Figure 2.5: Physical representation of diamagnetic drift

system, but this is an issue unique to linear devices.) Of more importance is the transport due to diffusion perpendicular to confining magnetic field lines. The question that summarizes this transport problem is: How are plasma particles able to move across field lines and why do the do so at a rate higher than generally expected?

Note, the notion of energy transport is associated with particle transport but is not necessarily directly connected; though the energy of a plasma is essentially the thermal energy of the particles, there can be situations where a plasma has significant energy or particle transport, but not the other, especially when broken down into directions parallel or perpendicular to a magnetic field. Though the detailed processes involved in energy transport will not be addressed here, there are some important effects on LAPD involving the differences between particle and energy transport which will be discussed in Chapter 3.

A review of what the generally expected diffusion rates are in a magnetized plasma is first presented here and then followed-up with the experimental observations that defy these expectations along with some theories which attempt to explain these deviations.

The process of particle diffusion defined as the statistical change in concentration between two adjacent regions of different concentrations. Obviously, this diffusion is generally—that is, the diffusion can be, for example, that of molecules of a neutral gas of higher density gradually moving into a region lacking the gas entirely. The processes is statistical because it is governed by a random walk process. If the neutral particles in the previous example had no motion whatsoever, the diffusion could not proceed as the system lacks the motion, and consequent collisions, which would facilitate any dynamic changes. The random-walk collisions between the particle over time causes a redistribution in the concentration; though each step a particle takes has an equal chance of being toward the region of high concentration or low concentration, the difference in concentration itself means there are numerically more steps from the high concentration to the low concentration region and vice-versa. The process continues until the concentrations and asymmetries are equalized. Mathematically, this process can be represented by a relationship between particle flux—the number of particles passing through an area per time—and the magnitude of the concentration difference,

represented by the gradient in the concentration, ∇n, as

$$\Gamma_p = -D\nabla n \tag{2.6}$$

where the quantity D is the diffusion coeffiecent or diffusivity and represents the physics of the particular transport process. The negative sign indicates that the change in concentration goes high to low regions. The diffusivity is not necessarily a numerical constant; however, if it is, as is likely in the simple case of the neutral gas molecules above, the above equation is called Fick's Law. The units of diffusivity (m^2/s) reflect the random-walk nature of the process—between each random-walk collision a particle to move on average a distance Δd and the frequency of such collisions $\nu = \Delta t^{-1}$ indicates how often these random steps occur. Thus the diffusion can increase given a larger step-size and larger frequency of collisions or decrease for smaller step-size and frequency quantities. The step-size and frequency of collisions is dependent on the physical nature of the system and it is often useful to approximate the general diffusivity of a system as

$$D = \frac{(\Delta x)^2}{\Delta t} \tag{2.7}$$

where Δx is the predominant step size for interactions of the system and $Deltat$ the predominant time-step for this interaction. For a simple system like the neutral gas, there is only one possible step-size—the average distance a particle travels between collisions, called the mean free path—and one collision frequency—the average time between collisions of molecules. Assuming these values are not dependent on the concentration, at least for a range of concentrations, then the diffusivity is constant and the system will follow Fick's Law.

In a plasma, the interaction physics between particles can be vastly different and consequently the diffusion is likely to be more complicated. However, it is still physically reasonable to simplify the diffusion process into a quantity that involves a step size and a time step. The first major difference is that rather than neutral particles, the plasma has charged particles which do not have billiard-ball like ballistic collisions like the neutral gas molecules, but have Coulomb collisions due to the respective electric fields of each particle. This has

implications for the collision frequency part of diffusion as Coulomb collisions are strongly modified by the temperature of thermal energy of the particles; the Coulombic cross-section goes as, $\sigma \sim v_{th}^{-4}$, where v_{th} is the thermal velocity—thus, collision frequency actually decreases between more energetic particles. Other complications arise due to the fact that most quasineutral plasmas consist both ions and electrons of vastly different masses, as well as neutral gas particles if the plasma is not fully ionized. Then, there is the added complication that arises due to a magnetic field. It is helpful then, to look separately at diffusion in different regimes: first, diffusion parallel and perpendicular to magnetic fields, and second, for fully and partially ionized plasmas.

2.4.1 Parallel Diffusion

Again, it is useful to refer to how step-size and time step changes. For particles in moving the parallel direction (or similarly for unmagnetized plasmas), the process regulating step-size and time-step is the likelihood of collisions between particles. The step-size is the mean free path can be defined as the inverse product of density and cross-section,

$$\lambda = \frac{1}{n\sigma} \tag{2.8}$$

and the time-step is the inverse collision frequency,

$$\tau = nu^{-1} = \frac{1}{n\sigma v} \tag{2.9}$$

where again σ is the collision cross section, n is particle density, and v is the particle velocity. This yields a general diffusivity as

$$D = \frac{(\Delta x)^2}{\Delta t} = \frac{1}{(n\sigma)^2}(n\sigma v) = \frac{v}{n\sigma} \tag{2.10}$$

This demonstrates that, in general, diffusivity is proportional to the velocity of the particles, and inversely proportional to the density and cross-section. Physically, this shows that diffusion is increased by the motion of particles, but decreased by the number and likelihood of collisions. This remains true for plasma particles moving parallel to a magnetic field. It

is convenient to recast the form of the diffusivity in 2.10 in terms of a particle temperature and collision frequency,

$$D = \frac{v}{n\sigma} = \frac{v^2}{n\sigma v} \sim \frac{T_e}{m\nu} \tag{2.11}$$

The form of the collision frequency depends on the ionization state of the plasma. For partially ionized plasmas, the collisions between electrons or ions with neutral gas molecules will dominate so the important collision frequency of the system is

$$\nu_{n\alpha} = n_n \sigma_{n\alpha} \sqrt{\frac{T_\alpha}{m_\alpha}} \tag{2.12}$$

for either species, α and where n_n is the neutral gas density and $\sigma n\alpha$ is the collision cross-section between each species and the neutral species respectively. The cross-section between electrons or ions and neutral particles does not vary significantly and can be approximated by $5 \times 10^{-15} cm^2$ [46]so that assuming relatively equal temperatures, the dominant differing quantity is mass. In the parallel direction, electrons have a significantly higher diffusion rate then do ions. For large enough plasmas (generally $\lambda_D << L$), this will result in a charge separation and the formation of ambipolar diffusion, but that will be discussed in a later section.

In a fully ionized plasma, the only collisions possible are Coulombic—that is, between electrons and ions. Compared to the partially ionized state, the cross-section of collisions is significantly different. From Chen [47], the cross-section for large-angle deflection collisions ($> 90°$) between ions and electrons can be approximated as

$$\sigma_{ei} \sim \frac{1}{m^2 v^3} \tag{2.13}$$

where m and v are the electron mass and thermal velocity respectively which shows that parallel diffusion generally greatly increases with temperature.

2.4.2 Perpendicular Diffusion

The evaluation of perpendicular diffusion in a plasma can again be started by estimating a step-size and time-step for the random walk of particles. For parallel diffusion the step-size

between collisions was consistent with the mean free path between collisions. Particles with motion perpendicular to the magnetic field will gyrate around a point called the gyro center. It can be shown that for collisions between like particles, the gyro center moves a distance about the length of the Larmor radius, r_L. This r_L serves as the step-size in the estimation for perpendicular diffusion instead of λ. Thus, assuming a time-step equal to the inverse of the collision frequency present in the system,

$$D_\perp = \frac{(\Delta x)^2}{\Delta t} = \frac{r_L^2}{\tau} = r_L^2 \nu \tag{2.14}$$

where clearly, unlike parallel diffusion, the perpendicular diffusion actually increases with collision frequency. This is clear physically because without collisions, a particle will remain in its gyro orbit. This relationship can be derived more rigorously using a force balance argument [47] but the form he is presented for its physical clarity. Rewriting the diffusivity in more plasma relevant parameters yields,

$$D_\perp = r_L^2 \nu \sim \frac{(mv)^2}{B^2}\nu = \frac{mT\nu}{B^2} \tag{2.15}$$

which shows that perpendicular diffusivity is inversely proportional to the square of the confining magnetic field. The dependence on temperature, however, ultimately depends on the ionization level. For partial ionization where neutral collisions are dominant, $D_{perp} \sim T^{3/2}$, since $\nu_{n\alpha} \sim T^{1/2}$. In fully ionized plasma (or in highly ionized plasmas like LAPD when ionization is $> 50\%$), the ion-electron collisions are dominant. This means that $D_\perp \sim T^{-1/2}$ since $\nu_{ei} \sim T^{-3/2}$. The nature of decreasing cross-section for more energetic particles is thus detetrimental to the ability for particles to collide and diffuse perpendicullary to a magnetic field.

This $1/B^2$ and $1/T^{1/2}$ scaling is extremely important in the realm of plasma confinement as it is indicative of the need for both strong magnetic fields to prevent the loss of particles as well as the need for high temperature plasmas. Diffusion with such as scaling is often referred to as "classical" diffusion. If classical diffusion were true for a wide range of plasma parameters, the plasma confinement problem, and the achievement of fusion energy would be much more easily achieved. However, nature, of course, does not work this simply, and

so deviations from classical diffusion are what ultimately drive the research presented in this dissertation.

2.4.3 Anomalous Diffusion

Work by Bohm, Burhop and Massey in 1946 showed that experimentally measured perpendicular diffusion appeared to be orders of magnitude larger than the models of classical diffusion would seem to predicted; this anomalous diffusion has since also become known as Bohm diffusion based on the empirical formula derived by Bohm et al's research which indicated a diffusion coefficient that scaled as $1/B$ rather than $1/B^2$ as in classical diffusion:

$$D_{Bohm} = \frac{1}{16}\frac{T_e}{B} \tag{2.16}$$

The 1/16 prefactor found by Bohm was not derived from first principles, but has been shown to fit a wide variety of fusion experiments within a factor of two or three. The T_e/B scaling can be heuristically derived by replacing particle collisions as the impetus for random-walk steps with local fluctuating $E \times B$ flows. First let, perpendicular particle flux be written as $\Gamma_p = nv_r$, with $v_r = cE/B$. Then, assuming that the maximum electric field fluctuation goes as,

$$E_{max} = \frac{e\phi_{max}}{L_n} \sim \frac{T_e}{L_n} \tag{2.17}$$

where the maximum plasma potential fluctuation is limited by Debye shielding to be on the order of the electron temperature, and the length scale is limited by the density gradient length scale. Then, the flux is written as,

$$\Gamma_p \sim n\frac{T_e}{L_n}\frac{1}{B} \tag{2.18}$$

where n/L_n can be taken as ∇n which leaves $D \sim \frac{T_e}{B}$.

Anomalous or Bohm diffusion can be further considered as turbulent diffusion as $E \times B$ fluctuations are generally present in turbulent plasmas.

2.5 Relevant Instabilities on a Linear Device

The main instabilities that arise in the edge of a linear device like LAPD consist of a universal instability—the resistive drift instability—an interchange instability—rotational interchange and a third called the Kelvin-Helmholtz. The resistive drift wave arises primarily from the radial density gradient from the plasma source core to the edge and has been shown to couple to shear Alfvén waves [48] forming resistive drift-Alfvén waves. The rotational interchange mode arises from the centrifugal forces due to bulk rotation of the plasma and Kelvin-Helmholtz is driven by sheared flow. All three instabilities can be present in the plasma at the same time and it has been shown in Popovich et al [49] that the growth rates for all three of the instabilities can be comparable on the LAPD.

Given the large size of LAPD, many different azimuthal modes can grow up on these various free-energy sources. These modes interact non-linearly eventually evolving into the state of broadband turbulence observed on LAPD. It has also been shown that non-linear modes themselves can be a primary instability on the LAPD [50], but these modes are beyond the scope of this dissertation.

2.5.1 Resistive Drift Wave Instability

Drift waves can be found to exist in any quasi-neutral magnetized plasma region that has a density gradient. (The gradient can be generalized to a pressure gradient where $p = nt$ for an isothermal plasma, but for simplicity of description only a density gradient is considered here.) Consider a small perturbation in the plasma consisting of small, evenly spaced fluctuations in density. If the electrons are assumed to follow a Boltzman distribution such that

$$\frac{\tilde{n}}{n_0} = \frac{\tilde{\phi}}{T_e} \tag{2.19}$$

the resulting potential variation produces electric fields that then drive $E \times B$ flow. If nothing restricts the electrons from the Boltzman response (i.e. no collisions, viscosity, etc.), then the $E \times B$ flow produced tends to push the displaced density in such a way that the perturbation

propagates in the direction perpendicular to both the initial density gradient direction and the magnetic field. In this case, the wave is stable and can be shown to propagate at a velocity equal to the electron diamagnetic drift velocity,

$$v_{De} = \frac{T_e}{B}\frac{\nabla n}{n} \tag{2.20}$$

giving the drift wave its name. If the parallel motion of the electrons is restricted in some way, such as from the collisionality of electrons on the ions, ν_{ei}, the phase between density and the generated electric field is shifted. Rather than merely pushing density to maintain the wave, the $E \times B$ flow tends to reinforce the perturbation, increasing the amplitude of the mode. The parallel resistivity caused by the ν_{in} allows the free energy in the density gradient to be extracted by the resistive drift wave instability. Drift waves are characterized by density and radial velocity fluctuations that at or near 90^{circ} out of phase (or by density and plasma potential fluctuations that are or nearly are completely in phase).

It should be emphasized that the distinguishing element of drift waves is the motion of the electrons parallel to the magnetic field. Consider again a perturbation in the density—say a bulge of density from a high density to a lower density region. A charge imbalance could develop within this perturbation if a force (other than electric field) were to cause drifts that would tend to separate electron and ion populations. One possible force, the pressure gradient, could drive diamagnetic drifts which could separate charge, but since the density gradient is always perpendicular to lines of constant density, a charge imbalance cannot build up anywhere along the perturbation. Thus, in the absence of any other force but the pressure or density gradient, any charge imbalance can only develop parallel to the field lines. Thus, drift waves can only be present in systems that have a finite parallel variation. In other words, drift waves must have a finite parallel wavelength. This is in contrast with the next two modes discussed which have no such requirement.

2.5.2 Rotational Interchange Instability

The rotational interchange instability can be found where a centrifugal force is present; for these cylindrical based experiments, this can be at any radial point where plasma rotation exists. As suggested in the previous section, a charge imbalance can develop in a perturbation when a force causes electrons and ions to drift in opposite directions. Unlike the pressure force, the centrifugal force caused by the column rotation is not restricted to the lines of constant density in a perturbation and thus can cause a charge imbalance to develop. This charge separation leads to the development of electric fields which can cause $E \times B$ flows to reinforce the perturbation in a similar manner as described for drift waves. The main difference here is that for rotational interchange modes to be unstable, the density fluctuations and potential must be between 45-90° out of phase, rather than nearly in phase. Also, since modes can grow from charge separation in the plane of the perturbation, the parallel dynamics need not come into play. The rotational interchange mode then can have an infinite parallel wavelength (known as flute modes). However, parallel electron motion can come into play as well, allowing interchange modes to couple to drift waves.

2.5.3 Kelvin-Helmholtz

The final mode type covered here is the Kelvin-Helmholtz mode. This mode arises in regions of sheared flow–at an interface where flow on one side is moving at a different velocity than flow on the other side. If there is a perturbation on this interface, such that plasma at one velocity enters a region of plasma at another velocity, the difference in rate can cause the slower plasma to be curled over onto itself. This process causes vortices of plasma to form as the two plasma regions mix. Like the rotational interchange mode, the KH mode can be a flute mode. It can be shown [51] that the growth of the KH mode can be associated with high plasma potential fluctuations and gradients in vorticity, defined as $\varpi = \nabla \times v$. Vorticity can be measured using Langmuir probes and is discussed in Chapter 3.

This chapter summarized the motivation for pursuing rotation experiments on LAPD as

well as lay a foundation for the physics concepts involved. The next section introduces the experimental device, the Large Plasma Device, as well as the primary diagnostics used for the biasing experiments.

CHAPTER 3

LAPD and Diagnostics

This chapter introduces the Large Plasma Device and the features which make it particularly useful for investigation into plasma turbulence. Then the primary diagnostics used for this dissertation are discussed as well as the techniques and formulas used to extract plasma parameters from probe signals. Detailed experimental conditions are also listed throughout this section.

3.1 The Large Plasma Device

The Large Plasma Device Upgrade (LAPD-U)[52] provides an extremely useful testbed for the study of turbulence and transport. It combines the ability to produce plasma at the size and scale of many fusion machines with the volumetric diagnostic accessibility of a linear device. While the plasma densities and temperatures are generally smaller than that of fusion level plasmas, the large axial and radial sizes allow for the growth of many modes, which can interact and develop into a broadband turbulent system. Moreover, the size and magnetization allow for ratios of the ion gyroradius or ion sound radius to the system size (ρ_i/a or ρ_s/a) to be on the order of that found on fusion tokamaks, ($\sim 1/100$ to $1/300$). Thus, the LAPD offers the opportunity to study basic turbulent processes, yet still have the ability to be relevant for turbulence and transport understanding on fusion-level devices [53, 54].

As indicated in Figure 3.1, the LAPD consists of a cylindrical vacuum chamber that is 20.7m from end to end and has an inner diameter of about 1m. An array of 90 magnetic coils produces a solenoidal magnetic field 17.54m long down the center of the chamber, just

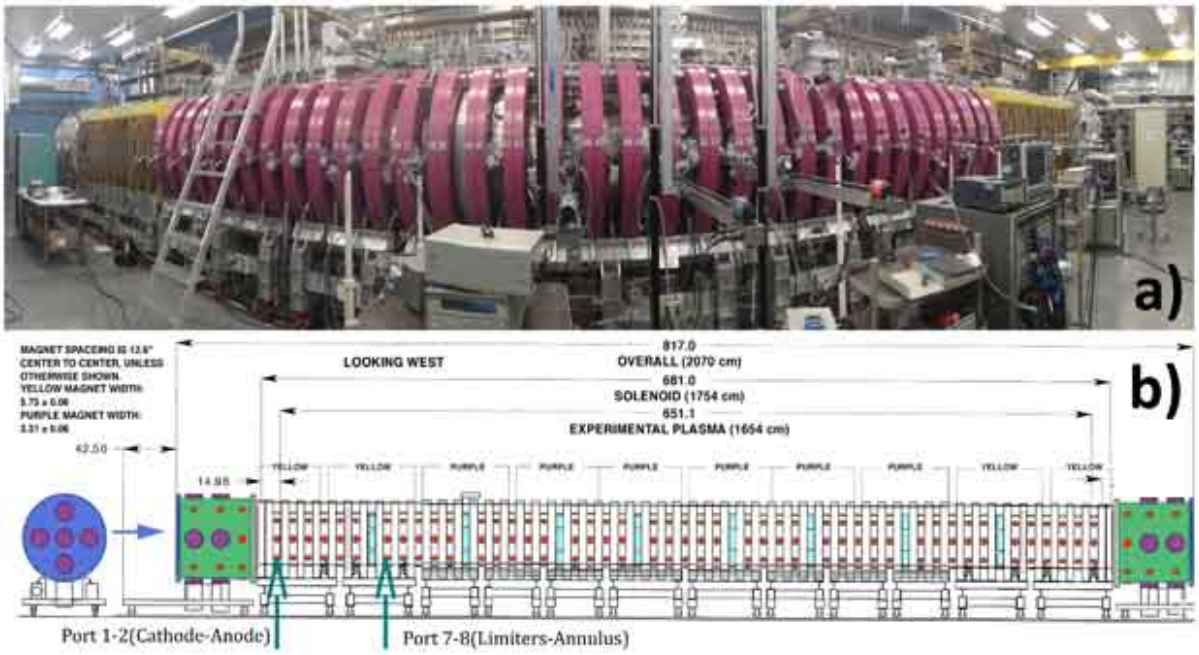

Figure 3.1: (a)Panoramic photo of the Large Plasma Device (using Fish-Eye-like lens) and (b)Diagram of the LAPD indicating relevant lengths and the position of the anode-cathode source as well as the limiters.

in-between the two end bell sections of the chamber. The magnets are divided and controlled by ten separate power supplies which can be individually set to different currents to produce non-uniform magnetic fields, though for these experiments the magnets were set to provide a uniform solenoidal field between 400 and 1800G. The coils are spaced at 32cm from center to center and produce a magnetic ripple of $\sim 0.1\%$. From left to right in Figure 3.1, the access ports are the sections of three red circles, starting just inside the left end-bell (green) and are labeled from Port 1 to Port 45; like the magnetic coils, they are separated by 32cm center to center. These ports numbers will often be referred to throughout this dissertation to indicate the positions of the source, the limiters or the probes and diagnostics.

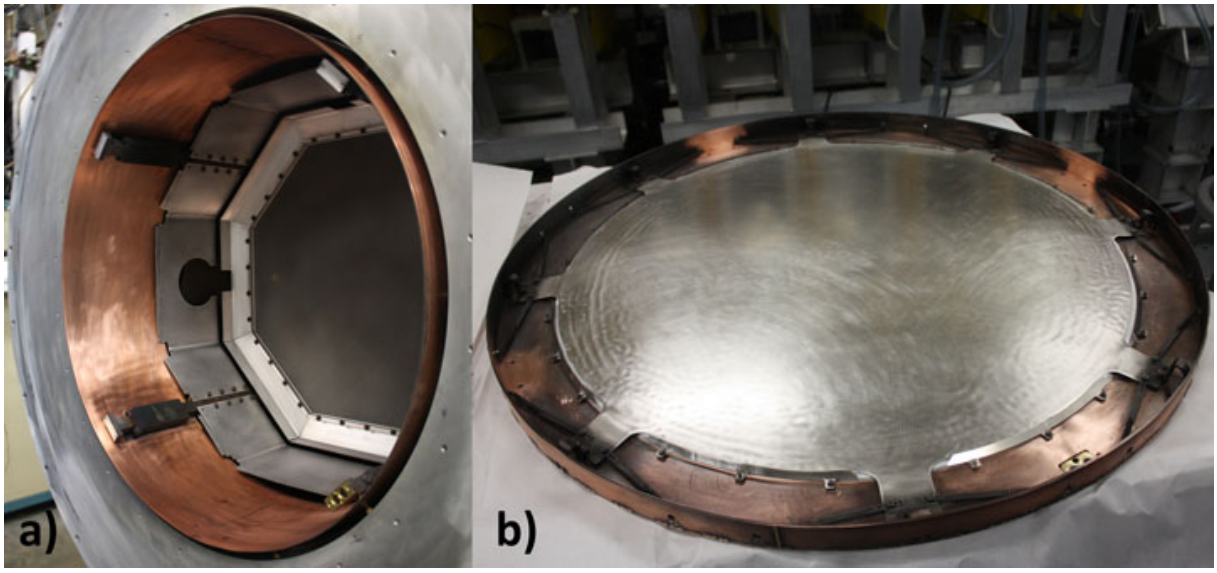

Figure 3.2: (a)The molybdenum mesh anode installed in the vacuum chamber and (b)the nickel cathode (without the barium oxide coating) shown extracted from the vacuum chamber.

The chamber is pumped down to a base pressure of about 5×10^{-8} Torr using 1500 liter/s turbo pumps, one attached to each end-bell section. It is then filled with a background gas (H_2, He, Ne, or Ar) using a mass-flow controller to a pressure of about 3×10^{-5} Torr. A plasma is produced inside the chamber using an electron beam created by a cathode-anode discharge. Located at port 1, the cathode source Figure 3.2(b) consists of a 70cm

diameter nickel plate that has a 60cm diameter coating of a barium oxide mixture on one side. When heated to 900°C by a graphite heater located just behind the cathode plate, the nickel/barium-oxide combination has a low work function which allows electrons to be thermally excited off the plate. Ahead about 30cm axially down the chamber, near port 2, an octagonal, molybdenum mesh anode, Figure 3.2(a), is located. A 60-70V potential between the anode and cathode is established using a 4-Farad capacitor bank and pulsed for between 10 and 20ms by an IGBT transistor switch, which causes the thermal electronics to be accelerated from the cathode source past the anode and into the remaining plasma chamber. The discharge current can be directly controlled and is set to be in the range of 2 to 5kA; since the anode mesh is about 50% transparent, approximately half of this dischrage current is absorbed by the anode while the other half forms an electron beam with an energy of about 50eV and a diameter of 54cm (the 60cm nickel/barium oxide source is mapped to a 54cm wide circle by an increasing magnetic field between the cathode region and the main plasma chamber region). The primary electrons in this beam initially ionize the fill gas producing thermal electrons of about 6-10eV which then continue to ionize the gas. Approximately 50% of the fill gas is ionized creating a steady-state plasma density of 1 to $5 \times 10^{12}\text{cm}^{-3}$. This level of plasma density exisits during the 10-20ms of the discharge (called the active phase) and measurements are typically taken in the last 5ms or so of the discharge when the plasma has reached steady-state. Once the heating source is stopped, the electron temperature drops immediately to non-ionizing values, though some plasma can persist for tens to hundreds of ms before diffusing to the walls and recombining; this phase is called the after-glow. This discharge can be repeated at 1Hz. Given the position of the anode, the length of the plasma beam can be estimated to be 16.54m from the end of the anode to the end of the solenoid.

At the far end of the machine, another mesh anode is attached to a hinge and can be rotated into the chamber to serve as an end boundary condition. Without the mesh, the plasma follow the field lines, which diverge beyond the last magnetic coil and eventually hit the chamber wall somewhere within the far end-bell. It will be shown in this dissertation

that any effect of differences in the end boundary condition was mostly non-existent. Thus, the far end boundary was generally not incorporated in these experiments especially for campaigns where the fast-framing camera (situated at the window at the far end) was used in order to avoid obstructing the camera view.

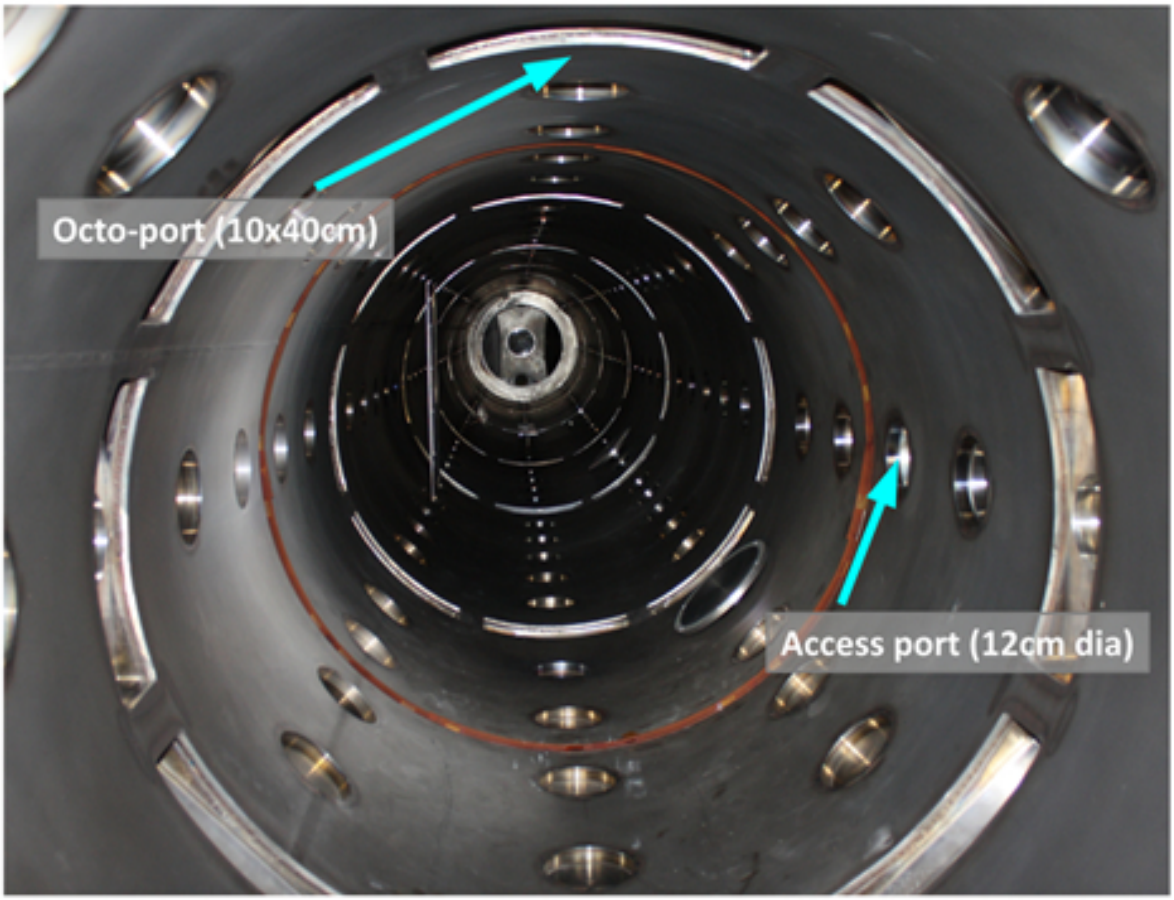

Figure 3.3: The inner chamber of the LAPD showing the many access ports and octo-ports for diagnostics.

Between each magnet loop are eight, 12cm diameter access ports and spaced periodically down the machine are sets of eight 10x40cm rectangular ports called octo-ports as shown in Figure 3.3. These ports allow access for diagnostic probes through vacuum feed-throughs or interlocks using standard KF40 or KF50 connectors as can be seen in Figure 3.4. These feed-throughs are mounted on a ball-joint which allows a probe to be moved in the x, y or z direction while inside the machine. The probes can be precisely positioned by stepper

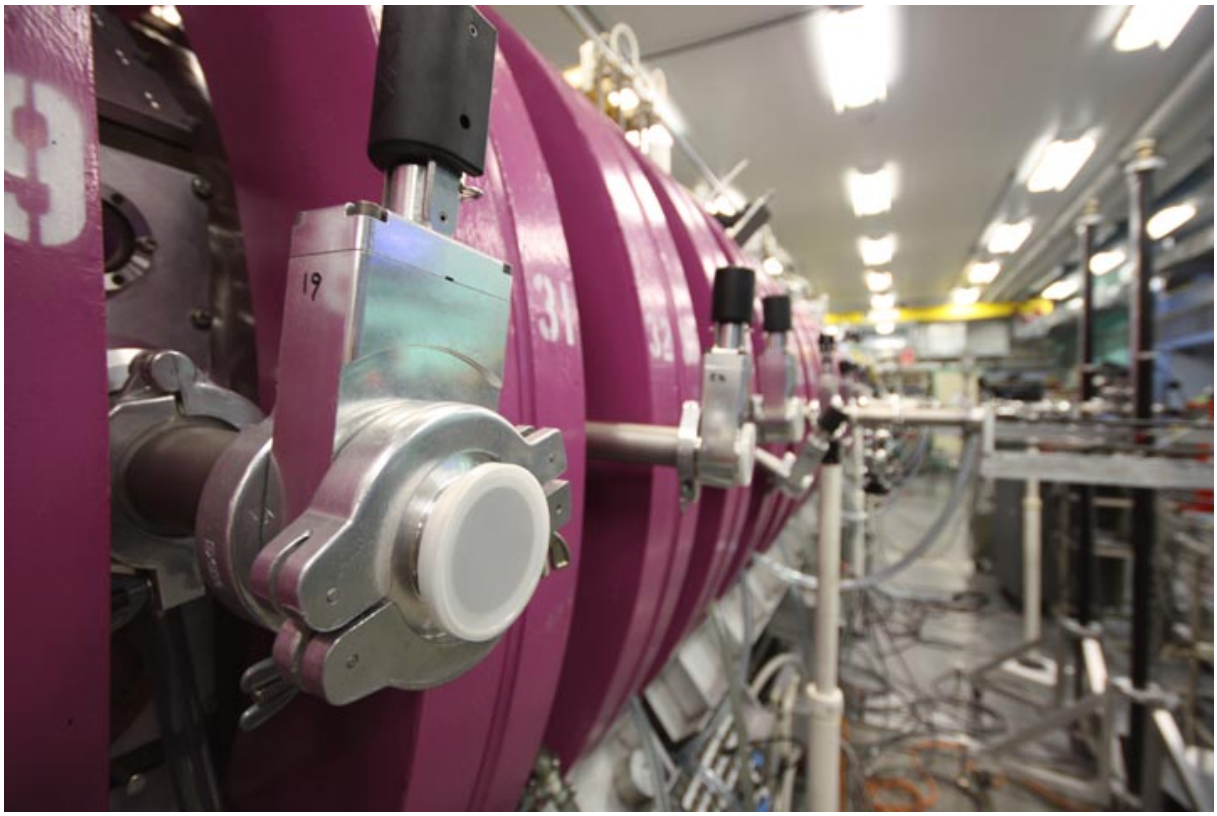

Figure 3.4: Close-up of a typical vacuum feed-through for insertion of a diagnostic probe.

Table 3.1: Control Parameters of the LAPD for this dataset. Note that the neutral pressure takes into account the calibration factor of 0.18 for helium in an ion-gauge.

Parameter	Value
Core Density	$1.5\times10^{12}\text{cm}^{-3}$
Neutral Pressure	1.28×10^{-4}Torr
Discharge Current	$\sim$ 3.5kA
Magnetic Field	1000G
Discharge Length	15ms

motor drives whose motion can be automated by computer. The probes are first pumped down using cryogenic pump-down stations to a base pressure of 1×10^{-6} Torr before being opened to the main chamber through the vacuum interlocks. This allows for the insertion and removal of probes without having to bring the entire chamber up to air. The heated barium oxide coating is extremely sensitive to oxidation and can be poisoned by an air leak; thus, maintaining vacuum is of utmost priority on LAPD.

Windows can also be placed in the access ports for passive or light based diagnostics such as interferometers, spectral analyzers, fast-framing cameras or lasers. Data collected by the various diagnostics is sent through a 14-bit, 100MHz sampling digitizer before processing and storage. The control parameters of LAPD include magnetic field (both magnitude and shape), discharge current, fill pressure and fill gas. A summary of typical control parameter values and typical experimental parameters for the data presented in this dissertation are shown in Table 3.1.

3.1.1 Axial versus Radial Transport

A major benefit of the size of LAPD is the ability to match the rate of radial transport to that of axial transport. First, we calculate the parallel end loss rate, $\tau_{\|}$. The parallel flux is

defined as

$$\Gamma_z = nv_e \tag{3.1}$$

where n is the plasma density and v is the velocity of the plasma. If we assume that the end boundary conditions form sheath boundary conditions, then the velocity of the plasma approaches the Bohm condition, $v = C_s$, so $\Gamma_z = nC_s$ where $C_s = \sqrt{(T_e + T_i)/m_i}$ is the ion sound speed. The end loss rate can then be defined as

$$\frac{d}{dz}(\Gamma_z) = \frac{\Gamma_z}{L_c} = 2\frac{nC_s}{L_c} \tag{3.2}$$

where L_c is the gradient scale length in the axial direction and the 2 arises from loss at both ends. The end loss rate, $\tau_\parallel$, is then defined as $\tau_\parallel = L_c/2C_s$. Given a $L_c = 16.54$m and $C_s = 9.79 \times 10^5\sqrt{(T_e)/\mu} = 9.79 \times 10^5\sqrt{((8)/4)} = 1.38 \times 10^6$cm/s so

$$\tau_\parallel = \frac{1}{2}\frac{1654\text{cm}}{1.38 \times 10^6(\text{cm/s})} = 0.6\text{ms} \tag{3.3}$$

This end loss is compared to a perpendicular loss. The radial flux is defined as

$$\Gamma_r = D\frac{dn}{dr} \tag{3.4}$$

The diffusivity is assumed to be Bohm,

$$D_B = \frac{6.25 \times 10^6 T_e}{B} = 5 \times 10^4\text{cm}^2/\text{s} \tag{3.5}$$

where $T_e = 8eV$ and $B = 1000G$. The radial loss rate is

$$\nabla \cdot \Gamma_r = \frac{d}{dr}(-D_B\frac{dn}{dr}) \approx -\frac{D_B n}{L_n^2} \tag{3.6}$$

where L_n is the radial gradient length scale. Assuming $D_B/L_n^2 = 1/\tau\perp$, then for $L_n = 10$cm,

$$\tau_\perp = \frac{L_n^2}{D_B} = \frac{10^2}{5 \times 10^4} = 2.000\text{ms} \tag{3.7}$$

so that the radial loss time, $\tau_\perp = 2.000$ms, is only a little bit larger than the end loss time, $\tau_\parallel = 0.6$ms.

Looking another way, the total particle loss,

$$\frac{dN}{dt} = \int \nabla \cdot \Gamma dA = \Gamma A = \Gamma_z A_{ends} + \Gamma_r A_{edge} \tag{3.8}$$

Assuming that the source for the perpendicular losses and the parallel losses is the same, the ratio of the two is,

$$\frac{dN/dt_{end}}{dN/dt_{edge}} \tag{3.9}$$

$$= \frac{\Gamma_z A_{end}}{\Gamma_r A_{edge}} \tag{3.10}$$

$$= \frac{nc_s(2\pi r^2)}{D_B dn/dr(2\pi r L)} \tag{3.11}$$

$$= \frac{C_s r L_n}{D_B L_c} \tag{3.12}$$

$$= \frac{\tau_\perp r}{\tau_\parallel L_n} \tag{3.13}$$

Given $r = 50$cm, $L_n = 10$cm, and $\tau_\perp/tau_\parallel = 1.776$, the ratio of end loss rate to edge loss rate is 8.88. Thus, the particle loss to the ends is only about an order of magnitude more than the radial particle losses. Compare this to a much smaller machine, with an L_c a quarter of that of the LAPD, but with the same radius. Then the ratio then becomes, ~ 36. For a tenth the size of L_c, the ratio is 88.8. The length of LAPD thus allows the radial particle loss to compete with the parallel loss rate; subsequently, edge radial profiles are set by perpendicular transport.

3.2 Diagnostics

3.2.1 Langmuir Probes

The most prevalent plasma diagnostic for these experiments is the Langmuir probe. Depending on the configuration and number of collecting tips, the probe is used to determine density, electron temperature, flow, floating potential, plasma potential, temporal and spatial fluctuation spectra, particle flux, Reynolds stress, vorticity and crossphase, but all of these measurements rely on the ability of a Langmuir probe to collect current from the plasma.

The most basic probe design is a single wire inserted into the plasma at one end and referenced to an electron source at the other end, generally either earth or chamber ground through a high-impedance resistor ($\sim 1M\Omega$) such that very little current can flow. In this

case, the potential of the inserted tip will reach a voltage called the floating potential,V_f, which for a Maxwellian plasma can be related to the plasma potential ,ϕ_p, as

$$V_f = \phi_p - \frac{1}{2} T_e \ln\left(\frac{2M}{\pi m}\right) \tag{3.14}$$

where M/m is the ion-electron mass ratio, and T_e is in eV. This difference in voltage between floating and actual plasma potential exists because of the presence of a sheath the develops at the collecting surface. This potential exists due to the difference in flux into the collecting tip between ions and electrons. If instead of a high-impedance reference, the probe is biased negatively (many factors more negative then the electron temperature), then the current entering the probe tip is primarily ion current (ions enter the sheath predominantly rather than electrons). From the Bohm sheath criterion, the saturated current collected by a negatively biased probe is

$$I_{\text{sat}} = neA_{\text{eff}} e^{-1/2} C_s \tag{3.15}$$

where C_s is the ion sound speed and A_{eff} is the effective area of the collection tip. For plasmas with a small Debye length, and for a flat tip surface, the effective collection area can be taken to be just that of the collection tip area or $A_{\text{eff}} = A_{\text{probe}}$. Density then can be precisely extracted from a measurement of the ion saturation current if the electron temperature is known. However, it is often difficult, in practicality, to determine the electron temperature. Thus for measurements of fluctuations and profiles, the ion saturation current is taken as a proxy for density, as is often done in the plasma community. These fluctuations and profiles can be related to density by scaling them to a separate measurement of density, usually an interferometer technique. For these experiments, the average measured saturated current in the core is scaled to the core density as measured by a microwave interferometer array.

3.2.2 Swept Probes

The biasing of a Langmuir probe can be expanded to a continuous sweep of values, producing a corresponding value of measured current through the probe that is the I-V curve for a Langmuir probe. From these swept measurements, values of electron temperature and

plasma potential can be determined, as well as the floating potential and ion saturation current already discussed.

For this dataset, each shot at each position is used to produce a swept-Langmuir I-V curve. Plotting the natural logarithm of the I_{sat} as a function of swept voltage, the linear region before the knee is fit to a line with the slope $= 1/T_e$. Then, a second fit of the linear region beyond the knee is made. The voltage at the intersection of the two linear fits is taken as the plasma potential.

The plasma potential measurements are primarily used to determine the radial plasma potential profile. From these profiles, the flow profile is determined by

$$V_\theta = \frac{cE}{B} = \frac{c}{B}\frac{d\phi_p(r)}{dr} \tag{3.16}$$

and the shearing rate as

$$\gamma_s = \frac{d}{dr}V_\theta(r) \tag{3.17}$$

3.2.3 Mach Probe

The second method for measuring cross-field flow is through a special configuration of Langmuir tips called a Mach or Gunderstrup probe. In general, a Mach probe has at least two equally sized ion-collecting surfaces facing in opposite directions and both biased negatively to draw saturated current as in a typical Langmuir probe. The Mach number of flow is calculated by comparing the level of ion saturation current measured by each face,

$$M_\parallel = M_c \ln(\frac{I_1}{I_2}) \tag{3.18}$$

where I_1 and I_2 refer to the saturation current measurements of each face and M_c is a magnetization factor which is equal to one for a strongly magnetized plasma.

The Mach number is specified as the parallel Mach number in 3.18 because in a magnetized plasma, a Mach probe with only two opposing faces can only measure flow parallel to the magnetic field. A measurement of the perpendicular or cross-field flow can be made by adding more opposing faces at angles to the magnetic field lines. The calculated $M_\perp$ though

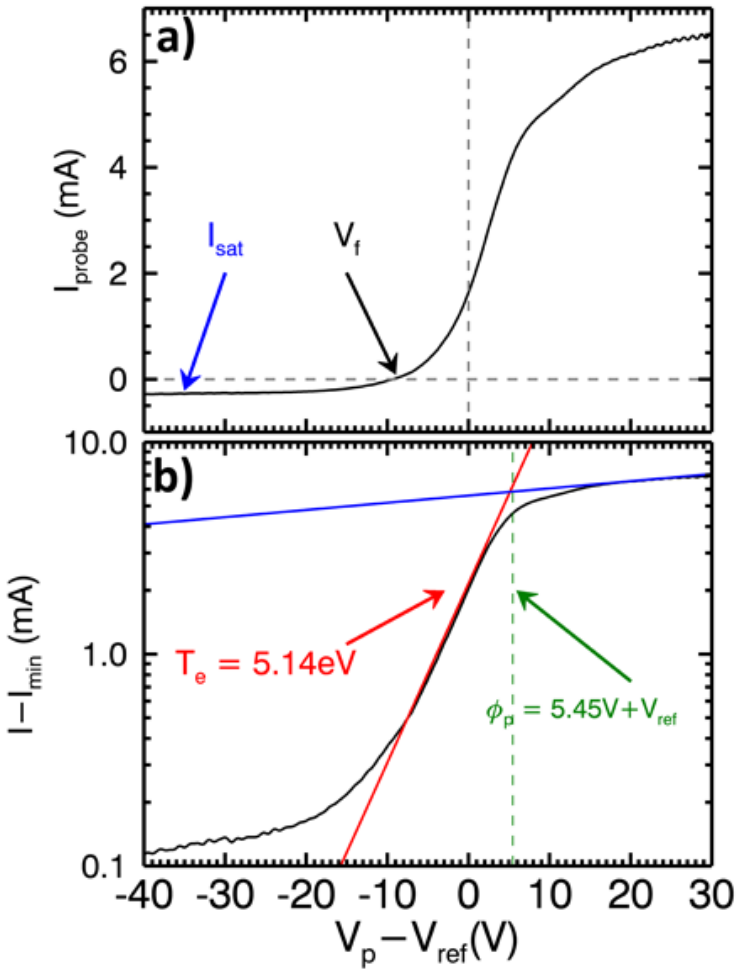

Figure 3.5: (a)A typical swept probe I-V curve in the LAPD core showing where I_{sat} and V_f are measured and (b) a logarithm of the current plot versus swept voltage to show the fitting of the exponential for a measurement of electron temperature, T_e and plasma potential ϕ. The value of V_{ref} depends on how the sweeper circuit was referenced and in this case, V_{ref} is the anode potential $\sim 20V$ above chamber ground.

is dependent on the measured $M_{\parallel}$ as

$$M_{\perp} = M_{\parallel} - \frac{M_c}{\cot(\alpha)} \ln(\frac{I_3}{I_4}) \tag{3.19}$$

where α is the angle the offset faces are to the magnetic field. This Mach number can be converted into a velocity, v, as $M = v/C_s$, where $C_s = \sqrt{((T_i + T_e)/m_i)}$ is the ion sound speed with ion temperature, T_i, electron temperature, T_e, and ion mass, m_i.

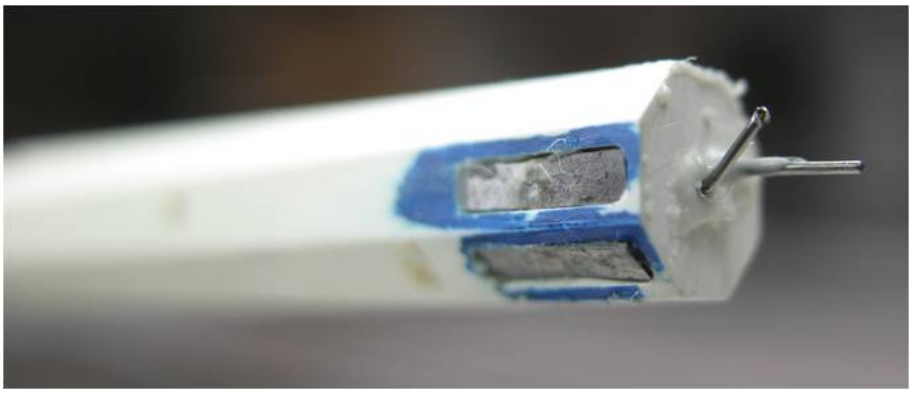

Figure 3.6: Picture of Mach Probe

The Mach probe built for this thesis consists of an octagonal frame made of boron nitride supporting six 1x4mm tantalum faces. Faces 2 and 5 comprise the standard two face-mach probe measuring flow parallel to the magnetic field, while faces 3 and 6, and, 1 and 4 are offset by a 45° angle as in Figure 3.7.

In this arrangement, two simultaneous measurements of perpendicular Mach flow can be made, which, when averaged, can cancel the contribution of the parallel Mach. Given the 45° angle of the tips, and assuming strong magnetization, the equation for cross-field Mach flow in this experiment becomes,

$$M_{\perp} = \frac{1}{2}(\ln(\frac{I_1}{I_4}) + \ln(\frac{I_3}{I_6})) \tag{3.20}$$

Given time-series measurements of ion saturation current, the probe yields a time-series of Mach number, making the particular probe useful in measurements of dynamically changing flows. However, there are a number of drawbacks of the probe which must be addressed.

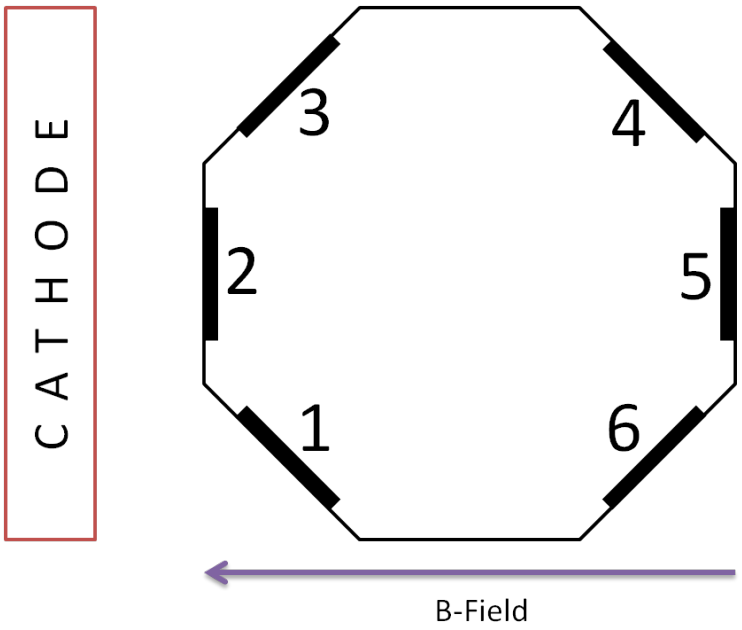

Figure 3.7: Diagram of mach probe

First, the probe can suffer from differences in collection areas between the tips. This can be remedied to an extent by calibration; first taking measurements with the probe oriented in one direction, then repeating the measurement with the probe rotated 180°. This allows for a calibration factor—the ratio of the measured saturated current of each tip in normal and flipped configurations—to be included in the Mach probe measurement. Even with this adjustment, minor offsets can remain and are especially apparent in regions where little to no flow should be measured. In this experiment, it is assumed that there is no flow at the very core of the machine. This assumption is borne out by plasma potential measurements using a swept probe. From this, any measured offset of Mach flow in the core can be taken as a global offset to shift an entire Mach probe profile.

A second drawback comes from the interpretation of the measurement itself. Hutchinson 2008 [55] showed numerically that original Mach number calculating includes diamagnetic drift contributions when a measurement is made in the presence of density or temperature gradients. Since these drifts do not contribute to a steady-state mean flow of the plasma, they must be taken into account in order to extract a true steady-state mean flow. Hutchison

expanded the original Mach number calculation to incorporate corrections due to diamagnetic drifts as,

$$\ln\left\{\frac{\Gamma_{\|p}}{nC_s}\right\} = -1 - M_{\|\infty} + \left[(1+M_{\|\infty})M_{T_e} + M_{D_i} + M_{E\times B} - \left(\frac{1-\sin\alpha}{1+\sin\alpha}\right)M_D\right]\cot\theta \quad (3.21)$$

where,

$$M_D = M_{D_i} - M_{D_e} = (M_{ni} + M_{Ti}) - (M_{ne} + M_{Te}) \quad (3.22)$$

represents the diamagnetic contribution to the flux, while $M_{E\times B}$ is the contribution due to $E \times B$ flow, which in this case is taken as the only component of cross-field flow. Given $\alpha = \theta = 45°$, the various diamagnetic components are as follows:

$$C_s M_{Te} = -(1.1716 + M_{\|})n\frac{dT_e}{dr} \quad (3.23)$$

$$C_s M_{Ti} = (0.8284)n\frac{dT_i}{dr} \quad (3.24)$$

$$C_s M_{ni} = (0.8284)T_i\frac{dn}{dr} \quad (3.25)$$

$$C_s M_{ne} = -(0.1716)T_e\frac{dn}{dr} \quad (3.26)$$

Given experimental measurements of density and temperature profiles, and using a measured Mach number, $M_\perp$, the steady-state Mach number is

$$M = M_\perp - (1.1716M_{Te} + 0.8284M_{ni} + 0.8284M_{Ti} + 0.1716M_{ne}) \quad (3.27)$$

With typical density and temperature profiles taken into account and an ion temperature that is assumed a constant 1eV (as is often assumed on LAPD), the dominant contribution to diamagnetic drifts is the electron temperature.

Now, while careful measurements of density and temperature could conceivably provide a reliable Mach probe measurement, any errors in these measurements would be compounded through the large calculated form. Thus, ultimately, while a correction to the Mach probe measurement is available, for this dataset, the Mach number presented will be the full Mach number.

3.2.4 Nine-Tip Langmuir Probe

The majority of measurements made for this dissertation were achieved using a single probe with a nine-tip array of Langmuir tips that is used to simultaneously measure ion saturation current, floating potential, and electric field fluctuations in order to make correlation measurements of particle flux, Reynolds stress and vorticity.

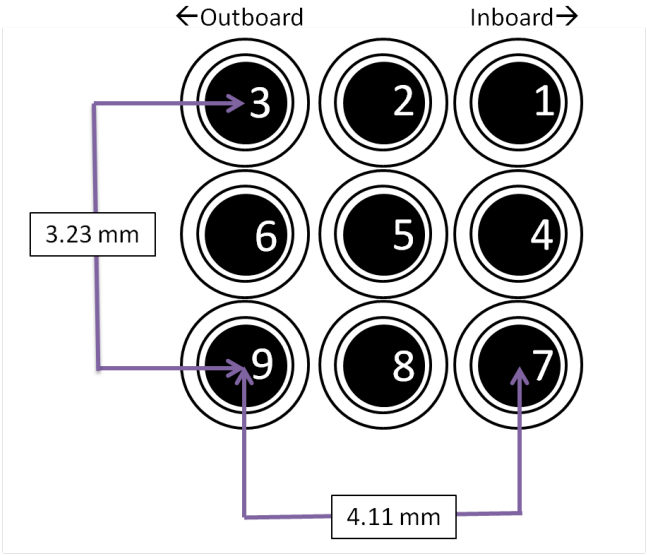

Figure 3.8: Diagram of Nine Tip Probe. $\Delta x = 4.11$mm and $\Delta y = 3.23$mm.

The probe is constructed by threading tantalum wire snuggly through thin single-bore alumina ceramic tubes which were cut diagonally and reattached at a right angle. The tubes arrayed in a 3x3 block and the edges sanded down so that the tantalum wire cross section is flush with the edge of the ceramic tube. Each tantalum tip can be separately biased negatively to collect saturated ion current or connected to a high-impedance circuit to measure floating potential. The tips are oriented in an L-shape such that the tip faces point perpendicular to the probe shaft. Thus, the tips can either face directly toward the cathode or away from it in the probe shadow. For the measurements taken in this experiment, the tips were always shadowed to avoid influence from the primary electrons on the signal.

3.2.4.1 Density

The ion saturation current was measured using a 67.5V battery to negatively bias the tip with respect to ground. Current flowed through a 330Ω resistor and the voltage across this resistor was recorded by the digitizer through either the Tektronix optoisolator unit, or a in-house buffer circuit (discussed in the appendix). Each voltage time-trace is offset such that the tail end of the time-trace, after the main plasma discharge has ended, is set to be zero. While a density could in theory be calculated using Equation 3.15, the density was determined instead by scaling the I_{cmrsat} profile to the density measured by a microwave interferometer permanently installed on the LAPD. Using the ion saturation current profile to determine a shape factor,

$$S = \int_{-r_{\max}}^{r_{\max}} \frac{n(t)}{n_{\max}} dr = \int_{-r_{\max}}^{r_{\max}} \frac{I_{\text{sat}}(t)}{I_{\text{sat}}^{\max}} dr \tag{3.28}$$

the line integrated density is

$$n(t) = \frac{\bar{n}_L V(t)}{S} \tag{3.29}$$

where V(t) is the voltage time-series recorded by the interferometer and $\bar{n}_L = 1.17 \times 10^{14}$ V/cm^2 is a calibration factor for the interferometer incorporating the output signal versus path length. Then, the peak density from n(t) is matched to the I_{sat} value in the core so that all I_{sat} values are scaled to this ratio. This is some systematic error in this measurement as the calibration factor is dependent on the density profile of the plasma column; this calibration factor might change slightly as the plasma is modified by biasing.

3.2.4.2 Floating Potential and Local Electric Field fluctuations

Floating potential is read directly off the tip using a high-impedance isolator. Electric field is calculated from two floating potential tips as,

$$E = -\frac{(V_f^2 - V_f^1)}{d} \tag{3.30}$$

where d is the center to center separation distance between two tantalum tips as indicated

in Figure 3.8. Fluctuating small scale velocity is assumed to be purely due to $E \times B$ forces so fluctuating velocity can be determined using the measured electric field, with two horizontally aligned tips determining azimuthal fluctuation flows, $\tilde{v_\theta}$, and two vertically aligned tips determining radial fluctuating flows, $\tilde{v_r}$.

3.2.4.3 Particle Flux, Reynolds Stress and Vorticity

With the ability to measure simultaneous time-series of saturated current (which can be scaled to density) and fluctuating plasma flows, it is possible to correlate these quantities to get particle flux, $\Gamma = \langle \tilde{n}\tilde{v} \rangle$ and Reynolds stress, $R = \langle \tilde{v}_r \tilde{v}_\theta \rangle$.

For flux measurements, the probe tips are connected such that tips 1, 3, 5, 7, and 9 measure floating potential and 2, 4, 6, and 8 collect saturated current. Thus radial particle flux can be calculated from isat tip 2 and the electric field from vf tips 1 and 7.

Both flux and Reynolds stress are calculated spectrally using the FFT of density and radial velocity fluctuations as well as their cross-spectrum defined as,

$$G(f, r) = \hat{x}^*(f, r)\hat{y}(f, r) \tag{3.31}$$

for two fluctuating quantities. The flux is then computed using [56],

$$\Gamma = 2 \int_0^\infty |n(f)||v_r(f)|\gamma_{(n,v_r)}(f) \cos[\phi_{(n,v_r)}(f)]df \tag{3.32}$$

where crossphase is computed from the cross-spectrum using,

$$\theta = \tan^{-1} \frac{\langle Q(f, r) \rangle_{f,r}}{\langle C(f, r) \rangle_{f,r}} \tag{3.33}$$

where Q and C are the imaginary and real parts of the cross-spectrum. Coherency, $\gamma_{(n,v_r}(f)$ is determined from the product of the autocorrelation power of each fluctuation quantity divided by the cross-spectral power.

Reynolds stress is calculated in the same manner by replacing density fluctuations with azimuthal velocity fluctuations.

Table 3.2: Data Acquisition settings for this dataset

Setting	Value
Samples	20480
Sampling Rate	1.5625MHz
Timestep	6.4×10^{-7}s
DAQ Trigger Delay	18.5ms
Shots Taken/Position	10-25

Vorticity, $\varpi = \nabla \times \mathbf{v}$, can also be determined from this arrangement. Given $v = cE/B = -(c\nabla\phi)/B$, the vorticity can be calculated using floating potential tips in a finite difference approximation method [57],

$$\varpi = \frac{1}{B}\frac{\left(V_f^{\text{tip1}} + V_f^{\text{tip3}} + V_f^{\text{tip7}} + V_f^{\text{tip9}} - 4V_f^{\text{tip5}}\right)}{\Delta x \Delta y} \tag{3.34}$$

where Δx and Δy are the separation distances between tips as indicated in Figure 3.8.

Lastly, an estimate for sheared flow can be made using this probe. First, the azimuthal flow is calculated using the V_f of tip 5 and the average of tips 3 and 9. Similarly, azimuthal flow between tip 5 and 1 and 7 are made. From these two flow values, a shearing rate, $\gamma = (E_1 - E_2)/\Delta x$ can be made.

3.2.5 Data Acquisition Settings

All the probe and surface potential data (limiters, anode, cathode, annulus) were recorded by the digitizer using the settings listed in Table 3.2:

3.2.5.1 Probe Axial Positions

The probe port position and axial position (as a function from the cathode) are listed in Table 3.3

Table 3.3: Axial port numbers and locations of Langmuir probes (z is distance from cathode).

Setting	Port Number	Axial Distance
Mach	25	z=7.5m
9-Tip	27	z=7.8m
Swept	29	z=8.1m
Rake	42	z=12.6m

3.2.6 Fast-Framing Camera

A final diagnostic used in this dissertation is a fast-framing camera, though the results were mainly used to qualitatively observe the changes in flow and level of fluctuations. The camera used is a Phantom V.7.3 and, for the movie shown in Figure 3.9, was situated at the end of the LAPD column opposite the cathode end. The camera is unfiltered and the light is integrated over the entire column. The camera can produce an image 64x64 pixels in height and width and at a sampling rate of up to 140kHz or an 128x128 pixels image at 86kHz. The movie qualitatively shows how strong driven rotation can modify the plasma turbulence.

The next chapter introduces the limiter biasing system and discusses how the biasing works and how the limiter modify the LAPD with and without biasing.

Figure 3.9: Movie of fast framing camera images of a full plasma discharge at 500G. (Viewable on pdf only. Click on image to start movie. Right click and select disable content to stop movie.)

CHAPTER 4

Bias-driven plasma rotation

The details of the biasing circuit, the limiters and their effect on plasma rotation are discussed in this chapter. The inclusion of the limiters represent a potentially significant change to the environment of the main chamber even when fully retracted. Comparisons to results from pre-limiter installation experiments are shown in this chapter. The changes arising from the insertion of the limiters (versus fully retracted) are also examined. This bias-driven plasma rotation and associated radial electric fields are also shown to be consistent with cross-field current that arises due to Pedersen conductivity.

4.1 The Limiters

The limiters installed in LAPD consist of two main sections: an aluminum plate annulus with an outer radius of about 50cm and an inner radius of 35cm is located at about port 8 of LAPD; a set of four movable quarter annulus aluminum-plates with inner radius of 30cm and outer radius of 40cm are situated about 30cm upstream from the full annulus at port 7. With the anode sitting approximately at port 1, the separate distance between the anode-cathode source and the limiters is about 2m. Both the annulus and limiter are electrically isolated from the chamber and each distinct section—the annulus and the four limiter plates—can be separately biased. While the full annulus is stationary—permanently providing a flat, known, axial boundary condition from 35 to 50cm—the quarter annulus limiters can separately be moved radially through vacuum feedthrough to the chamber exterior, starting completely behind the annulus when fully extended, to a radius of about 20cm when fully inserted. Given the shape of the four limiters, a perfectly circular aperture is achieved only when the

inner edge of each limiter is set to 30cm, which is about 2cm outside of the radial extend of the cathode source (typically about 28cm given a standard magnetic field setup).

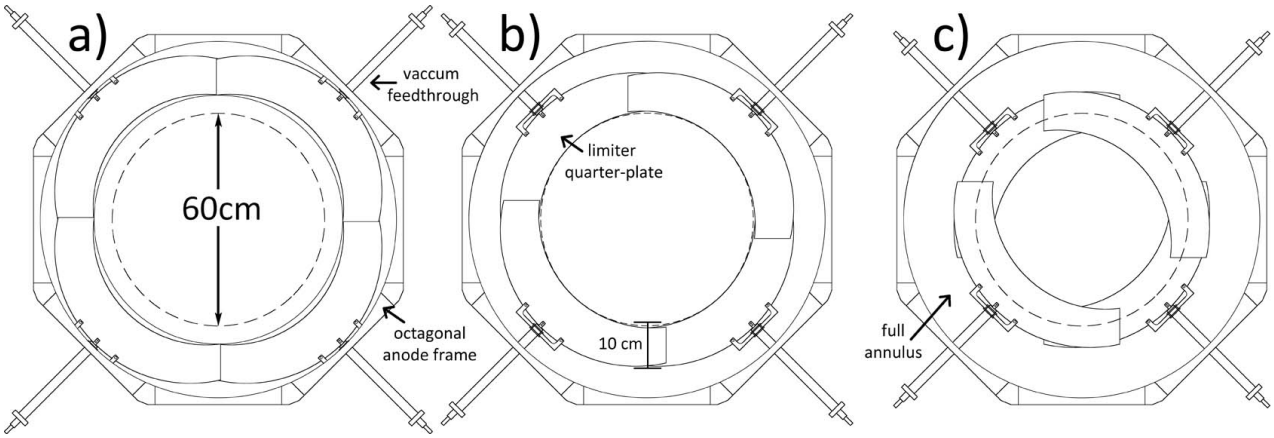

Figure 4.1: Sketches of the limiter quarter-plates and full annulus with view from cathode. (a)Quarter-plate limiters full retracted behind annulus. (b)Inserted to an inner radius of 30cm to form a circle. (c)Maximum insertion of limiters without gapping between quarter–plate limiters and annulus at a an inner radius of about 25cm.

For the data in this dissertation, the limiters were set to provide an aperture of about 26cm in radius, just inside the cathode source edge. The four plates were electrically linked to one another through cabling outside the chamber and then attached to the biasing circuit. The annulus was not connected to the circuit and left electrically floating.

4.2 The Biasing Circuit

The biasing circuit consists of a 0.2F, 450V capacitor bank that is pulse discharged through an isolated gate bipolar transistor (IGBT) switch. A 250V, 1.5A Agilent network controlled power supply sets the voltage on the capacitor bank. The discharge circuit shown in Figure 4.4 supplies a voltage to the limiters through the capacitor bank/IGBT circuit and referenced to the cathode of the plasma discharge circuit. A 0.2Ω wire resistor is placed in series in order to monitor the current of the bias discharge. The cathode-anode discharge circuit is normally isolated from the chamber and chamber ground, but for these experiments,

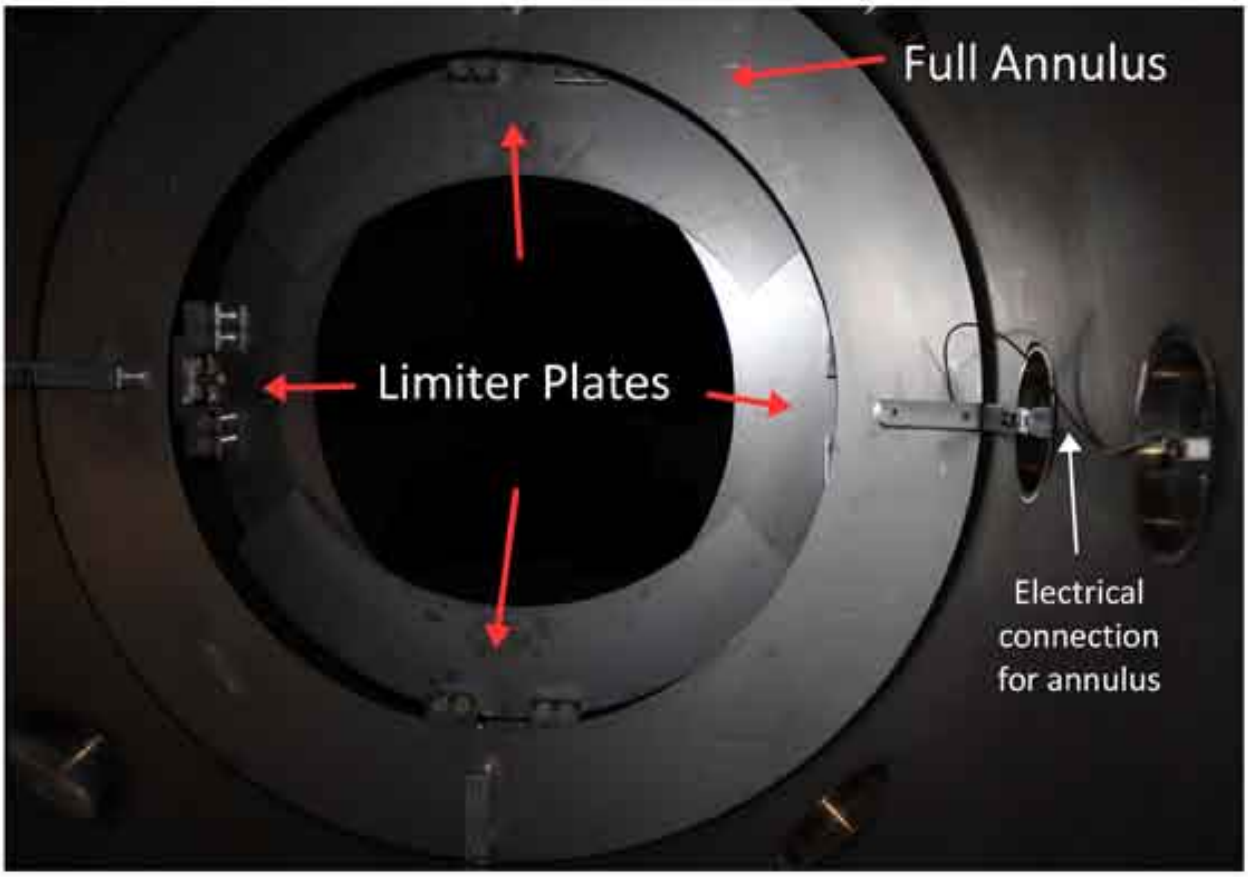

Figure 4.2: Picture of the limiters inserted to an of 52cm (26cm radius) and the annulus from the point of view of the main plasma chamber.

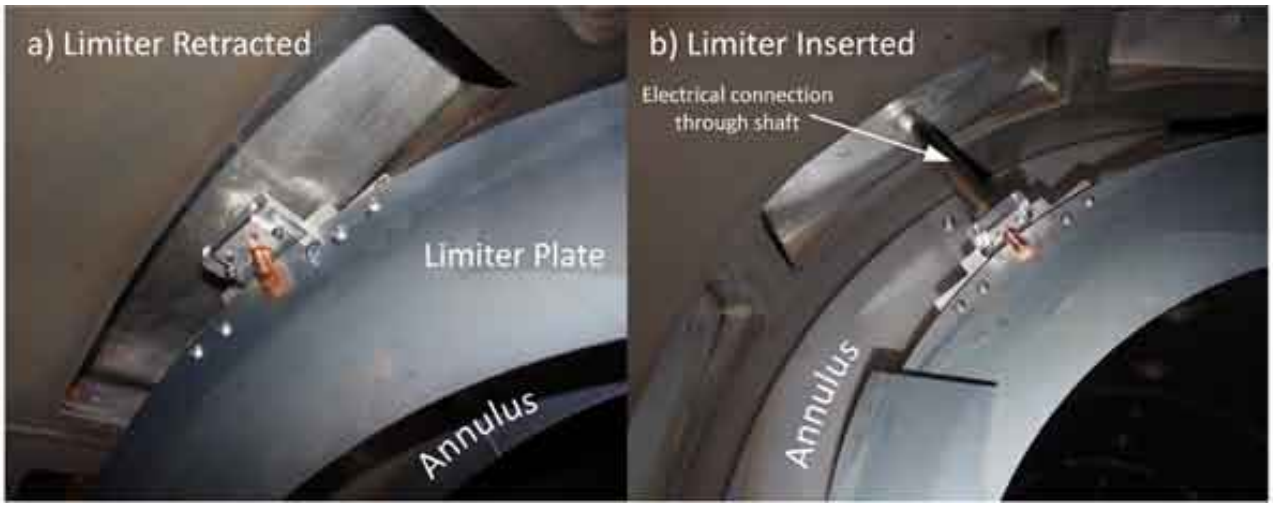

Figure 4.3: Picture of a limiter quarter-plate (a) fully retracted and (b) inserted to 26cm exposing the annulus behind it

a 7.2Ω, 100W resistor is connected between the cathode and chamber ground. When the bias circuit is connected to the discharging plasma, but not given a voltage output from the network power supply, the limiters will collect charge from the plasma and begin to reach a floating potential on the order of 35V above chamber ground. This limits the ability of the biasing circuit to provide a bias less then floating potential; consequently, a discharge current is only observed when the power supply provides capacitor bank voltages above floating potential.

The main biasing circuit loop is schematically represented in Figure 4.5. From the cathode reference, the capacitor bank supplies a voltage of V_{bias} up to 250V. A voltage drop occurs across the 0.2Ω wire resistor; given a discharge current that can run into the tens of amperes, this drop can be on the order of 10-20 volts. From the anode to the cathode, there is a voltage drop that is set by the overall plasma discharge circuit, which, during the bias discharge time, is usually about 45V. The remaining voltage drop to complete the circuit is believed to arise from the perpendicular resistivity of the plasma itself. It will be shown below that this resistivity is consistent with the cross-field Pedersen conductivity due to ion-neutral collisions from limiter connected field lines and anode connected field lines. The resistivity

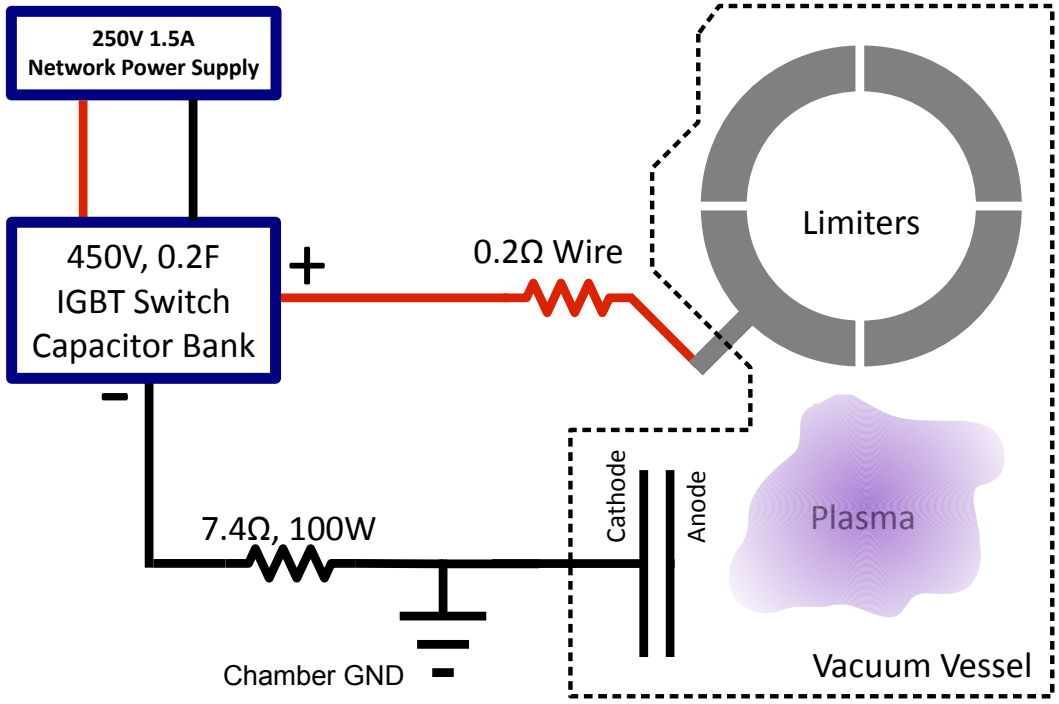

Figure 4.4: Symbolic diagram of biasing circuit showing capacitor bank, network power supply, circuit resistors, limiters/anode/cathode.

for electrons along field lines to complete the current is small, on the order of 0.01Ω.

It should be noted that given the placement of the limiters at 26cm, there is a slight overlap of the cathode source and limiter plates consisting of a thin ring. At the moment of bias turn-on, there is an immediate path for current from the cathode to flow to the limiters through electrons. This results in an immediate current through the bias circuit. However, current also begins to flow cross-field. After the plasma reaches a steady state, about 2ms after bias turn-on, the total current through the circuit is a combination of this direct current between the cathode and the limiters and the current that crosses from limiter-connected field lines and anode-connected field lines. This second current component is approximated by subtracting immediate current at bias turn-on from the eventual steady-state bias current.

A small amount of current may complete the circuit directly from the limiter to chamber ground to the cathode or from the anode to chamber ground to the cathode, but these currents cannot be measured at this time. They are assumed to be small corrections to the measured bias current, especially for high bias cases where discharge current is large, but may be important in the unbiased and no-flow cases.

During each shot on LAPD, the time-series potential of the anode, cathode, capacitor bank output, limiters, and annulus were monitored through high-impedance voltage dividers referenced to ground (see Appendix 3). The potential across the 0.2Ω wire resistor was also monitored for calculating of discharge current.

The IGBT switch is connected to the plasma discharge trigger through a delay box. In these experiments, the bias discharge was delayed to begin approximately 8ms after the initial plasma discharge trigger and the switch is closed for 5ms. For a plasma discharge time of about 15ms, this places the bias discharge in the tail end of the plasma discharge when plasma conditions have reached steady-state and just before the plasma current ramp-down begins. The bias voltage and current take approximately 1ms to reach its steady-state value from the trigger time, with this time decreasing with increasing magnetic field.

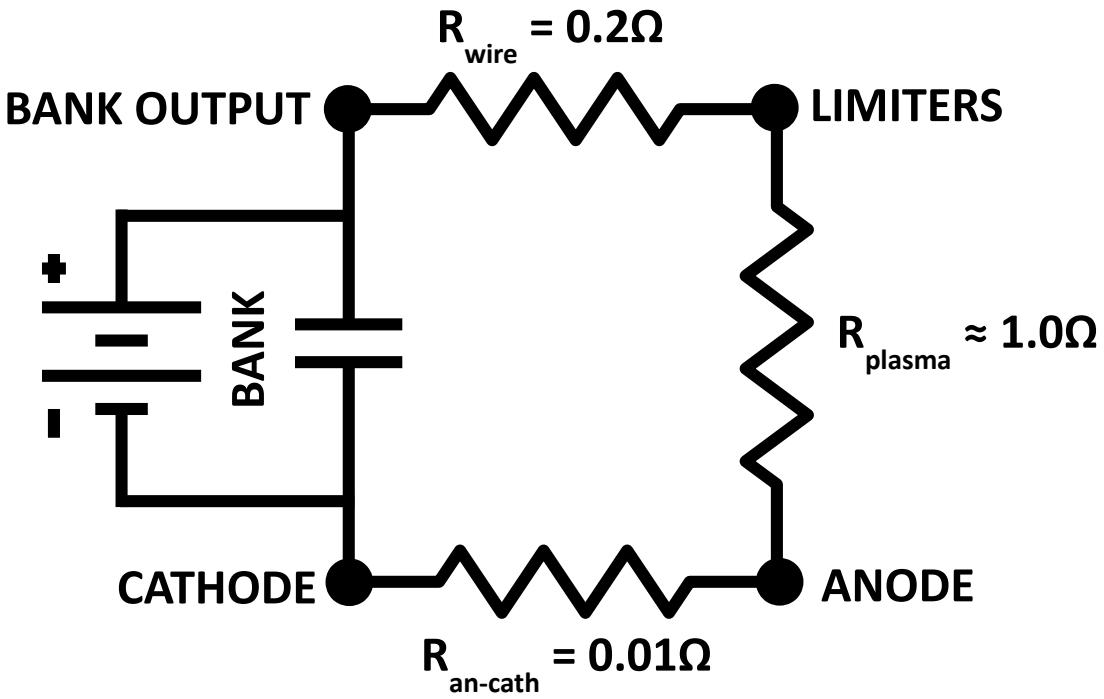

Figure 4.5: Schematic diagram of bias discharge current loop.

4.3 Limiter Voltage and Discharge Current Response with Bias

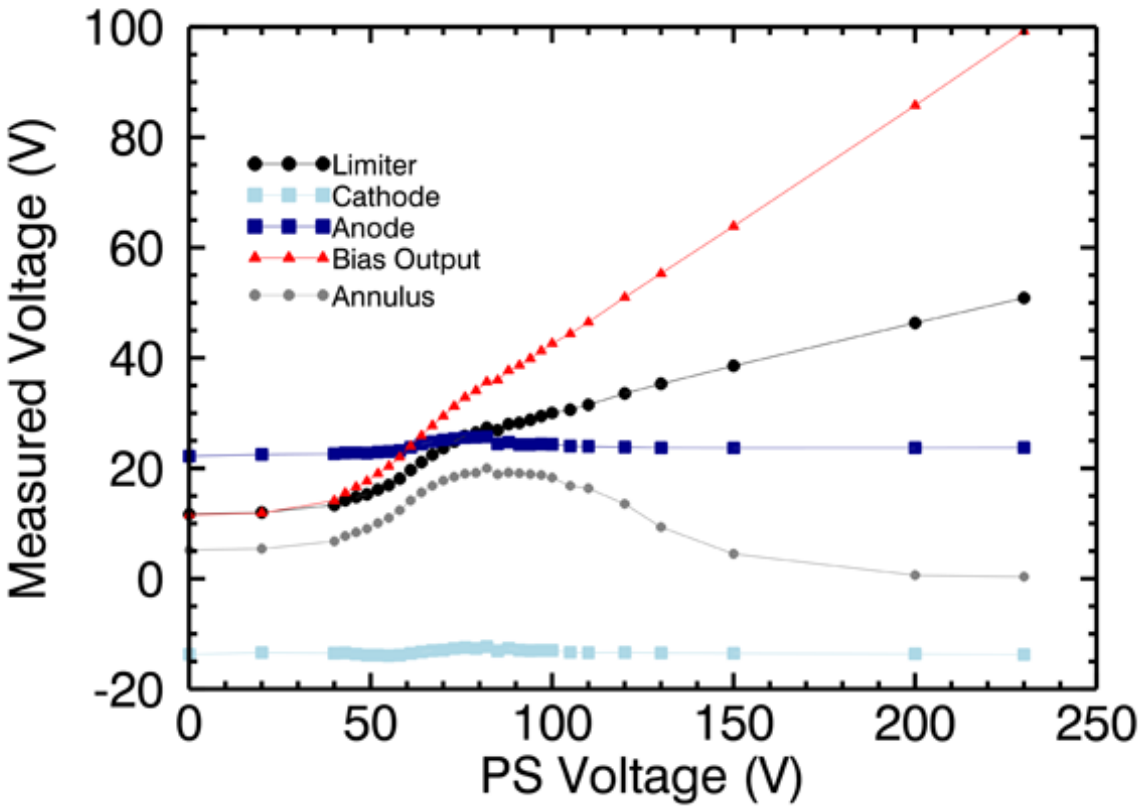

Figure 4.6: Voltage monitoring of limiters, anode, cathode

A summary of the voltage response of the anode, cathode, bias output, limiters and annulus averaged over a period of 3.2ms in the steady-state regime, is shown in Figure 4.6, all referenced to chamber ground. The bias output (red curve) reflects the potential at the output of the capacitor bank. The limiter (black curve) reflects the direct potential measurement of the limiters. Both curves begin at an absolute voltage of 10V, 25V above the cathode potential. This value is held constant until the power supply voltage is increased above 25V. Up to this point, the plasma currents tend to charge the capacitors to the floating potential of the plasma. Only once the biasing power supply is set to a voltage above the floating potential—and can charge the capacitors above floating potential—does the bias

circuit register a temporal change in the current and output or limiter potentials. The output voltage is higher than the limiter voltage because of the voltage drop across the wire resistor.

The slope of the limiter voltage curve appears to increase until it reaches the same voltages as the anode. Then, the slope decreases slightly before reaching a generally constant value. The voltage of the anode and cathode remain relatively constant with increasing voltage on the power supply, with the exception of a slight bump that appears at the intersection of the limiter and anode voltages. The cathode actually drops below ground, but the voltage difference between the anode and cathode is essentially constant throughout (the voltage difference between anode and cathode is set by the overall LAPD plasma discharge). From the bias circuit loop in Figure 4.5, it is clear that the voltage most important for rotation is that between the limiter and the anode as this value reflects the amount of cross-field current. Bias voltages quoted throughout this thesis will be referenced either by their power supply value or by the anode-limiter voltage difference.

The dynamics of the voltage and current response to the bias turn-on for various capacitor bank settings are shown in Figure 4.7, which show time traces for the voltage difference between anode and limiter plates and the bias current averaged over multiple shots. The time $t = 0$ corresponds to the moment the IGBT switch is triggered and current can begin flowing through the bias circuit. As the power supply voltage is increased, the potential reached by the limiter is clearly increased (the anode voltage is constant) and the amount of total current flowing through the bias circuit increases as well. As can be seen in Figure 4.7(a), the voltage difference between the limiter plates and the anode reach a steady flat value after about 2ms. achieved after about 2ms. Similarly, the bias discharge current (as measured using the wire resistor and shown in Figure 4.7(b)) also reaches a fairly steady value after about 2ms, though the current value does not stay as constant as does the voltage in the steady-state regime of the bias discharge. At 5ms, the IGBT switch is opened, and both the voltage and current drop very rapidly to pre-bias values, on the order of about 100μs. Chapter 8 will go into more details regarding the dynamics of bias turn-on and turn-off as

well as the dynamics of the changing plasma parameters.

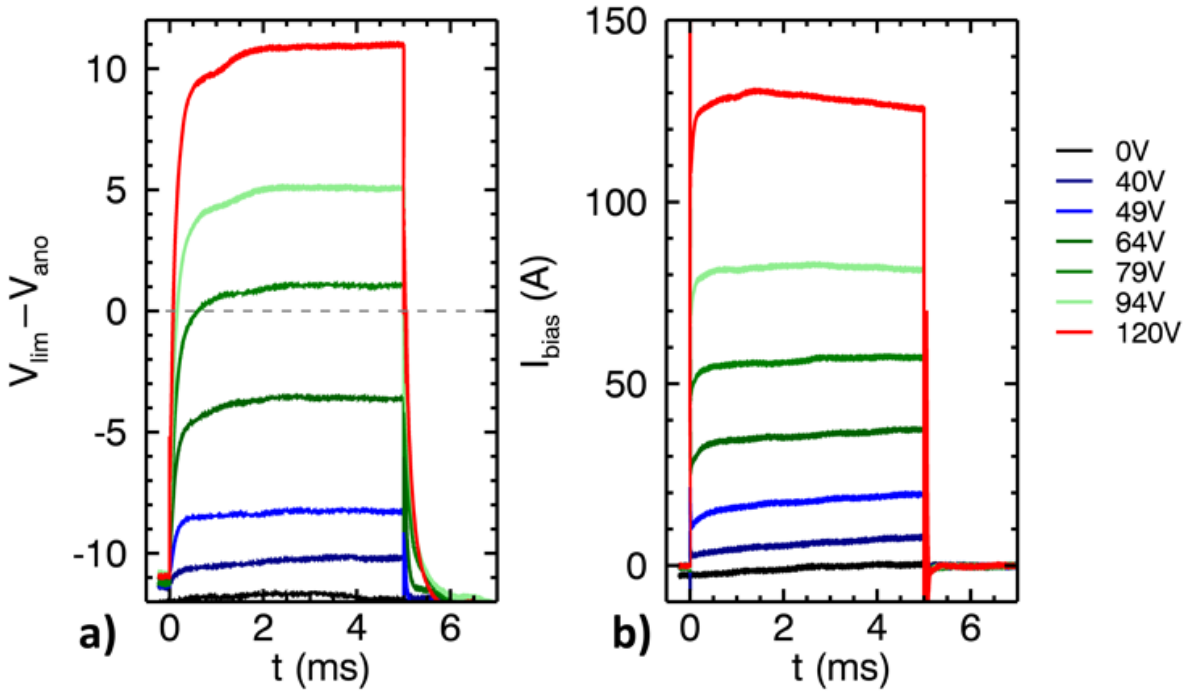

Figure 4.7: (a)Voltage difference between limiter plates and anode as a function of time for different power supply voltage settings. (b)Current as measured through the wire resistor for the same power supply settings in (a). The time $t = 0$ corresponds to the moment the IGBT switch is triggered and the entire bias lasts 5ms.

The total discharge current, calculated from the voltage across the wire resistor, is plotted as the black curve against the total capacitor voltage set by the power supplies in Figure 4.8(a). As mentioned before, this total current must be broken into a part that represents current directly between the cathode and the limiters along the cathode connected field-lines carried by the primary electrons and a part that connects to the cathode by first traversing perpendicularly across field lines. The cross-field current can be estimated by first subtracting the initial current measured from the saturated steady-state current. This initial current is determined just after transients have died away (about 0.01ms) as shown in Figure 4.8(b), indicated by the dotted line. The blue and green curves in Figure 4.8(a) show the values of the initial current and cross-field current estimate as a function of power

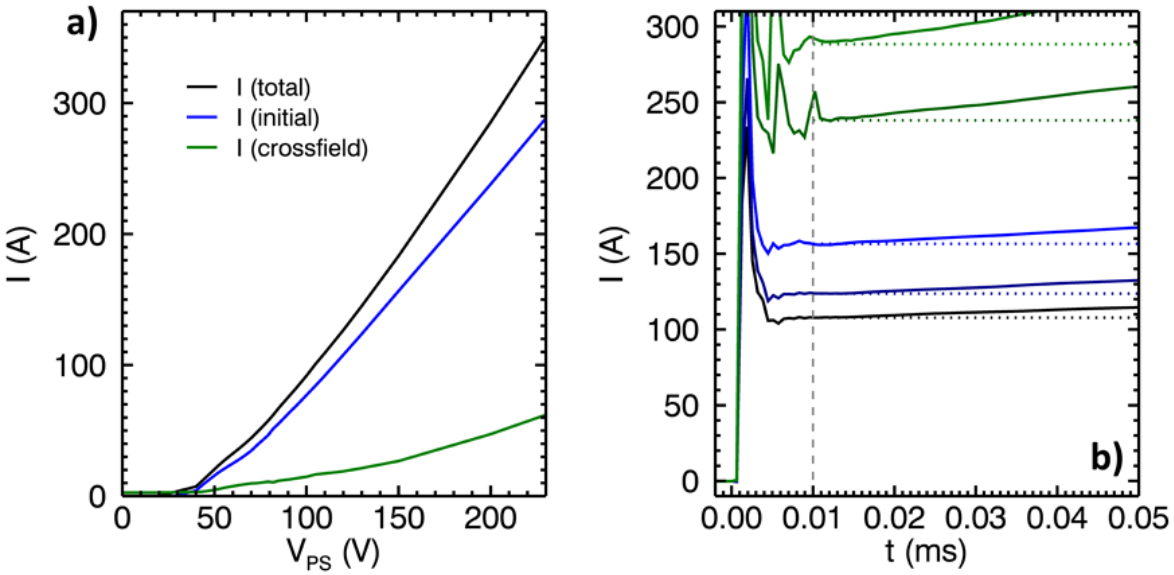

Figure 4.8: (a) Bias circuit current versus power supply voltage showing total(black), initial(blue), and the crossfield estimate(green) determined the difference between total and initial currents. (b) Time traces for various biases, increasing from black to green. Bias turns on at t=0 and undergoes transients until about 0.01ms. The current just beyond the dashed grey line at 0.01ms is taken as the initial current and the dashed colored horizontal lines shows the current increasing beyond this initial amount.

supply voltage.

As a rough estimate as to how much resistance the plasma provides, the two current channels are plotted as functions of the most likely voltage difference that generates the current: cathode-limiter potential just after bias turn-on for the initial current and steady-state anode-limiter potential for the cross-field current.

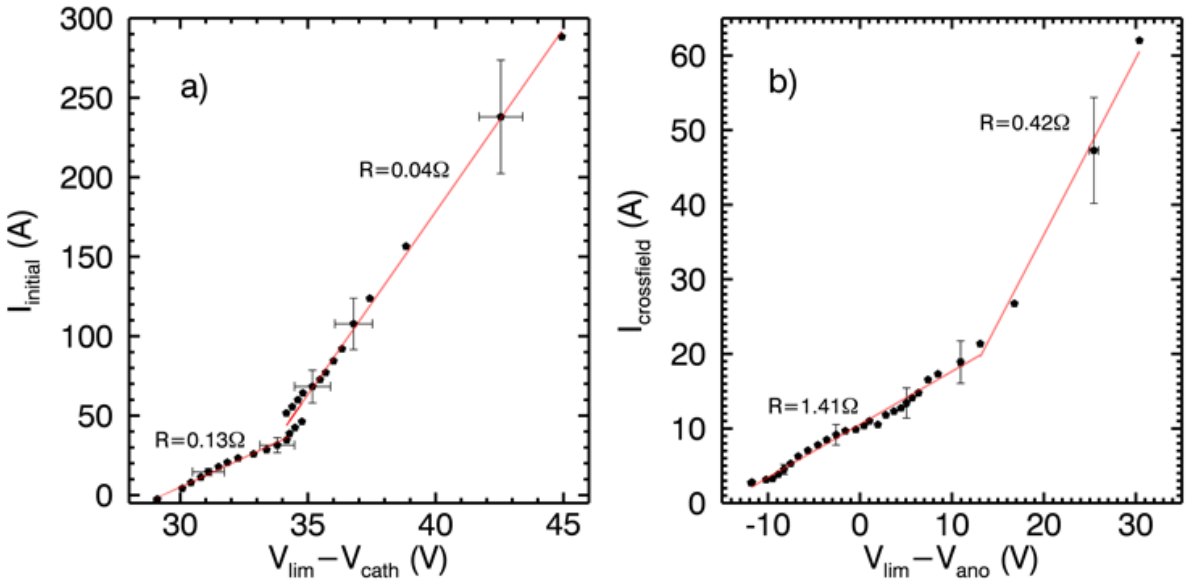

Figure 4.9: Initial current versus initial limiter voltage minus cathode voltage and (b) steady-state crossfield current versus steady-state limiter voltage minus anode voltage. Fit lines in both give an estimate of the resistance provided by the plasma assuming a Ohmic relationship between voltage and current.

Figure 4.9(a) shows the initial current as a function of the initial limiter-cathode voltage different. The values are taken just after transients have died out, about 0.01μs after bias turn-on. An estimate of the resistance provided by the plasma parallel to the field lines between the cathode and the limiters is made by taking the slope of the I-V curve. There are two distinct regions of linearity: for low power supply bias voltages, the apparent parallel resistance is about 0.13Ω, while for high biases, the parallel resistance drops to 0.04Ω. These values are consistent with the estimated parallel resistance from the anode-cathode discharge of about 0.01Ω. Figure 4.9(b) shows the estimated cross-field current as a function of the

limiter-anode voltage difference in the steady-state regime. The fits represent the cross-field resistance of the plasma which is fairly consistent for the majority of the biases measured here at 1.41Ω. For the three very highest biases recorded, the resistance appears to drop to 0.42Ω. It will be shown at the end of this chapter that this cross-field current is consistent with current predictions made assuming the perpendicular conductivity is due to Pedersen conductivity.

4.3.1 Field Variations

Before moving on to how the limiter biasing scheme modifies plasma parameters, the effect of magnetic field on the limiter I-V curves and estimated plasma resistance is examined.

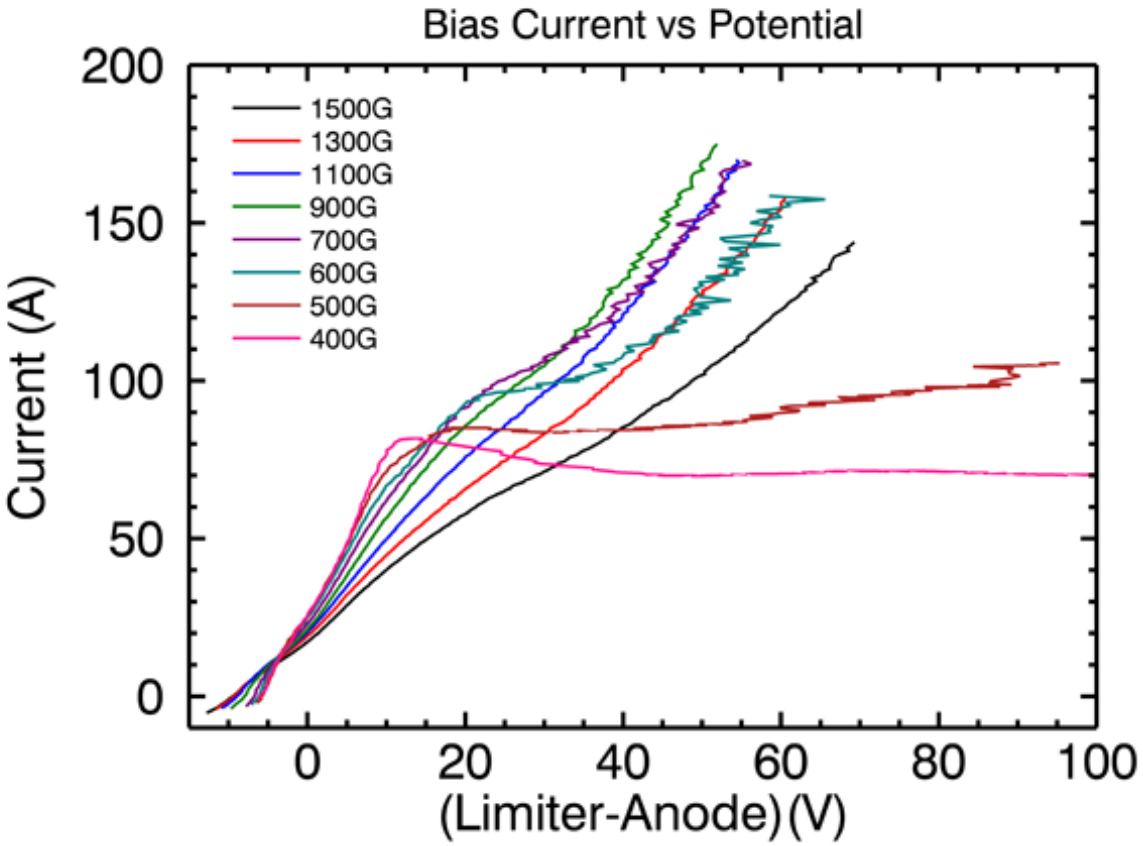

Figure 4.10: Total bias circuit current versus limiter-anode voltage difference

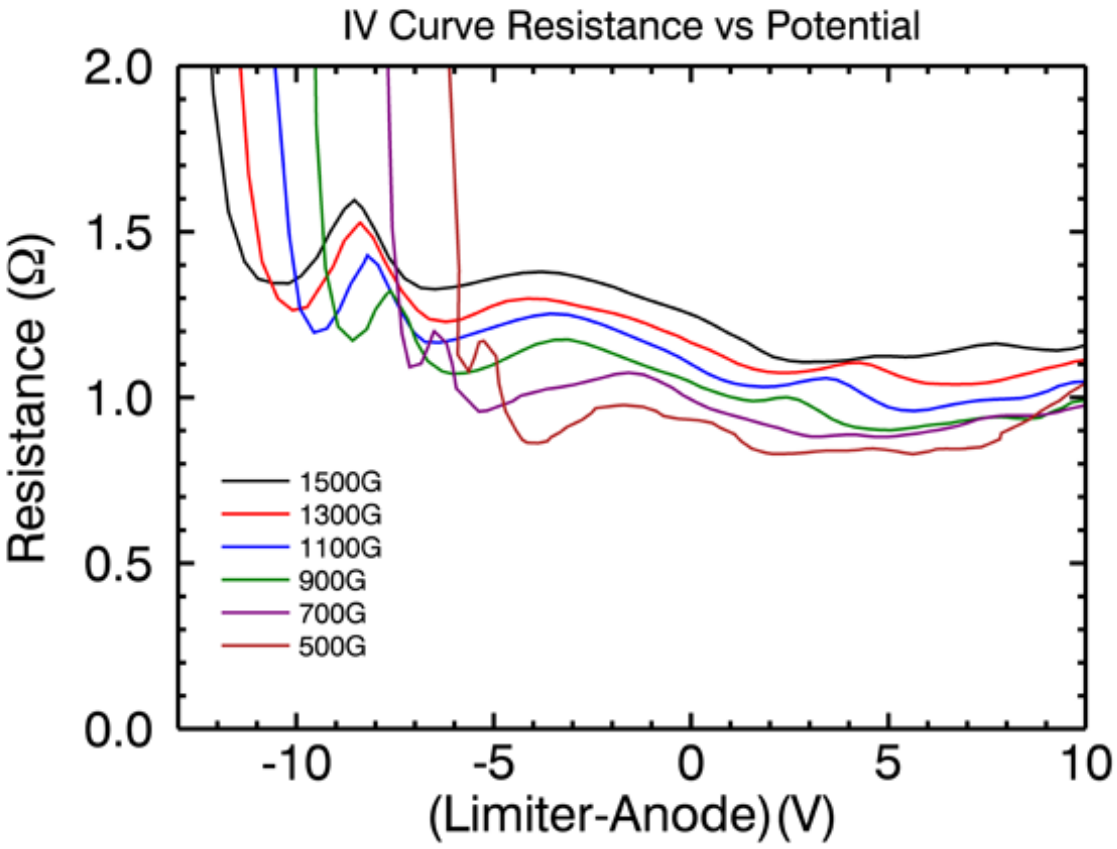

Figure 4.11: Local R vs limiter-anode voltage difference

Plotting current against the anode-limiter difference voltage to produce an I-V curve for the biasing circuit as in Figure 4.10, which shows that plasma resistance changes as the bias voltage is increased. A plot of resistance calculated from the slope of the IV curve and zoomed in on the region where limiter and anode voltages intersect, is shown as a function of limiter-anode voltage potential for various magnetic fields in Figure 4.11. Note how the apparent resistance of the plasma increases with magnetic field, which is consistent with the idea that the conductivity arises from ion-neutral collisions. The average collision step size is on the order of the gyroradius, which is larger for lower fields, and allows cross-field current to occur more easily for lower fields. Also, the asymptotic behavior of the resistance curves is indicative of the power supply voltage dropping below floating potential and thus current going to zero. The trend in field suggests that the floating potential achieved by the limiters decreases with magnetic field. The behavior of the current at low fields and high biases—where the slope falls over—is not completely understood at this time though it may also be due to an increasing collision step-size (i.e. the plasma reaches a point where the collision frequency is so low that the ions are essentially free streaming and thus can have negative resistance or nearly infinite conductivity.)

4.4 Modification of Plasma due to the presence of Limiter Plates

Before getting into the details of how the biasing modifies the plasma, it is worth showing how the presence of the limiters appears to modify the natural flow and turbulence in LAPD.

The introduction of the limiters into the LAPD represents a potentially significant change to the nature of plasma parameters observed on the machine. Though the limiters were designed to be moved completely out of the radial extend of the cathode (approximately 28 cm), the plasma chamber was nevertheless permanently changed. Even when fully retracted, the limiters and annulus remained present for the final 15cm of cylindrical radius. Results from run campaigns before and after the installation of these limiters were made in an effort to document any significant changes to the "'natural"' LAPD plasma.

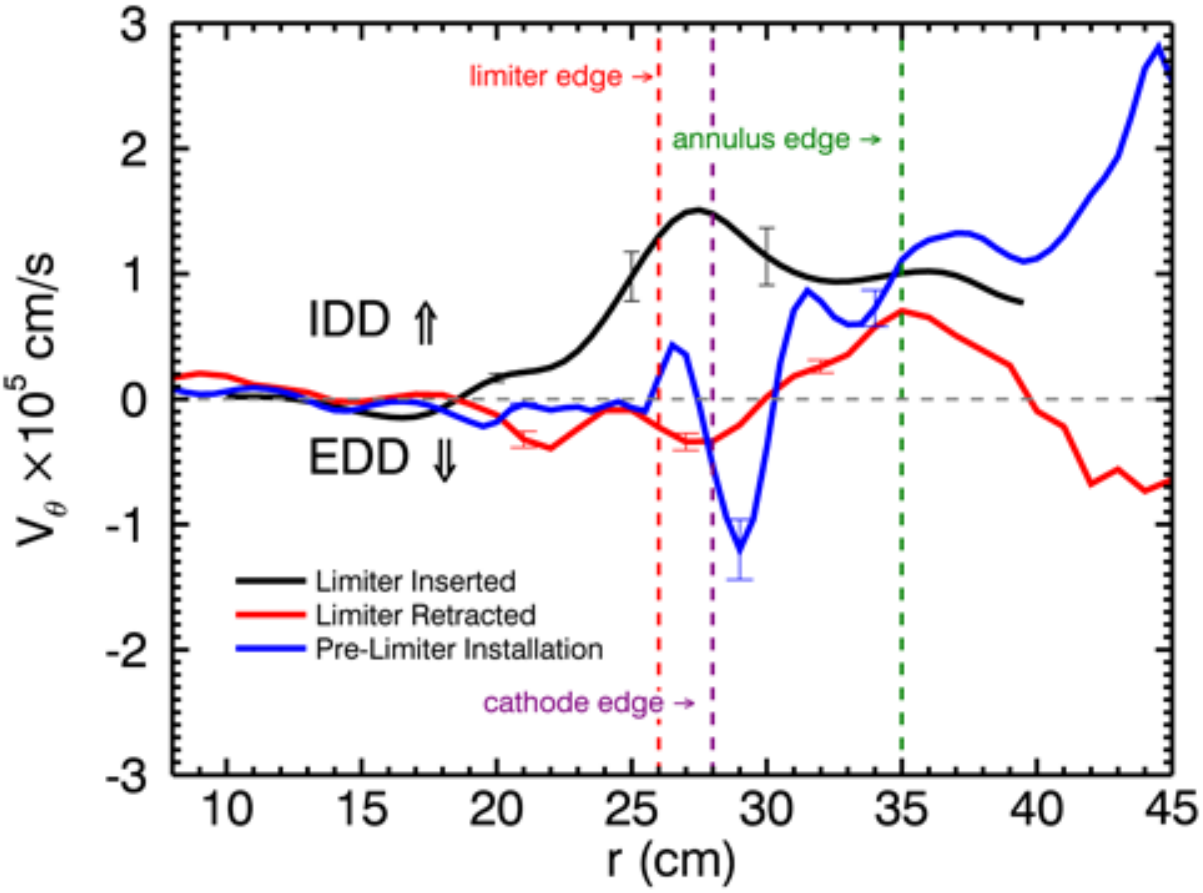

Figure 4.12: Swept-probe measured flow profiles for three limiter arrangements.

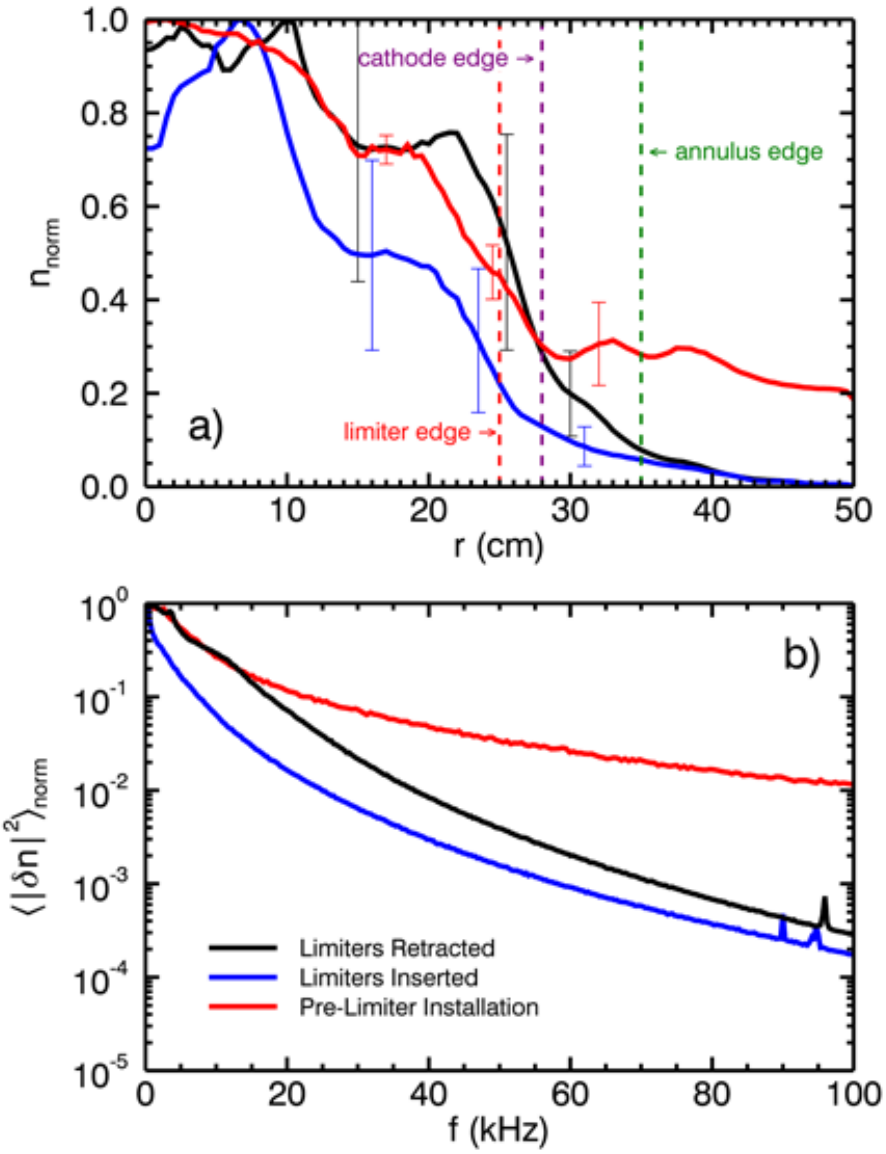

Figure 4.13: (a) Density profiles for three limiter arrangements. (b)Density edge spectra summed over 20-35cm for three limiter arrangements.

Figure 4.12 shows swept-probe measured flow profiles for three different limiter cases. The blue curve shows a flow profile for the LAPD before the limiters were installed. The red curve, then, shows the flow profile with the limiters installed, but retracted behind the annulus. The black curve shows the flow for the limiter inserted up to a radius of 26cm. Without the limiters installed, the flow dips down into the EDD direction just outside the cathode edge, but then reverses into the IDD toward the chamber wall. With the limiters in, but retracted, the flow profile is similar, with a dip in the EDD direction, and reversal into the IDD, but diverges from the limiter-less profile behind 35cm, where the annulus begins. With the limiters inserted, on the other hand, the flow profile is completely changed, with flow peaking in the IDD instead of the EDD. The flow profiles show that the pre-limiter installation flow profile can be recovered with the limiters completely retracted, except, perhaps beyond the annular edge.

The density comparison is similar amongst the three limiter arrangements. Figure 4.13(a) shows density profiles with the same colors corresponding to the limiter state in the previous plot. The profiles are scaled to the maximum value of each curve as each curve is from a different dataset with slightly different plasma conditions. Again, the profiles of the pre-limiter installation density and the limiter retracted density are most similar up to the cathode edge. The limiter-free state appears to have more density in the far edge than the limiter retracted state. The limiter inserted state has a density profile that is reduced in magnitude at almost all points as the limiter overlapping with the cathode source clearly has an effect on how much density is produced in the core.

Comparison amongst fluctuations are made in Figure 4.13(b) for the edge region of 20 to 35cm. The normalized density fluctuation spectra of the pre-limiter state and the limiter retracted state are again the most similar; the curves are nearly identical up to 20kHz, but diverge greatly at higher frequencies. The fluctuation level drops for the limiter inserted state and has somewhat of a steeper decrease in fluctuation amplitude with frequency than the other two cases.

Overall, the comparison shows considerable modifications in flow, density and fluctua-

tions when the limiters are installed and inserted compared to the pre-limiter LAPD state. However, the retracted limiters are able to replicate the pre-limiter LAPD plasma at least up to the annulus edge at 35cm.

4.5 Setting Plasma Potential, Flow and Shear with Biasing

The main objective of the biasing limiter is to modify the plasma potential so as to control the azimuthal, cross-field flow and flow shear. It is instructive to first look back at biasing experiments before the limiters were installed when the entire main chamber was biased. In the chamber biasing experiments, the middle three vacuum chamber sections are isolated from ground by removing all the bolts that attach the sections together. The chambers are already isolated from the main chassis frame by plastic blocks and the individual sections have Kapton tape inserted between them. The bolts then serve as the only conductive connection between the sections. The end bell chambers are permanently grounded through the turbo vacuum pumps. Once isolated, the middle chamber is biased using the same circuit as described above. While the probes inserted into the middle chamber are normally isolated from the chamber by the vacuum O-rings, they are also given an isolating coating to help prevent against arcing during biasing.

The results from chamber biasing on LAPD have been published [38, 39] for 400G magnetic field cases. The papers showed the ability to drive large flows in the electron diamagnetic drift direction as well as a reduction in cross-field transport and improved radial confinement with increased flow and flow shear. However, fine control of the flow could not be achieved for reasons discussed now, eventually leading to the development of the limiter biasing method.

For more direct comparison with the later results of this dissertation, Mach number flow profiles and density profiles for a magnetic field of 1000G are shown in Figure 4.14 during a biasing experiment just before the installation of the limiters. The chamber biasing clearly has an overall effect on the plasma flow; however, much of the flow modification occurs

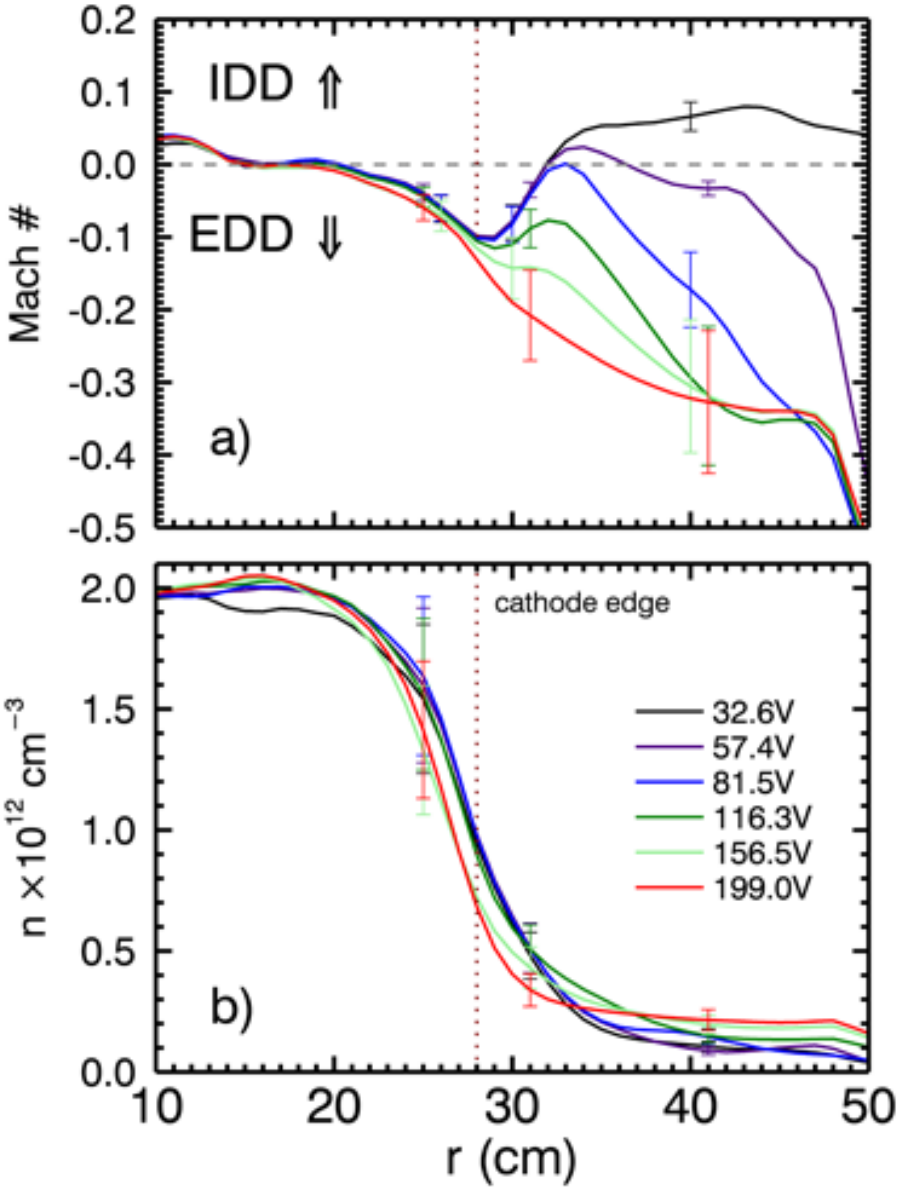

Figure 4.14: Profiles of (a)Mach number and (b)density for various power supply bias voltages at 1000G for a dataset prior to the installation of the limiter plates and annulus where biasing was achieved using the entire middle section of the LAPD chamber.

beyond 35cm where the plasma density tends to be very low. It is not until a power supply voltage of 120V is reached the flow profile changes significantly in regions of high density, $r < 30$cm. Beyond this bias, the flow continues to be modified in the region near the cathode edge at 28cm. At these high biases, the density profile near the cathode edge also begins to be affected; a very slight steepened gradient can be observed. At lower biases, the density is only slightly affected, and only in the region beyond 30cm.

While the flow profile can be modified using the chamber biasing technique, flow does not penetrate radially until a high bias is reached—about 120V. Thus, the chamber biasing technique can access only two flow realms: an unbiased state, and a strongly biased, high flow state. This results in, like in the published rotation studies, threshold behavior for modification of the flow, density and turbulence. The root of the problem is traced back to how the flow develops through cross-field current. In order for the plasma to be rotated, a torque must be applied. In this case, the torque is due to a $j \times B$ force with the current density supplied by the biasing circuit. With the chamber biasing, the ion current must cross a span of nearly 22cm of fairly low density plasma until it can be met by electron current flowing along the anode-connected field lines and connect the main biasing circuit loop. For low biases, the current only can penetrate a short distance and apply a torque only on the outer regions of the plasma. Eventually, a high enough bias is reached that cross-field ion current can penetrate all the way to the plasma core, and from that point on, can apply an increasingly larger torque on the plasma, supplying the flow and flow shear needed for modification of turbulence and transport.

The benefit of using limiters inside the chamber rather than the chamber itself is the ability to address this current penetration problem. By inserting the limiters radially into the plasma, the gap through which ion current must flow—limiter-connected field lines to anode-connected field lines—is extremely reduced. Even at low biases, and thus low current, there is full current penetration and the torque applied to the plasma can be observed from small values on up to the high values observed in the chamber biasing experiments.

Thus, the new limiters are able to more finely set the plasma potential a region of high

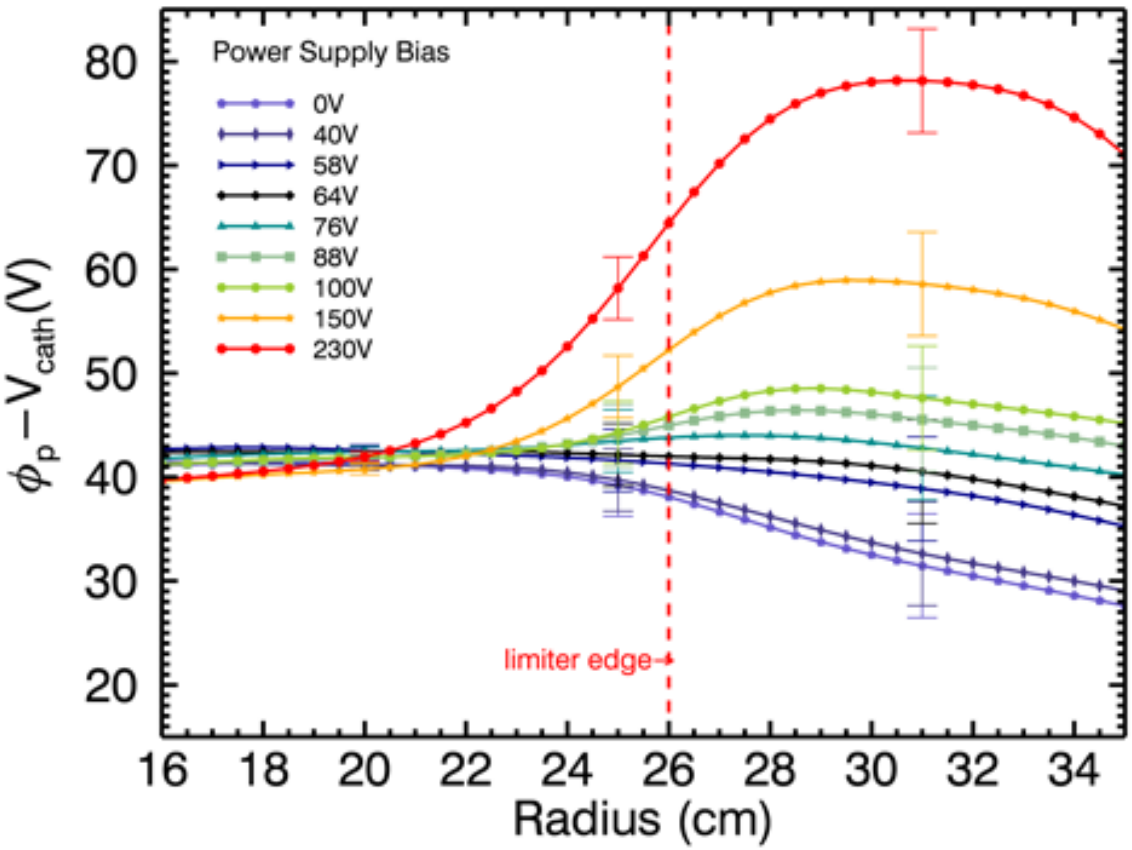

Figure 4.15: Plasma Potential profiles

density just around the limiter edge and further radially toward the chamber edge as shown in Figure 4.15 measured using the swept Langmuir technique again at a field of 1000G. In these limiter biasing experiments, the aperture of the limiters is set to be about 26cm, which is just inside the edge of the cathode. The boundary conditions are completely set by the limiters and the cathode. The annulus, serves as the boundary condition for regions beyond 35cm and in these experiments is left floating (i.e. only the movable quarter-plate limiters are biased). The rest of the chamber itself is connected to ground through the bolts to the end-bell chambers.

For this dataset, 30 biases were used and Table 4.1 and 4.2 show the bias number, power supply setting bias with the corresponding steady-state limiter minus anode voltage and steady-state total bias current. Note that the limiter minus anode voltages and bias currents are slightly different from those reported in Section 4.3. This difference arises from the fact that the anode-cathode potentials relative to ground were slightly different for the voltage monitoring data used in Section 4.3 and the probe data used in the remainder of this dissertation.

The unbiased plasma potential profile (Power Supply potential = 0V) is nearly constant at about 35V through the core, up to a few centimeters short of the limiter edge. Beyond the limiter edge, the plasma potential drops continuously toward the chamber edge. The profiles only begin to be modified when the power supply voltage surpasses the plasma potential referenced to the cathode, with a slight increase in the plasma potential beyond the limiter edge. Increasing the bias causes this outside plasma potential to continue to increase as well, until a power supply bias of about 64V is reached, whereupon the potential is nearly constant across the limiter edge and into the far edge. Meanwhile the core potential, which is ultimately set by the anode-cathode circuit, remains nearly constant. Increasing further, the plasma potential outside the limiter begins to be higher than the core potential, reaching values nearly twice that of the core.

From the plasma potential profiles, it is straightforward to calculate the velocity profiles

Table 4.1: Bias Index (0-15) listing Power supply setting, limiter-anode voltage difference and current as measured in the steady-state regime.

Bias Index	Power Supply (V)	Lim-Anode (V)	Bias Current (A)
0	0	-9.728	-0.636
1	20	-9.711	-0.715
2	40	-8.478	5.306
3	43	-7.681	8.775
4	46	-6.989	12.327
5	49	-6.398	15.892
6	52	-5.694	19.518
7	55	-4.951	22.884
8	58	-4.106	26.012
9	61	-3.171	29.036
10	64	-2.282	32.137
11	67	-1.674	35.455
12	70	-0.880	38.895
13	73	-0.199	42.749
14	76	0.425	46.642
15	79	1.076	50.769

Table 4.2: Bias Index (16-29) listing Power supply setting, limiter-anode voltage difference and current as measured in the steady-state regime.

Bias Index	Power Supply (V)	Lim-Anode (V)	Bias Current (A)
16	82	1.632	55.410
17	85	2.272	60.469
18	88	2.732	65.053
19	91	3.175	69.564
20	94	3.677	74.050
21	97	4.156	78.855
22	100	4.656	83.948
23	105	5.620	91.967
24	110	6.688	99.824
25	120	8.363	116.163
26	130	9.920	133.365
27	150	13.144	168.727
28	200	21.223	262.743
29	230	25.905	322.421

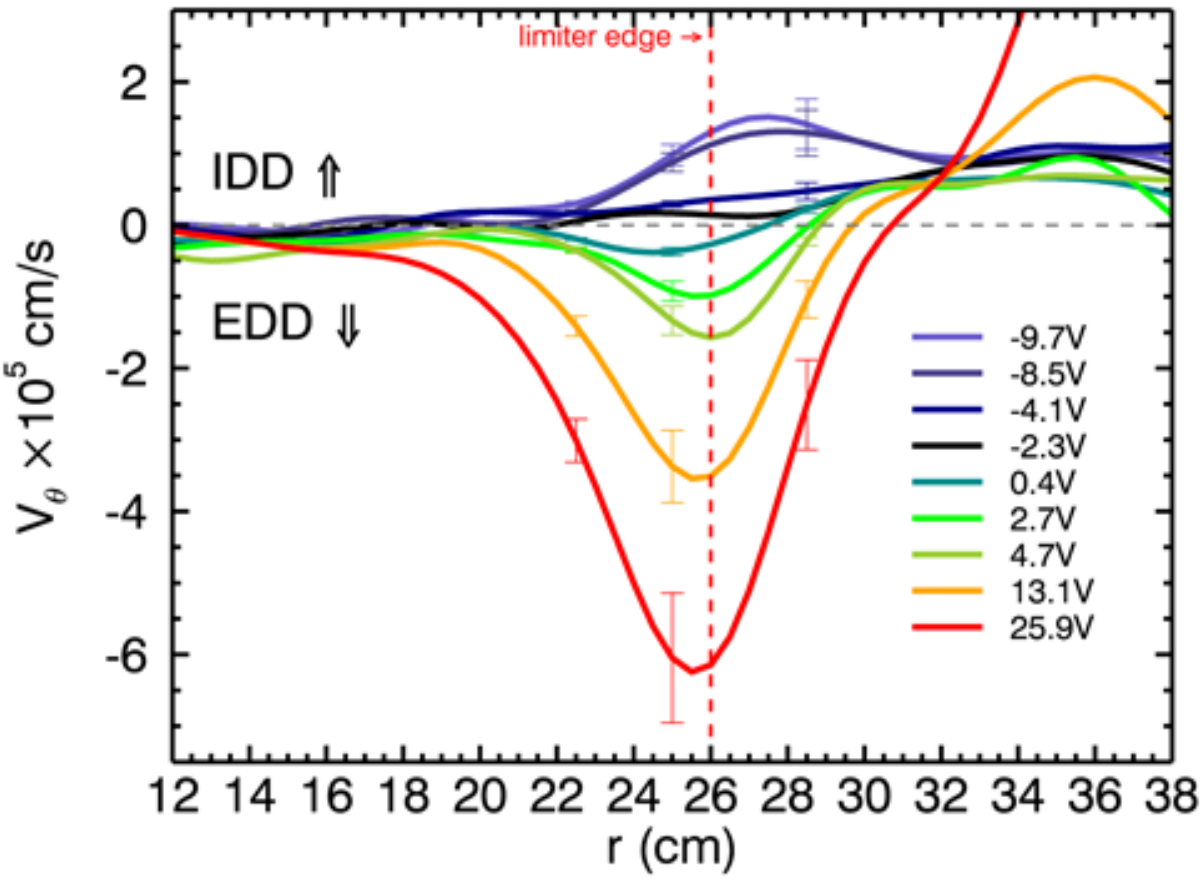

Figure 4.16: Azimuthal Velocity profiles from gradient of radial plasma potential profiles with each color corresponding to the voltage difference between the limiter and the anode.

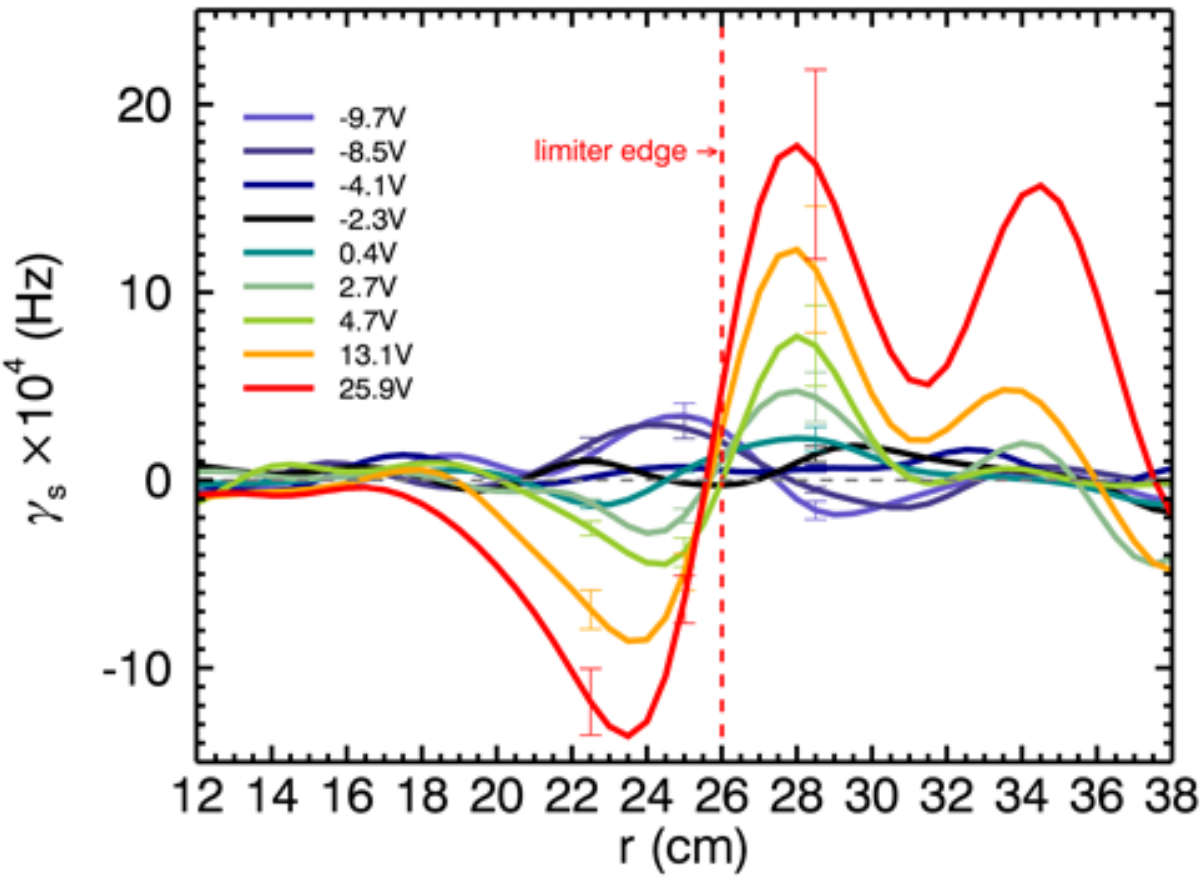

Figure 4.17: Shearing rate profiles from radial gradient of azimuthal velocity profiles with each color corresponding to the voltage difference between the limiter and the anode. These profiles are the derivative of those in Figure 4.16

Table 4.3: Limiter and Bias Circuit Settings Summary. Note: the bias trigger delay is in reference to the main trigger which is set by achieving a threshold current in the plasma discharge.

Setting	Value
Bias Trigger Delay	8ms
Bias Duration	5ms
Lim Insertion Spacing	4in
Limiter Edge	$r = 26$cm

assuming the rotation is due solely to $E \times B$ flows, as in,

$$v_\theta = \frac{c(E \times B)}{B^2} = \frac{cE_r}{B_0} = \frac{-c}{B_0}\frac{d}{dr}\phi \tag{4.1}$$

where c is the speed of light and B_0 is the background magnetic field. The resulting profiles are shown in Figure 4.16 for varying biases. The decreasing plasma potential of the unbiased case results in a spontaneous rotation in the ion diamagnetic direction peaked just outside the limiter edge. As the bias increases and the plasma potential levels out, the overall flow goes to zero. As the biasing pushes the plasma potential outside the limiter edge above that of the core, the resulting flow is reversed into the electron diamagnetic direction, peaking at the limiter edge. The sound speed, $C_s = \sqrt{(T_e)/m_i}$ ranges from 7×10^5cm/s in the far edge ($T_e \sim 1$eV) to 1×10^6cm/s in the core ($T_e \sim 4$eV). In high biases, the electron temperature can reach 6-7eV near the limiter edge. In these regions, C_s can reach up to 1.4×10^6cm/s. The peak flows then have Mach numbers, $M_\theta = V_\theta/C_s$, on the order of 0.5-0.75.

The flow shear as defined by

$$\gamma_s = \frac{d}{dr}v_\theta \tag{4.2}$$

is also finely modified by the increase in limiter bias as shown in Figure 4.17.

4.6 Cross-field Current and Pedersen Conductivity

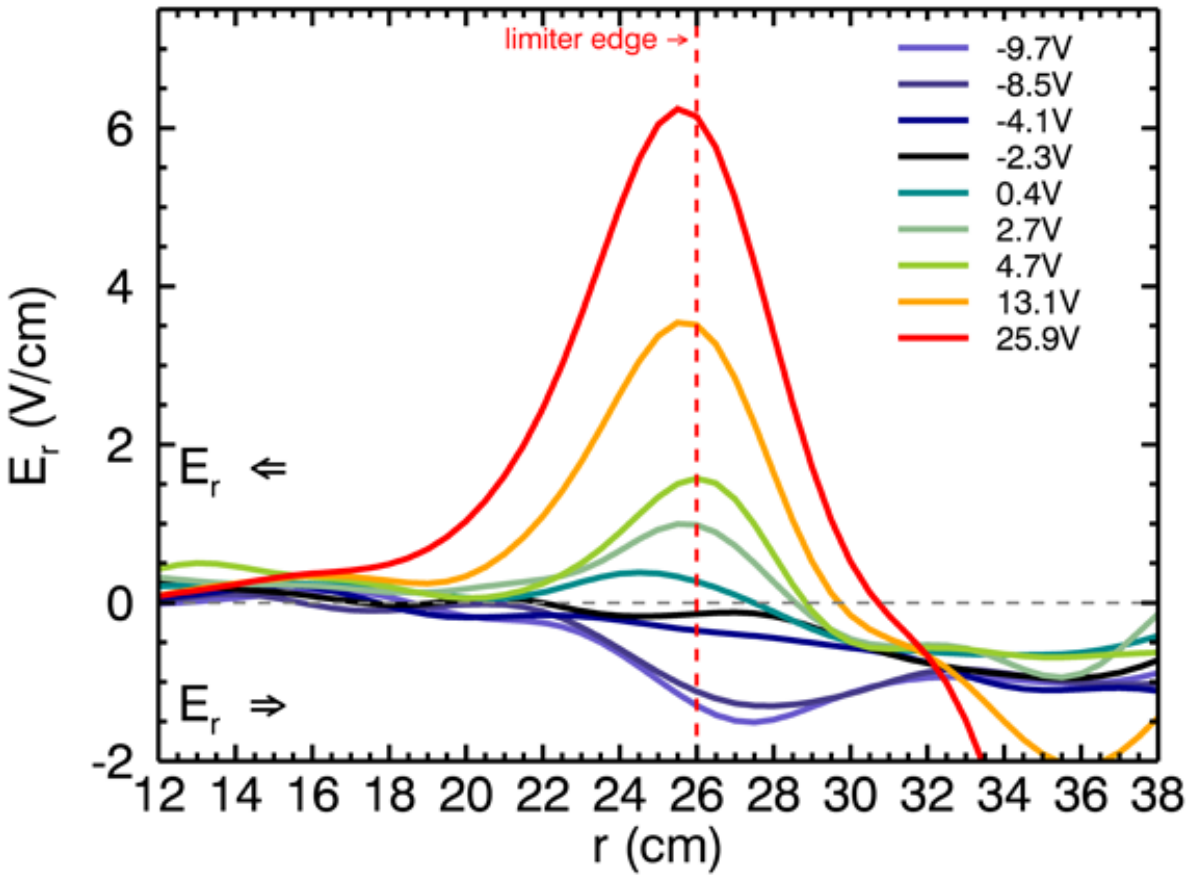

Figure 4.18: Swept determined Electric field profiles from the radial gradient of azimuthal velocity profiles with each color corresponding to the voltage difference between the limiter and the anode.

Finally, from the plasma potential, the radial electric field can be calculated and is shown in Figure 4.18. These measured electric fields can be assumed to be generated by a cross-field current density, $J_\perp = \sigma E_r$ where the conductivity, σ incorporates the physics of the plasma in question. As discussed in Chapter 2, the mobility of particles perpendicular to the magnetic field is dependent on gyroradius. Given that $\rho_i >> \rho_e$ for LAPD plasmas in general, it can be assumed that the dominant cross-field current carrier will be the ions and the collision mechanism that facilitates cross-field transport the ion-neutral collision rate. This means

that the conductivity for this plasma can be approximated as Pedersen conductivity defined as,

$$\sigma_P = \frac{ne^2\nu_{in}/m_i}{\nu_{in}^2 + \omega_{ci}^2} = \frac{nec\nu_{in}}{B\omega_{ci}} \tag{4.3}$$

where the fundamental quantity is ν_{in}, the ion-neutral collision rate. This quantity can be calculated as

$$\nu_{in} = n_0\sigma_s^{(i/n)}v_i \tag{4.4}$$

Neutral density, n_0, can be found using the equation of state, $p_0 = n_0kT$ with the neutral helium temperature assumed to be about $T = 300K$ and its pressure measured as 1.28×10^{-4} Torr. The ion velocity can be either determined by estimating the ion temperature as in, $v_i = \sqrt{T_i/m_i}$—typically $\sim 1eV$—or by approximating the ion velocity as the measured flow velocity, v_θ. The final factor, σ_s is the cross-section for collisions between the helium ions and the neutral helium atoms. This quantity must be measured experimentally; a value of 5×10^{-15} cm^2 is used [38].

A profile of ion-neutral collision frequencies is determined using these quantities where for each bias, the larger of the ion velocities—temperature based or flow based—is used. This yields a range of values: 10.038kHz$< \nu_{in} <$12.638kHz.

To be able to compare directly to the estimated cross-field current, a radial location must be chosen so that any calculated current density can be converted into current. Since the electric field peaks at the limiter edge, this point can be used as this reference (r=26cm). The Pedersen current that would be needed to give rise to the experimental electric fields, then, is plotted in blue (absolute value) in Figure 4.19(a) along with the estimated cross-field current from Figure 4.8(b) in black triangles as a function of limiter-anode voltage difference. Also compared is the predicted velocity at the limiter edge the measured cross-field current to the measured velocity shown in Figure 4.19(b).

For positive difference values (limiter potential $>$ anode potential), the peak plasma rotation is in the electron diamagnetic drift direction, the Pedersen current is a decent match to the estimated measured cross-field current given the level of error. The plot emphasizes

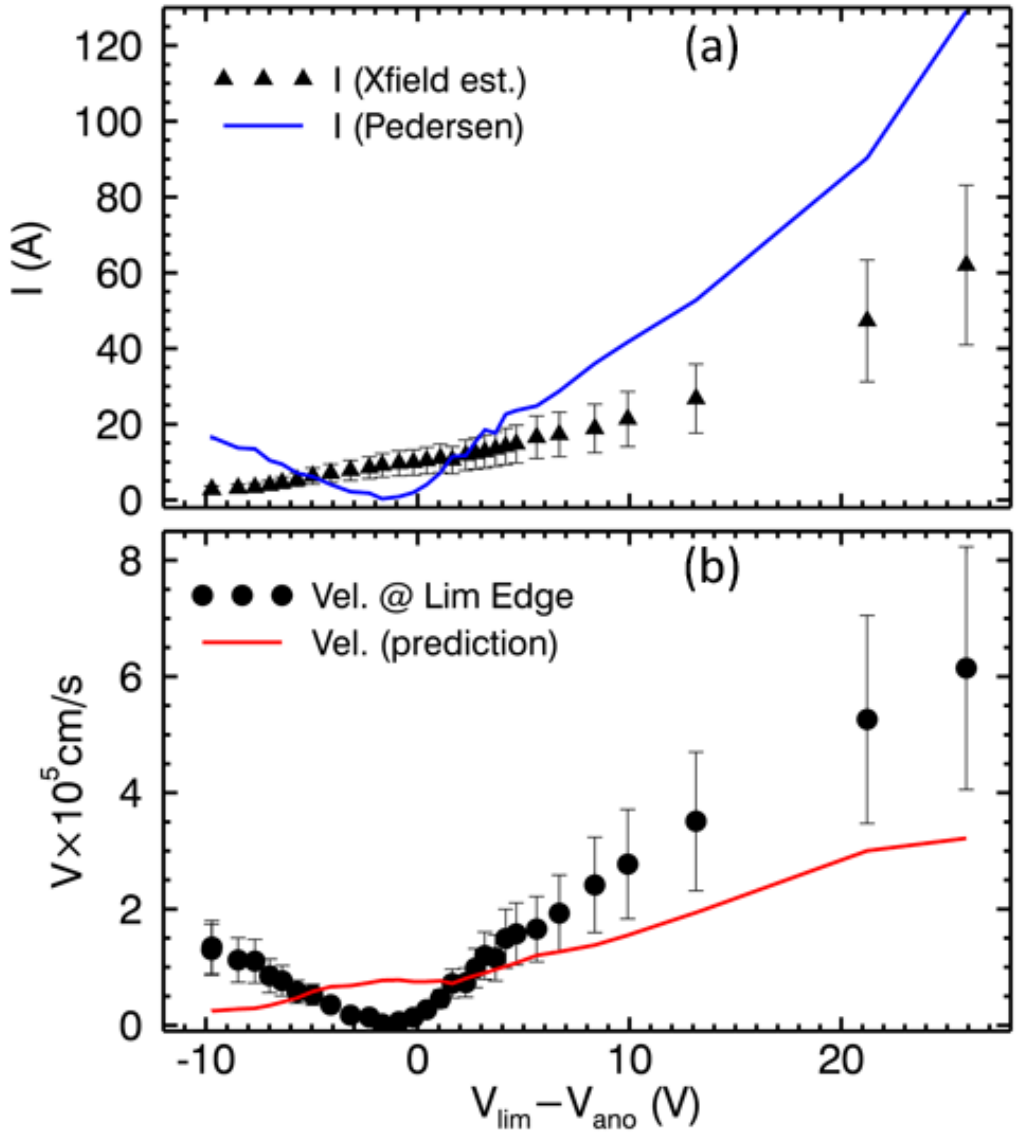

Figure 4.19: (a) Current as expected given Pedersen conductivity as a function of limiter anode potential difference compared to the cross-field current estimate. The solid blue curve is the Pedersen current found using an ion-neutral collision frequency that is calculated using relevant experimental values. The black triangles to the cross-field current estimate. (b) Velocity at the limiter edge as expected given the measured cross-field current (red curve) as compared to the actual measured limiter edge velocity (black circles).

that most of the current measured in the bias circuit likely does not travel cross-field and produce rotation, instead reaching the cathode through other paths, such as the direct limiter-cathode path along the field lines. However, beyond a voltage difference of 3V, the predicted current begins to outpace the estimated cross-field current. This could suggest that the method of estimating the cross-field current by subtracting the initial current from the saturated current is not completely accurate and that some of the initial current value should be put into the cross-field current column. Nevertheless, the predicted cross-field current never exceeds the amount of current injected for positive voltage differences showing that the bias current is always enough to account for the cross-field flow and resulting electric fields generated. The fact that the predicted current for the unbiased case is higher than the injected current suggests that the measured electric field here is due to a cross-field current not generated by the biasing circuit (or at least not measurable). The origin of this spontaneous generation of flow is an entire thesis topic on its own, though biasing techniques can be used to investigate it.

Lastly, the distribution of velocity profiles is compared in Figure 4.20 which shows a set of biased velocity profiles all normalized to the peak velocity of each curve. If the relationship between injected current and velocity were linear, one might expect that the width of the curves would be self-similar. This appears to be mostly true for the moderately biased states up to about a limiter-anode voltage difference of 4.2V (light blue curve). However, at higher biases, the width of the profile begins to widen indicating deeper penetration of the current from the limiter edge into the plasma core. This possible non-linear effect has not been characterized or modeled and could be an avenue of further study.

Given the establishment of a range of flow and sheared flow profiles, the next step is to examine how plasma parameters such as density and temperature are modified as well as how fluctuations and turbulence are affected. A more global look at the changes is taken up in Chapter 5 while a local analysis of changes with shearing rate is made in Chapter 6.

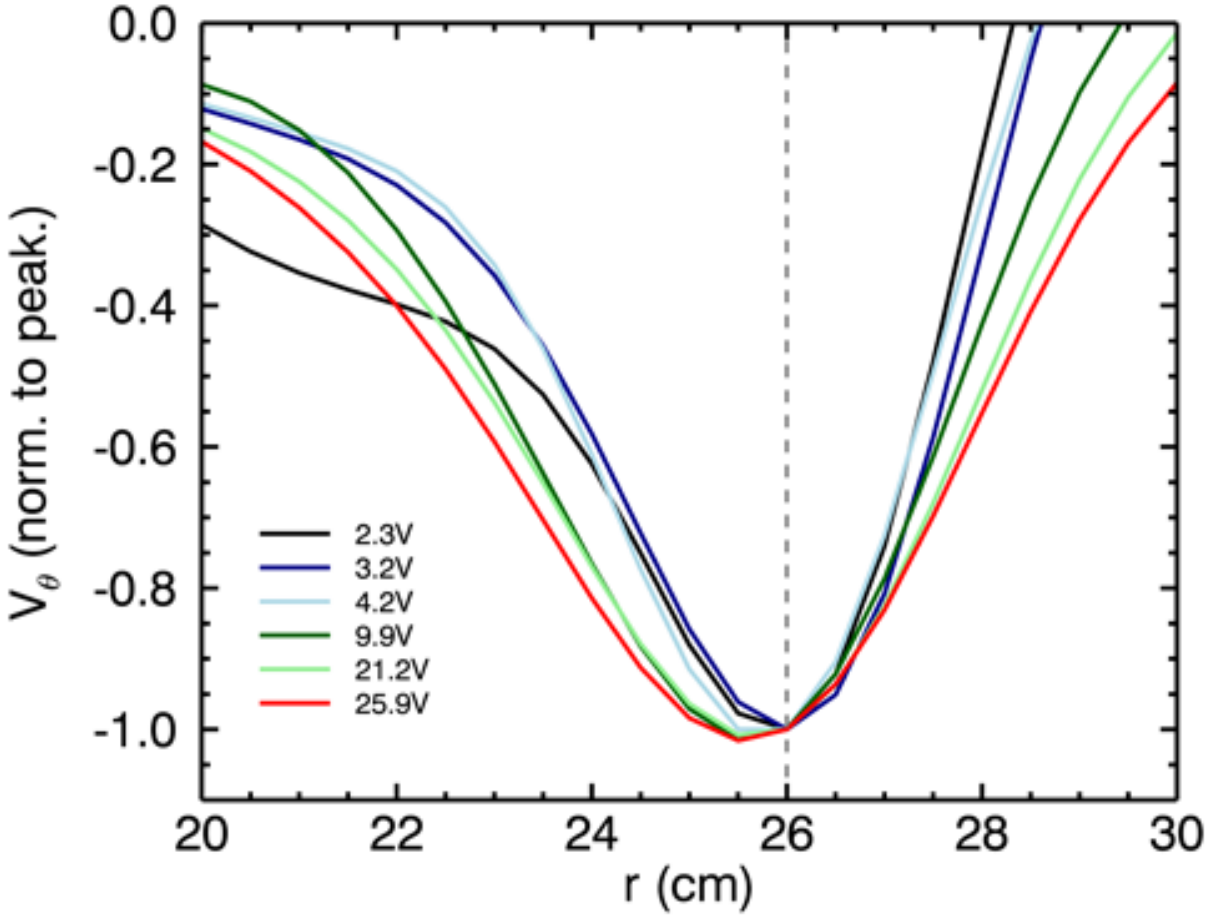

Figure 4.20: Velocity profiles normalized to the peak velocity in each curve. Self similar profiles suggest a linear relationship between current and velocity while the spreading shape of the profiles at higher biases suggest a non-linear effect.

CHAPTER 5

Modification of LAPD turbulence with steady-state biased rotation

Given the establishment of a range of flow states using the limiter biasing setup, as discussed in Chapter 4, the response of radial profiles of density, temperature, and the fluctuation profiles of density, floating potential, and radial velocity are examined in this chapter. Moreover, the effect on radial transport will begin to be explored by looking at changes to the radial profile of particle flux and diffusivity. The structure of the turbulence will also be explored through correlation plane studies. The discussion will expand into an analysis of how the instabilities that contribute to the plasma turbulence are changed through both experimental observations—fluctuation ratios, identification of free-energy sources, and two-point correlation spectral density—and through comparisons to the linear growth rates calculated by a Braginskii fluid model.

5.1 Profile Modification

5.1.1 Density and Temperature Profiles

The modification of the plasma potential profile has already been covered in the previous chapter, as this is the basis for how the rotation states on the LAPD are established, as well as the flow and flow shear profiles. The density reaches a steepened steady-state profile for flow states with significant flow and flow shear. This change will be shown to correlate best to flow shear and is ultimately due to a response in radial particle transport. The initial, unbiased density profile is shown as the black curve in Figure 5.1 in a range of 15cm to 35cm.

The density in the core is around $1.5 \times 10^{12} cm^{-3}$ and falls fairly evenly and consistently to a little less than $5 \times 10^{11} cm^{-3}$ at 35cm where the biased limiter plate transitions to the floating annulus plate boundary condition. The limiter edge is at 26cm and represents the transition from core region (plasma source connected field lines) and the edge region (limiter-connected field lines). Thus, while the core extends radially to 26cm, the density begins to decrease nearly 10cm before the edge, indicating a significant level of cross-field transport in the unbiased state.

With a slight increase in bias voltage, such that the limiter voltage sits about 5 volts below the anode, particle transport is actually enhanced and the density profile relaxes with core density decreasing and edge density increasing. It will be shown in the next chapter that this confinement degradation corresponds to the minimum shearing state of the plasma flow. As increased bias begins to drive flow in the EDD direction, the particle transport begins to decrease again. The density profiles first return to the level of confinement seen in the unbiased state, but then further steepens as flow is driven beyond the level that can be achieved spontaneously. The level of confinement saturates to a profile consistent with the yellow curve in Figure 5.1.

An interesting feature appears for the highest biases inside a radius of 20cm. At this range, the density profile exhibits a hollowed profile (a decrease in density toward the core) rather than the monotonically decreasing density observed in the unbiased and lower biased states. The nature of this change is not fully understood although there are possible implications related to non-local transport. This is discussed further in the section on particle flux.

The electron temperature as measured by swept Langmuir probe is also modified by biasing, but in a different way then the density. The unbiased electron temperature is shown in Figure 5.2 for three biases: unbiased, small bias near zero rotation, and a high bias with strong rotation. Unlike the density profile, the temperature profile maintains its core temperature of about 4eV very close to the core-limiter transition, then drops rapidly beyond the limiter edge to an edge value of about 1eV. This is consistent with the dominance

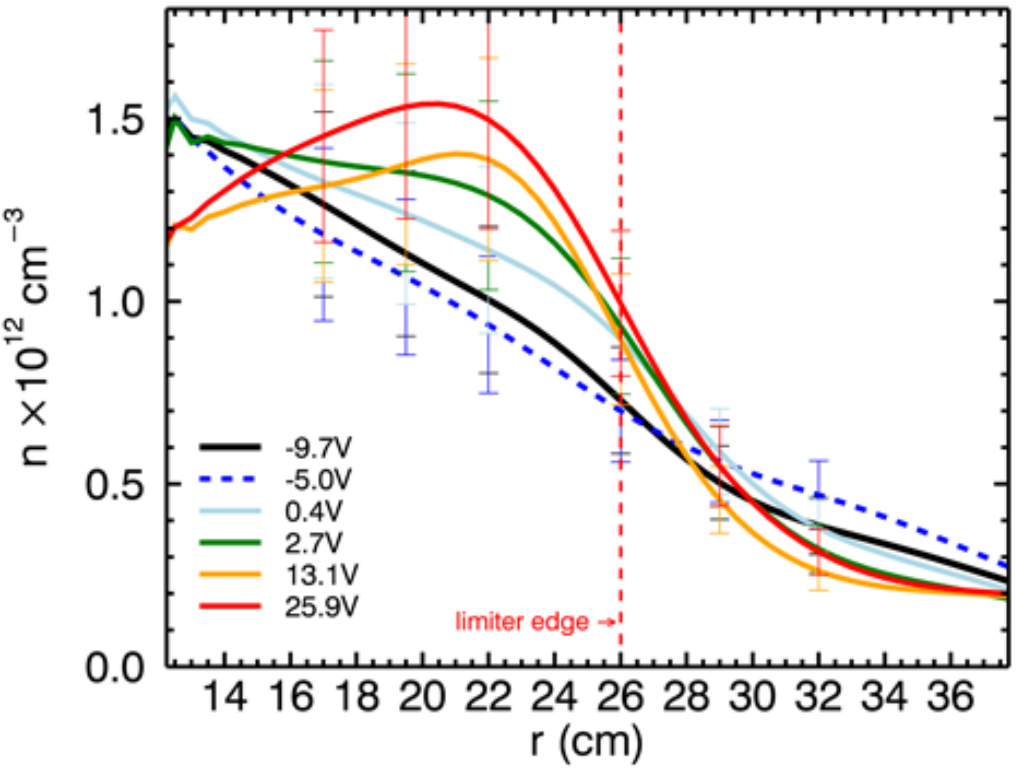

Figure 5.1: Density profiles for various bias states with each color corresponding to the voltage difference between the limiter and the anode.

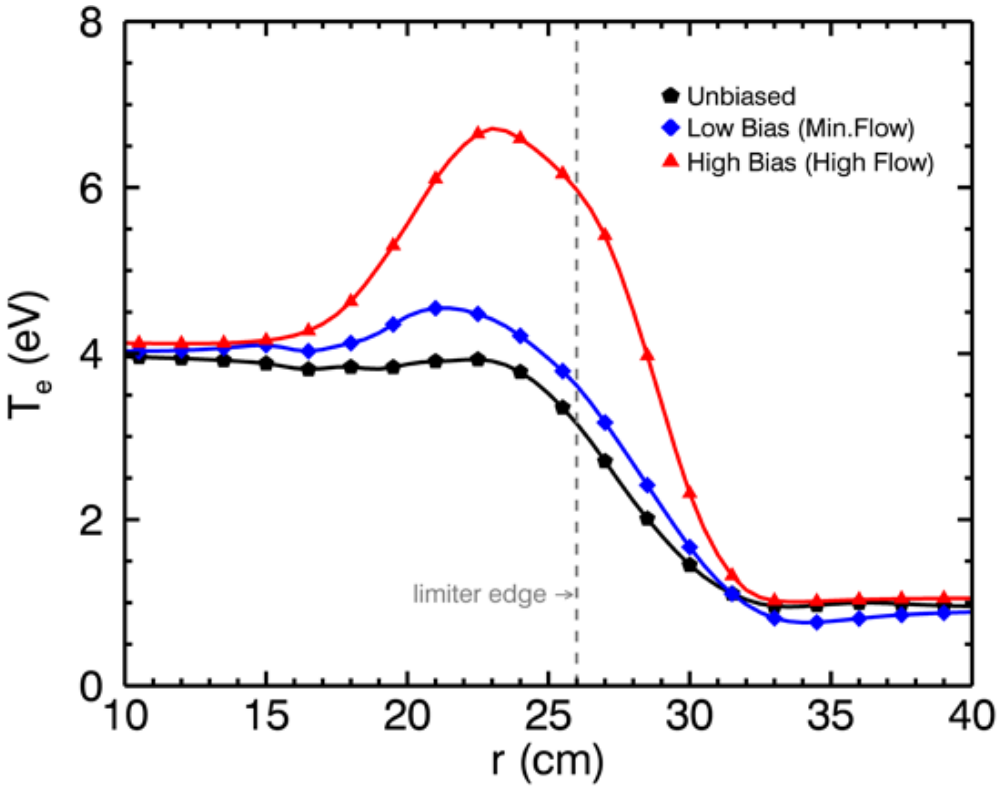

Figure 5.2: Electron temperature profiles for various bias states with each color corresponding to the voltage difference between the limiter and the anode.

of parallel over perpendicular heat transport in LAPD. The electron temperature which is sourced by the fast electrons from the anode is not carried radially easily by the electrons and instead is transmitted quickly down the field lines to the ends of the machine. Unlike the density profile, the temperature profile does not exhibit a steepening as the bias and rotation is increased. Instead, there appears to be heating just inside the limiter edge. For biases associated with the minimum shearing state, a peak temperature of about 4.5eV is observed about 4cm inside the cathode edge, while a slight increase in temperature is seen everywhere else in the profile. The core temperature of 4eV is very slightly modified above its unbiased value. With high biasing, there is a peak temperature of nearly 7eV just inside the cathode edge. By a radius of 30cm, the temperature of all three measured biases reaches about 1eV. Thus, despite increased electron temperatures at the edge, the heat transport properties of the plasma do not appear to be significantly changed by the biasing or plasma rotation.

It should be noted that the actual measured values of swept electron temperature were actually twice the values listed in Figure 5.2. The reason for this discrepancy is thought to be an error in the electronics (such as a burned out resistor on the digitizer which would have caused a factor of two error due to the loss of 50Ω impedance matching) but has not been definitively tracked down. There are a number of justifications for assuming the halved temperature profiles are correct. One, previous rotation runs have yield core swept temperature measurements on the order of 4-5eV rather than the 8eV measured in this dataset. Two, the amount of electron temperature heating suggested by the high bias case (nearly 14eV) is highly unlikely given the amount of power being injected into the plasma by the biasing circuit. Taking the maximum amount of biasing current measured($\sim$ 350A)and the highest potential difference between cathode and limiter plates ($\sim$ 70V), the maximum possible power injected by the biasing scheme is $P_{bias} = 24.5kW$. However, given a plasma discharge that injects 3.5kA of current across initially $\sim$ 70V between anode and cathode, the background power is $P_{dis} = 245kW$. Thus, the biasing represents an injection of power on the order of 10% that of the intial discharge. Given an initial temperature of 8eV, 10%

more power is unlikely to yield 6 more eV. On the other hand, it is conceivable for an intial plasma of temperature of 4eV to be raised by 2-3eV by the injection of such power. The third reasoning involves comparison of data with transport modeling developed by Maggs, Carter and Taylor [38], which will be discussed shortly, but that essentially show that core temperatures of 8-14eV produce vastly more plasma than would be expected, while profiles of 4-7eV fit the data very well.

The nature of the heating is not fully understood, though was observed in previous rotations experiments on LAPD as well [38, 39]. Heating of plasma ions might be expected due to viscous dissipation of the driven flow. Also, increased current along field lines between the cathode and the limiter could increase electron temperature directly, though would be confined to the region behind the limiter. Unfortunately, no direct measurements of ion temperature were able to made for these experiments to verify a change did in fact occur with biasing. Nevertheless, the observed temperature increase is in the electron temperature and the coupling between electron and ion temperatures on LAPD is not high—in addition to the fact that ion temperature is generally much lower than electron temperature. More focused measurements of temperature are needed to fully explain the phenomena and will be discussed a bit further in the discussion of future work.

The fact remains though that an increase in electron temperature is observed in the core and especially just inside the limiter edge. The higher temperature complicates the picture of the density profile since higher temperatures can increase local plasma production. In fact, the density profiles appear to reflect a local increase in plasma production; the yellow curve of density at high bias in Figure 5.1 shows a peak in the density just inside the limiter edge, comparable to the radial location of the temperature increase. Support for this plasma increase comes from calculations using a transport modeling code developed in Maggs et al [38] which predicts the temporal and radial distribution of plasma production given a source and temperature profile and assuming set levels of radial and axial transport. The details of this model are provided in Appendix A. A comparison between experimental data profiles and modeled profiles is shown in Figure 5.3. The unbiased experimental density

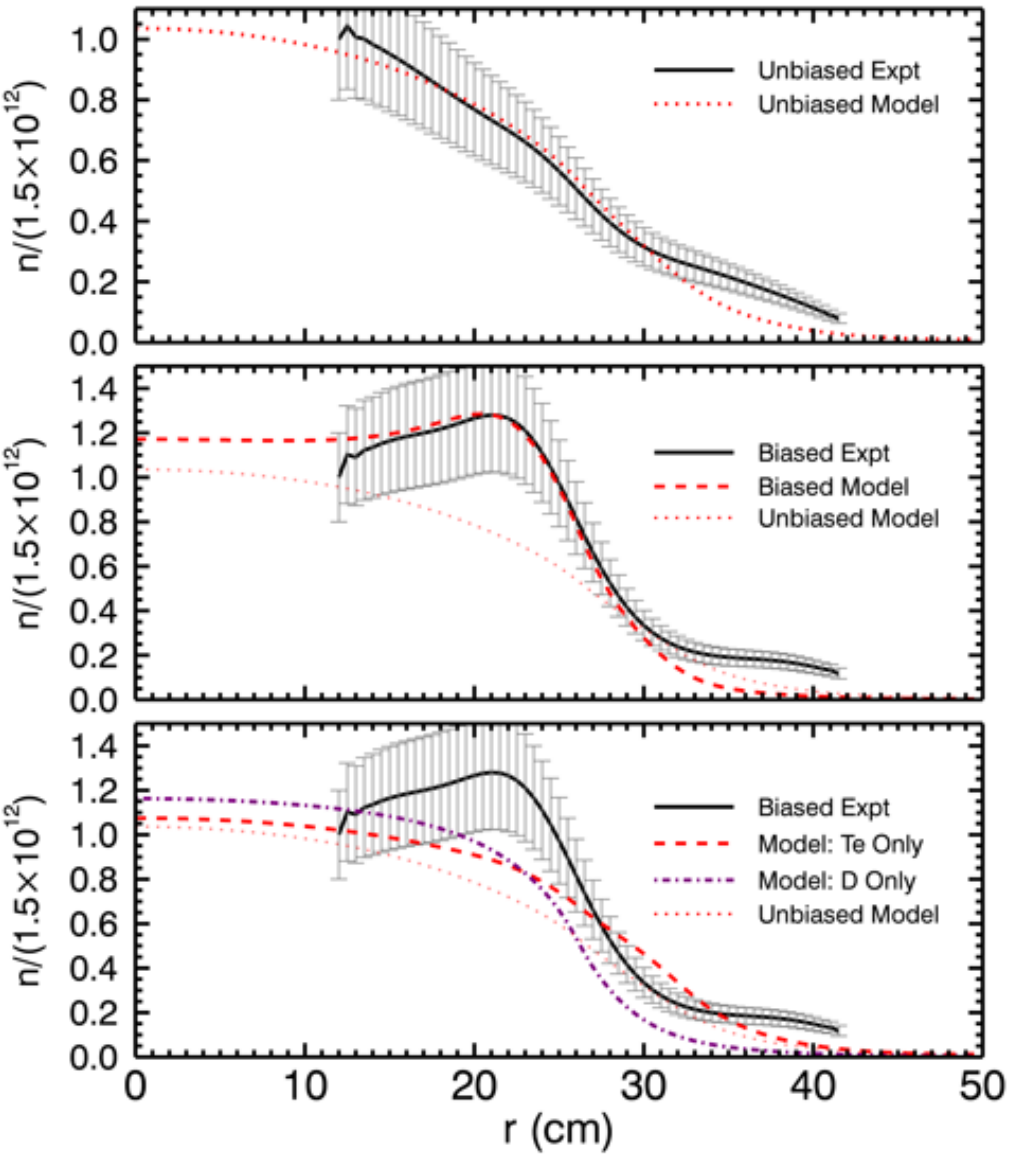

Figure 5.3: Comparison of data to transport models: (a) The unbiased experimental density profile (black curve) with best fit transport model calculated density profile (dotted red curve). (b) The experimental density profile for Bias 27 (black curve) with best fit transport model density (dashed red). The calculated curve in (a) is shown as a reference in (b). (c) The steepened experimental density profile shown in comparison with calculated profiles using only temperature changes (dashed red) or transport changes (dash-dotted purple), again with the original calculated profile shown as a reference (dotted red).

profile in Figure 5.3(a) is matched to the model using a source function radius matched to the limiter aperture opening of 26cm, an endloss rate of $250s^{-1}$ for $r < 26$cm and $500s^{-1}$ for $r > 26$cm, and a diffusion coefficient set to Bohm diffusion,

$$D = D_B = \frac{1}{16}\frac{T_e}{B} \tag{5.1}$$

The temperature profile used is the unbiased temperature profile in Figure 5.2. The calculated density profile can be modified by either changing the temperature profile, which changes the plasma production rate, or the diffusion coefficient, which modifies the radial transport, or a combination of both. The changes to the temperature or diffusion coefficient are done immediately (i.e. no gradual transition), but the density is allowed to evolved given these changed parameters eventually reaching a new steady-state profile. In order to match this modified model profile to the experimental density gradient of Bias 27, at an anode-limiter potential difference of 13.1V, both the temperature and the diffusion coefficient must be modified. The best fit, as shown in Figure 5.3(b) is achieved by changing the temperature profile from the unbiased version to a profile that peaks at 6eV and by changing the diffusivity at each radial position from D_B to $0.2D_B$.

If only the temperature profile or diffusion coefficient is changed, the agreement is significantly worse. Figure 5.3(c) show the experimental density profile compared to model curves where only the temperature was modified (red curve) and only the diffusion coefficient is modified (purple curve). The red curve shows increased plasma production compared to the unbiased case consistent with higher temperatures. The purple curves shows a steeper gradient consistent with reduced transport and improved confinement. However, only the combination of these two changes can match the experimental data well. Also, the model is matched to the experimental data for temperature change on the order of 2eV, rather than the 4-6eV that would have occurred has the measured temperature profiles not be modified. This further supports the modification of the measured temperature profiles by one-half as discussed previously.

Comparison to transport modeling shows that in addition to changes in plasma produc-

tion due to temperature increases, the steepened density gradients a result decreased radial transport as well. This leads to an examination of radial particle flux which shows changes in transport from a local point of view, rather than the more global picture a density profile provides. Moreover, once flux is known, an effective source term, $\nabla \cdot \Gamma_r$, can be calculated. These we be discussed in detailed in a later section.

5.1.2 Density, Potential and Velocity Fluctuation Profiles

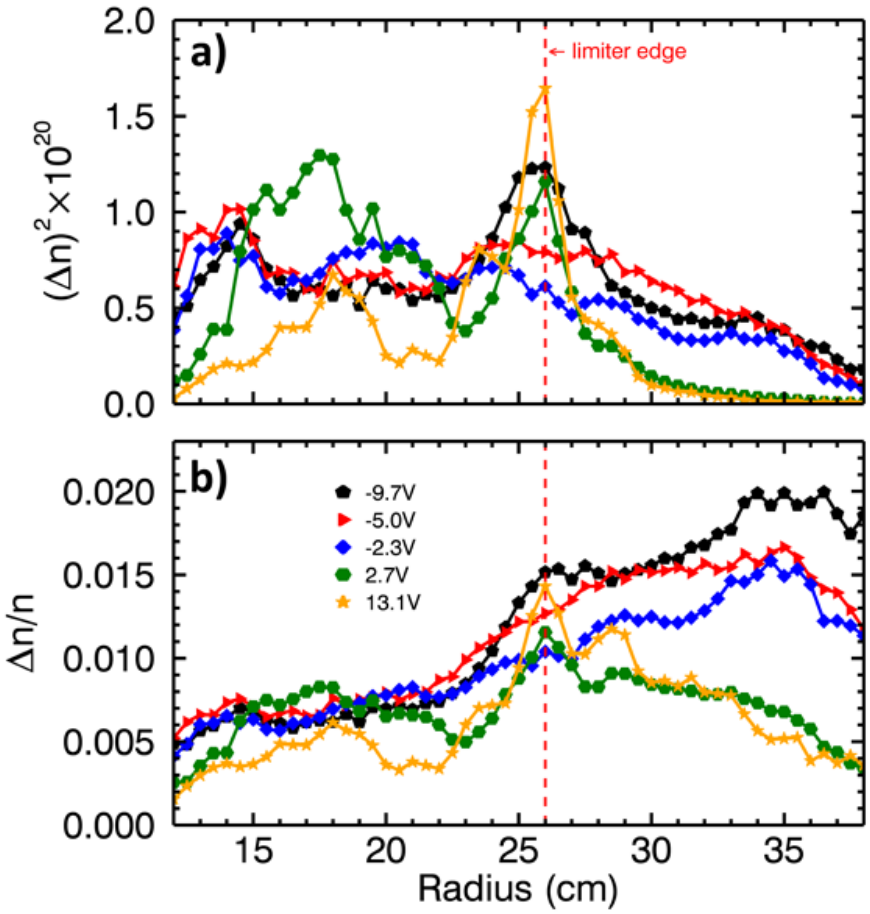

Figure 5.4: (a) Density fluctuation power profiles summed over the frequency range of 0.3125-250kHz for various bias states (b)Density fluctuation amplitude divided by the mean density profile summed over the same frequency band as in (a).

The general effect of biasing on fluctuations profiles is summarized in Figures 5.4 and 5.5.

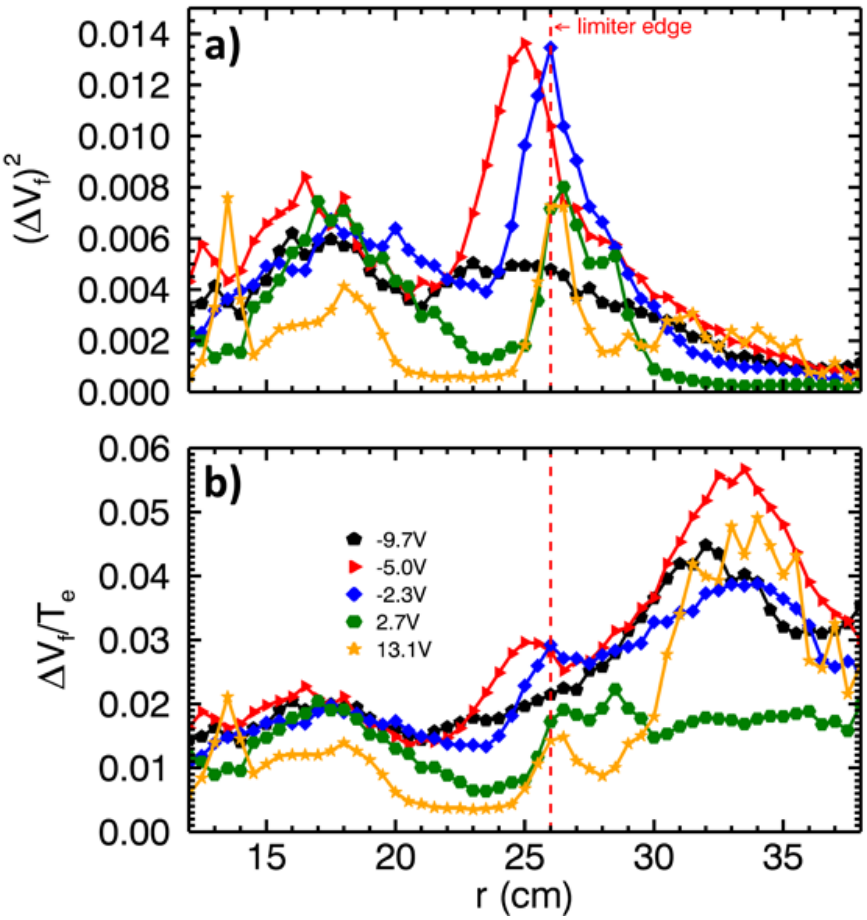

Figure 5.5: (a) V_f fluctuation power profiles summed over the frequency range of 0.3125-250kHz for various bias states (b)V_f fluctuation amplitude divided by the mean density profile summed over the same frequency band as in (a).

The fluctuation amplitude is calculated by first taking the unfiltered Fast Fourier Transform (FFT) of the time-series. For density, the saturated current time-series is scaled to the interferometer density as described in Chapter 3. After subtracting the mean value of the time series (here, 5000 samples or 3.2ms) and taking the FFT, the transformed power, $\tilde{n}(f)$ for example, is summed over a given range of frequency as in

$$\Delta n = 2\sqrt{\sum_{f=f_1}^{f_2} \tilde{n}(f)\Delta f} \tag{5.2}$$

yielding a fluctuation amplitude where for these plots the starting frequency is the second frequency bin from the FFT, $f_1 = 312Hz$ and the second is cutoff at $f_2 = 250kHz$ with $\Delta f = 312.5Hz$. For both Figures 5.4 and 5.5 the top plot shows the summed fluctuation power $(\Delta n)^2$ or $(\Delta v_f)^2$, while the second plot shows the amplitude normalized to the mean density or temperature profile respectively, to give a percent fluctuation value.

Both plots show that fluctuations values are modified by the changing bias, but the trends are different for different radial locations. In the region just beyond the limiter edge, density fluctuations initially increase as the bias is increased and the flow is slowed. They then decrease again as bias and flow are increased. At the limiter edge, the trend is slightly reversed: density fluctuations initial decrease as flow is nulled, but then peaks up again with increased driven flow. This trend is likely due to the growth of a coherent mode that appears at the limiter edge. Floating potential fluctuations have similar trends outside the limiter and at the limiter edge as the density fluctuations. Inside the cathode edge, there are slight modifications in fluctuation levels for both, but a consistent trend is not obvious.

Figure 5.7 show a comparison of density fluctuations overlayed with the density profile for three representative biases. Regions of high fluctuations correspond to regions of gradient in the density profile suggesting that at least some of the fluctuation power is driven by density gradient instabilities such as drift-waves. The changes in fluctuation profile are consistent with changes in the density profile. A shallowing of the profile at the limiter edge corresponds to the decrease in the peak in the fluctuation profile in Figure 5.7(b). The increase in fluctuations outside the limiter edge are instead due to changes in the shearing

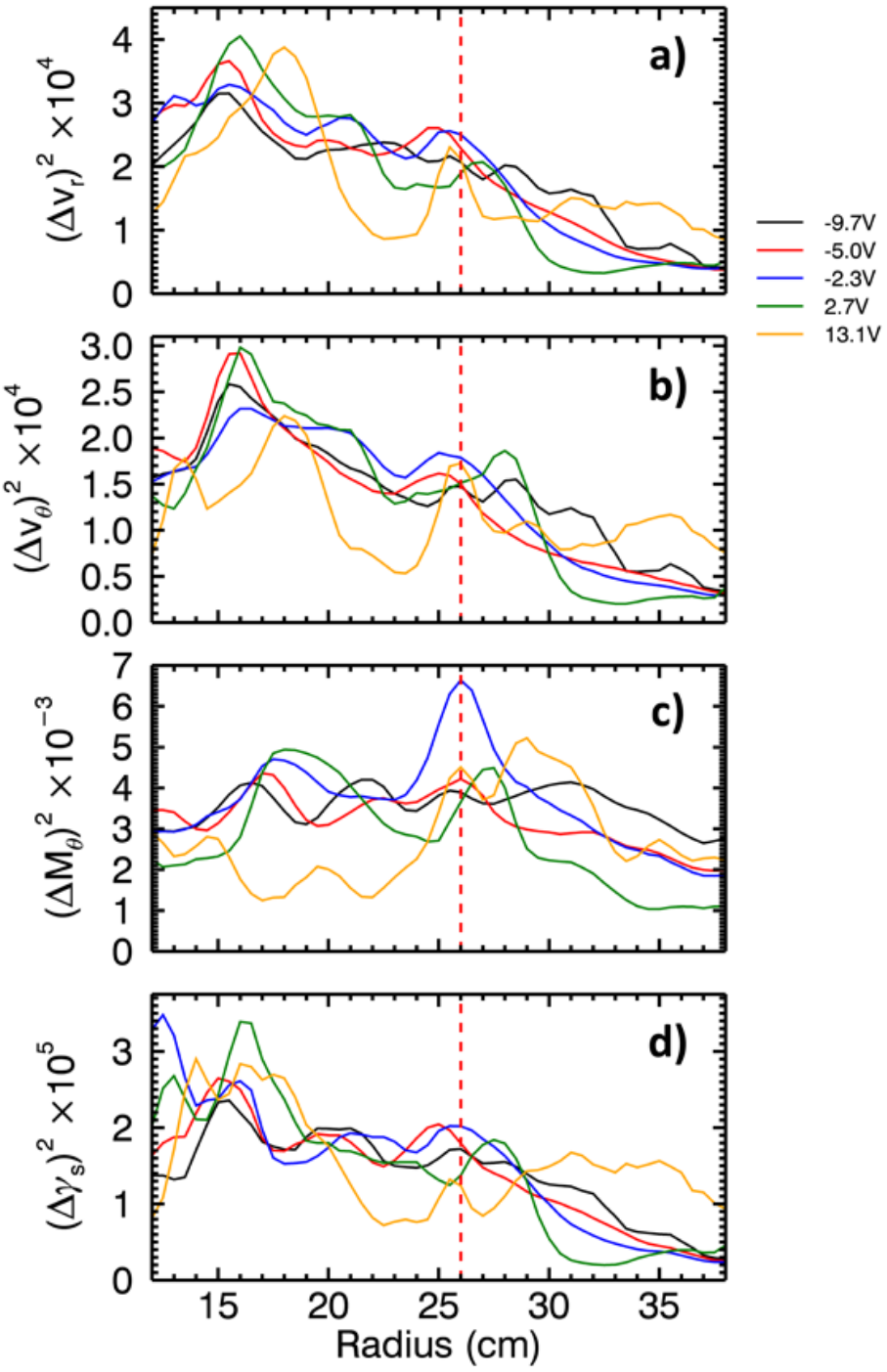

Figure 5.6: Velocity fluctuation power profiles summed up to 250kHz for various bias states including (a) radial velocity, (b) azimuthal velocity, (c) perpendicular Mach number, and (d) shearing rate.

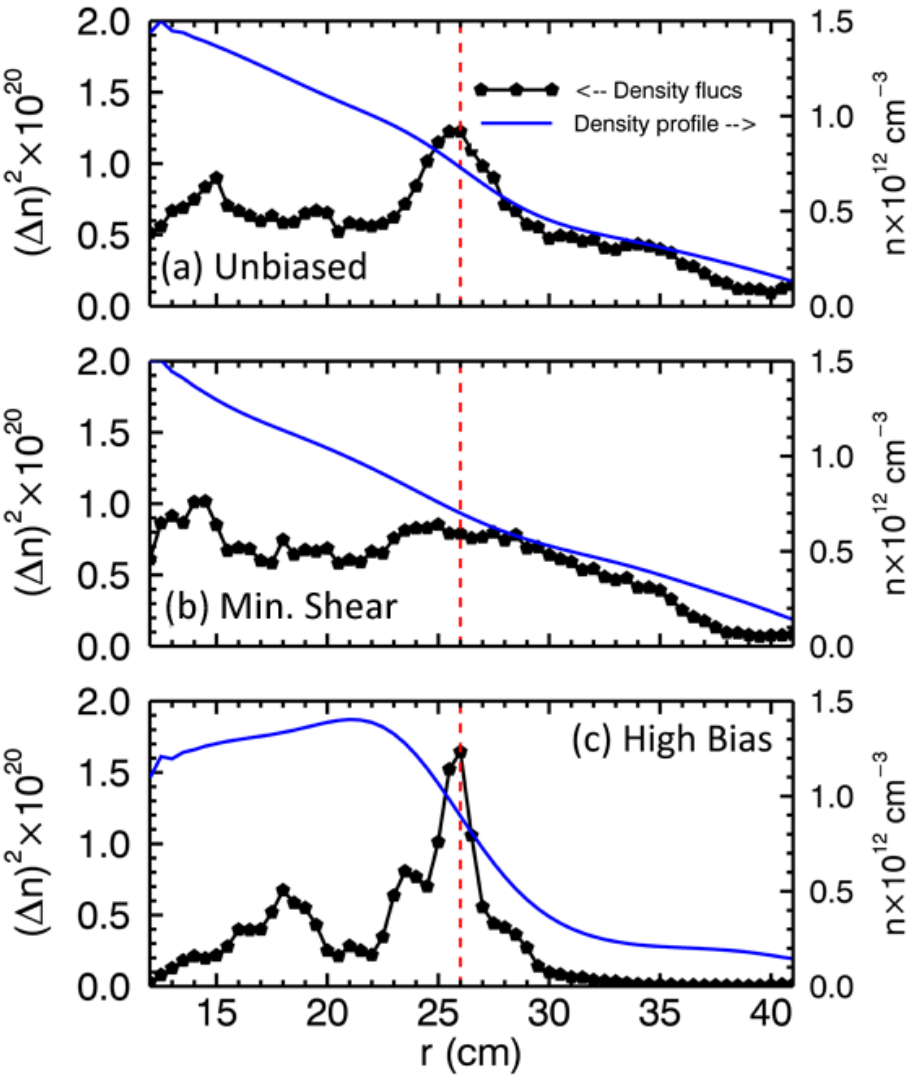

Figure 5.7: Density fluctuation profiles overlayed with the corresponding density profile for (a) the unbiased case, (b) a low bias case corresponding to a low flow state and the minimum shearing rate, and (c) large bias, flow shear.

profile and changes in turbulence suppression rather than directly due to the change in the instability drive. In the high bias case, the peaked fluctuation profile returns with the advent of a coherent mode. Inside 20cm, where the hollowed density profile appears, a peak in the fluctuation profile appears in the middle of the outward pointing gradient.

A similar plot for fluctuating velocity power of various types is shown in Figure 5.6 as well as shearing rate fluctuation power. The top two plots show a radial and azimuthal velocity fluctuation power determined from the times-series of electric field fluctuations calculated from the two V_f measurements as discussed in Chapter 3. The third plot shows perpendicular Mach number fluctuation power. The last plot displays the fluctuation power of a shearing rate measurement made using the 9-tip flux probe (rather than the swept plasma potential) as described in Chapter 3.

The main observation from these plots is the fact that biasing does not change the velocity fluctuation levels very much especially in the region surrounding the limiter edge. In the highest bias shown, the effect of the coherent mode at the limiter edge does appear, but it is not as pronounced as in density or floating potential. The Mach probe fluctuation power does show a peak at the limiter edge for the -2.3V bias case. This corresponds to the lowest flow state and is likely due to errors in the Mach probe measurement that become more pronounced at low flow values.

5.1.3 Particle Flux and Diffusivity Profiles

Turbulent particle flux is a correlation calculation that determines how much density on average is advected by turbulent velocity fluctuations at a given point. That is, symbolically, particle flux is

$$\Gamma_p(r) = \langle n(r,t)v(r,t)\rangle \tag{5.3}$$

where n—density—and v—velocity—are functions of time and position and the brackets indicate a time average. The particle flux of most interest here is the radial particle flux which can be determined by specifying $v(r,t)$ as v_r in Equation 5.3. Physically, this quantity

represents the likelihood for a parcel of density to be moved radially inward or outward by the plasma flow. The measurement of flux can be calculated spectrally as was discussed in Chapter 3. The flux here is integrated over frequencies between 350Hz to 100kHz.

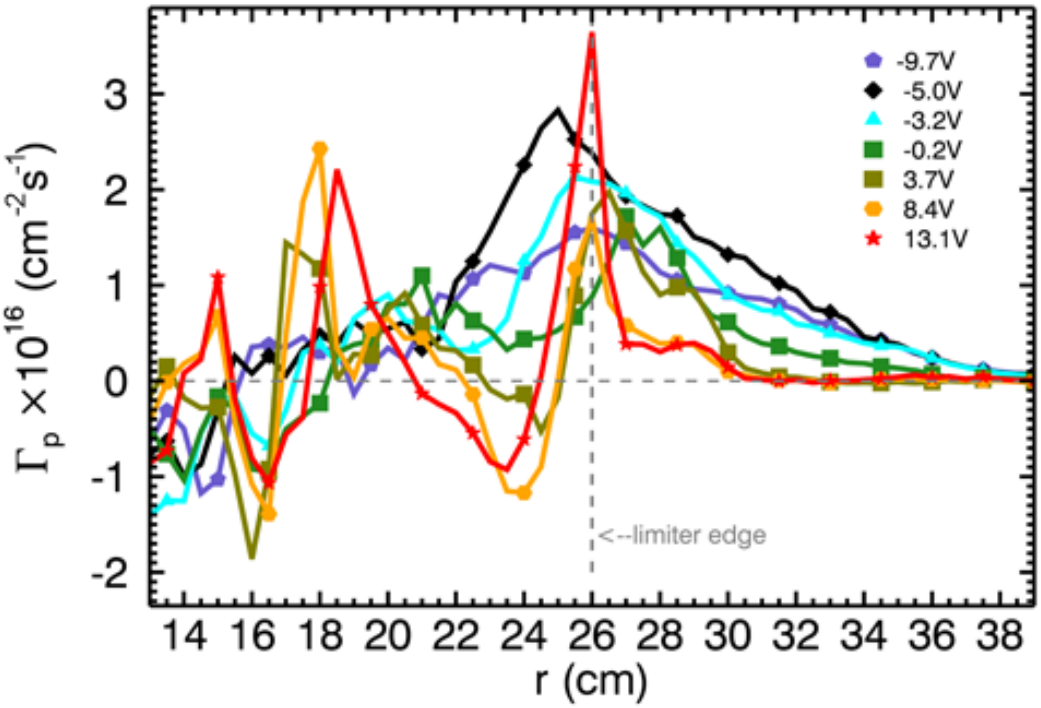

Figure 5.8: Particle flux profiles for various bias states with each color corresponding to the voltage difference between the limiter and the anode.

Figure 5.8 shows radial profiles of Γ_p for increasing biases. The blue, pentagon-marked curve shows the unbiased flux profile, indicating an average flux around $1.5 \times 10^{16} cm^{-2}/s$ for 13 to 39cm which corresponds to the evenly decreasing gradient region of the density profile. A constant flux such as this is consistent with the type of density profile that develops—smoothly and evenly decreasing. At a bias where rotation is nullified, the flux profile increase by about 50% overally while the peak, located just inside the limiter edge, reaches a value about twice the peak of the unbiased state. This global increase is indictative of a wide-spread change in transport properties rather than a local change due to local increase heating.

While the peak flux may be enhanced by the increase temperature bump seen in the blue curve of Figure 5.2, there is increased particle flux in regions where the temperature has not changed such as radii beyond 30cm.

The picture becomes somewhat more complicated with higher biases. While the teal curve for a limiter-anode potential difference of 3.2V appears to return to the something close to the unbiased profile—just as the density profile at this bias appears to match the unbiased density profile—biases beyond this state introduce both increased rotation and shear as well as slightly increased temperatures just inside the limiter edge.

At the higher biases, the changes in flux appear to be less global. The flux profiles of the higher biases, such as the orange and red curves of Figure 5.8, show significant decreases in local particle flux especially in regions of high shearing rate (20-24cm and 27-31cm), but increased flux just inside the cathode edge, and peaked flux at the cathode edge. This observation is in contrast to conclusions made by Maggs and Carter [38, 39] which showed that changes due to shearing rates were global—that is, even if the sheared flow was relatively localized, the transport changes would be observed widespread. The contrasting results may arise from the difference in magnetic field: the previous experiment was conducted at 400G rather than 1000G. This means that the radial correlation length of the earlier data was generally wider and may have allowed for better "communication" of the effect of the shearing rate. Another difference may be the effect of the coherent modes which appear at the limiter edge and produce increased fluctuations in density which were not observed in the previous experiment. These modes appear with flow in the EDD direction and are discussed in more detail later in this chapter. There may also be a small contribution from increased plasma production due to peaking temperature just inside the cathode edge (temperature increase in previous rotation studies were only observed outside of the cathode-source region).

Negative flux for high biases in regions within the cathode edge are also observed. Negative values are only achievable for this measured flux if the crossphase between density and radial velocity fluctuations is negative. It will be shown in Chapter 6 that the suppression of density fluctuations is the main contributer to decrease transport, at least in the region out-

side of the limiter edge, but this observation of negative flux shows that crossphase changes due to biasing may also play a role in transport changes. It can also be an indication of non-local transport. This possibility will be discussed in more detail later.

The measured particle flux profiles can also be used to calculate an effective source for the radial transport of particles, written as,

$$S_{eff} = \nabla \cdot \Gamma_p = \frac{1}{r}\frac{d}{dr}\left(r\Gamma_p\right) \tag{5.4}$$

where Γ_p is the measured radial particle flux and the second form is specifically for cylindrical coordinates. The effective source profile can indicate a change in plasma production due to biasing. Three calculated effective source profiles are shown in Figure 5.9 for three different bias states—low bias with IDD flow, medium bias with null flow, and high bias with strong EDD flow—all compared to the unbiased source profile. Positive values indicate a source of plasma while negative values correspond to plasma sinks; the units are arbitrary. The main observation is that any amount of biasing appears to have an impact on the plasma source with the the most pronounce affect occurring just inside the limiter edge. This location corresponds to the region of increase electron temperatures that are observed suggesting that this heating is indeed associated with increased plasma production.

While the transport changes in this biasing experiment probably cannot be explained entirely by a simple diffusion model as indicated by the changes in the source, it is is still useful to make calculations of experimental diffusivity, $D_{exp} = \Gamma_p/\nabla n$ in order to compare to local diffusion models such as Bohm diffusion or classical diffusion. Three profiles of D_{exp} are shown in Figure 5.10 for an unbiased state, a low flow state and a high flow state. Each profile is scaled to a profile of calculated Bohm Diffusion using the Equation 5.1. It should be noted that this quantity, D_{exp} is not well defined when $\nabla n = 0$ which for these profiles occurs only in the highest flow state (red) at about 21cm.

The profiles show that as the unbiased state actually has a transport rate that is about $7D_B$ and that by decreasing the flow and flow shear, this transport can be increased to a value more like $15D_B$. High bias and strong driven flow, the transport is reduced to diffusion

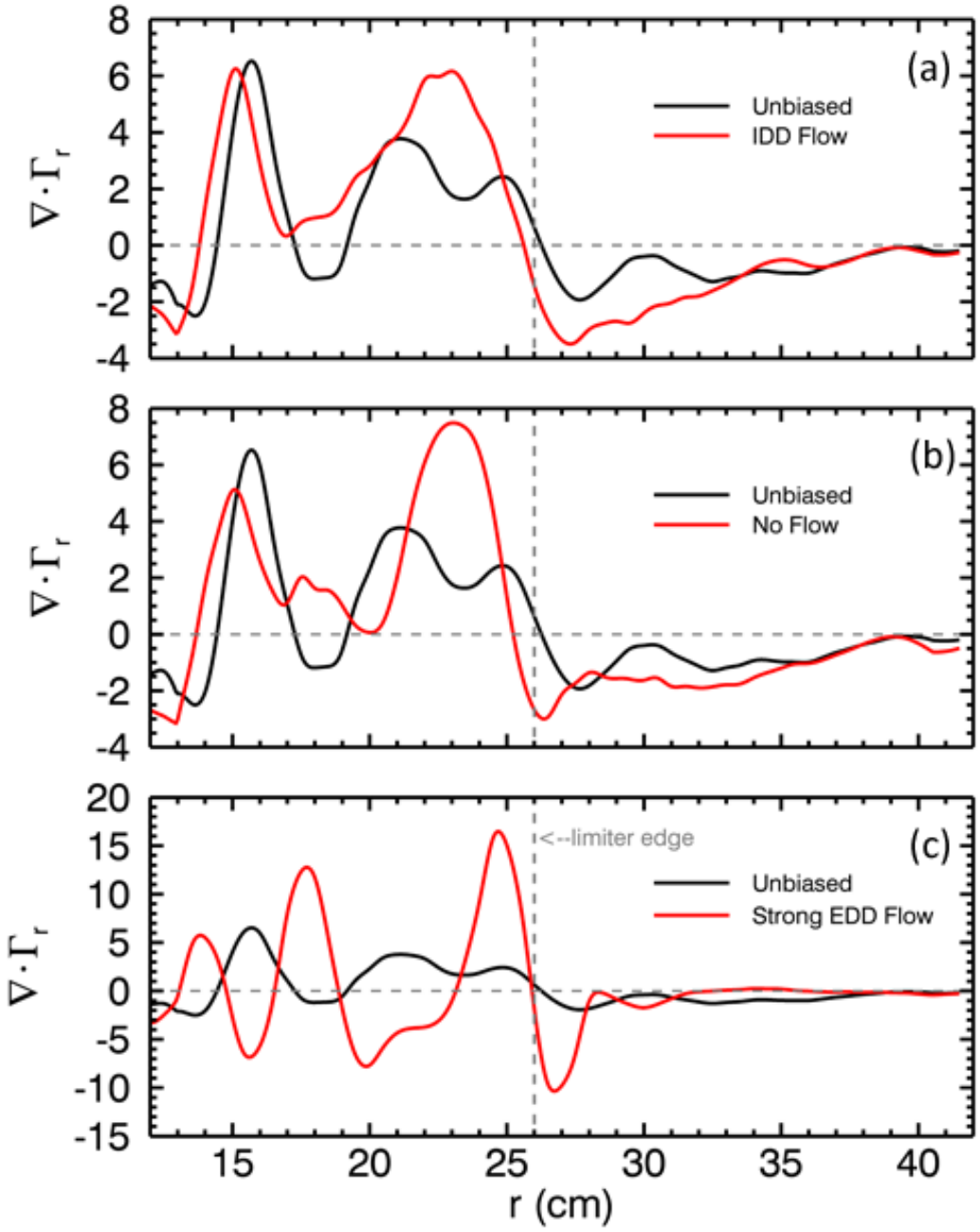

Figure 5.9: Source profiles for (a) a low bias, IDD rotation state, (b) a medium bias, null rotation state, and (c) a high bias, strong EDD rotation state. Each plot has the unbiased source superimposed for comparison.

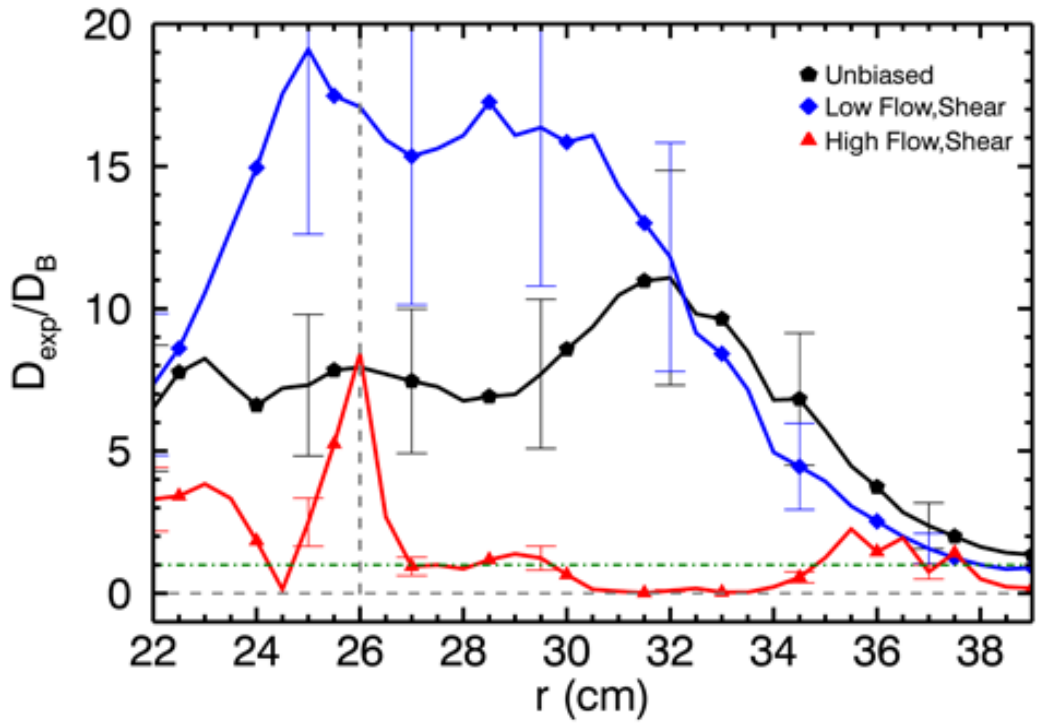

Figure 5.10: Diffusivity profiles scaled to the value of Bohm diffusion for the unbiased state, a zero flow/shear state, and a high-bias, high flow state. The diffusivity is undefined at r=21cm for the higest biases as $\nabla n = 0$ at this point. The direction of the gradient also reverses direction for radial points inward of r=21cm. The gradient for all other points and biases points radially inward.

levels below D_B except for a region around the limiter edge. Note that while particle flux may peak at the limiter edge for the high biases, D_{exp}, though also peaked at the edge, remains consistently below the unbiased profile. Again, this peak in D_{exp} is thought to be the result of the coherent mode at the limiter edge.

As mentioned previously, however, the transport model calculations suggest a much more modest change in diffusion coefficient values: from $1.0 \times D_B$ in the unbiased case to $0.2 D_B$ in the high bias case. The main difference is that this diffusion coefficient is assumed constant across the entire profile while D_{exp} clearly changes with radius. Perhaps the comparison of coefficients would be closer if the model incorporated a profile rather than constant value for diffusivity. Nevertheless, both D_{exp} and the model comparison show a significant decrease in diffusivity with increased bias.

In Chapter 6, the experimental diffusion is calculated only for a region outside the limiter edge and is shown to decrease by a factor of about 30 with increased sheared flow in that spatial region.

The local model suggested by identification of a diffusion coefficient appears to break down in the highest bias and rotation states. Instead, evidence of non-local transport can be observed through a comparison of measured flux and density gradient. In a local transport model, such as a model that follows, $\Gamma = -D\nabla n$, the direction of flux is dictated only by the direction of the gradient. It is local in the sense that transport occurs only due to the environment immediately surrounding it—namely the nature of the gradient driving the transport. Non-local transport, on the other hand, can be due to mechanisms other than the local gradient. This can manifest, for example as observed flux that occurs in a direction opposite of that prescribed by the local gradient. Figure 5.11 shows four bias cases with measured flux overlayed with the corresponding density gradient. A Bohm flux, calculated using experimental temperature and density profiles and Eq 5.1, is also overlayed to demonstrate what a typical local transport model would predict the flux to be. Of the first four plots, Figures 5.11(a)-(c), have density gradients that always point inward, while the last plot, representing a very high bias and strong EDD flow state, has a density gradient

which reverses direction to be outward pointing inside of about 20cm.

A local transport model, such as that represented by Bohm transport, predicts flux that points only in the directing opposite of the gradient. As shown by the red curves in Figure 5.11, the predicted Bohm flux is always outward for (a)-(c) while reverse direction in (d). The measured flux, on the other hand, exhibits regions where the flux is opposite that of the Bohm flux, indicative of a possible non-local transport effect. This negative flux appears to be consistent in the radial region 12-15cm, though given that this flux does not appear to change much throughout the varying biases, it could be a measurement error. However, negative flux is also observed in regions that do exhibit changes with bias such as the radial region of 21-25cm in the highest bias plot. The contrast between the measured flux and the Bohm flux is most apparent in this region; while Bohm flux, a local model, would predicted outward flux in this region based on the direction of the gradient, the measured flux is clearly inward pointing, suggesting particle movement against driving gradient. This can only be achieved using a non-local transport mechanism. Similarly, the Bohm flux for high bias in the radial region of 18-21cm is inward pointing, but outward measured flux is outward pointing. The cumulative effect of this varying transport could possibly be related to the formation of the hollow density profile. Moreover, the nature of the non-local transport mechanism could be related to the strong flow and flow shear which would provide the free energy needed to cause particles to move against the density gradient.

5.2 Spectrum Modification

In addition to changes in basic plasma parameter profiles, the biasing has makes significant changes to the overall nature of the turbulence; in addition to modification of the amplitude of the turbulent fluctuations itself, both the spatial distribution and frequency distribution of these fluctuations are affected by changes in bias/flow states. The location of free energy sources are shifted. The nature of the turbulence shape appears to be modified as well which is indicative of the character of the fluctuations themselves.

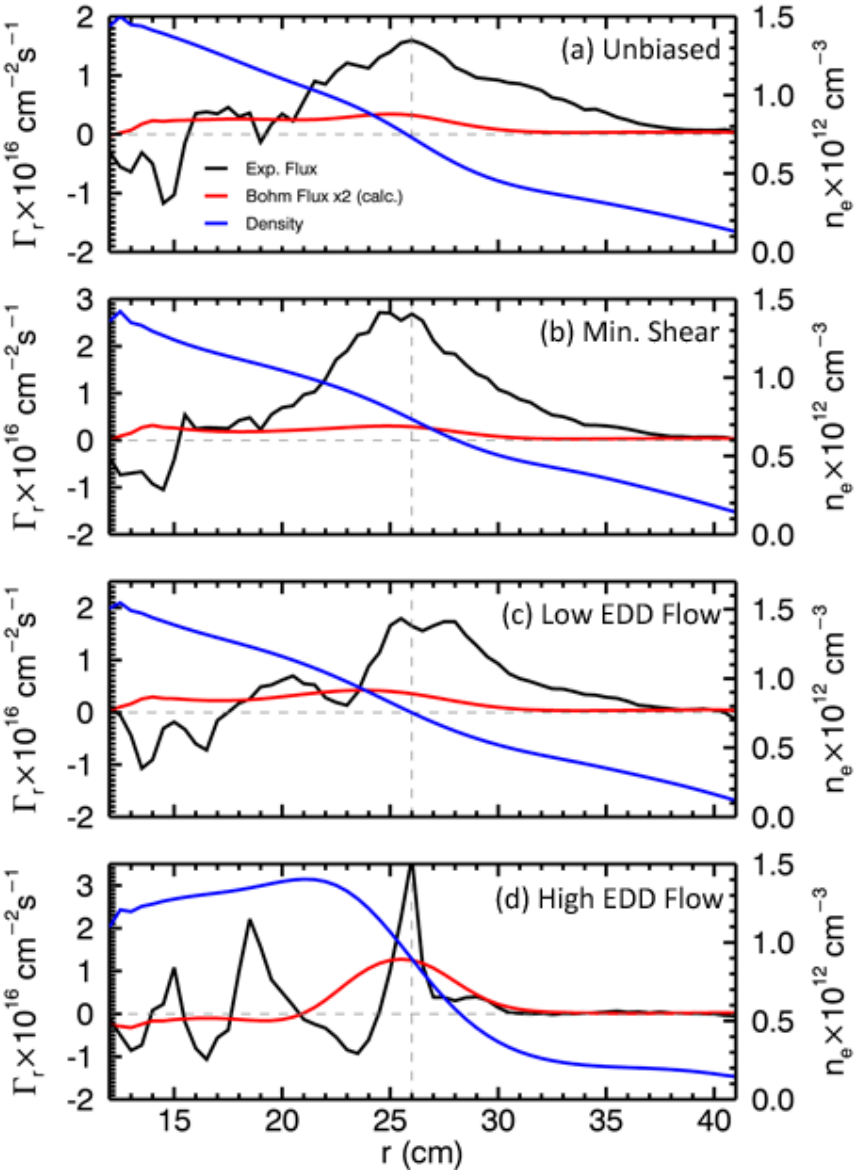

Figure 5.11: Measured flux overlayed with density profiles for (a) an unbiased (low IDD flow) case, (b) a null flow case, (c) a low EDD flow case and (d) a strong EDD flow. Each plot has a curve calculated assuming a Bohm transport model which is a local model and depends on the direction of the gradient. The regions where measured flux is opposite that of Bohm predicted flux is evidence of possible non-local transport.

5.2.1 Frequency Spectral Distribution

Figure 5.12 shows spatially averaged spectra of density and floating potential fluctuation power for three spatial regions—core, limiter-cathode transition, and edge—for the unbiased state as indicated by the black, blue and red curves respectively. The core curve comprises the mean spectrum curves for each radial position between 12 and 22cm. The limiter-cathode interface region spans a radial range of 24 to 27cm and edge region contains 27 to 31cm fluctuations. The first column plots the fluctuations in a log-linear form while the second column presents the log-log form. First, the spectra are clearly turbulent and broadband—there are no bumps indicating a coherent mode. The next noticeable difference is that core fluctuations in the unbiased state have a much lower amplitude—on average about two orders of magnitude—then the transition and edge regions. This is, of course, not surprising considering that the gradients supplying free-energy are mostly located in the transition and edge regions. The third, more interesting distinguishing feature is in the shape of the spectra: compared to the other regions, the core region spectra exhibits a much more power-law like decrease in power versus frequency. This is more obvious in the log-log plots, Figure 5.12(b) and (d), where the black curve is more linear than the red or blue. The transition and edge region spectral distributions, meanwhile, exhibit a more exponential shape, characterized by a generally linear trend in the log-linear plots, (a) and (c). Such exponential spectra would be expected for turbulent fluctuations dominated by pulses which have a Lorentzian shape in time [44, 45, 58]. The curves are not perfectly linear however, though it is conceivable that such spectra are generated by the overlay of two or more Lorentzian fluctuation widths which can occur with spatial averaging of the spectra. It should also be noted that the floating potential spectra are generally more power-law like than exponential suggesting that potential fluctuations are less characterized by Lorentzian structures than density.

Since the likelihood of a spectra containing multiple Lorentzian structures can be increased by spatial averaging it is instructive to study single point spectra as shown in Figure 5.13. The spectra is arrayed at three single point radial locations (12cm, 26cm and 30cm)

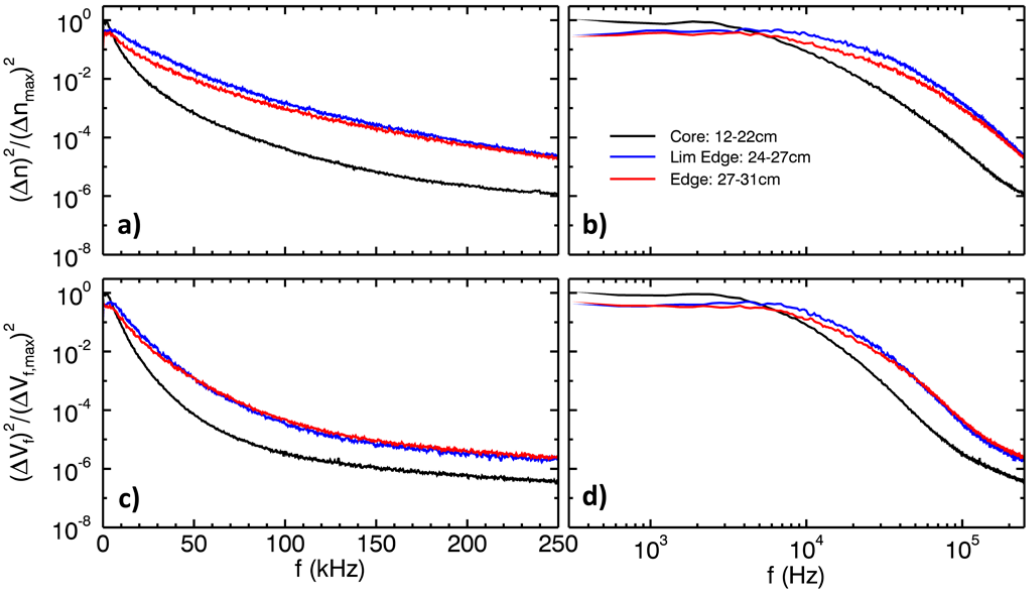

Figure 5.12: Unbiased log-linear spectra for density(a) and floating potential(c) and log-log spectra for density(b) and floating potential(d).

and four bias/flow states (unbiased, IDD flow, low IDD flow, no flow, and strong EDD flow). There is, again, a clear distinction in shape between core fluctuations and those at the limiter edge and beyond. The core spectra are extremely curved while the edge fluctuations exhibit the more exponential-like spectra. The fluctuations at 26cm, right on the limiter edge, tend to be the most linear suggesting that they are dominated by a single time width Lorentzian pulse while the other two locations contain more than one time-width Lorentzian pulses. A trend increasing biases is also observed; at the minimum flow state, the spectra are more concave then those with flow in either azimuthal direction.

These observations are consistent with the time series data for each of the three regions in each of the representative bias/flow states. To guide the time resolution needed to be able to observe the Lorentzian structures, a fit was made to the most linear spectra in Figure 5.13, which was the high bias spectra at 26cm. The fit is indicated by the dashed red line. Assuming an exponential of the form [54]

$$e^{-2f/f_s} = e^{-4\pi\tau f} \tag{5.5}$$

where f is frequency and τ is the characteristic time of a Lorentzian pulse such that

$$L(t) = \frac{\tau^2}{t^2 + \tau^2} \tag{5.6}$$

For this fit, a $\tau = 0.8\mu s$ is found, so the time resolution needed to see Lorentzian structures is on the order of 1μs. Figure 5.14 shows a single-shot time series of the original saturation current measurement zoomed in on a section between 2.10 and 2.40ms after the bias turn-on for the same biases shown in Figure 5.13. Figure 5.14(d) thus represents a time series for the spectra that was fit with the $\tau = 0.8\mu s$. The plot shows the shape of a Lorentzian of $1\mu s$ as a reference. Clearly, the most common small time scale fluctuations in the time trace resemble the $1\mu s$ Lorentzian which is consistent with the linearity of the spectrum. The longer time scale fluctuation (lower frequency), on the other hand, is due to the coherent mode. Comparatively, the other three plots above do not exhibit a single width Lorentzian shape or do not have strong Lorentzian shapes at all. The no flow case does appear to have any clear Lorentzian fluctuations shapes. The IDD flow cases Figures 5.14(a) and (b), have much larger Lorentzian structures, as seen in comparison to a $10\mu s$ Lorentzian, but also show more variation in Lorentzian sizes. This leads to both a less linear shaped spectrum (more diversity) and a generally steeper slope (wider pulses). Figure 5.15 shows similar time traces for a point at 30cm, outside the limiter edge, for the same four biases. Like the first three plots of the previous figure, the signals show evidence of Lorentzian structure, but without a single Lorentzian pulse shape which is again consistent with the spectra shown. Figure 5.16, however, shows essentially no Lorentzian structure at this time resolution. Thus, the spectra are much less linear in Figure 5.13.

The Lorentzian structures, then, appear to be correlated to the biasing, and most likely, the flow state of the plasma. The null flow state and the core region (which see no flow either) show the least amount of Lorentzian structure or exponential spectra. The states with flow in either the IDD or EDD direction have more Lorentzian structure though a consistent trend in temporal shape of pulses is not observed with changing bias or flow.

Turning to spatially averaged spectra, Figures 5.17 and 5.18 illustrate the modification of

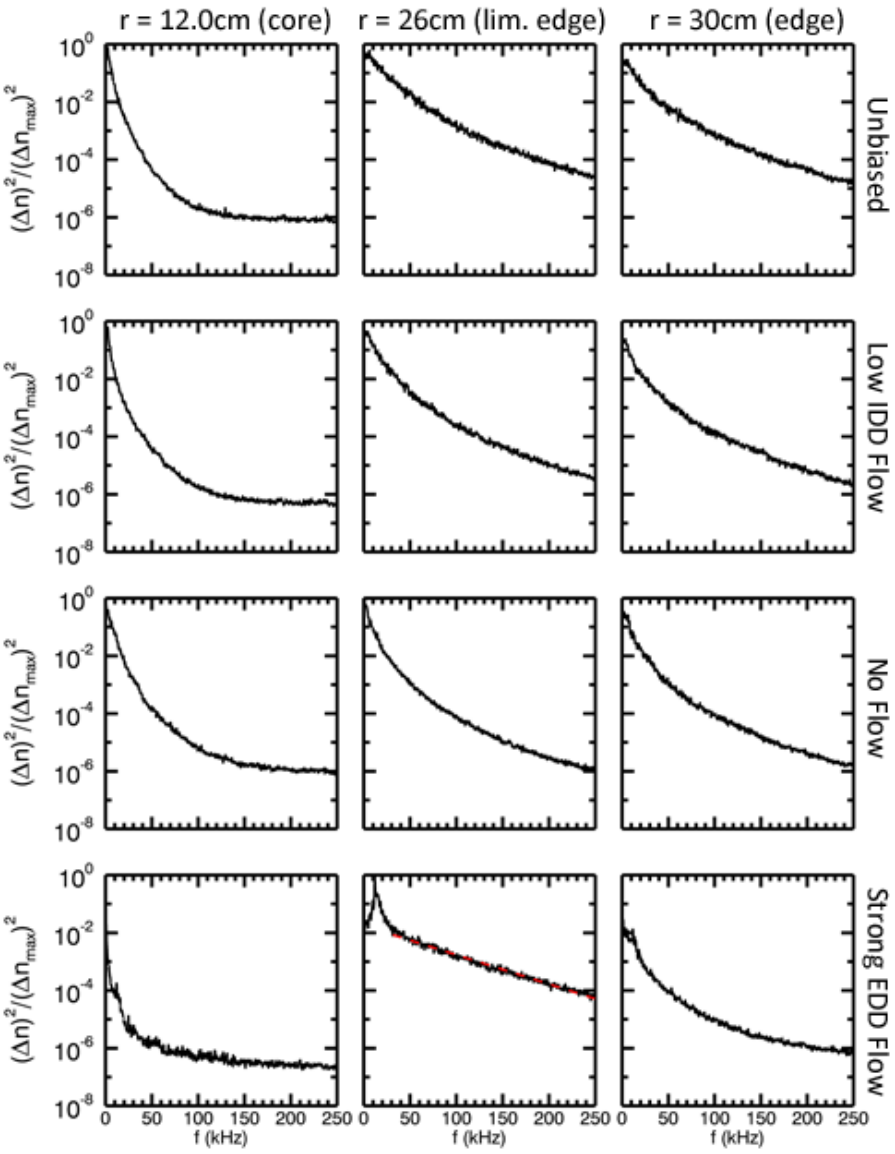

Figure 5.13: Local log-linear spectra for various locations and biases. Each column contains a shot-averaged spectrum for three radial locations: 12cm (core), 26cm (limiter edge) and 30cm (far edge). Each row represents a different bias state: unbiased (Bias 0), low IDD flow (Bias 5), null flow (Bias 10), and strong EDD flow (Bias 27). The bottom row, middle column spectum has an exponential fit indicated by a red dashed line that corresponds to a $\tau = 0.8\mu s$.

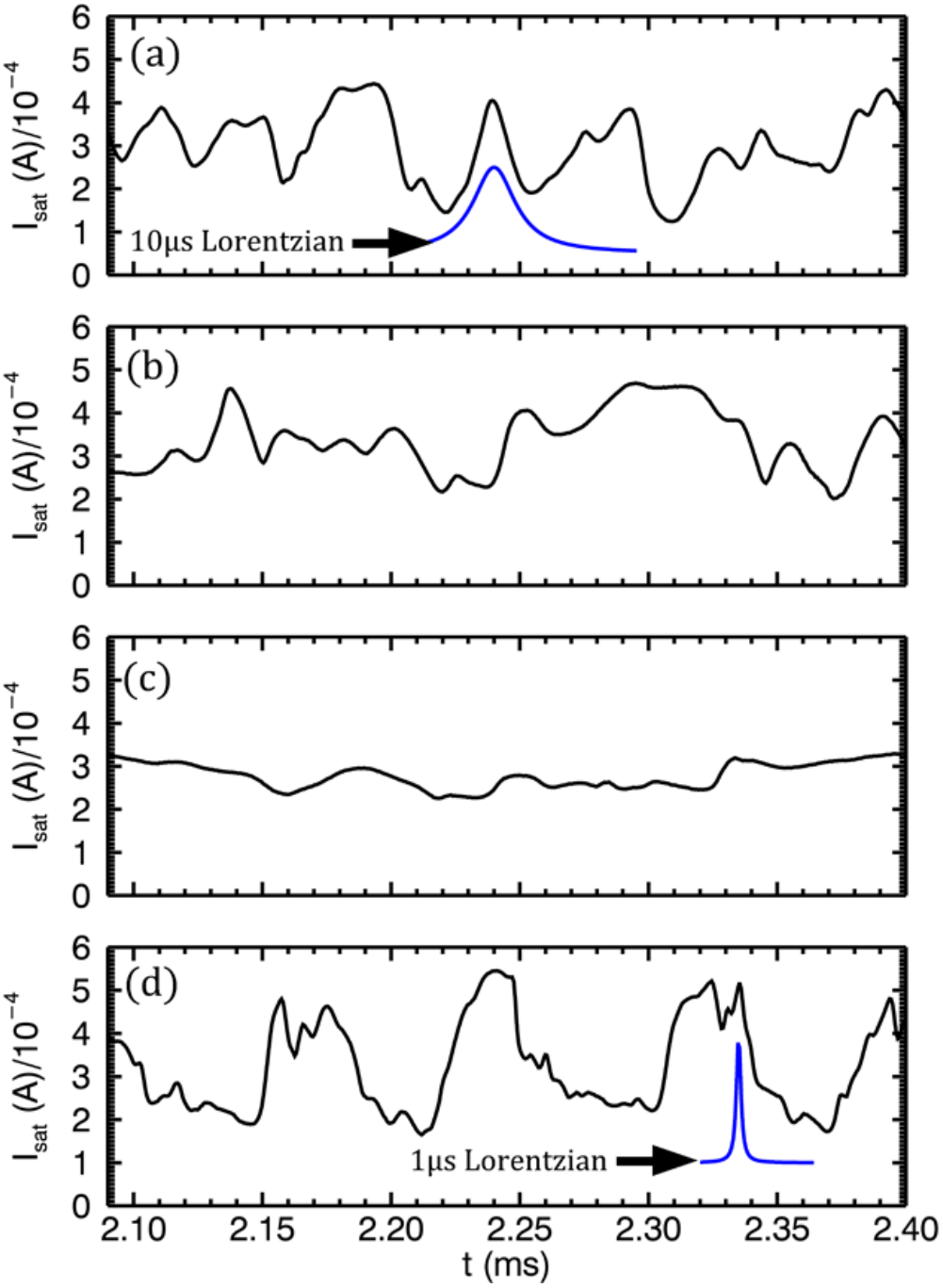

Figure 5.14: A single shot (no average) time series at 26cm (limiter edge) of the saturation current single used to determine density for the same four bias states described in Figure 5.13, labeled respectively as (a)-(d). The time resolution is high enough to resolve a Lorentzian pulse on the order of 1μs as shown in (d). A 10μs pulse is also shown for reference in (a).

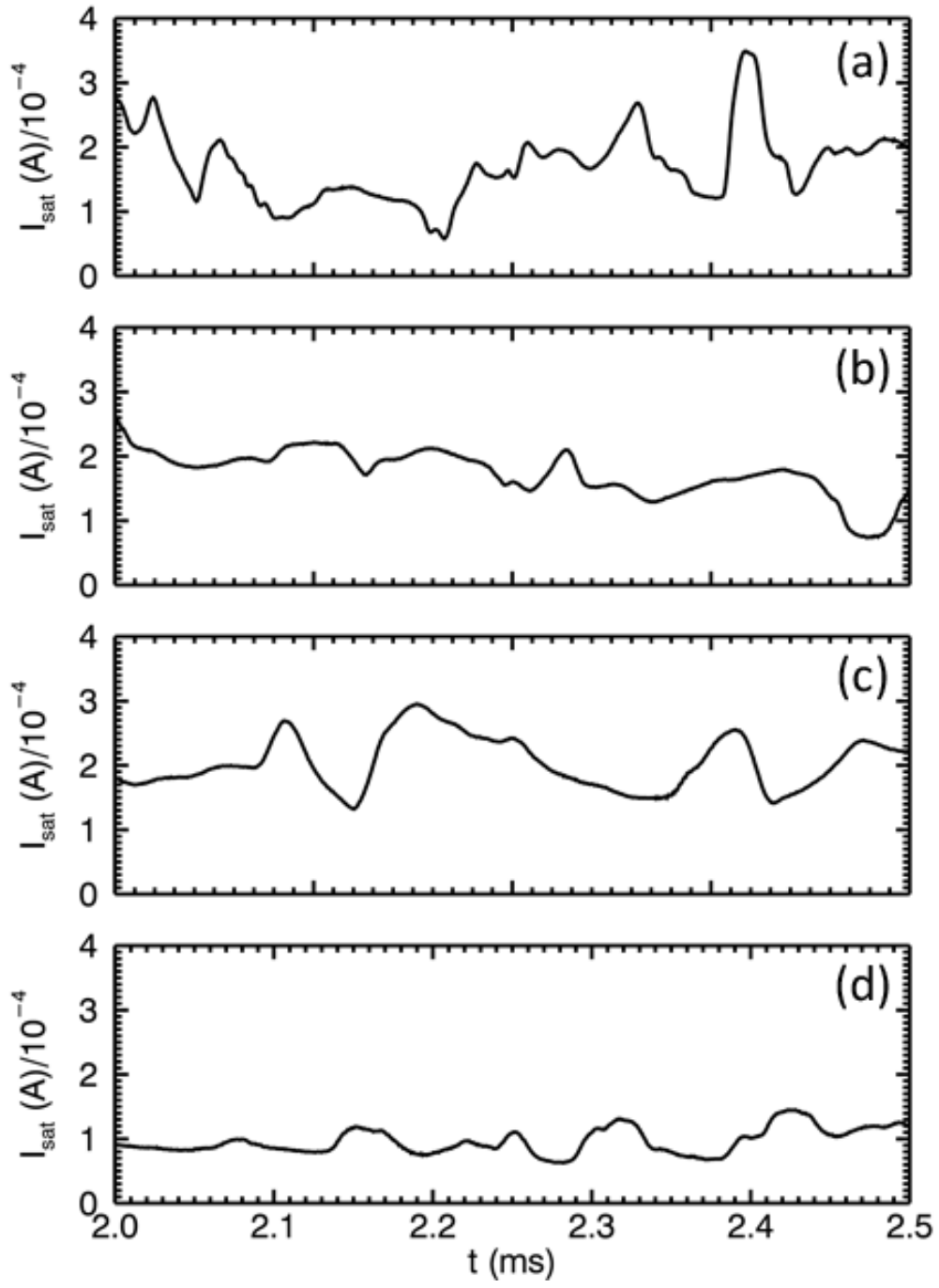

Figure 5.15: A single shot (no average) time series at 30cm (far edge) of the saturation current single used to determine density for the same four bias states described in Figure 5.13, labeled respectively as (a)-(d).

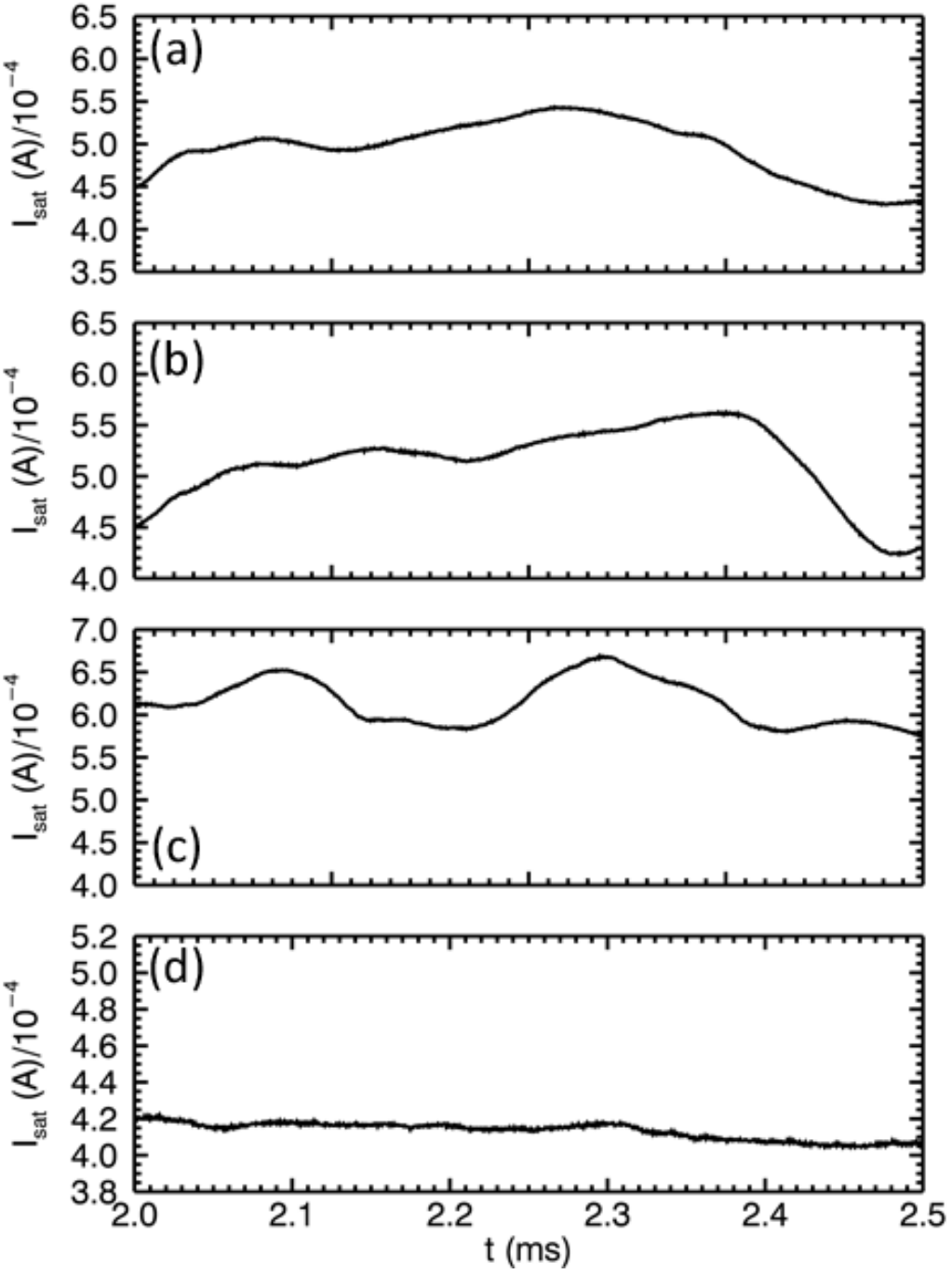

Figure 5.16: A single shot (no average) time series at 12cm (core) of the saturation current single used to determine density for the same four bias states described in Figure 5.13, labeled respectively as (a)-(d).

the turbulent spectral distributions for the density fluctuation power and floating potential fluctuation power respectively. Each plot shows the (a)core, (b)limiter-cathode transition, and (c)edge regions averaged over the same radial ranges indicated for Figure 5.12. Five different limiter bias states are used as referenced to the anode: -9.7V, -5.0V, -2.3V, 2.7V and 13.1V. These five states correspond to five bias states shown in Figure 4.16 and represent roughly a unbiased state, a minimum shearing state, a minimum flow state, a small EDD flow state and a strong EDD flow state. In the core, Figure 5.17(a), there is almost no variation with bias; the first few biases are almost identical up to about 50kHz and there is only a spread in normalized amplitude of about half an order of magnitude. The highest bias shown, however, does exhibit a substantial decrease in amplitude over all frequencies. The shape of the spectrum does not really change at all remaining a power-law like decrease throughout bias states. The floating potential similar shows even less change in the core. The edge and transition region spectra undergo significant changes, on the other hand. In both regions and for both density and floating potential fluctuations, compared to each spectra's unbiased state, there is generally a decrease in fluctuation amplitude though very importantly, there is actually an *increase* in fluctuation amplitude for low frequencies $\lesssim$ 20kHz. This change will be discussed separately and comprises a bulk of the Chapter 6 focus.

Lastly, the coherent modes mentioned previously can be seen to emerge in the spectra as bias is increased. The most prominent mode seems to begin about at 7kHz and reaches a peak frequency just under 20kHz. There is also evidence for a lower frequency mode that appears around 3kHz. The modes are most apparent in the transition region; it was clear in the fluctuation power and amplitude profiles that the peak fluctuations occurred at the limiter edge. The origins of these modes are discussed in much more detail later in this chapter.

Overall, these spectra demonstrate that the biasing clearly modifies the nature of the turbulence and that these changes appear to be correlated to the overall rotation state of the plasma.

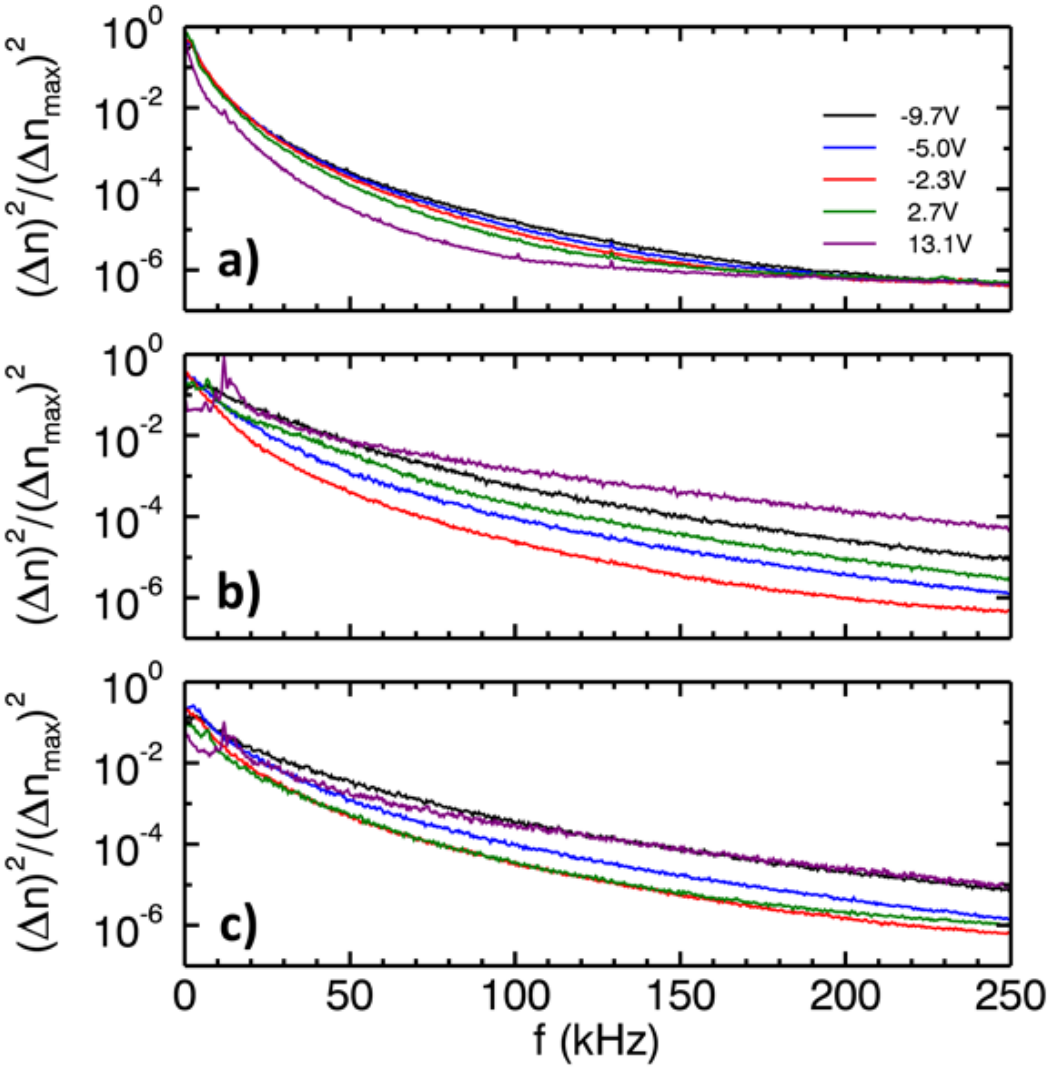

Figure 5.17: Spatially averaged log-linear spectra for density for (a)core (b)limiter-edge (c)outer edge regions for various biases

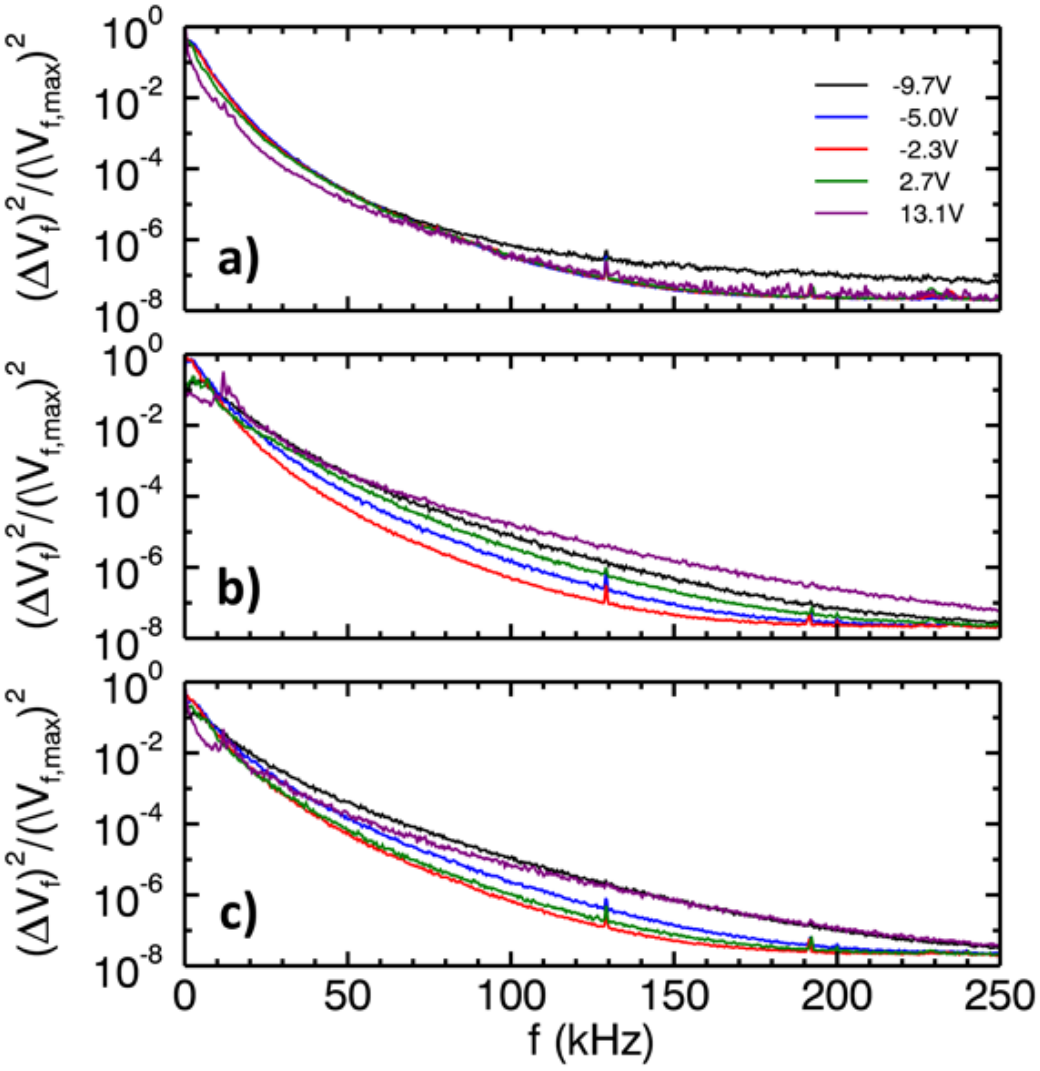

Figure 5.18: Spatially averaged log-linear spectra for vf for (a)core (b)limiter-edge (c)outer edge regions for various biases

5.2.2 Turbulent Spatial Distribution

Figure 5.19 show the spatial distribution of turbulent fluctuations for four different biases: (a) an unbiased state with small IDD flow, (b) a minimum shearing state, (c)a small EDD flow, and (d) a strong EDD flow state. Each of the four contour plots show the logarithm of the density fluctuation power as a function of both radius and frequency with the limiter edge indicated by the dashed line at 26cm. All four plots are normalized to the same maximum fluctuation value. In the first plot, (a), the fluctuation power is generally fairly evenly distributed radially. As mentioned before, most of the fluctuation power is concentrated in the band $< 10kHz$. There is a slight spreading of power in frequency at the limiter edge. This could be due partially to Doppler shifting of the frequency from the spontaneous flow, though the peak flow in this stage occurs at about 28cm. There is also a local maximum of fluctuation amplitude at the limiter edge.

Though the previous spectral distribution plots showed that the core region usually had a smaller amount of fluctuation power overall, in this very low frequency regime, the core region tends to have the highest absolute fluctuation amplitude. Evidence for this trend was also observed in the fluctuation profiles as in Figure 5.4. However, as that same figure shows, it is clear that the core region generally has the lowest percentage fluctuation amplitude when compared to the density level.

Figures 5.19(b) and 5.19(c) show the modification of the spatial distribution as the limiter bias is increased to -6.3V below the anode(b) and 0.22V above the anode(c) respectively. The -6.3V bias has low flow and nearly zero shear. The fluctuation power is shifted back toward lower frequencies as seen in the line cut plots and is even more evenly spatially distributed than the unbiased state. This is possibly due to the lack of flow to Doppler shift some of the frequencies; however, as will be discussed in Chapter 6, the elimination of sheared flow in the system correlates to increased density fluctuations in frequencies $<$ 20kHz. As the bias surpasses the anode voltage in (c) and the flow begins to go in the opposite azimuthal direction, the main effect appears to be a decrease in fluctuation amplitude in the edge region.

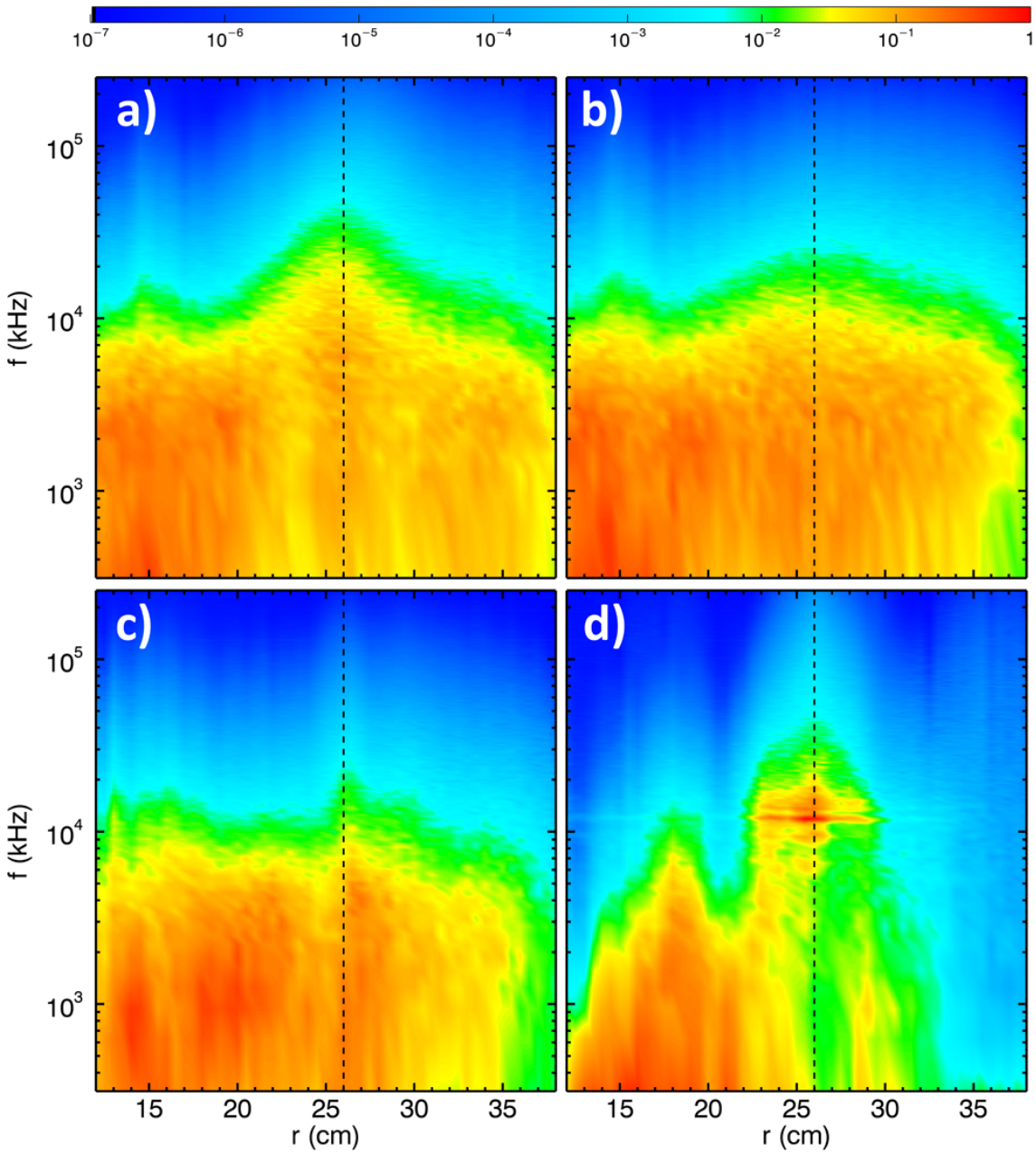

Figure 5.19: Contour Plots of Density fluctuation power (normalized to the maximum value) versus frequency and radius for (a)0bias, (b)Bias 7, (c)Bias18, (d)Bias27

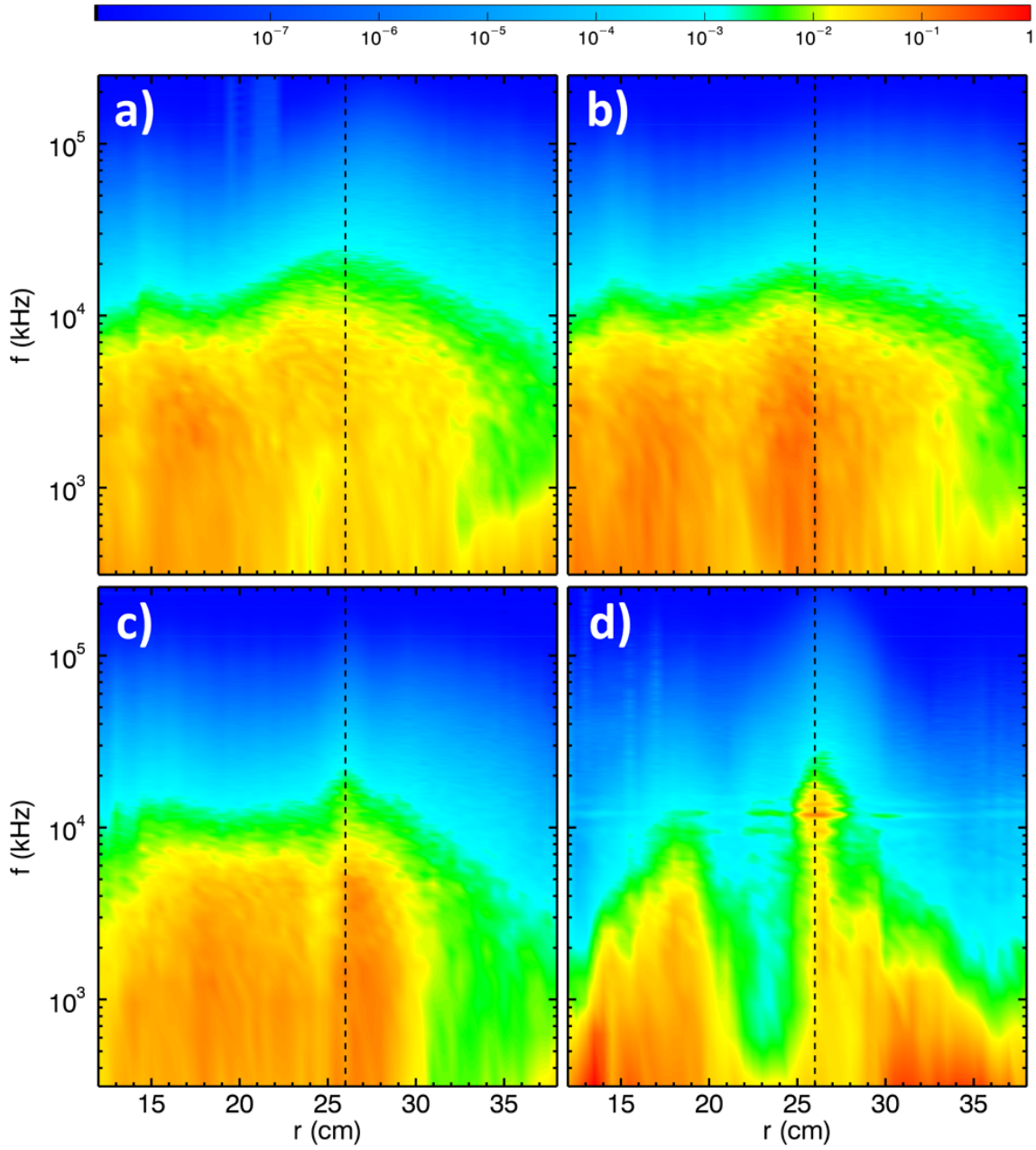

Figure 5.20: Contour Plots of vf fluctuation power versus frequency and radius for (a)0bias, (b)Bias 7, (c)Bias18,(d)Bias27

One of the coherent modes can be seen emerging at the limiter edge at about 5kHz. Finally in Figure 5.19(d), at a bias of 13.1V above the anode and in a highly EDD flowing state, the highest fluctuation power appears in the coherent mode now at a frequency of 10kHz. Fluctuations outside the limiter edge are almost completely removed, having decreased an order of magnitude or more compared to their peak values. Even the core fluctuations are spatially modified with peaks concentrated in the region between 15 and 20cm. This core change could be related to a modification of the density gradient which actually slightly reverses to point outward in this 15-20cm region as can be seen in Figure 5.1. Clearly, though, the most change in spatial turbulence occurs in the higher biases, with the highest rotation states achieved. Since the free-energy sources are most modified by the biases—steepest density gradients, highest flow and flow shear states—its very likely the turbulence modification is due to this change in drive.

Figure 5.20 shows a similar set of contour plots as Figure 5.19 but for floating potential rather than density fluctuations. Overall, the spatial distribution of floating potential fluctuation power appears to undergo less change than the density, and at least for plots (a),(b), and (c) follow similar trends in change. The high bias state shows some peaking at the point of the coherent mode as in the density plots, but also strong fluctuations in the core and far edge with most of the fluctuation reduction occurring just inside the limiter edge rather than outside as for the density. A curious feature does appear at high biases where the floating potential fluctuations decrease dramatically in a region 21 to 25cm for frequencies $>$ 10kHz. This reason for this drop is not understood but could be related to the increased heating and plasma production that occurs in this region (see Figure 5.2.

5.2.3 Wavenumber and M-Number Spectra

In addition to temporal fluctuation spectra, spatial spectra can be used to analyze turbulent properties of the plasma. The most accurate way to determine a spatial spectrum—that is, the distribution of fluctuation power broken into spatial eigenmodes—would be to have a simultaneous measurement of plasma parameters (I_{sat},V_f) at a high resolution of multiple

positions. While this can be partly achieved using multiple tipped Langmuir probes (such as the rake probe described in Chapter 3), such a probe offers far too little spatial resolution to be of very much use. Instead, the high temporal resolution available to the Langmuir probe signals can be used to approximate a local wavenumber spectrum using a two-point correlation technique. This method uses the time correlation between two points to measure a relative phase, and with a known separation distance, a local wavenumber, $k_l = \theta/d$. Given a large enough number of statistics, a distribution of local wavenumber as a function of frequency and position can be created. The details of this process are discussed in detail in Appendix B. The results of such an analysis yield spectral density functions which is a histogram of fluctuation power binned by wavenumber and frequency.

Since the LAPD is a cylindrical device, it is most natural to cast eigenmodes of the system with as having an azimuthal component $\sim e^{im\theta}$ with mode number, m; an axial component $\sim e^{inz}$, with eigenvalue n; and a radial eigenfunction f(r). The stability of the relevant modes depend most on the azimuthal mode number, m, (and consequently the resulting transport)and is thus of most interest for turbulence study. Though m-numbers are the more physically relevant quantity, the two-point correlation method used here determines an azimuthal wavenumber first, where $k_\theta = m/r$. The results will be shown first cast in terms of k_θ and a frequently used ratio, $k_\theta \rho_s$, but will also be shown in terms of azimuthal mode numbers.

Figure 5.21 shows fluctuation power as a function wavenumber, $k = 2\pi/\lambda(\mathrm{cm}^{-1})$, for the same set of biases shown for the time-domain spectra plots above. These are made by summing the spectral density functions over the time frequency dimension. The plots are also broken into the three spatial regions, core, limiter-cathode transition, and edge regions as before.

The most notable difference between the spatial and temporal spectra is the presence of negative wavenumbers. Signs correspond to the propagation direction of the mode which is ultimately determined by the relative lead or lag in the phase between the two correlation points. Given the experimental arrangement of tips on the probe, the negative values

correspond to modes propagating azimuthally in the ion diamagnetic drift direction while positive values correspond to the electron diamagnetic drift direction.

In the core, values of k_θ appear to change very little with biasing with respect to amplitude, shape or distribution in direction. This is similar to what was observed in the temporal fluctuation spectra and reinforces the notion that core turbulence is mostly unaffected by the biasing scheme—though density gradient *is* modified.

The second two plots showing the transition and edge regions show significant modification of spectra. In both regions, there is an overall shift in fluctuation power from IDD direction propagating modes to EDD direction modes. This shift is reflected in both the summed power over wavenumbers and in the peak fluctuation amplitude. Again, like the temporal spectra, there is a change in the distribution shape with bias. In the unbiased state, the IDD direction propagating modes have higher amplitude and a linear slope indicating an exponential nature to the fluctuations, while the EDD modes have much lower amplitudes and resemble more of a power-law like composition. This trend is balanced out between directions as the bias is increased into the minimal flow regime, with the linearity of the slope less apparent in the IDD direction. In a definitely EDD direction rotation plasma, the nature of the slopes has reversed, with EDD modes demonstrating a generally linear shape and IDD modes showing a more power-law-like shape. This difference and shift indicates the flow has a substantial effect on the turbulent fluctuations as very linear slopes in the log-linear spectra appear to occur only with significant flow—again, similar to what is observed in the temporal spectra. However, the wavenumber spectra appears to add the importance of direction of flow; turbulent modes that propagate in the same direction of rotation would appear to have a more Lorentzian nature than those that propagate in the opposite direction.

The wavenumber spectra can also be cast in terms of azimuthal mode numbers, m, as shown in Figure 5.22. From this plot, it can be seen that the peak mode number in the unbiased edge regions is about m=15. At the limiter edge, this corresponds to a wavenumber of $k = m/r = 0.577\text{cm}^{-1}$ or a wavelength of $\lambda = 10.9\text{cm}$. In the strongly biased regime,

the peak switches to m=10 in the EDD direction which is $k = 0.384$ or $\lambda = 16.3$cm at the limiter edge. Since the growth of the coherent mode is strongest at the limiter edge, its is likely that these modes generate the peak at m=10.

Examples of the full spectral density histogram is shown in Figure 5.23 for four different bias regions. The spectral amplitude is histograms into bins 312Hz wide in frequency, and 0.01 cm^{-1} wide in wavenumber space. Spectral density histogram (a) is averaged over all radial locations from 12-32cm and over Bias 0,1, and 2, which are essentially all unbiased cases (they are all biases less than the floating potential). Histogram (b) shows the average of three biases around where the plasma rotation nulls out—Bias 10,11 and 12. Histogram (c) averages biases in the low to medium EDD flow regime—Bias 16,17, and 18. Finally, Histogram (d) averages some strong EDD flow biases—Bias 25,26 and 27.

As with the line plots above, these spectral density functions show the overall shift in propagation direction for the modes as the bias is increased. These plots show that the vast majority of the fluctuation power resides in the frequency space less than 10kHz and within a wavenumber space less than 2.0 cm^{-1} or, assuming an ion sound radius of $\rho_s \sim 0.5$cm, within a $k_\perp \rho_s < 1$. Power does expand out into a narrow band that increases approximately linearly in both frequency and wavenumber. In the unbiased state, a line fit along this strip would have a slope that corresponded to a phase velocity, $v_p = f/k = 2 \times 10^4$cm/s which is about an order of magnitude less than the peak flows observed in this state. This confirms that these distributions are not set entirely by the Doppler shift.

As the bias is increased to the point where plasma rotation minimized, fluctuation amplitude begins to be concentrated toward smaller wavenumber and frequency. Both the frequency and wavenumber of the linear feature in the IDD direction decreases and its slope decreases slightly to a phase velocity of 1.5×10^4 cm/s which shows the slight impact of Doppler shifting on phase velocity. There is also slightly more power in the EDD direction. It should be noted, though that even in the minimum flow state, there is still moderate amounts of flow in the IDD at the far edge or $r > 30$cm as can be seen in Figure 4.16. In fact, the far edge flow appears to be consistently in the IDD beyond 30cm even for the flow

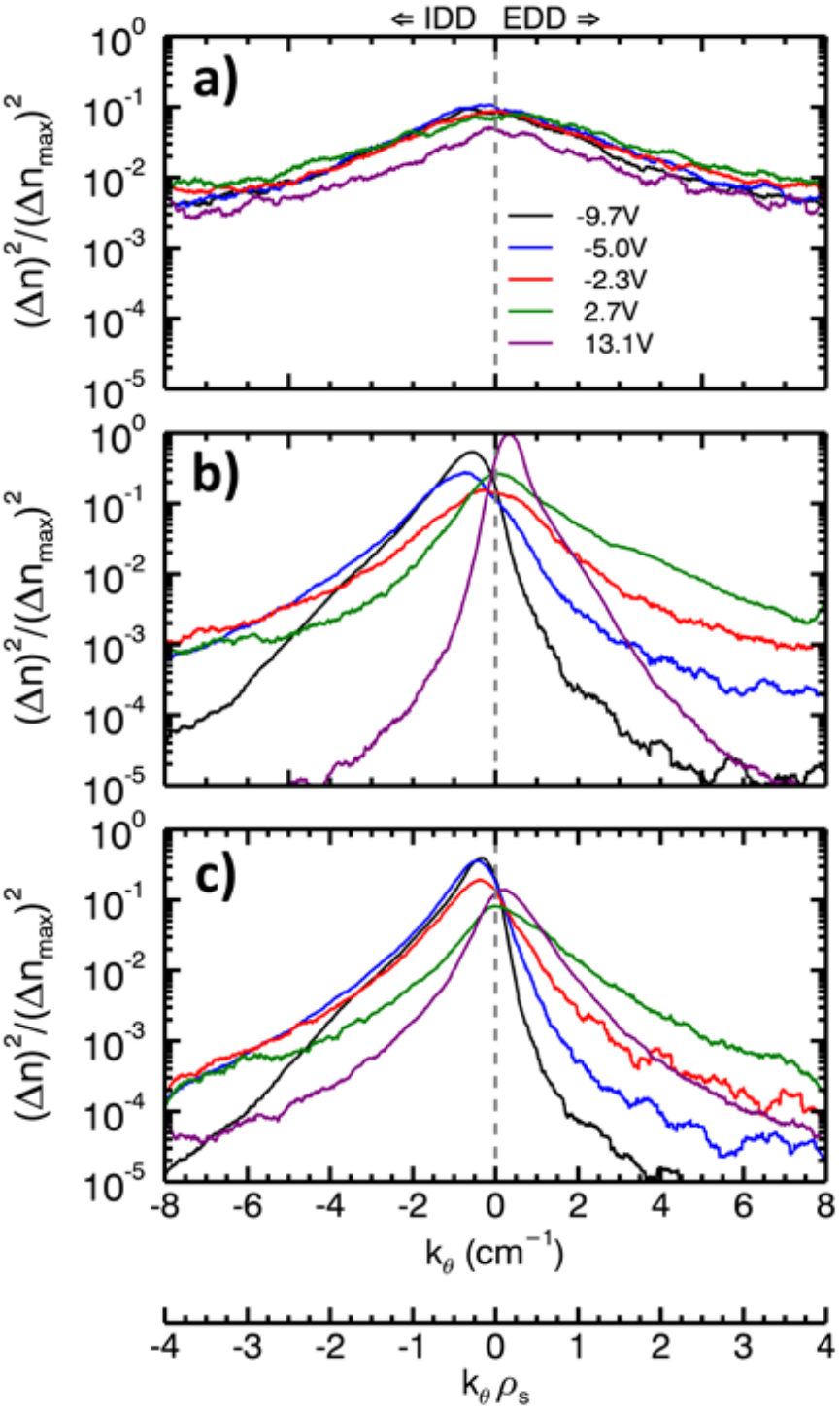

Figure 5.21: Perp Wavenumber spectra for (a)core, (b)transition, and (c)edge regions for various bias states

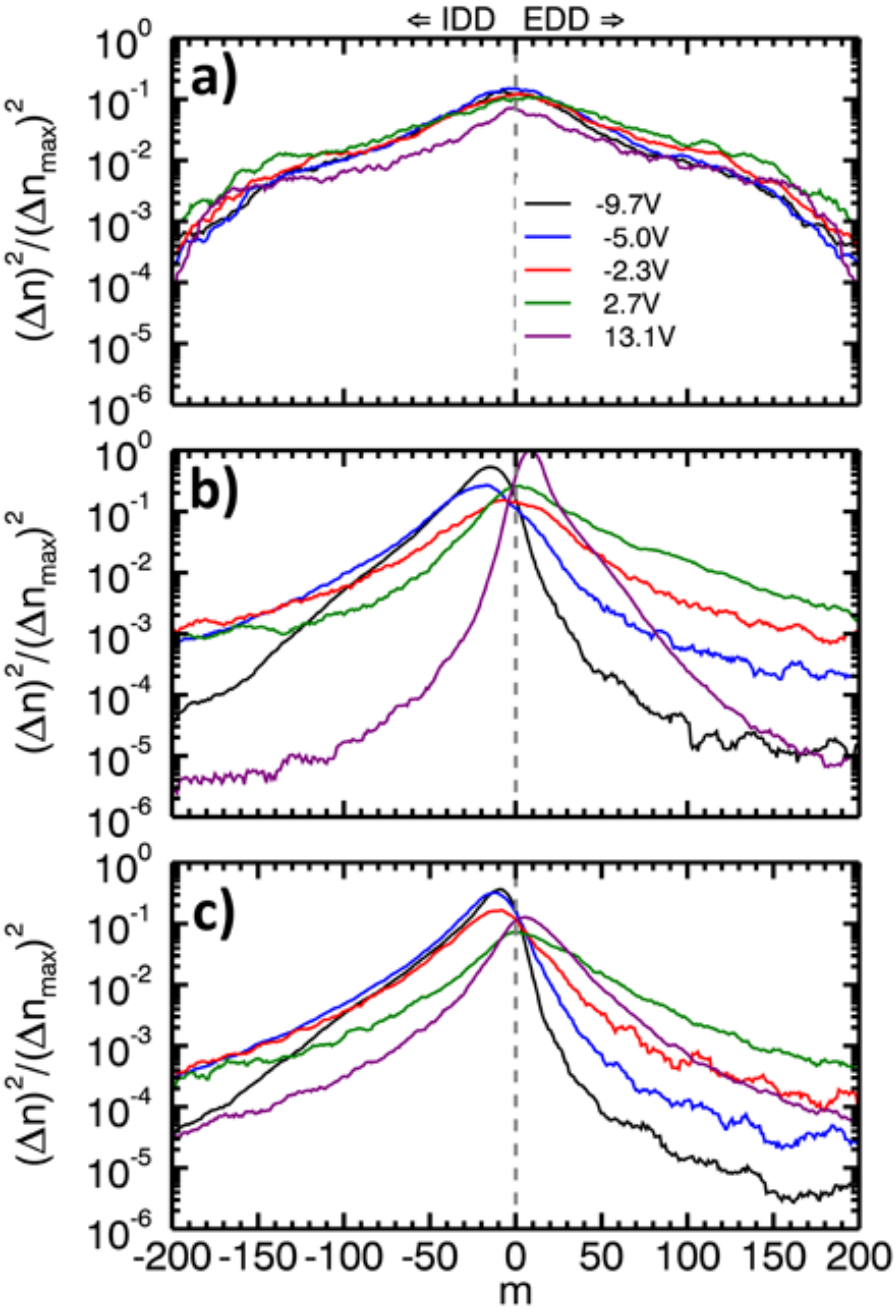

Figure 5.22: Azimuthal mode number m spectra for (a)core, (b)transition, and (c)edge regions for various bias states

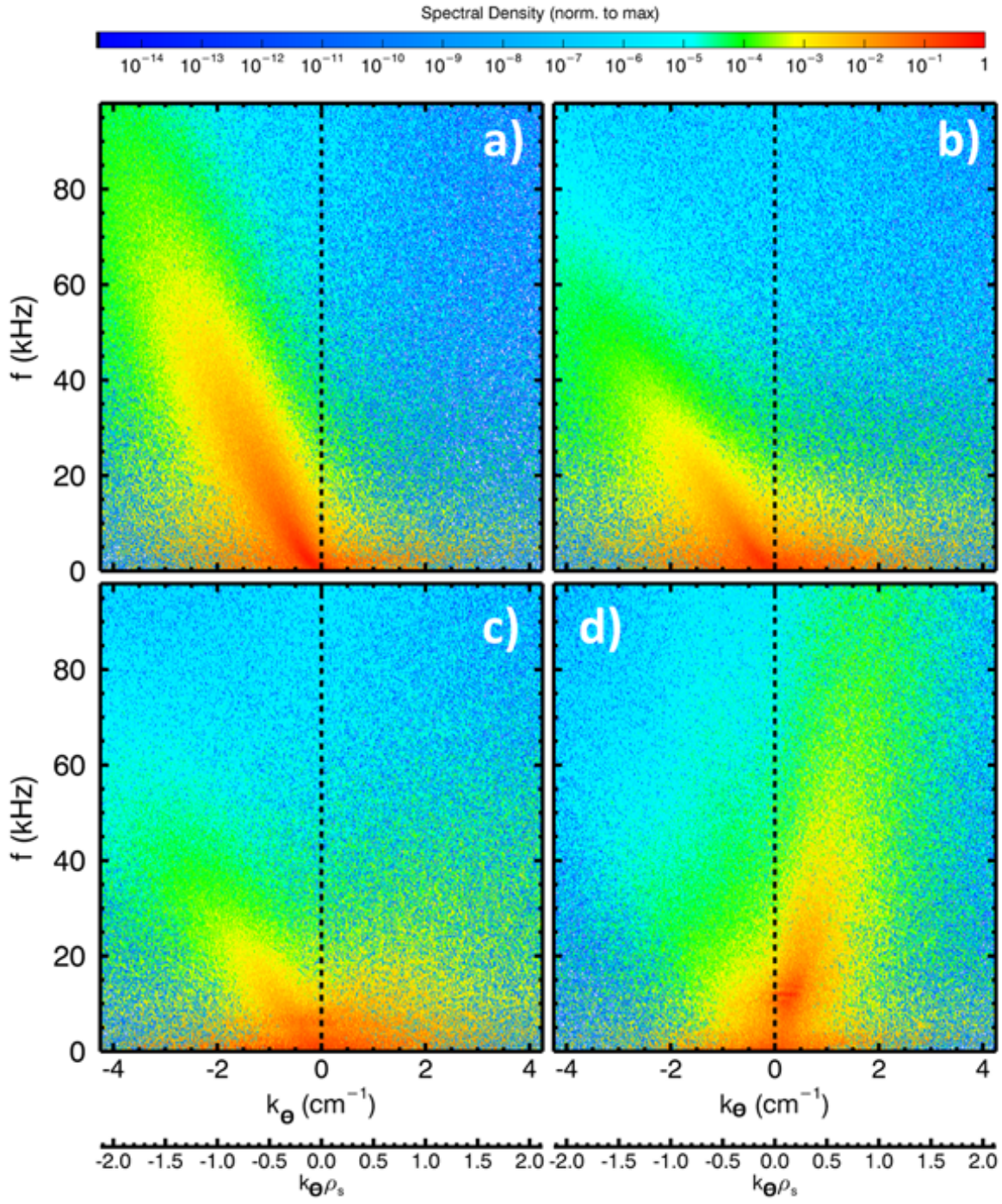

Figure 5.23: Perp Wavenumber spectra for four different bias groups (a)Low/Unbiased IDD flow Bias0-2, (b)Min Flow Bias10-12 (c)Low EDD Flow Bias 16-18 and (d)Strong EDD flow Bias 25-27

states with the highest peak driven flow. This can be seen in these four plots by the presence of power in the IDD which is never completely eliminated.

For biases that cause plasma to rotate a low to medium rates in the EDD direction, as in Figure 5.23(c), there is a clear difference in distribution for modes that propagate in the EDD and those still propagating in the IDD. The IDD modes maintain the narrow lobe shape that is reminiscent of the unbiased case and can somewhat still be fit by a linear dispersion relation with phase velocity on the order of $\sim 1.5 - 2 \times 10^4$ cm/s. The EDD modes on the other hand are more broadly distributed in the range from 0-40kHz and 0-4 cm^{-1}. No dispersion relation can be approximated in this region. This difference is perhaps an indication of differing origins of the turbulence and evidence that the biasing is changing the free energy drive of the turbulent fluctuations.

The highest measured biases show the most significant change in the spectral distribution showing both the coherent mode at approximately f=10kHz and k=0.5cm^{-1}, but also fluctuation power in modes propagating predominantly in the EDD direction. Rather than being diffuse, a narrow lobe is formed like in the unbiased state, but with a steeper slope. An approximate fit to this slope yields a phase velocity more like $v_p \sim 4 \times 10^4$ cm/s. This could be due to a change in the underlying instability drive and resulting mode, or from the influence of the stronger EDD rotation in this state. Nevertheless, there is a clear transition in the nature of the turbulence not only from the unbiased state to the high biased, high rotation state, but even between the lower EDD rotation and higher EDD rotation states as in Figure 5.23(c) and (d).

The questions of the underlying modes are taken up in the next section.

5.3 Mode Analysis

The nature of the types of instabilities found in the LAPD plasmas can have important effects on the resulting turbulence and transport. One example of this effect is in the scaling of turbulence and transport suppression with shear as discussed in the variations of decor-

relation models of shear suppression which make different assumptions on the instabilities present and driving the turbulence. Instability identification in a turbulent setting can be an extremely difficult task as there are many simultaneous sources of free energy as well as the fact that non-linear fluctuation behavior can be vastly different than the linear modes that might originate it. Nevertheless, mode identification (or at least categorization) can be useful in understanding the physical mechanisms in turbulence and transport so any attempt is worthy.

This biasing experiment in LAPD provides a useful approach to mode identification as it has been shown that biasing can significantly modify the plasma gradients present thus changing the drive of different linear instabilities. The three main linear instabilities that will be analyzed in this section are the resistive drift-wave (hereafter DW), the rotational interchange mode (RI), and the Kelvin-Helmholtz instability (KH). The resistive pressure-gradient driven instability or drift-wave has been shown to be present in the LAPD in [59]. Investigations and identification of the KH mode was made on the LAPD in [57, 60]. Linear calculations using a Braginskii fluid model (discussed later in the section) has shown that given experimental profiles—those taken from previous biasing experiments on LAPD [38, 39]—the activity of all three of these instabilities are present and the growth rates for all three modes are comparable [49].

Simulations of LAPD turbulence using the BOUT++ code have revealed the presence of a nonlinear instability which overtakes the linear modes in establishing the resulting turbulent state [50]. Thus it is possible that linear modes do not have any connection to the turbulent state in LAPD. It should be noted however, that simulations have only been performed for the "null flow" state and that linear instabilities may explain the fluctuation spectrum (in particular the coherent mode) at higher biases.

Since the experimental data is taken from the steady-state portion of the plasma discharge, when growing linear instabilities will not only have already saturated, but will likely have already non-linearly interacted to form a broadband turbulent state, mode identification cannot rely entirely on the clues from the fluctuation and spectral data. The spectral

information is combined with examination of location and strength of gradients which can drive the instabilities, the direction of propagation of these modes and comparison to the growth rates and frequencies of linear modes as calculated using a Braginskii fluid equation eigenfunction solver to narrow down the likelihood of contributions to the turbulence due to each of the three instabilities. The appearance of a distinct coherent mode in the highest biases is also helpful in distinguishing between mode types especially when compared to linear growth rates. While a full 3D non-linear simulation like BOUT++ can provide much better comparisons, the combination of the approaches mentioned can be highly suggestive.

The varying features of the spectral density functions—calculated using the two-point correlation technique—are used to distinguish amongst modes. By calculating the spectral density for different regions and different groupings of bias states, the features can be used to compare to both radial and bias locations of driving gradients as well as to growth rates from linear calculations restricted to similar spatial regions and bias groupings.

5.3.1 Instability Drive

As a starting point, it is useful to identify what inhomogeneities are most likely to drive which instabilities. Drift waves can originate from gradients in pressure, $p = nT$, which indicates that gradients in either density or temperature are likely to drive drift waves. For simplicity, the temperature gradient is not considered in this analysis despite the fact that there is obviously a temperature gradient in the profile. The temperature profile does change somewhat with biasing, but not significantly and it is justified to take the temperature gradient to be constant for the level of detail of this analysis. Rotational interchange is driven by the flow and thus tied to gradients in the plasma potential profile. Kelvin-Helmholtz also is a flow driven mode, but requires a finite second derivative in the flow to be active—this can be observed by looking either directly at the gradient in shearing rate (second derivative in flow) or by measuring a quantity called vorticity defined as, $\varpi = \nabla \times v_\theta$. As will be shown, the contribution of KH modes in the linear eigenfunction solver can be derived explicitly from the gradient in the vorticity. The vorticity can be measured using the 9-tip flux probe

as described in Chapter 3. Figure 5.24 shows a few of these vorticity profiles, but more importantly, indicates where the gradient of the vorticity is largest and thus potentially where the KH modes would be most active.

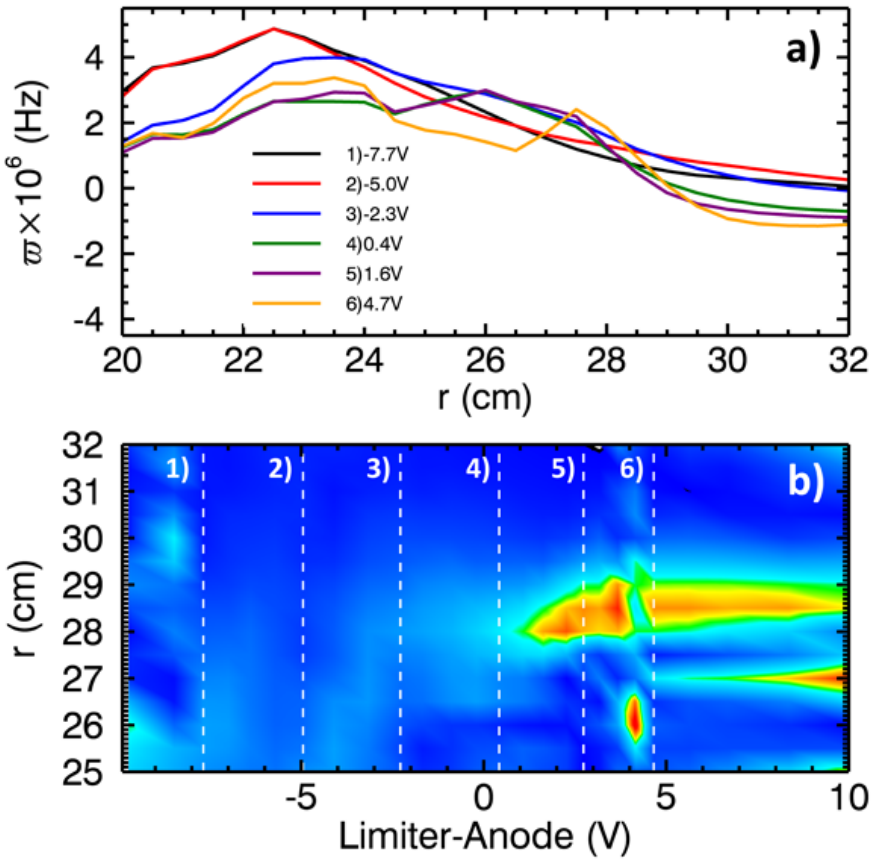

Figure 5.24: (a) Vorticity profiles for various bias states and (b) contour showing the gradient of vorticity as a function of radius and bias state as indicated by limiter-anode voltage difference. The different colored profiles correspond to the dashed line cuts in the contour plot.

The changes to the density gradient (as in Figure 5.1) and flow as a function of bias state (displayed in Figure 4.16) has been discussed in earlier sections. The key points that help in mode identification are highlighted again. Since the flow can be nulled out, eliminating the drive for both RI and KH modes and leaving only a density gradient to drive drift waves, the contribution of drift-waves on the turbulent wavenumber and frequency spectra can be

isolated. Moreover, the flow, when it is present, is generally localized around the limiter edge while the density gradient penetrates deeper into the core of the plasma. This can allow for some spatial distinction between drift-waves and flow driven modes. Also, since the flow can be reversed, the propagation direction of RI modes can be tracked—that is, flow in the IDD will likely result in modes that propagate in the IDD. Connected to that is the fact that linear modes of drift-waves propagate in the EDD and since the overall density gradient is in the same direction throughout the biasing, the direction of *linear* drift-wave modes should as well (though it should be noted that this is *not* necessarily true of non-linear drift modes as well as the fact that turbulent saturation properties can diminish this asymmetry). Finally, as indicated in Figure 5.24,strong KH mode growth might be likely localized to a region just beyond the limiter edge, for high biases voltages which can be used to distinguish from both RI and DW modes.

5.4 Fluctuation Ratios

The relative amplitude of density and plasma potential fluctuations is also an experimental method for distinguishing between modes. The ratio of floating potential fluctuations (as usual, used as a proxy for plasma potential) scaled to the unbiased temperature profile over density fluctuations scaled to the density profile is shown in Figure 5.25 for a set of biases that characterize the variations in this ratio.

It can be shown [51] that the ratio of $R = |\tilde{\phi}/T_e|/|\tilde{n}/n|$ should be $\lesssim 1$ for drift-waves and $\gtrsim 1$ for rotational interchange modes. KH modes, on the other hand, would be expected to have $R >> 1$. Of course, these numbers are for linear modes and presumably less reliable in comparison to saturated turbulence. However, there are trends in the profiles which can be observed. First, the ratio for all the profiles remains generally around 1. The unbiased profile starts off with ratio values $R > 1$ but gradually decreases below 1 toward the limiter edge, before return above 1 in the far edge. As bias in increased throughout, the core ratio is mostly not affected within 22cm (except with the highest bias difference, 25.9V). This is

consistent with the previous core spectra data generally being unaffected by bias. As the bias increases to no shear and no flow states, the limiter edge and far ratio begins to increase above 1 peaking at the limiter edge. This trend is somewhat curious since $R > 1$ would tend to imply stronger potential fluctuations relative to temperature than density fluctuations relative to the mean density, though the plasma would only have a density gradient driving fluctuations at this point. The difference could arise from a general increase in mean density in the edge (which will be shown to occur at the minimum shear state) which would offset increases in density fluctuation. As the bias continues to increase, the ratio at the limiter edge drops back down to a value just above 1, while the ratio just outside the limiter edge begins to grow (green to purple), then drops down again at the highest bias (orange). These peaks correspond to the region and set of biases where peaks in the vorticity gradient where also observed. Since KH modes tend to have larger values of R, this could further indicate the presence of KH mode drive in the region just outside the limiter edge.

5.5 Linear Analysis Fluid Equations

To elucidate the contribution among mode types in the LAPD turbulence, it is useful to compare to results to a Braginskii fluid model which attempts to closely represent the collisional LAPD plasma. The following section discusses comparison between linear growth rates as calculated from a linearized set of Braginskii fluid equations with the fluctuation amplitudes as measured experimentally. While there is obvious interpretive difficulty in attempting to match saturated turbulent fluctuation amplitude with calculated growth rates of linear modes, any connects observed can be used to in concert with many experimental observations to get an idea of what physical processes may be at work.

The basic Brakinskii fluid equations combine the density, ion momentum and electron momentum and charge conservation equation with collisional damping amongst ions, electrons and neutrals included:

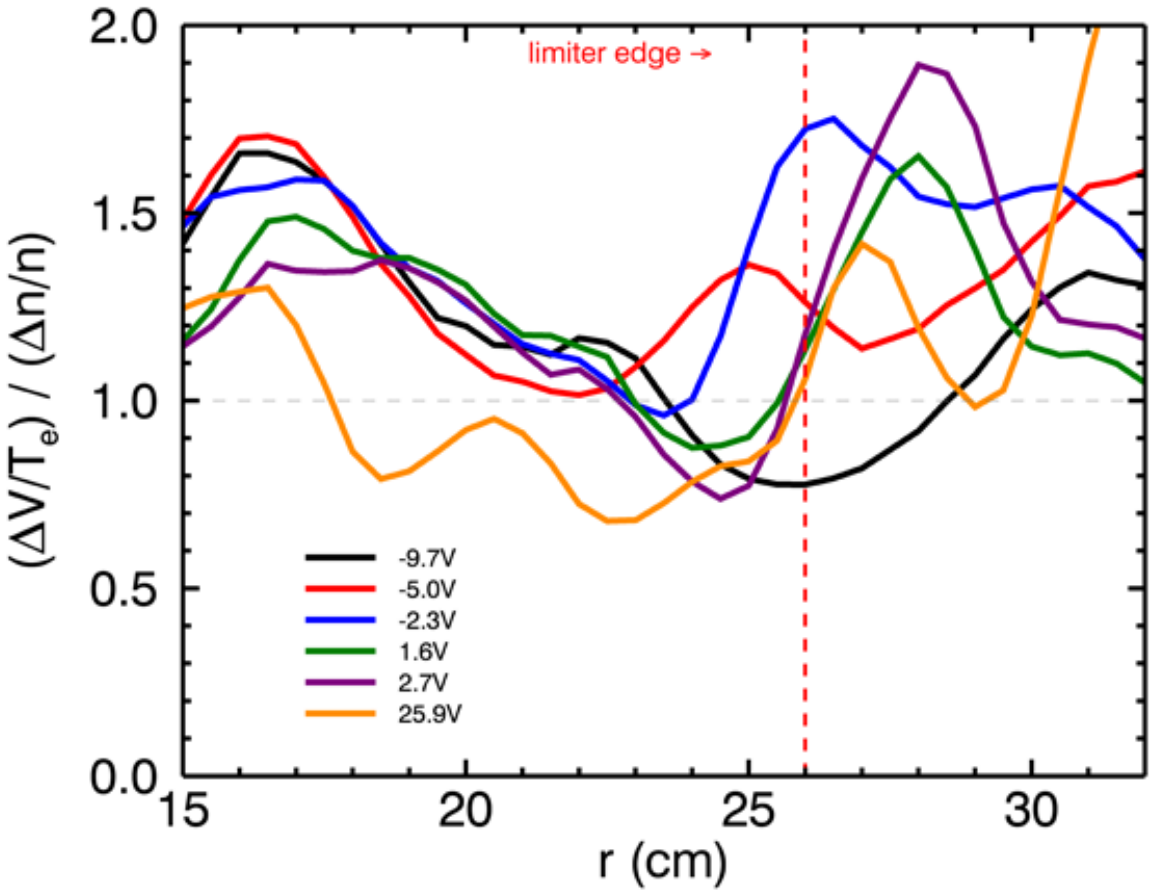

Figure 5.25: Profiles of ratios of floating potential fluctuations to density fluctuations for various biases.

$$\frac{\partial}{\partial t}(N) + (\mathbf{v}_e \cdot \nabla)N = 0 \tag{5.7}$$

$$Nm_e(\frac{\partial}{\partial t}(\mathbf{v}_e) + (\mathbf{v}_e \cdot \nabla)\mathbf{v}_e) = -\nabla(Nk_bT_e) - Ne\left(\mathbf{E} + \frac{\mathbf{v}_e}{c} \times \mathbf{B}\right) - Nm_e\nu_{ei}(\mathbf{v}_e - \mathbf{v}_i) - Nm_e\nu_{en}\mathbf{v}_e \tag{5.8}$$

$$Nm_i(\frac{\partial}{\partial t}(\mathbf{v}_i) + (\mathbf{v}_i \cdot \nabla)\mathbf{v}_i) = -Ne\left(\mathbf{E} + \frac{\mathbf{v}_i}{c} \times \mathbf{B}\right) - Nm_i\nu_{in}\mathbf{v}_i \tag{5.9}$$

$$\nabla \cdot \Big(eN(\mathbf{v}_{i\|} - \mathbf{v}_{e\|}) + eN(\mathbf{v}_{i\perp} - \mathbf{v}_{e\perp})\Big) = 0 \tag{5.10}$$

The following equations are a modified set of Braginskii fluid equations—augmented by the inclusion of radial density diffusion and ion-ion viscosity—used in an eigenmode solver code to calculate the growth rates and associated radially eigenfunctions of the modes present.

$$\frac{\partial}{\partial t}(N) = -\mathbf{v}_\mathbf{E} \cdot \nabla N - \frac{\partial}{\partial z}(v_{\|e}N) - D_n\nabla_\perp^2 N \tag{5.11}$$

$$\frac{\partial}{\partial t}(v_{\|e}) = -\mathbf{v}_\mathbf{E} \cdot \nabla v_{\|e} - \frac{m_i}{m_e}\frac{T_{e0}}{N_0}\frac{\partial}{\partial z}(N) - \frac{m_i}{m_e}\frac{\partial}{\partial z}(\phi) + 1.71\frac{m_i}{m_e}\frac{\partial}{\partial z}(T_e) - \nu_e v_{\|e} \tag{5.12}$$

$$\frac{\partial}{\partial t}(\varpi) = -\mathbf{v}_\mathbf{E} \cdot \nabla\varpi - \frac{\partial}{\partial z}(v_{\|e}N) + b \times \nabla N \cdot \frac{\nabla^2 v_E}{2} - \nu_{in}\varpi - \mu_{ii}\nabla_\perp^2\varpi \tag{5.13}$$

where $\varpi = \nabla_\perp \cdot (N\nabla_\perp\phi)$ is the definition of vorticity. Cast in cylindrical geometry, with $\mathbf{x} = (r, \theta, z)$, the solutions of the form

$$f(\mathbf{x}) = f(r)exp(im_\theta\theta + ik_\| z - i\omega t) \tag{5.14}$$

are sought for density, N, parallel electron flow, $v_{\|e}$, and vorticity, ϖ, where m_θ is the azimuthal mode number and $k_\|$ is the axial wavelength which can be case in terms of an axial eigenvalue, n_z.

The origins of the three different instabilities can be highlighted from the many various terms in Equations 5.13. First the growth of resistive drift-waves can be narrowed down to

the following subset of equations,

$$\frac{\partial}{\partial t}(N) = -\mathbf{v_E} \cdot \nabla N - \frac{\partial}{\partial z}(v_{\|e} N) \tag{5.15}$$

$$\frac{\partial}{\partial t}(v_{\|e}) = -\mathbf{v_E} \cdot \nabla v_{\|e} - \frac{m_i}{m_e}\frac{T_{e0}}{N_0}\frac{\partial}{\partial z}(N) - \frac{m_i}{m_e}\frac{\partial}{\partial z}(\phi) - \nu_e v_{\|e} \tag{5.16}$$

$$\frac{\partial}{\partial t}(\varpi) = -\frac{\partial}{\partial z}(v_{\|e} N) \tag{5.17}$$

which highlight the DW drive dependence on the gradient in density as well as the parallel electron response. In order for the DW to be unstable, a phase shift between the density and plasma potential is necessary and in these equations is provided by the resistivity due to electron collisions (found in the term $\nu_e v_{\|e}$).

Similarly, the origin of rotational interchange is contained in the subset,

$$\frac{\partial}{\partial t}(N) = -\mathbf{v_E} \cdot \nabla N \tag{5.18}$$

$$\frac{\partial}{\partial t}(\varpi) = -\mathbf{v_E} \cdot \nabla \varpi + b \times \nabla N \cdot \frac{\nabla^2 v_E}{2} - \nu_{in}\varpi \tag{5.19}$$

where the $b \times \nabla N \cdot \frac{\nabla^2 v_E}{2}$ terms serves as the centrifugal force terms which initiates the mixing inherent in the interchange instability.

Lastly, the KH modes arise due to the gradient in the vorticity as in,

$$\frac{\partial}{\partial t}(\varpi) = -\mathbf{v_E} \cdot \nabla \varpi \tag{5.20}$$

The remaining terms represent dissipative effects including perpendicular diffusion contained in the term $D_n \nabla_\perp^2 N$, where D_n taken to be classical diffusion in the code, and damping due to ion-ion viscosity contained in the term $\mu_{ii}\nabla_\perp^2 \varpi$.

Of course, in the full set of equations coupling can take place between modes (e.g. drift-interchange modes). However, it should be noted that drift waves can only occur when a parallel wavelength is present; in other words, when there is a non-zero parallel eigennumber, n. For n=0, only rotational interchange and Kelvin-Helmholtz modes can be active. For comparisons to these experiments, only values of n_z =0 and 0.5 are used which correspond to infinite wavelength flute-like modes for $n_z = 0$ and wavelengths of the order of twice the

machine length ($n_z = 0.5$), similar to the fundamental mode of a column with one open boundary condition and one closed boundary condition.

Using experimental profiles of density, temperature, and plasma potential for a given bias, Equations 5.13 are solved as an algebraic eigenvalue problem for each azimuthal eigenmode number, m, and parallel eigenmode number, n. The range of m numbers used for this analysis was $m = 1 - 80$ while n=0 or 0.5 as mentioned previously. The solutions consist of radial eigenfunctions for density, parallel velocity, and plasma potential of the form in Equation 5.14 coupled with a growth rate, γ, and a frequency, $\omega = 2\pi f$. A positive(negative) growth rate indicates an unstable(stable) mode while the sign of the frequency indicates the propagation direction of the mode. For this analysis, only the density eigenfunctions, growth rates and frequencies were used.

Figure 5.26 shows typical results from the profiles of four different biases(Bias#/(Limiter-Anode) potential : (a) Bias 1/-9.7V representing the unbiased IDD flow state, (b)Bias 8/-4.1V representing the zero flow state, (c)Bias 20/3.7V represented the moderate EDD flow state and (d)Bias 27/13.1V representing the strong EDD flow state. The growth rate and mode number for the fastest growing mode for each m-number is shown with the blue curves indicating calculations for n=0 and green for n=0.5. The mode selected is restricted to have a peak in its corresponding density eigenfunction within the a certain radial range; here, the modes are selected to be within radii of 20 and 32cm. If the fastest growing mode does not have a peak in its eigenfunction within the selected range, the next fastest growing mode is chosen and so on until all the possible modes are exhausted. This procedure ensures comparison to modes driven by the experimentally relevant gradients and not due to numerical artifacts.

The variations amongst the four biases shown demonstrate how the linear growth of instabilities are modified by the changes in the plasma profiles. In general, the n=0 modes appear to dominate the growth when both are present, certainly at lower m numbers. The exceptions are for small regions in the unbiased case and for m numbers larger than 20 in the moderate EDD flow case. In the zero flow case, only drift-waves can be active so only

n=0.5 modes will be unstable. The portions of Figure 5.26 which show the frequency of the corresponding growing mode indicate the direction of propagation of the modes. In the unbiased case, the n=0 modes propagate in the positive direction which given the experimental arrangement corresponds to the IDD direction. In the EDD flow biases, the frequency sign is now negative indicating propagation in the EDD direction. In the highest bias shown, the frequencies are in the EDD for all m numbers suggesting that all of these modes are predominately interchange driven modes. The moderate EDD mode has frequencies in both directions. The lower m number modes are likely rotational interchange, but the higher m number modes can either be interchange modes driven by flow in the IDD (which does occur in the very far radial end of this bias) or are KH modes which do not have to propagate in the direction of the flow. The zero flow state with only drift waves shows that drift-waves propagate only in the EDD.

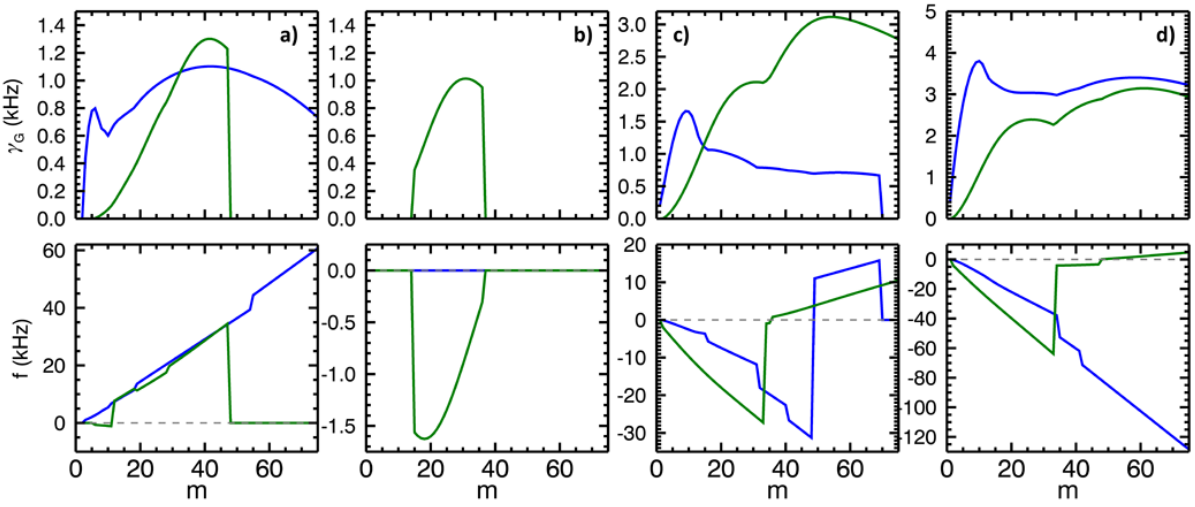

Figure 5.26: Plots of the linear calculated growth rate and frequency of the fastest growing mode for each m number. Blue curves represent calculations using n=0. Green curves represent calculations with n=0.5. Column(a) shows calculations for Bias 1, (b) for Bias 8, (c) for Bias 20 and (d)for Bias 27.

In order to facilitate comparisons to the experimental spectral density functions, a "growth rate density" function is constructed using the eigenfunctions, growth rates and frequencies

of the Braginskii equation solutions. First, the normalized eigenfunction of the fastest growing mode for each m number is scaled to the value of the growth rate to create a localized growth function—that is, the strength of the growing mode is maximum at the peak of the eigenfunction and reduced accordingly away from the peak. This radial distribution of growth rate is broken into wavenumbers, k, given the m number and radius. Connected to each value of k is the frequency of the mode, and the sign of the frequency is converted into a sign of the wavenumber. Then, this collection of signed wavenumbers or frequencies is histogrammed into wavenumber and frequency bins and then averaged according to the histogram count. What results is a contour of average growth rate as a function of wavenumber and frequency which can then be compared directly to the spectral density functions from experiment.

Figure 5.27 shows the "growth" density functions created using the same data presented in Figure 5.26 separated into different bias groupings and parallel eigenvalue n. The growth density functions shown were averaged for three bias regions: Row (a)Bias 0-9 representing all the biases with flow in the IDD; (b)Bias 10-14 representing the region near zero flow and just into the EDD flow; and (c)Bias 15-29 representing moderate to strong EDD flow. The first column shows these growth density functions calculated for n=0 and the second for n=0.5. The negative signed wavenumbers indicate mode propagation in the IDD while positive signed wavenumbers indicate EDD. The features of these plots will be explored in more detail when being compared to experimental data.

5.5.1 Experimental Spectra vs Linear Growth

To compare to the linear growth rate density functions shown in Figure 5.27, the spectral density plots for the same bias groupings and radial extent displayed in Figure 5.28.

A comparison of the two sets of plots yields similar overall features: 1) Both show an overall trend of mode propagation from the IDD to the EDD direction as bias is increased. In the experimental data there is a clear lean toward IDD wavenumbers in the low bias states.

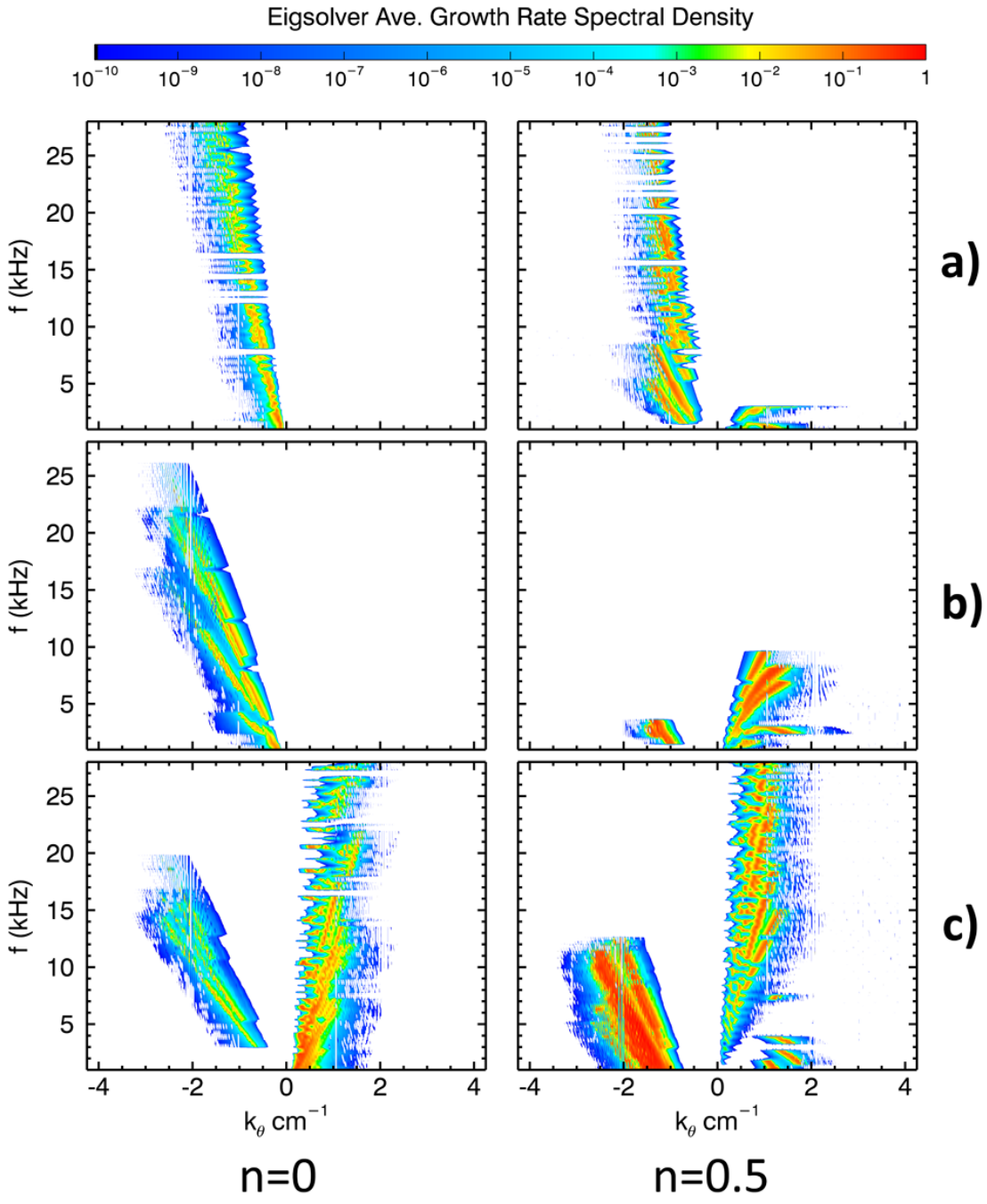

Figure 5.27: Growth Density functions from linear eigensolver calculations for 3 bias groupings: (a)Bias0-9, (b)Bias 10-14, and (c)Bias 15-29. Growth rates were restricted to the radial region of 20 to 32cm.

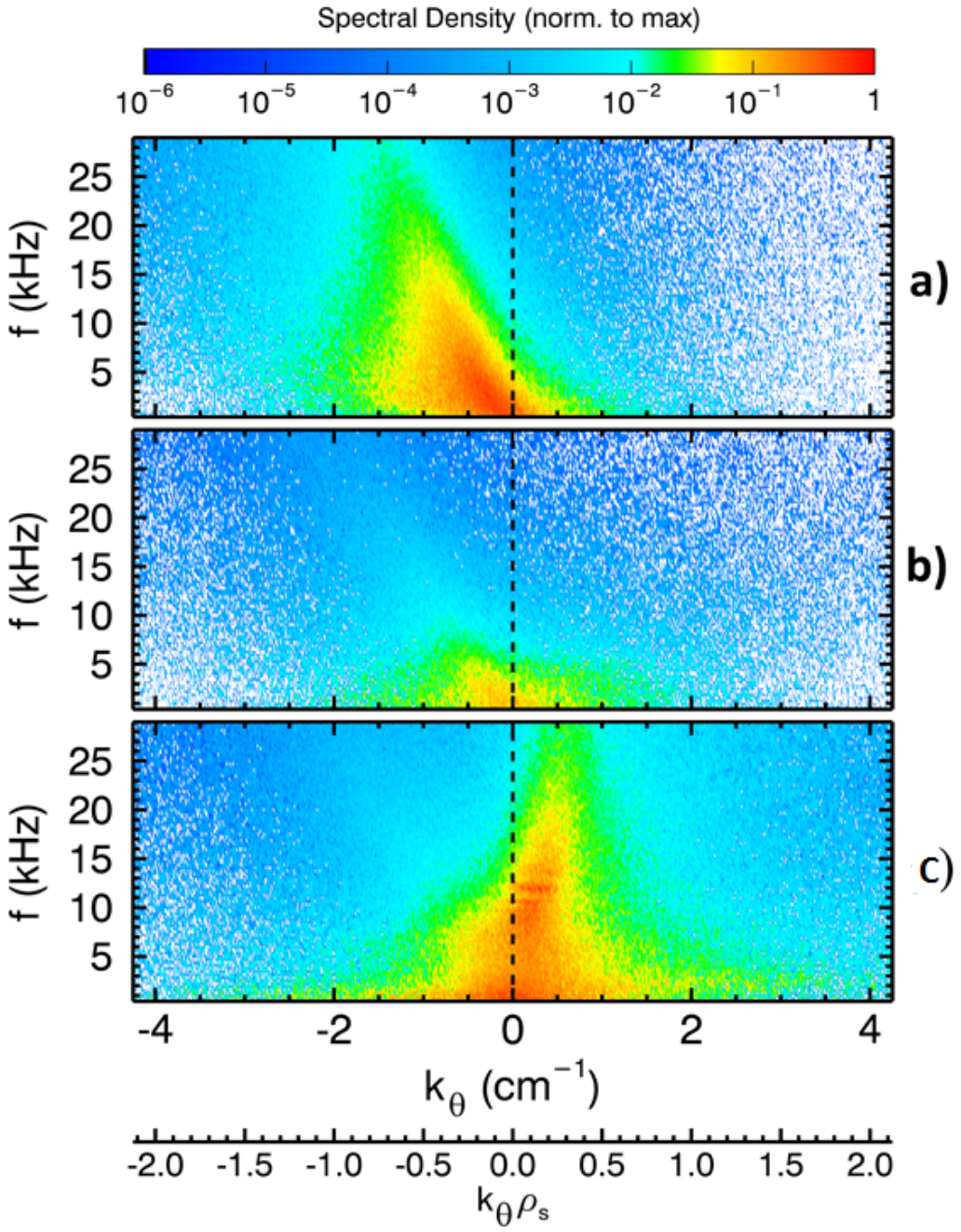

Figure 5.28: Perp Wavenumber spectra for three different bias groupings in the 20-32cm region (a)Bias 0-9 (b)Bias 10-14, and (c)Bias 15-29.

Similarly, in the growth density functions, the growth of modes is primarily in the IDD direction as well, form both n=0 and n=0.5 parallel eigenvalues. The low bias spectral density plots due show some power in the EDD and the growth density plots show some growth at low frequency and wavenumber in the EDD direction as well—characteristic of drift wave modes. Additionally, both spectral density and growth density plots for the low bias states have values which increase in frequency space with increasing wavenumbers. 2)Both low/zero flow bias groupings show a shift in density magnitude from high frequency to low frequency values. The low flow spectral density plot shows very little power beyond 5-10kHz and appears to be more evenly distributed between IDD and EDD directions, though there is still a slight tilt in the IDD. Meanwhile, the growth density plots also show a shift to lower frequency especially in the n=0.5, IDD direction. Meanwhile, there is a concentration of growth density in the n=0.5, EDD direction. Since these middle biases correspond to the states of lowest flow, this growth is likely the emergence of a dominant drift-wave mode. 3)Moving into the high bias, high EDD flow regimes, there is a clear shift into EDD propagating modes. Direct comparison of the top and bottom plots of both spectral density and growth density highlight this change. The experimental data shows an overall lean to the EDD and the appearance of the coherent mode is clear between 8 and 12kHz where the red is darkest. Despite this overall shift, there is still significant fluctuations propagating in both directions; the width in wavenumbers space for frequencies less than 10kHz is generally wider than the low bias groupings. In the calculated growth density plots, there is clearly more growth in the EDD for n=0, though growth in the IDD is not entirely eliminated. The n=0.5 column has the most activity with strong growth in both azimuthal directions. Since the high bias states have flow and density profiles that would both tend to drive their corresponding instability in the EDD, the strong growth in the IDD is a possible indication of KH growth.

To narrow down the possible origins of the features in both the spectral and growth density plots, cuts in radius and bias can be made to highlight the regions where only certain gradients are present. The first cut is made to radius in order to separate density gradient only regions from regions with density and flow. Figure 5.29 shows spectral density

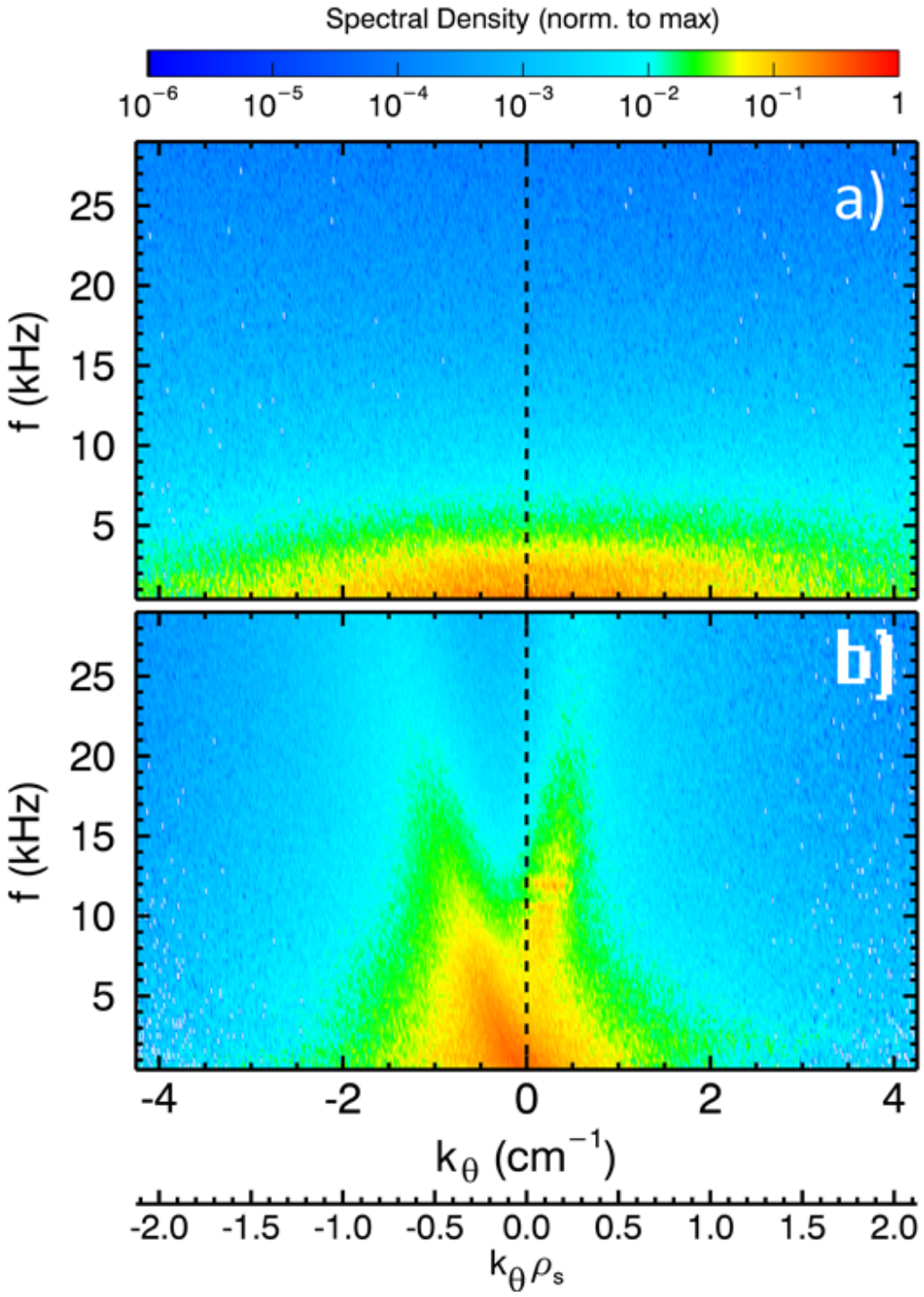

Figure 5.29: Perp Wavenumber spectra for two different gradient regions (a)Density gradient only, no flow (12-20cm) and (b) Density gradient, temperature gradient, and flow (20-32cm).

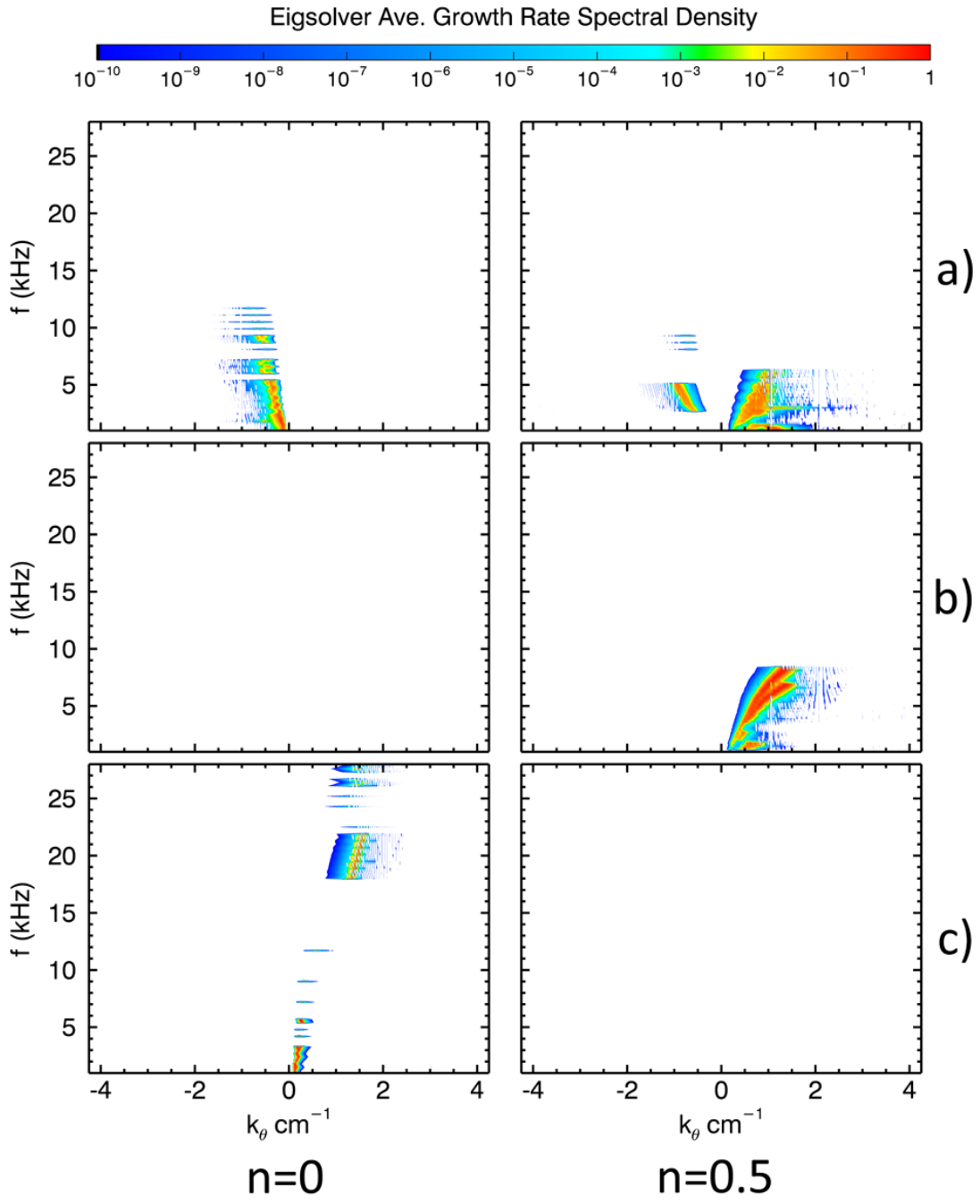

Figure 5.30: Growth Density functions from linear eigensolver calculations for 3 bias groupings: (a)Bias0-9, (b)Bias 10-14, and (c)Bias 15-29. Growth rates were restricted to the radial region of 12 to 25cm.

plots for all biases, but restricted to either 12-20cm (top) or 20-32cm (bottom); this cut-off in radius approximates where the rotation in the edge no longer penetrates into the core (even at the highest biases). The distinction is striking; turbulent fluctuations in the core region are broad in wavenumber space, spanning both azimuthal directions, but very restricted in frequency space, with fluctuation amplitude dropping by at least 3 orders of magnitude beyond 5kHz. The edge region, in contrast, is much more narrowly confined in wavenumber space, but expands into large frequencies, reaching significant amplitudes up to 20kHz.

Linear calculations appear to somewhat mirror this differences observed in the spectral density plots. Figure 5.30 shows the growth density for the same sets of biases in Figure 5.27, but restricted to modes that peak in the region 12 to 25cm, again where density gradients are the primary gradient drive. Comparison between these plots and those in Figure 5.27 show that without flow, the only modes that grow are those which were speculated to be drift-waves. Like the spectral density plots, the growth density plots are localized to low frequencies, less than 10kHz. The growth rate features in the IDD that spanned the large range in frequencies are not present, though there is some evidence of possible flow driven modes (this is possible since the cutoff for calculated growth is wider than the experimental cutoff and some flows exist in the 20 to 25cm region.) Assuming that n=0.5, EDD propagating modes in the top and middle row plots are indeed drift waves, the modes can be characterized by generally low frequency and for having a light curve in the apparent dispersion relation, as the frequency increase with wavenumber appears to level off. This then can be distinguished from the flow modes in Figure 5.27 which have a more linear dispersion relation. It should also be noted that while the bottom row of Figure 5.30 would seem to indicate no drift-wave growth despite the steepened gradient at high bias, the likely reason for this is that the density gradient is strongest in the region beyond 25cm for high biases; in fact, looking at the density profiles for high bias show that there is comparatively little density gradient for high biases in the 12-20cm region. Looking instead at the edge growth density plots in Figure 5.27(c), there appears to be some drift-wave like mode growth in the region $< 5kHz$, distinct from the flow driven modes in the higher frequency.

Since the main difference between these two regions is the presence or lack of a flow profile, while a density gradient is present throughout both, it is tempting to attribute the turbulent spectral density of Figure 5.29(a) as being generated by drift-wave turbulence; however, this is too simplistic a conclusion to make as other modes can be active, such as the non-linear modes mentioned earlier [50]. Trying to connect the nature of the turbulence in the core seen in the experiment to growing linear drift waves is impossible without taking into account these non-linear and saturation mechanisms. Indeed, the linear calculations show that linear drift waves should propagate in the EDD direction while the saturated turbulence is clearly symmetrically distributed. What can be concluded is that the introduction of flow has a significant impact on the eventual saturated turbulence either through the generation of pure rotational flute modes or through coupling to the modes already present (e.g. drift-interchange modes). The shape of the spectral density distribution in Figure 5.29(b) compares much more favorably to the growth rate distribution shape for the edge region modes in Figure 5.27 suggesting that these flow driven modes may retain more of their linear nature than the modes in the core. In fact, it can will shown that the coherent modes observed in the driven states can be fairly conclusively attributed to the growth of both a pure (n=0) interchange mode and a coupled (n=0.5) drift-interchange mode.

An attempt to distinguish between rotational interchange and Kelvin-Helmholtz modes can be made. Again referring to the edge spectral density plots in Figure 5.28, the modes that change direction from IDD to EDD are most likely to be driven by interchange. In the full range growth density plots, the IDD flow biases show significant growth in the IDD direction for both n=0 and n=0.5 which is indicative of interchange modes; however, it is conceivable that KH modes would be present as well. When the flow is reverse into the EDD, as in the bottom row plots, there is now significant EDD growth for both n=0 and n=0.5, consistent with rotational interchange modes driven by EDD flow; however there remains growth in the IDD. Since the flow is almost entirely in the EDD for these biases, the strong IDD growth probably cannot be RI, leaving KH as the likely candidate. This can be supported noting where KH drive is likely to exist. In Figure 5.24, the gradient of the vorticity reaches its

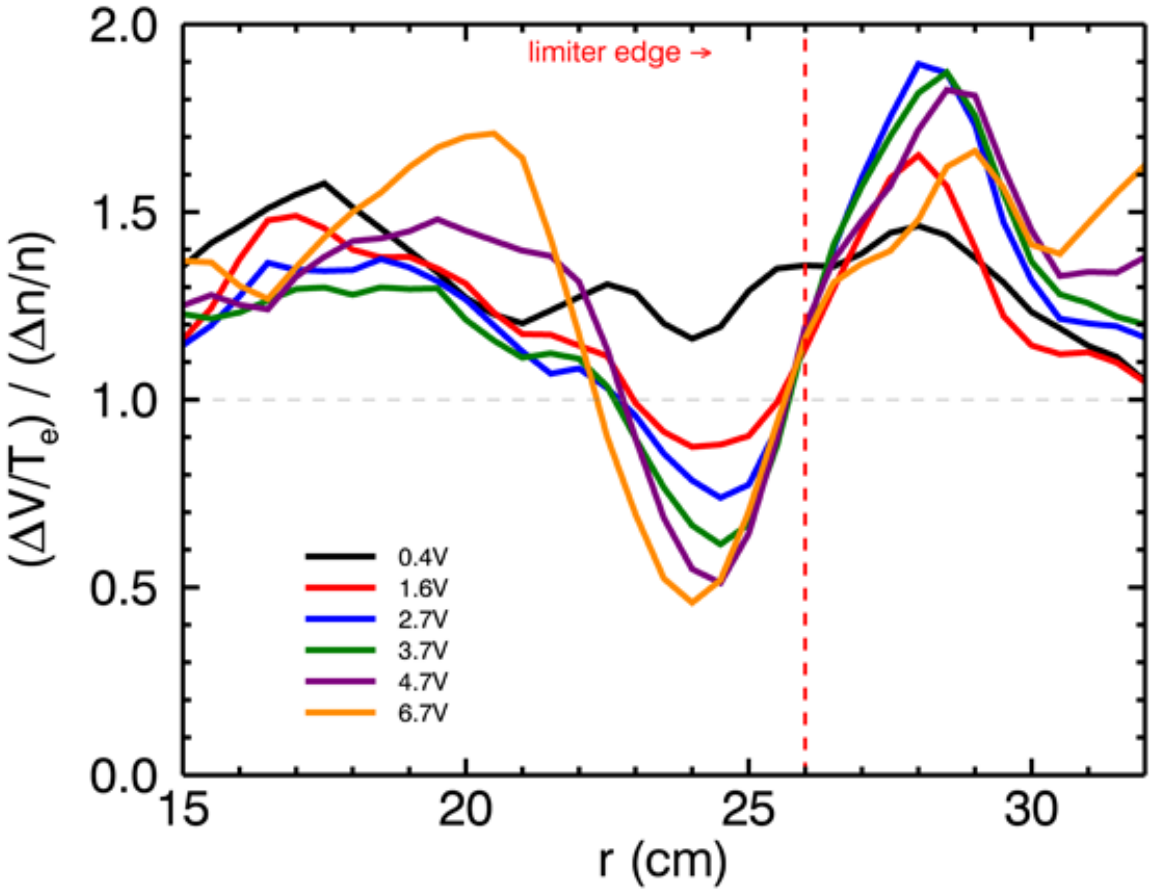

Figure 5.31: Profiles of ratios of floating potential fluctuations to density fluctuations biases that exhibit a coherent mode as well as a strong vorticity gradient.

largest values when the limiter is between 1 and 10V above the anode—corresponding to Biases 15-25—as well as localized in a region just outside the limiter edge. Similarly, the fluctuation ratio profiles shows peak values in this radial region for the bias range listed, shown in Figure 5.31. KH modes would generally have fluctuation ratios $R >> 1$. While ratios just under 2 cannot be considered large, the higher values are consistent with KH drive in that region.

Finally, linear calculations also support the KH mode hypothesis. Figure 5.32 shows the growth density now restricted to the range 27.5 to 31cm and with biases grouped differently. The top plot is still low biases Bias 0-9, but the middle plot now averages Biases 15 to 25 and the bottom plot shows Bias 27 through 29. It is clear in comparison to the full range, bottom plot of Figure 5.27 that the modes growing in the IDD for both n=0 and n=0.5 really only grow in the biases and in the region that has significant vorticity gradient. This can be compared to spectral density plots for the same region and biases of Figure 5.33. Like the growth density plots, the spectral density does not exhibit the long linear features that presumably are characteristic of the rotational interchange modes. Rather they feature squatter shapes in frequency and wavenumber space similar to those growth density features in Figure 5.32.

5.5.2 Evaluation of the Coherent Mode

Finally, given the categorization of the probable contributions for DW, RI, and KH modes, the origin of the coherent mode can be explored. Figure 5.34 shows the frequency spectra for various biases zoomed in to frequencies less than 50kHz and focused in the region right around the limiter edge, where the presense of the coherent mode is strongest. Compared to the minimum flow case (Limiter-Anode = -5.0V), where the fluctuation spectrum is broadband, a clear peaks in the spectra emerge starting at a Limiter-Anode voltage difference of 2.7V and increasing in power and frequency up to a voltage difference of 13.1V. The highest bias listed, with a voltage difference of 25.9V, shows a reduction in power and less distinct peaks.

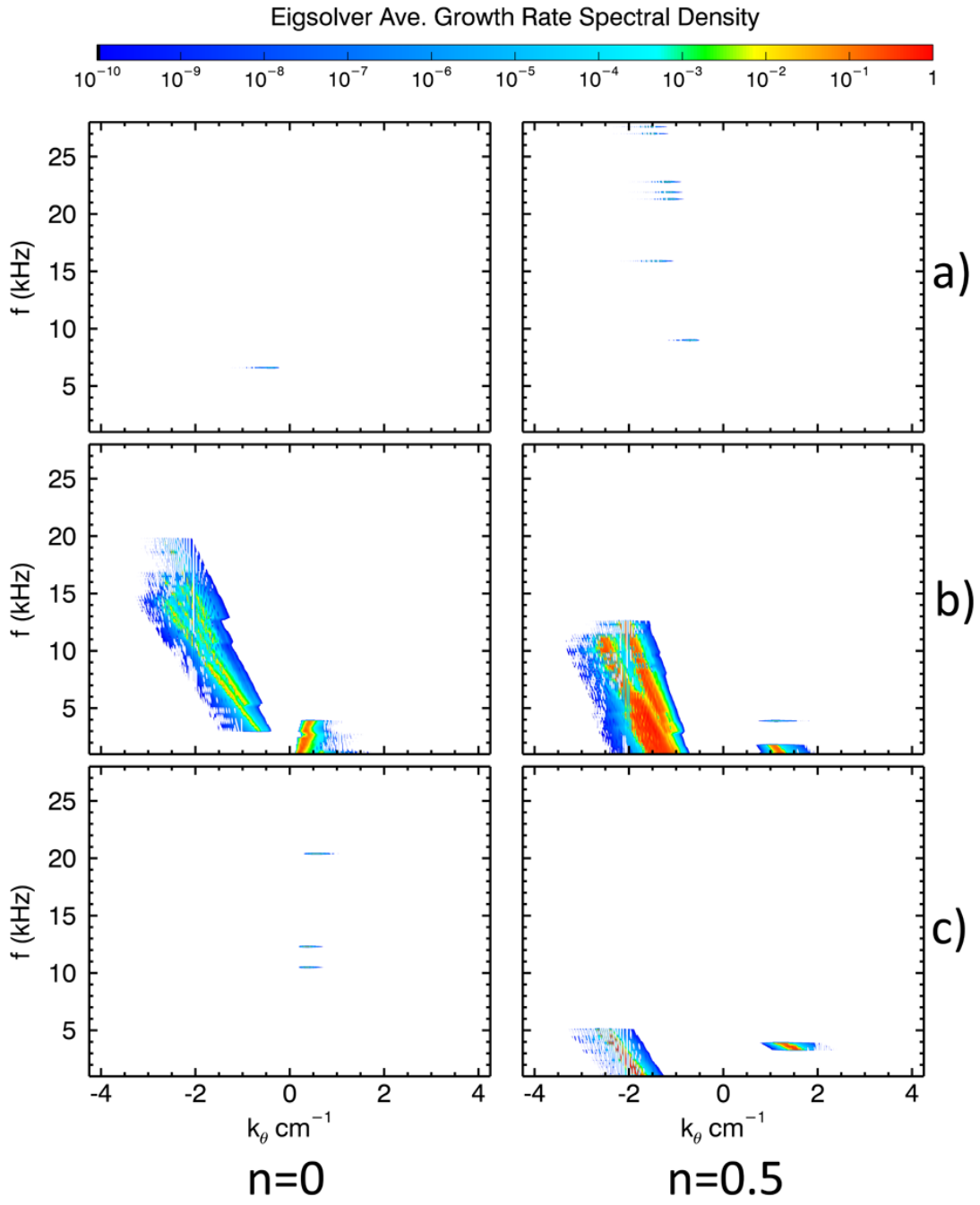

Figure 5.32: Growth Density functions from linear eigensolver calculations for 3 bias groupings: (a)Bias0-9, (b)Bias 15-25, and (c)Bias 27-29. Growth rates were restricted to the radial region of 27.5 to 31cm.

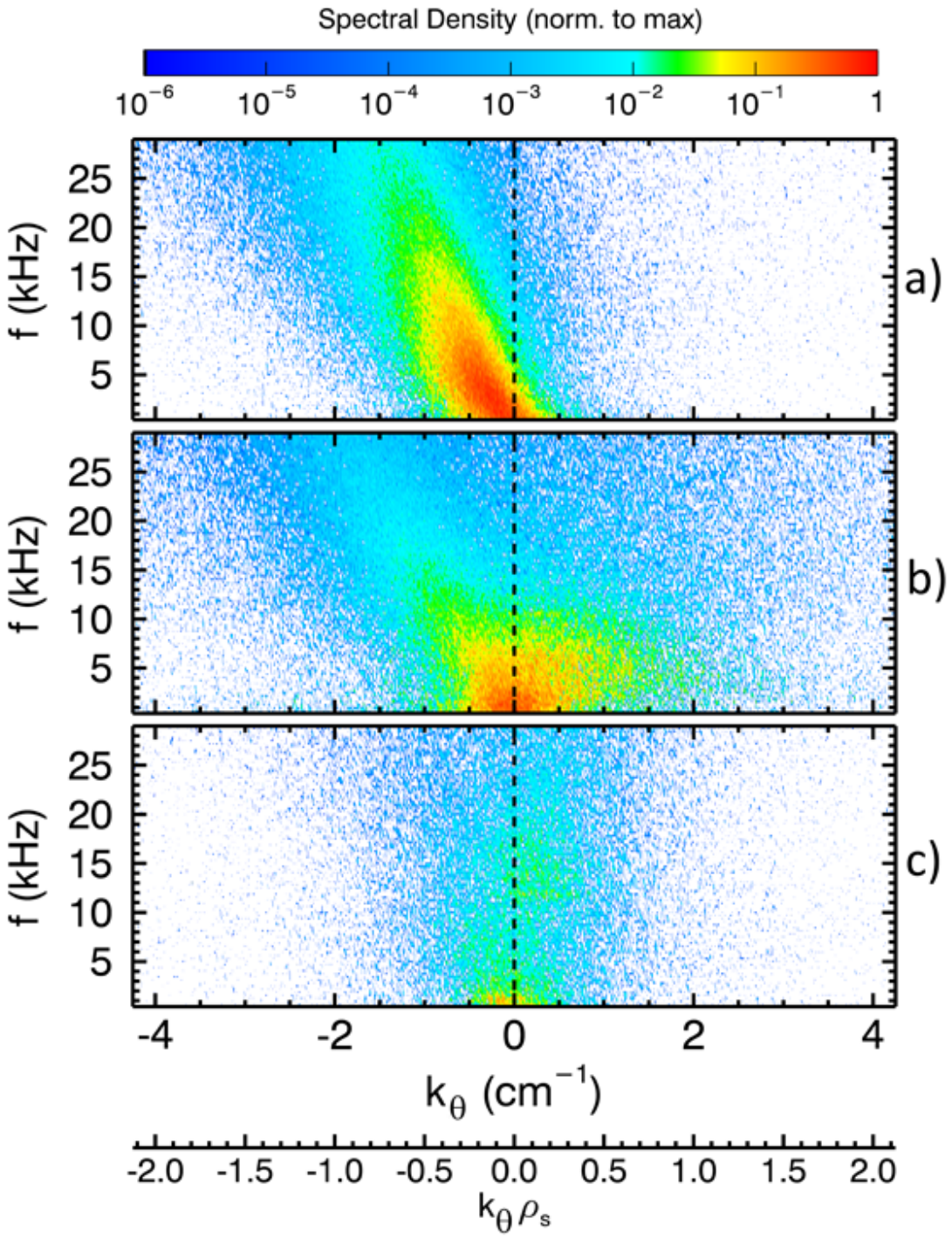

Figure 5.33: Spectral density for (a)Bias 0-9, (b)Bias 15-25 and (c)Bias 27-29 restricted in the region outside the limiter edge, 27.5 to 31cm.

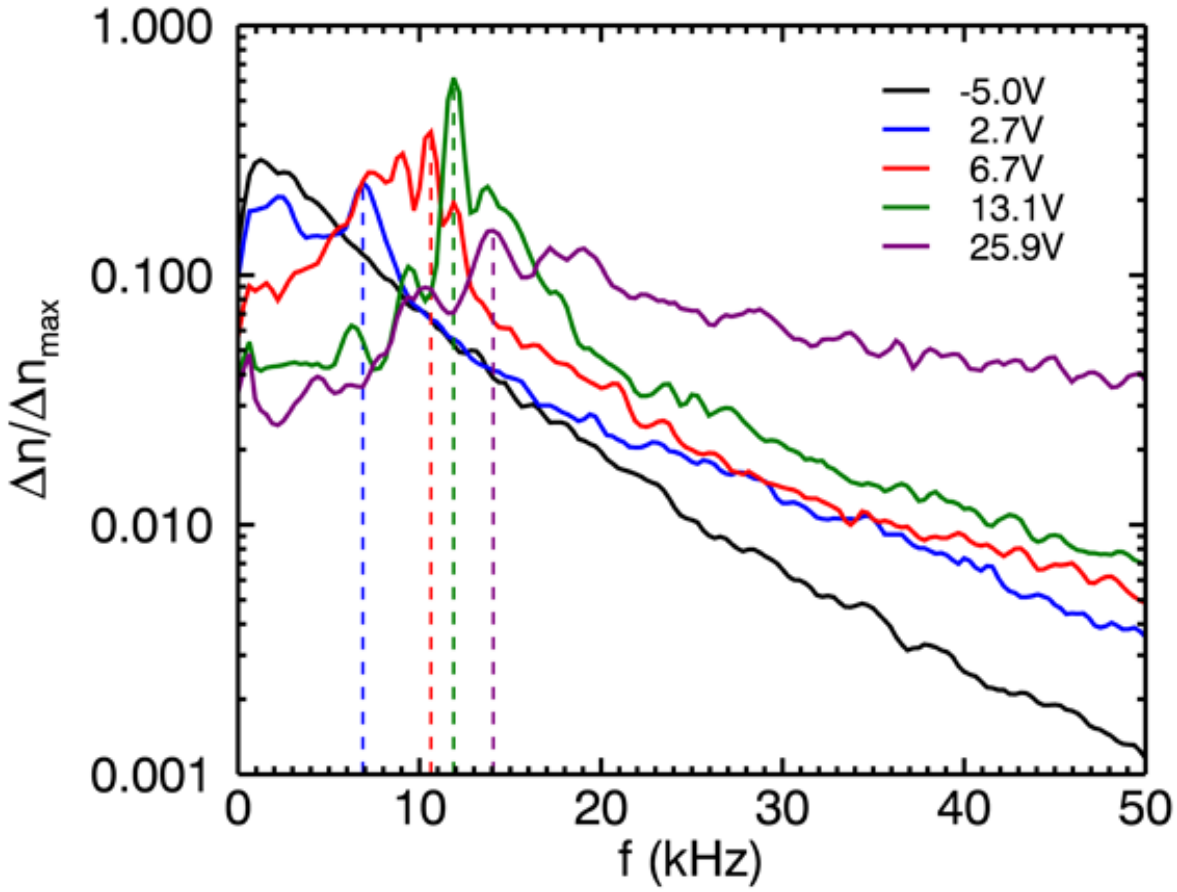

Figure 5.34: Coherent modes for various biases

The very localized nature of the coherent mode (or modes) can helps in determining its underlying instability. The mode peaks at the limiter edge which is precisely where the azimuthal flow peaks (see Figure 4.16)suggesting this mode is purely rotation interchange driven; however, the density profiles show that this point is also where the steepest density gradient occurs implying the strongest drive for drift waves would also occur at this point.

Given the lack of strong flow shear at this point ($\gamma_s = 0$ at the flow max), the mode is unlikely driven by the Kelvin-Helmholtz instability. It was also shown in Figure 5.32 that the KH drive appears to be localized to a region outside the limiter edge.

Since the coherent mode is generally observed in the same biases where the vorticity gradient peak is observed, Figure 5.31, shows that the fluctuation ratio for the limiter edge region sit fairly consistently at a value just above 1, consistant with what would be expected for interchange modes.

Spectrally, the mode does not begin to emerge as a distinctly coherent mode until the plasma is rotating in the EDD direction. Indeed, as shown in Figure 5.35(c) which shows the average spectral density for all the EDD flow states, the peaks in the spectra density indicating the coherent mode are situated only in the EDD propagation direction. Neither (a) or (b), representing the IDD flow or non-rotating bias states show coherent mode behavior. However, this directionality cannot rule out contribution from drift waves to the mode.

Comparison with the linear calculations, however, appears to offer the clinching evidence for rotational interchange. Figure 5.36 shows a similar set of growth density plots and bias groupings as in Figure 5.27, but restricted now to 24 to 28cm. Again for the regions of flow, the top and bottom plots, the only growth rate shown are those characteristic of rotational interchange modes. The n=0.5, high bias bottom right plot does not show features characteristic of the IDD KH modes or the low frequency EDD DW modes. The only growth in this region is due to rotational interchange modes; however, there is growth for both n=0 and n=0.5 modes. Which of these modes then drives the coherent mode?

The frequency of the calculated modes can be examined and compared to the experi-

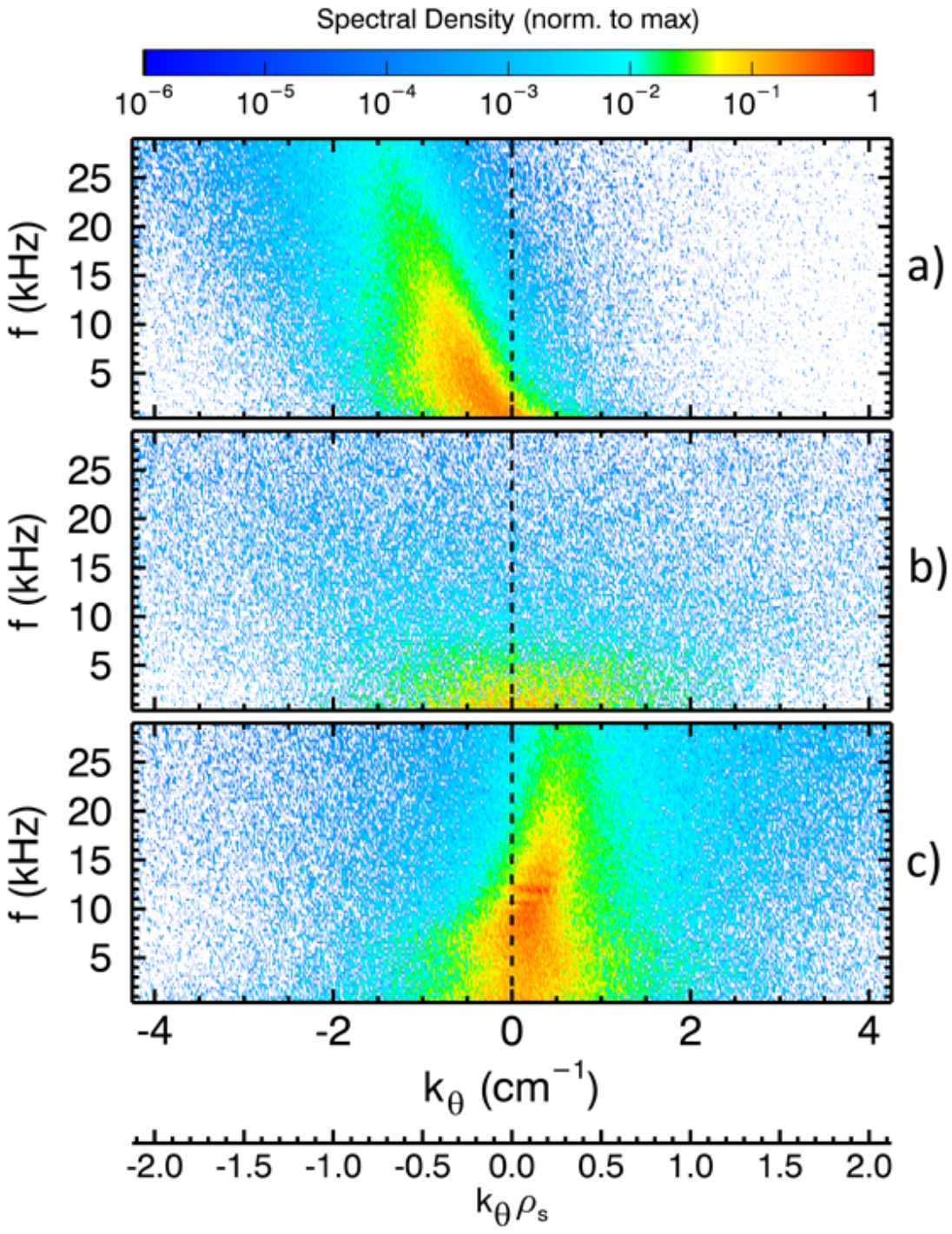

Figure 5.35: Spectral density for (a)Bias 0-9, (b)Bias 10-14 and (c)Bias 15-29 restricted in the region right around the limiter edge, 24 to 28cm.

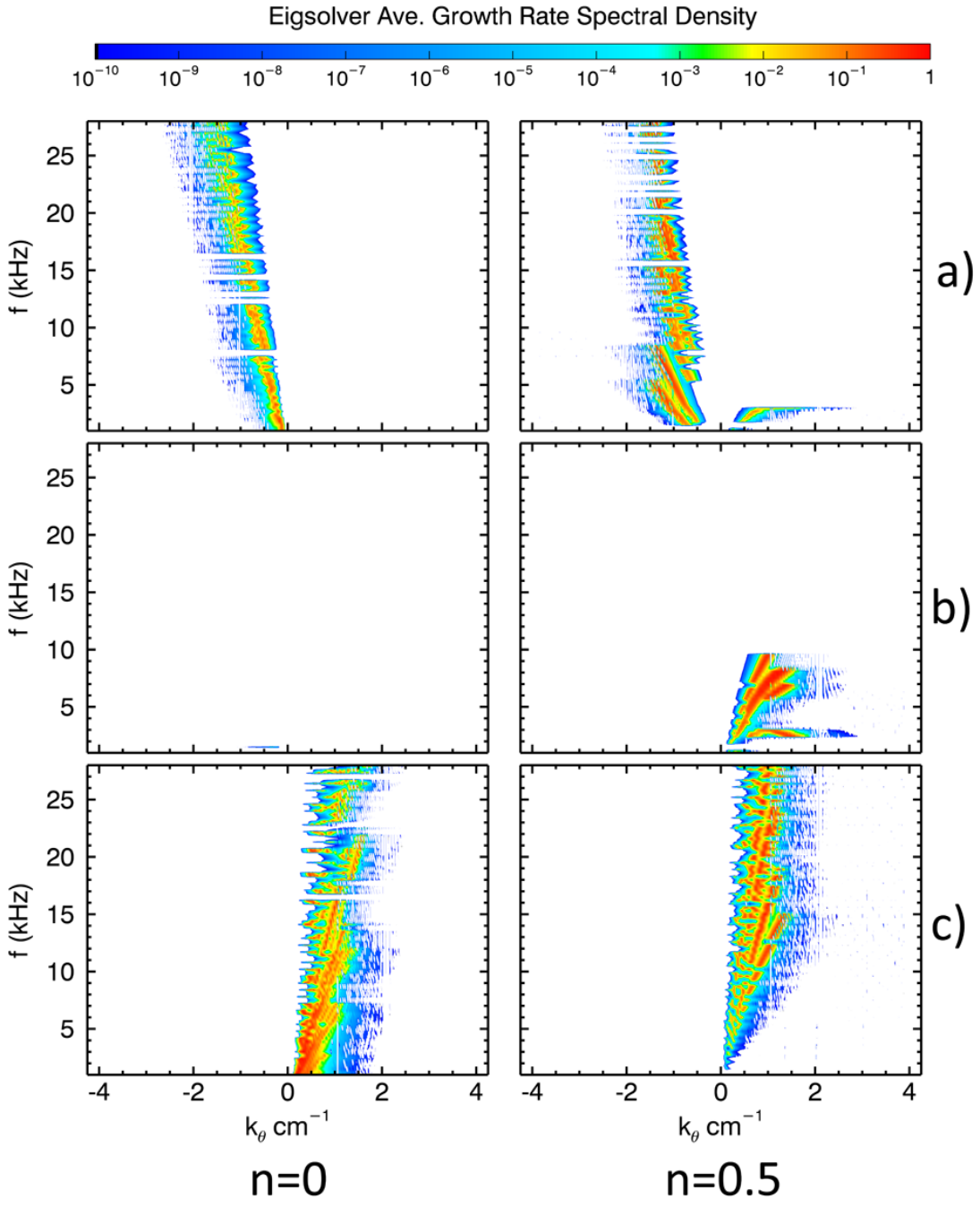

Figure 5.36: "Growth" Density functions from linear eigensolver calculations for 3 bias groupings: (a)Bias0-9, (b)Bias 10-14, and (c)Bias 15-29. Growth rates were restricted to the radial region of 24 to 28cm which surrounds the limiter edge and location of the coherent mode.

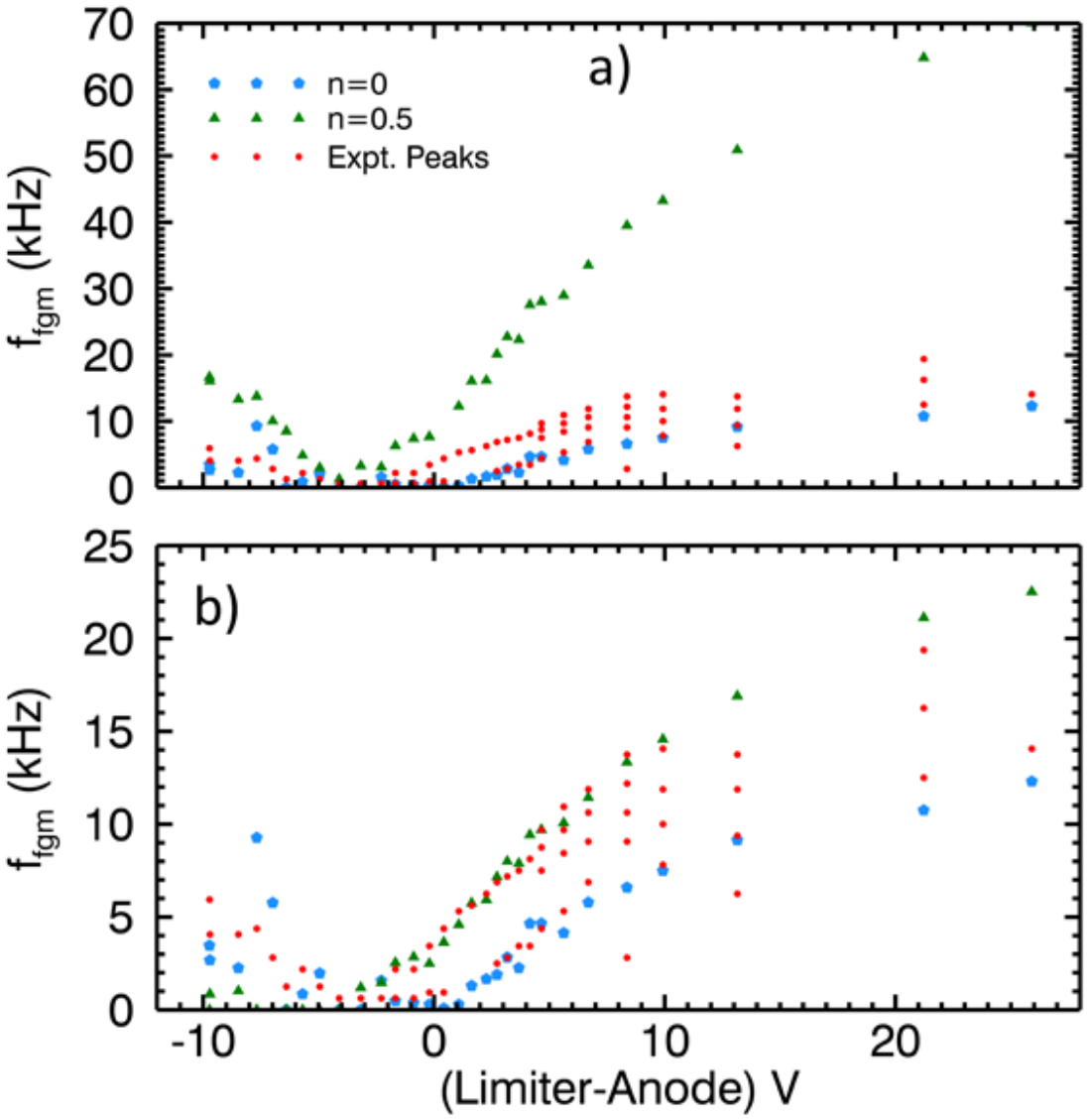

Figure 5.37: Linear eigensolver calculated fastest growing modes for each bias state for n=0 (blue pentagon) and n=0.5 (green triangle) with peaks in the experimental spectra of each bias (red circles). If the spectra show multiple distinct peaks, a red circle is placed to indicates the frequency of each peak. The top plot (a) shows frequency of the maximum growing m-number mode per bias with m-number restricted to 1-25 for both n=0 and m=1-25 for n=0.5. The bottom plot (b) is the same, but with the range restricted to m=1-25 for n=0 and m=1-7 for n=0.5. These restrictions are motivated by the experimental m-numbers measured.

mental frequency peaks from the measured spectra. Returning to the original forms of the calculated values of growth rate and frequency as in Figure 5.26, the frequency of the fastest growing m number mode for each frequency and for both n=0 and n=0.5 is plotted against limiter bias in Figure 5.37. Close examination of the frequency spectra shows that there are actually two peaks that begin to appear with EDD flow; one at a lower frequency and one at a higher one. For example, the blue curve in Figure 5.34 exhibits a clear peak at a frequency of about 7kHz as indicated by the dotted line, but a second peak at about 2kHz can also be seen. With increasing bias, the frequencies of both peaks increase, with the one starting at a lower frequency originally increase slightly faster than the high frequency peak. As the frequencies merge, there appears to be a mode interaction and sidebands appear resulting in multiple peaks. The red and green curves of Figure 5.34 show this behavior. The multiple peaks are plotted as a function of limiter bias in 5.37 indicated by the small red dots. For low bias voltages, the peak is just taken as the peak of the broadband spectra. As more distinct peaks emerge, there appears to be two lines of increasing frequency forming with increasing bias. At a limiter minus anode voltage of about 5V, more than two peaks begin to appear and the two lines merge into a range of peaks which continue to increase in frequency with bias.

The experimental peaks can be then compared to the frequencies of the fastest growing modes for each bias. Since the linear growth rates do not incorporate any saturation mechanisms, a limit on the range of m numbers must be set manually. Referring to the experimental m eigenvalue distributions in Figure 5.22, it is clear that the fluctuations power as a function of m number falls off by about an order of magnitude by about m=25. The top plot in 5.37 shows the frequency for the fastest growing m number mode within this m=1-25 range. The frequency of the fastest growing n=0 modes appear to generally follow the lower frequency line of experimental peaks. The fastest growing n=0.5 growing modes though tend to outpace the increase in frequency of the second experimental line. However, by limiting the m number range of the calculated fastest growing mode, the frequency of the n=0.5 modes can be reduced. The bottom plot displays the same data as the top, but

with m numbers for the n=0.5 modes restricted to m=1-7. Forcing this low m number is not entirely unreasonable considering that the experimental m-number peak for limiter edge fluctuations as seen in Figure 5.22(b) is just under m=10. Given this restriction the n=0.5 calculated frequencies line up almost exactly with the line of high frequency experimental peaks.

Figure 5.38 shows calculated eigenfunctions for given m and n eigenvalues compared to a frequency filtered density profile which can serve as an experimental radial eigenfunction. Figures 5.38(a) and (c) show the radial eigenfunctions for two lower frequency, n=0 modes while (b) and (d) show the eigenfunctions for two higher frequency n=0.5 modes. The m-numbers of the modes correspond to the fastest growing mode m-number as indicated by Figure 5.37(b). The experimental density fluctuation profile is filtered to a small bandwidth that nearly matches the frequency of the fastest growing mode. The comparison shows that for (b) and (d) that the peak of the eigenfunction corresponds to the peak of the experimental fluctuation profile. On the other hand, plots (a) and (c) show that the eigenfunction match up to a local peak, but not peak with the most power. This suggests that the n=0 modes—(a) and (c)—correspond to a peak just outside the limiter edge while the n=0.5 modes—(b) and (d)—correspond to a peak directly on the limiter edge.

The conclusion from this analysis is that the coherent mode observed at the limiter edge is in fact two coherent modes; one driven by pure n=0 rotational interchange and the other driven by n=0.5 rotational interchange. Since the parallel eigenvalue of this second mode is non-zero, it is in a way coupling to the mechanism that drives drift-waves. Thus non-zero parallel eigenvalue rotational modes are often called drift-interchange modes. As the rotation, and thus drive and frequency of these modes, increases, the interchange and drift-interchange modes appear to interact creating multiple sideband peaks. At even high biases, this linear interaction seems to evolve into non-linear broadband turbulence. In the highest measured bias spectra, shown as the purple line in Figure 5.34, the intensity of the coherent mode has collapsed, turning into a more broadband like structure, and its energy possibly going into high frequency values. Comparison of the radial location of peaks between Figures 5.38(a)

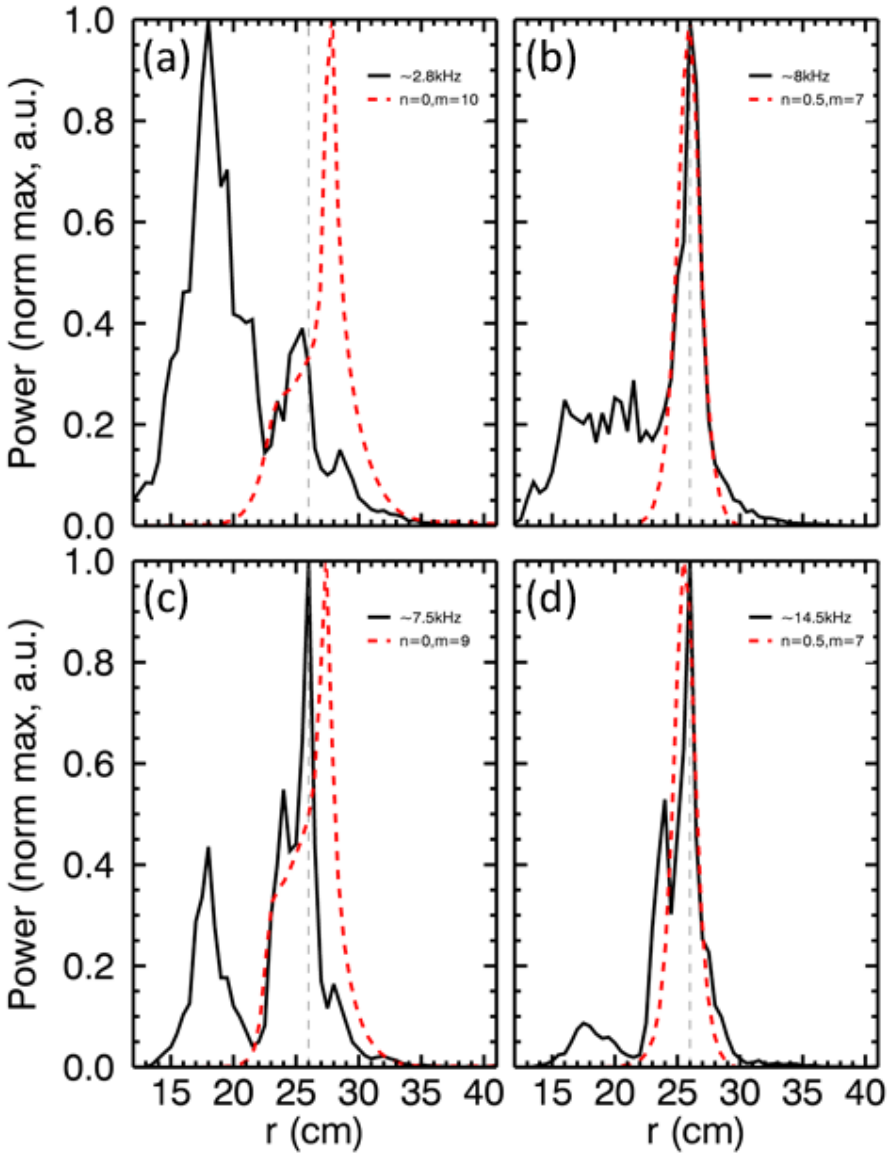

Figure 5.38: Comparison of radial eigenfunctions calculated using the Braginskii eigenmode solver with filtered density fluctuation profiles. (a) Shows the eigenfunction (red) for the fastest growing mode for n=0 for a moderately biased, medium EDD flow case, which is also found to have m=10 and a frequency of about 2kHz. The density fluctuation profile (black) for his same bias is bandwidth filtered just around 2kHz. (b) Shows a similar plot for this same bias case but for the fastest growing n=0.5 mode which has an m=7 and frequency of 8kHz. (c) and (d) show the same as (a) and (b) but for a high bias, high EDD flow case.

and (c) also seems to show that the radial location of the n=0 mode begins to shift slightly inward with increasing bias. This is likely a contributing cause to the increasing interaction and sideband production.

The results of this mode analysis suggest that the saturated LAPD plasma consists of a combination of low frequency drift modes overlayed with higher frequency linear rotational interchange and drift wave modes. All plasma states appear to share a common bed of low frequency (<5kHz), broadband fluctuations approximately equally distributed in both electron and ion diamagnetic drift directions, most likely saturated drift-wave turbulence. If rotation is present in any amount, higher frequency (5-15kHz) modes appear on top of this broadband foundation. In the unbiased state, these rotational interchange modes propagate in the ion diamagnetic drift direction and remain broadband in nature as reflected in both frequency spectra and spectral density. In strongly biases states, while the low frequency drift-wave base remains, a higher frequency coherent mode emerges out of the broadband spectrum as well as the appearance of KH modes. The coherent modes are a rotational interchange and rotational drift-interchange mode that can be seen to grow up, interact and eventually spread out into additional broadband turbulence.

5.6 Turbulent Structure and Modification

The turbulent structure refers to the level of spatial correlation observed between fluctuating quantities. This correlation plane can indicate the amount of radial and axial correlation between two points which is an indication of the amount of turbulence, which would tend to decrease this spatial correlation. Moreover, the correlation structures can indicate the influence of flows in modifying the shape of the structure through shearing.

Correlation plane measurements are taken by calculating the correlation between a stationary reference probe measuring either saturated current or floating potential, and a second motion probe which maps out a spatial region around the reference probe with a similar measurement. In LAPD, the axial variation of fluctuating quantities is low so the reference probe

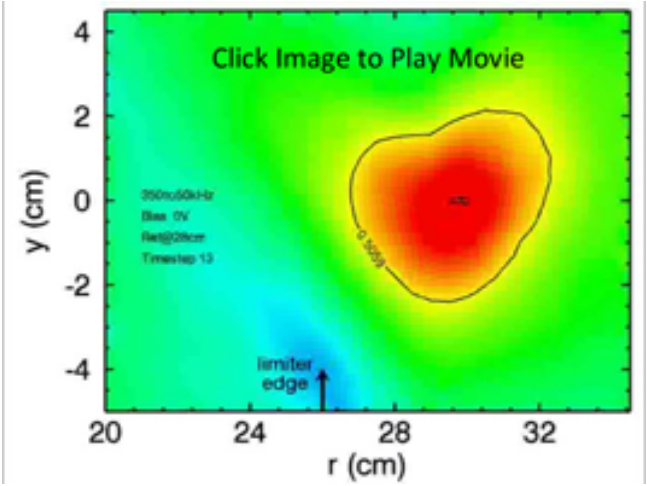

Figure 5.39: Movie of correlation plane as a function of time-delay τ. (Viewable on pdf only. Click on image to start movie. Right click and select disable content to stop movie.)

and motion probe can be located at different axial ports. For these experiments, the reference probe used was the multi-tipped rake probe measuring saturated current with tips at 26.5, 27.0, 27.5, 28.5, 29.5 and 31.5cm. A second Langmuir probe measuring saturated current was used as the motion probe and swept in a planer region of 20 to 34.5cm in radius and -5 to 4.5cm y. The correlation function can be calculated in two ways: it can be either directly computed as time-averaged product of two time-series, or as the integral of the product of the Fourier transforms of the two time-series.

When computing directly in the time domain, it is straightforward to introduce a time-delay, τ in the correlation, as in

$$C(x, y, \tau) = \langle I_{ref}(x, y, t) I_{mot}(x, y, t + \tau) \rangle \tag{5.21}$$

where the brackets indicate an average over time, t. Viewing the changes in correlation function with time-delay can indicate its general direction of propagation and evolution over time. This effect can be observed in Figure 5.39 which shows the correlation function, $C(x, y, \tau)$ normalized by C_{max} for each time-step for both negative and positive delay times. The peak correlation with the reference probe begins near the bottom when the motion time-series is leading the reference time series. As the delay time is shortened, the peak

correlation moves upward indicating an overall plasma motion in the ion diamagnetic drift direction and continues upward into positive delay times.

While examining time-delay correlations can be useful for determining propagation direction, the must interesting information comes from the $\tau = 0$ correlation. In this case, the correlation function can be rewritten in terms of an integral over the cross-spectrum between the two time-series as

$$C(x, y, \tau = 0) = \langle I_{ref}(x, y, t) I_{mot}(x, y, t) \rangle = 2 \int_{f_1}^{f_2} |\tilde{I}_{ref}(x, y, f)||\tilde{I}_{mot}(x, y, f)| \cos(\theta) \gamma df \tag{5.22}$$

where $C(x, y)$ is again normalized to C_{max} and $f_1 = 350$Hz and $f_2 = 100$kHz. θ is the spectral crossphase between the reference I_{sat} fluctuations and the motion I_{mot} while γ is the coherency between the two quantities. The benefit of the integral form is the ability to include a bandwidth in the calculation of the correlation function. This will be particular useful in high bias situations as it will be shown that a coherent mode in about the 8-12kHz range will have an impact on the correlation plane.

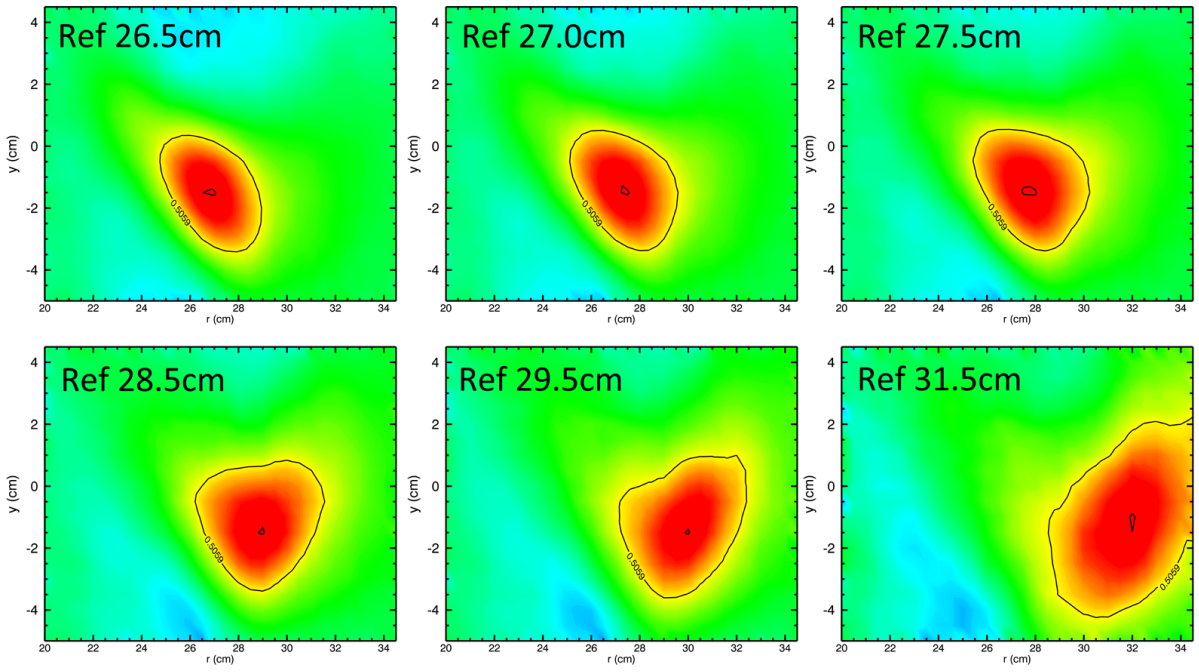

Figure 5.40: Correlation function planes for six reference points

The unbiased correlation function $C(x,y)/C_{max}$ is shown in Figure 5.40 for all six reference positions. The black curve indicates where the correlation function has decreased by half and is here defined as the correlation distance. That is, a distance from black curve to black curve through the maximum point in the radial direction is defined as the radial correlation length and the azimuthal correlation length if along the y-direction.

From Figure 5.40, the most obvious change in turbulence structure as the reference location is changed is in the shape; in other words, the shape of the correlation function is modified by the flow profile. In general, flow appears to modify the correlation function by stretching it in the direction that the flow is originating from; higher flow connects the fluctuations from wider azimuthally separated points better then lower flow. In the unbiased case, the peak flow is at about 28cm and the structure becomes most elongated about the 28cm radius, while regions about this flow are less elongated. This results in tilted structures such as in Ref 26.5 or 31.5 when the flow differential exists on only one side of the structure, to more triangular shapes when the shear is on both sides of the structure as in Ref 28.5 and 29.5. For the level of flows and shear in the unbiased case, at least, the shearing or flow does not appear to shorten the radial correlation length, instead tilting the structures themselves. In fact, for regions around a peak flow, the radial correlation is lengthened by the tilting effect of the sheared flow, going from about 3cm in Ref 26.5 to about 4cm in Ref 28.5. The radial correlation length of Ref 31.5 appears to be even larger, but harder to determine as the structure begins to extend beyond the region measured by the motion probe. The azimuthal correlation length, on the other hand, does not appear to be significantly changed by the radial location of the reference probe. While the unbiased flow profile does appear to change the tilting of the turbulent structure, the size of the structure is not significantly increased or decreased. At a bias of 60V, the flow profile flattens out as can be seen in the correlation movie with time-delay of Figure 5.41 where the structure in the movie is moving more more slowly. Finally, at a bias of 100V, the propagation has reversed completely into the electron diamagnetic direction as seen in the Figure 5.42.

As summary of the correlation structure at zero time delay for each bias is shown in Fig-

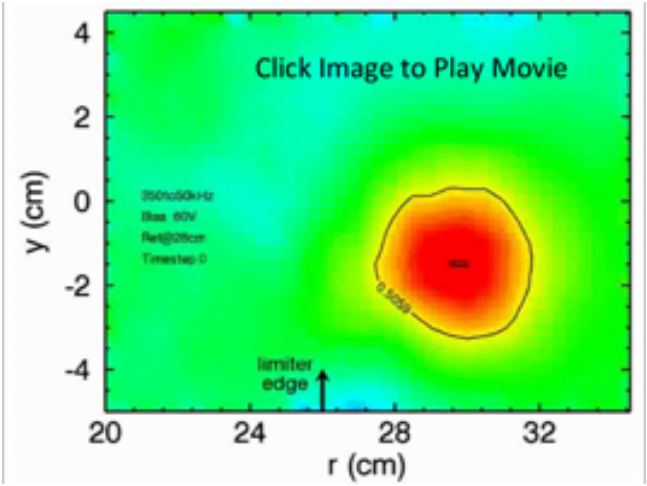

Figure 5.41: Movie of correlation plane as a function of time-delay τ for a bias of 60V. (Viewable on pdf only. Click on image to start movie. Right click and select disable content to stop movie.)

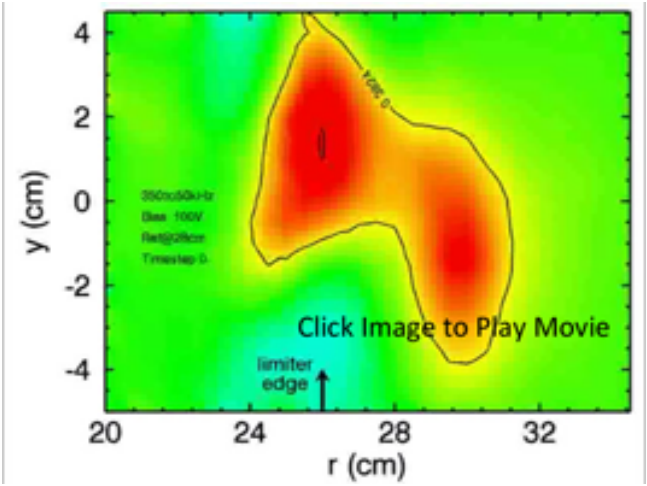

Figure 5.42: Movie of correlation plane as a function of time-delay τ for a bias of 60V. (Viewable on pdf only. Click on image to start movie. Right click and select disable content to stop movie.)

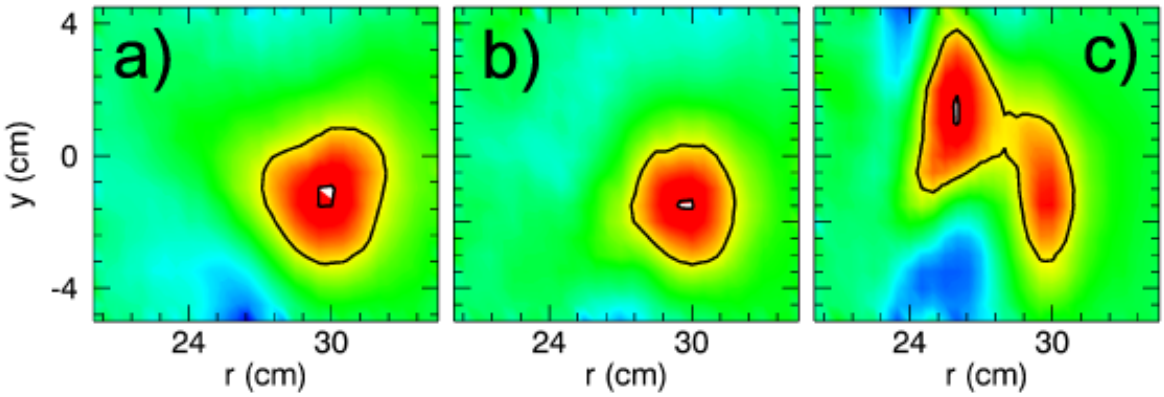

Figure 5.43: Correlation function planes for three different biases: (a) unbiased, (b) 60V power suppply bias (near minimum sheared flow) and (c) 100V power supply bias (rotation in EDD direction).

ure 5.43. The shape and size of the turbulent structure clearly varies as the bias is changed. For the 60V bias, the state with the minimum amount of sheared flow, the correlation structure has the most even shape, almost circular. In contrast, the correlation structures with sheared flow present are more elongated azimuthally as can be seen in Figure 5.43(a) and (c). In the unbiased state, the spontaneous sheared flow causes a slight elongation of the structure into a triangular shape as shown in Figure 5.40. In the strongly biased case, with high amounts of sheared flow, the turbulent strucutre, identified as the right most lobe in Figure 5.43(c), is elongated, but not tilted. This can be an indication of a reduced radial correlation length due to shear suppression, but more likely, the reduced length here is because of the increased density gradient which can also reduce radial correlation extent. This distinction will be discussed in more detail in Chapter 6 where the radial correlation length is plotted for different values of the shearing rate. The left lobe structure is identified as a mode pattern resulting from the coherent mode; this mode pattern sits at the limiter edge and can be removed by removing the contribution to the correlation plane of the 8-12kHz frequencies. Why the mode pattern would show correlation to the turbulent structure is not known.

This chapter summarized the large scale effects on density, temperature, fluctuations,

modes and turbulent structures as a function of changing bias and rotation state. The next chapter presents an analysis of the changes to these quantities in a localized region in order to develop a quantitative scaling. This scalings are then used in Chapter 7 to compare to models of shear suppression in the literature.

CHAPTER 6

Local analysis of the variation of turbulence and transport with shearing rate

While Chapter 5 provided a broader overview of the effect of varying flow state on various plasma parameters, this chapter focuses on a local variation of these quantities for a region just outside the limiter edge where the variation in flow shear is greatest through the different biases. A clear suppression of particle flux is observed in this region as a function of shearing rate. The shearing rate is normalized to the inverse autocorrelation time which provides a numerical comparison as to the level of temporal decorrelation of fluctuations that are due to the background turbulence or to sheared flow. The decrease in particle flux is shown to be due mainly to the reduction of density fluctuation power, though reduction of other components of particle flux are modified as well. The chapter also discusses the reduction in radial correlation length as a function of shearing rate.

6.1 Flow and Density

The flow response to biasing is summarized in Figure 6.1. For this chapter, the focus will be on a region just outside the limiter edge, 27 to 31cm. In this region, the radial average flow and flow shear scale approximately linearly with the anode-limiter voltage difference as seen in Figure 6.1(c). The other quantities presented in this chapter are also radially averaged over this region unless otherwise noted. Figure 6.2 shows the density profiles again, but with the averaging range indicated by the dotted black lines at 27 and 31cm.

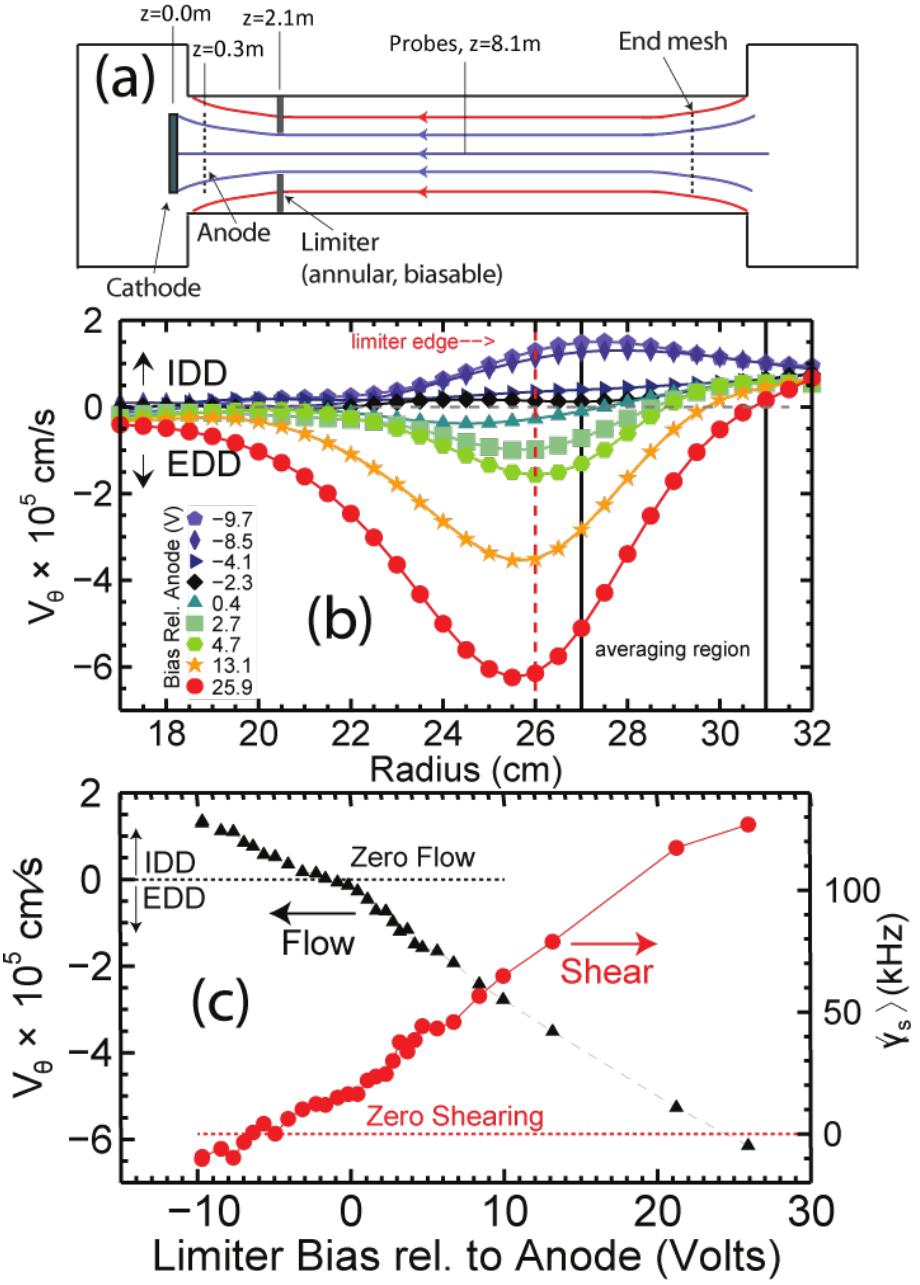

Figure 6.1: (a) Diagram of the LAPD device showing axial position of cathode, anode, annular limiters, and Langmuir probes. (b) Velocity profiles using plasma potential from swept measurements. (c) Flow at the limiter edge (black, triangles) and mean shearing rate, averaged over $27 < r < 31$cm (red, circles).

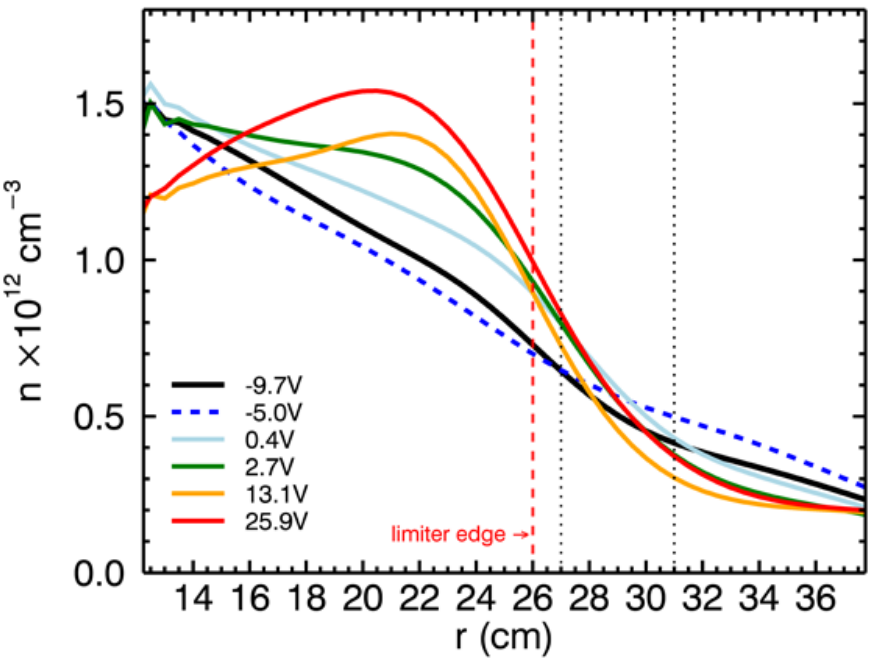

Figure 6.2: Profiles of density for various biases for 1000G with the averaging region for shear suppression comparison noted by dotted lines at 27 and 31 cm.

6.2 Decorrelation Rate

Before approaching the shear suppression results, the normalization for shearing rate used in this chapter is first discussed. The decorrelation rate (or inverse autocorrelation time) in this context is a measure of the time it takes for a signal to be randomized to a certain level by turbulent fluctuations. To calculate this decorrelation rate, the autocorrelation of the signal must be first determined, defined as

$$C_{xx}(\tau) = \langle x(t)x(t+\tau)\rangle \tag{6.1}$$

where x(t) is a time signal, τ represents a time delay and the brackets indicate both an ensemble and time average. An example of this quantity is plotted as the black curves in Figure 6.3 for two I_{cmrsat} time-series at different radial locations. Roughly, this equation represents how close in value the signal A at time t is compared to signal B at a time $t+\tau$ or $t-\tau$. In this sense, correlation measures how quickly a signal is randomized. If correlation is high for large values of the delay time τ, then fluctuations or modes present in the signal will persist for larger amounts of time; if correlation is low, then the fluctuations are quickly modified by some physical mechanism (e.g. shearing rate.)

A timescale representing the rate of this randomization can be defined in the following rigorous way. First, an envelope function is determined for this autocorrelation function using another quantity called the Hilbert Transform, which for a function u(t) is defined as,

$$H(t) = \text{P.V.}\frac{1}{\pi}\int_{-\infty}^{\infty}\frac{u(\tau)}{t-\tau}d\tau \tag{6.2}$$

The envelope function is found by combining the Hilbert Transform of the autocorrelation function and the autocorrelation function itself as,

$$A(\tau) = \sqrt{((C_{xx}(\tau))^2 + Re((H(\tau))^2))} \tag{6.3}$$

This envelope function is plotted in red along side the original autocorrelation functions in black in Figure 6.3. An autocorrelation time, τ_{ac} is now defined as the half-width at half-max of the envelope function. A large τ_{ac}, as in Figure 6.3(a), suggests a time signal

which randomizes slowly while a small τ_{ac}, Figure 6.3(b) suggests one that "decorrelates" very quickly. Finally, the decorrelation rate is defined as the inverse autocorrelation time, $\gamma_d = \tau_{ac}^{-1}$.

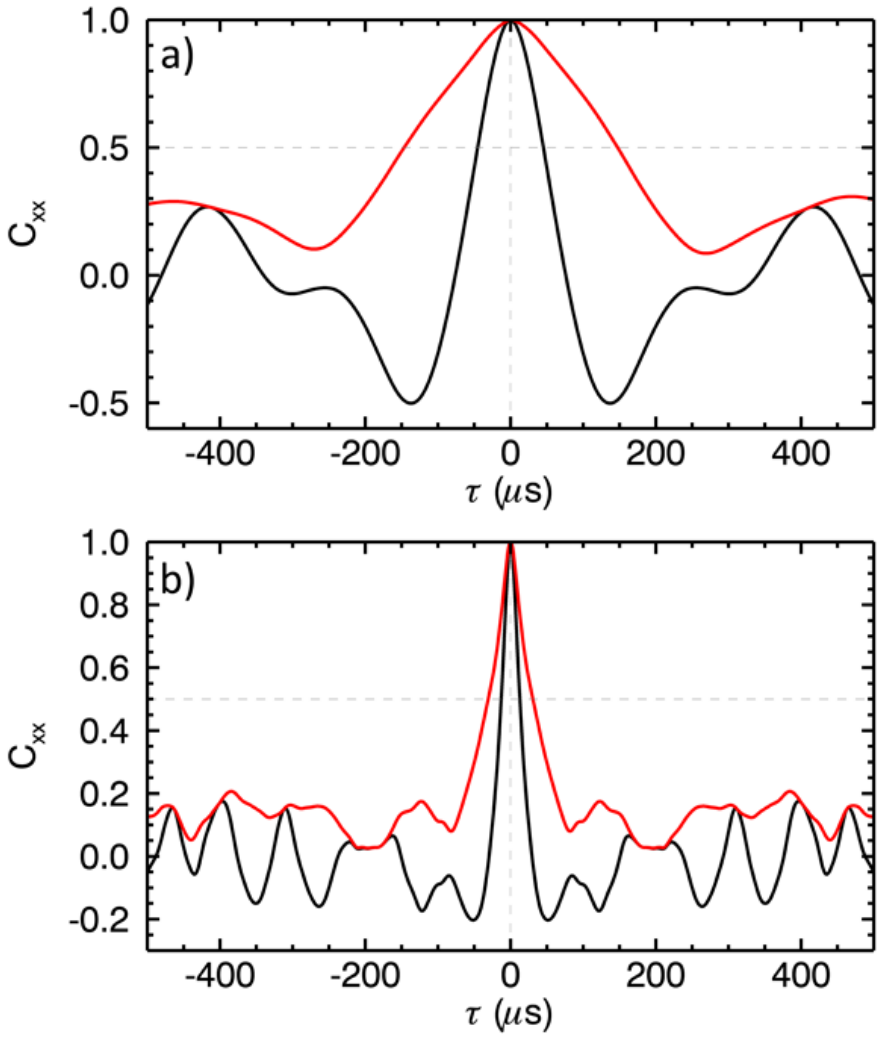

Figure 6.3: Autocorrelation function and Hilbert Envelope for an density signal with (a) a large autocorrelation time (small decorrelation rate and (b) a small decorrelation rate (large decorrelation time). Plot (b) is the kind of autocorrelation function observed in the gradient region of an unsheared plasma, while (a) is in the core in a much less turbulent region.

The motivation for seeking the decorrelation rate in shear suppression studies arises from

the fact that shearing rate can play the role of the physical mechanism which modifies the randomization of a fluctuation signal. Specifically, in so-called decorrelation models of shear suppression, the autocorrelation time of a fluctuation signal is decreased by the tendency of sheared flow to disrupt turbulent eddies (these models will be discussed in more detail in the next chapter). Formally, the ratio of the shearing rate, γ_s and the decorrelation rate of the signal absent any shear, τ_{ac}^{-1}, can be used to determine the level of this disruption. The ratio of $\gamma_s \tau_{ac} < 1$ is considered weak shear while $\gamma_s \tau_{ac} > 1$ is called strong shear. Many theories of shear suppression require a certain level of shearing rate compared to the unsheared decorrelation rate to be present in a system to be able to significantly modify fluctuations levels and so this ratio is used in this experimental study.

The unsheared decorrelation rate is measured here in the bias state which exhibits the least amount of sheared flow. Using the method detailed above, an average autocorrelation time of $36\mu s$ is found for the 27 to 31cm radial region which translates into an average decorrelation rate of 28kHz.

6.3 Density Gradient Modification

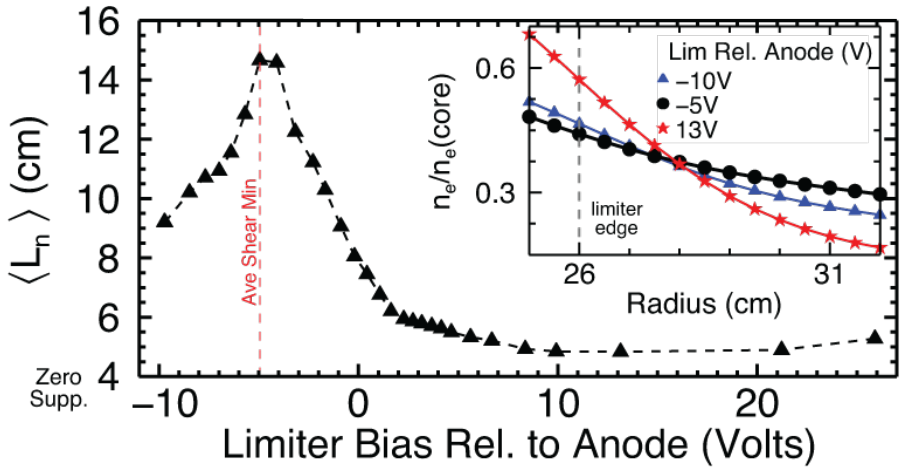

Figure 6.4: Density gradient length scale versus limiter bias. Inset shows density profile at three bias values.

Figure 6.4 shows the variation in the spatially-averaged density gradient length scale, $L_n = |\nabla \ln n|^{-1}$ with increasing limiter bias. As the limiter bias is increased, reducing the IDD flow, an increase in the gradient scale length is observed, indicating a degradation of radial particle confinement. The gradient scale length peaks when the averaged shearing rate is near zero. As the bias is increased further, reversing the flow and again increasing the shearing rate, the gradient gradually steepens and the scale length is lowered, indicating improved radial particle confinement.

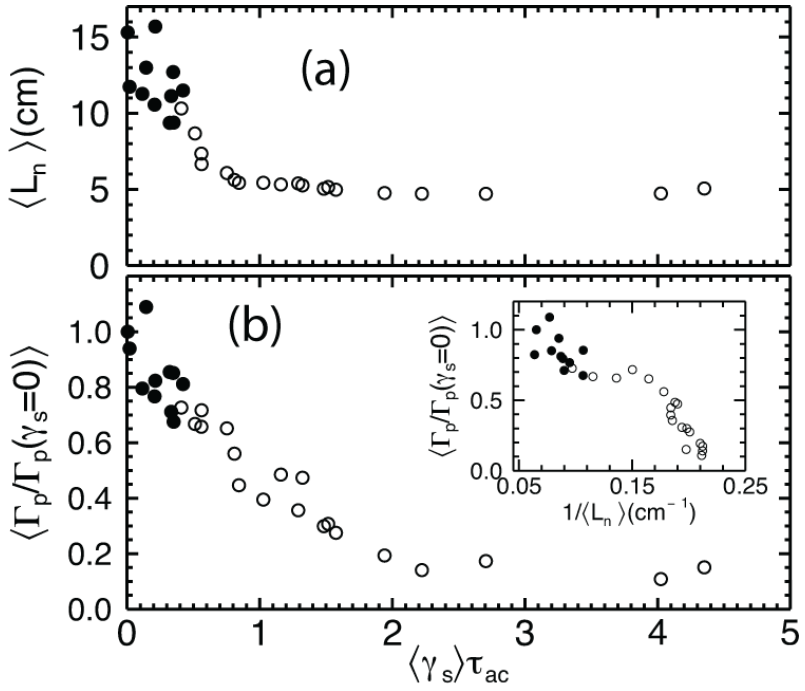

Figure 6.5: (a)Gradient scale length versus shearing rate. (b)Particle flux normalized to no-shear flux as a function of normalized shearing rate. Filled symbols represent points with flow in the IDD. Inset: Measured turbulent particle flux versus gradient scale length.

The observed variation of $\langle L_n \rangle$ with bias is best organized when compared to the shearing rate, γ_s, as is shown in Figure 6.5(a) normalized to the decorrelation rate as discussed in the above section. Confinement improvement (decreased $\langle L_n \rangle$) occurs continuously and gradually with increasing γ_s and reaches saturation for $\gamma_s \approx \tau_{ac}^{-1}$ (a normalized γ_s of 1). The profile steepening appears to be largely independent of the direction of the flow (or radial

electric field): IDD (filled points) and EDD (open points) flow cases follow the same trend when plotted against normalized shearing rate.

6.4 Turbulence and Transport Suppression

Measured changes in turbulence and turbulent particle flux are consistent with the observed changes in the density profile. The turbulent particle flux can be written[56]:

$$\Gamma = 2\int_0^\infty |n(f)||v_r(f)|\gamma_{(n,v_r)}(f)\cos[\phi_{(n,v_r)}(f)]df \tag{6.4}$$

where $n(f)$ and $v_r = cE_\theta(f)/B$ are the Fourier transforms of the density and radial velocity fluctuations (as determined from azimuthal electric field fluctuations assuming $E \times B$ flow only as discussed in Section 2.3); $\gamma_{(n,vr)}$ is the coherency between density and electric field; and $\phi_{(n,vr)}$ is the cross-phase angle between density and electric field.

Before summing over frequencies, the integrand of Equation 6.4 or flux kernel, is shown in Figure 6.6 as a function of normalized shearing rate and frequency, radially averaged over 27 to 31cm as usual.

The figure shows that fluctuations at frequencies less than 10kHz dominate the contribution to the flux integral. The value of the flux kernel drops off with increasing shearing rate and increasing frequency except for a narrow region that begins around a normalized shearing rate of 1 and frequency of 5kHz, and stretches into a thin region around 12kHz. These features are clearly the effect on particle flux of the rotational interchange driven coherent modes in the region beyond the limiter edge; though the particle flux due to this mode is initially relatively high, its contribution decreases with increasing sheared flow for reasons discussed below. Summing over various frequency regions, line plots of particle flux normalized to the unsheared value versus normalized shearing are shown in Figure 6.6(b). The plot again emphasizes the fact that most of the radial particle flux occurs at fluctuations frequencies less than 10kHz.

Isolating the plot that sums over frequencies from 312Hz to 100kHz, Figure 6.5(b) shows

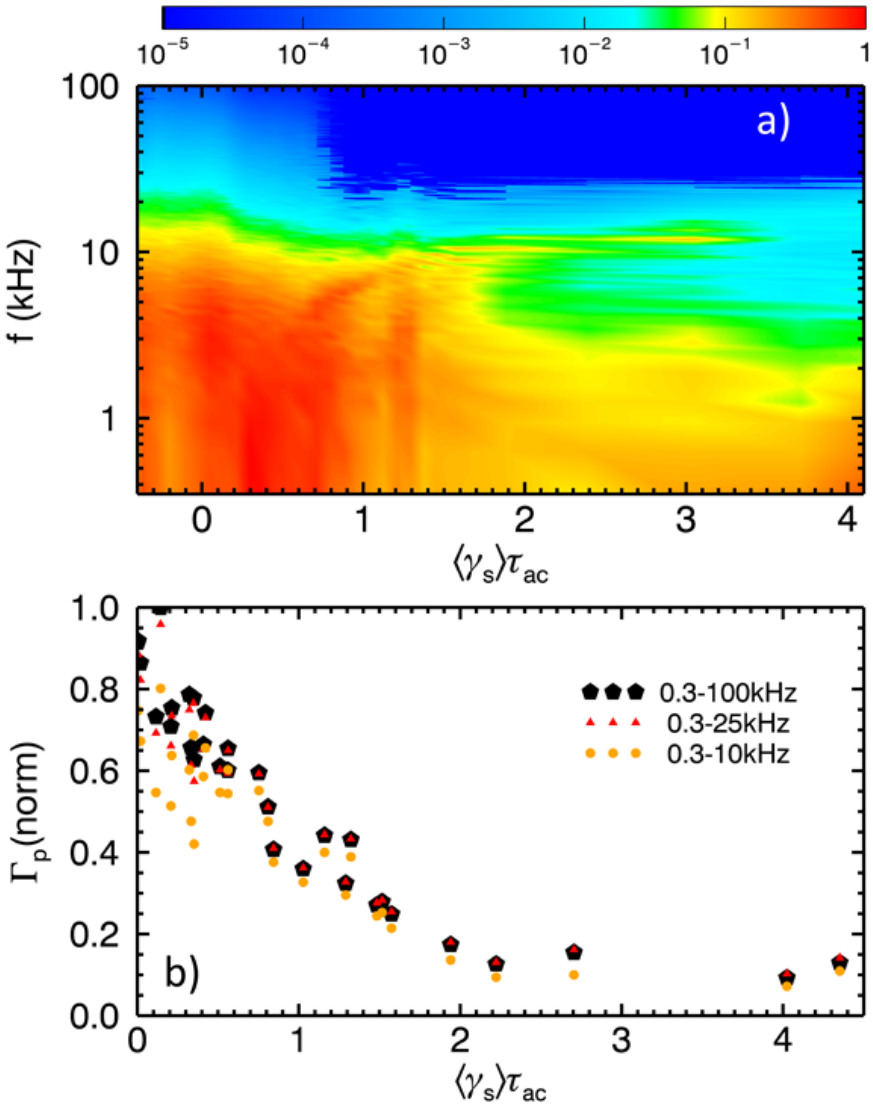

Figure 6.6: (a) Log-scaled contour plot of particle flux versus shearing rate and frequency and (b) Line plots showing summed flux over different frequency bands as a function of sheared flow. It should be noted that the shearing rate scales are slightly different between contour and line plots. In order to properly display the contour plots, a monotonically increasing function of shear versus bias is fit to the sheared flow data. Since the line plots are scatter plots, the shearing rate shown is exactly what is measured.

the summed and spatially-averaged turbulent particle flux as a function of normalized shearing rate compared to the gradient scale length as a function of shearing rate. The turbulent flux decreases continuously with increasing shearing rate; however the observed decrease is slightly gentler than that observed for L_n.

The trend in reduced particle flux is the same for either direction of flow (IDD or EDD). That is, there does not appear to be a preferred direction of flow or sheared flow which causes a decrease in turbulent transport. This is consistent with many theoretical decorrelation models which do not distinguish flow direction (or radial electric field direction) for suppression.

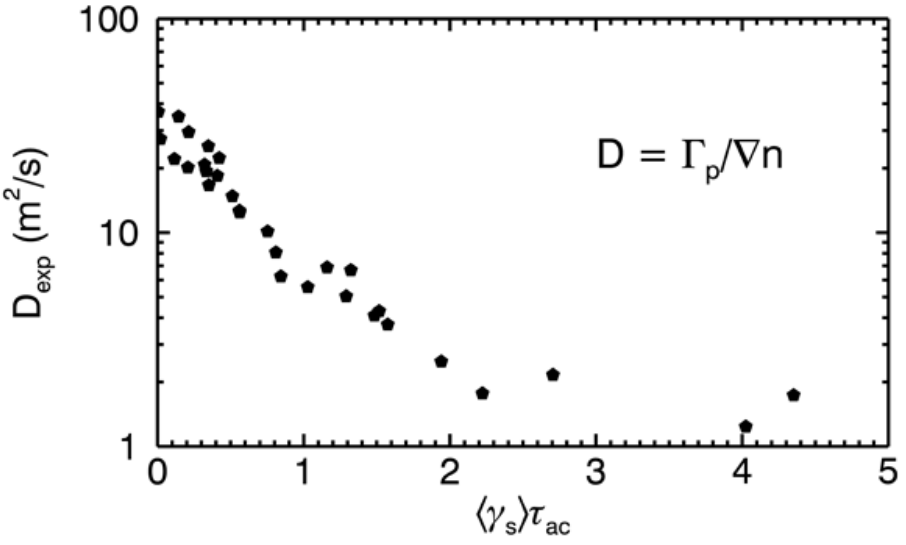

Figure 6.7: Diffusion coefficient as a function of normalized shearing

The inset in Figure 6.5(b) shows that the variation in turbulent flux is correlated with the changes in L_n (but scales in a way that is inconsistent with Fick's law using a fixed diffusion coefficient). Since the diffusion coefficient (or diffusivity),$D_{exp} = \Gamma_p/\nabla n$, is not a constant as in Fick's Law, its value can also be tracked as function of shearing rate as in Figure 6.7. The suppression of the diffusivity shows that reduction of radial transport is large enough to compensate for any potential increased transport due to the steepened density gradient.

The physical mechanisms that generate a decrease in particle flux has generally fallen into

two camps: a reduction in density fluctuation amplitude or a reduction in crossphase between density fluctuations and radial velocity fluctuations. Thus, the cause for the reduction in turbulent particle flux can be explored by considering individual terms in the integrand of Eqn. 6.4 as functions of normalized shearing.

6.4.1 Density Fluctuations

Density fluctuations, the first component of turbulent particle flux considered, were reduced significantly with increasing shearing in these experiments. Figure 6.8(a) shows changes in the spatially-averaged density fluctuation spectrum with shearing rate in a similar format to that made for flux in Figure 6.6. The shearing rate is signed in this figure, and negative shearing rates occur for flow in the IDD. Most of the power is located in frequencies < 10kHz and in this range, power decreases overall with increasing shearing rate. A decrease of about one order of magnitude in fluctuation power is seen between the minimum shear state and the high shear regime where L_n and particle flux are minimized; this is made more clear in Figure 6.9(b) where low frequency power peaks at the minimum shearing bias. At higher shearing rates, $\gamma_s \gtrsim \tau_{ac}^{-1}$, the coherent mode becomes quite visible in density fluctuations, and much more apparent than in the overall flux kernel. This can be seen in the upward shift of points between normalized shearing rates of 2 and 3 in Figure 6.8(b). The first point showing a change in the downward trend (around $\gamma_s \tau_{ac} = 2.75$) shows additional power in high frequencies (red triangles) compared to the low frequencies which does not change much from the previous point. This indicates the contribution of the higher frequency coherent mode. The last two points show an upward trend in both high and low frequency bands. Since measurements of shearing rate were not made beyond about $\gamma_s \tau_{ac} = 4.5$, it is difficult to interpret this trend in the data with only two data points.

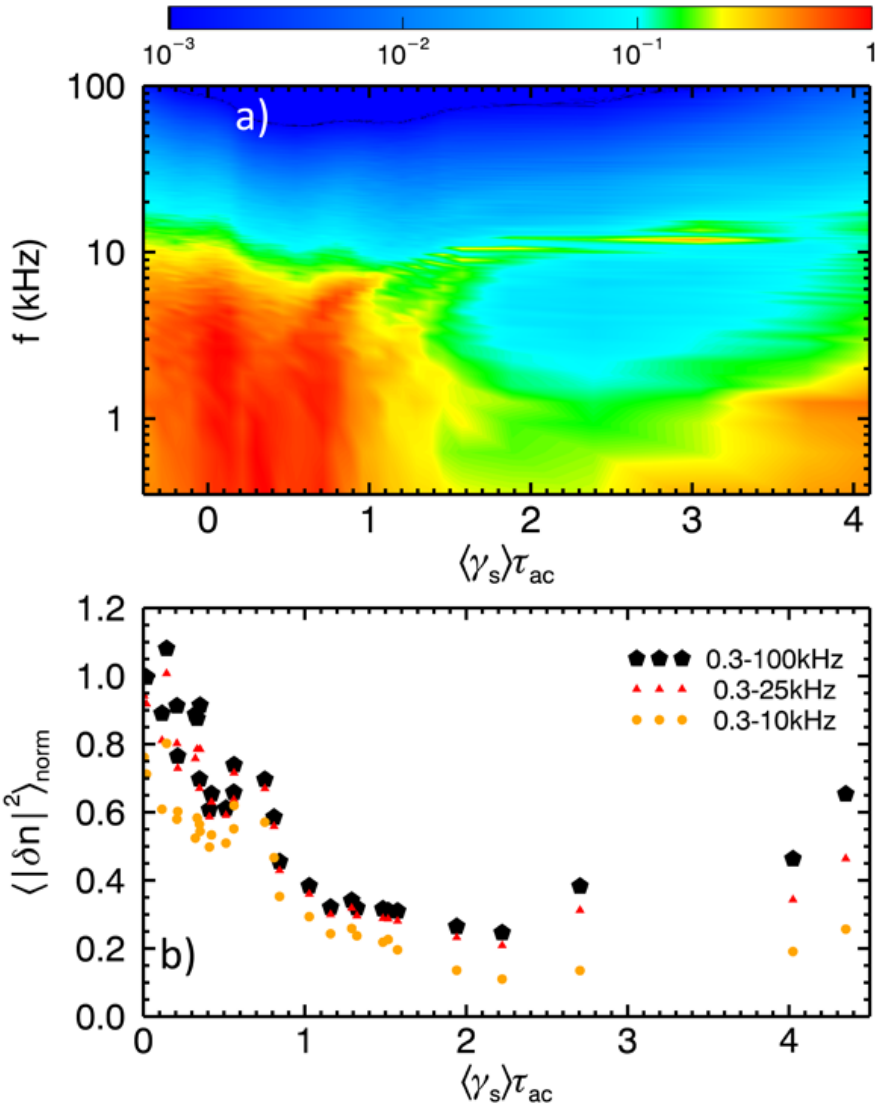

Figure 6.8: (a) Contour plot of density fluctuations versus shearing rate and frequency and (b) Line plots showing summed fluctuation power over different frequency bands as a function of sheared flow. A decrease in fluctuation power is clearly observed with shearing rate up to a normalized shearing rate of about 2.5. The fluctuations begin to increase due to the presence of the coherent mode. It should be noted that the shearing rate scales are slightly different between contour and line plots. In order to properly display the contour plots, a monotonically increasing function of shear versus bias is fit to the sheared flow data. Since the line plots are scatter plots, the shearing rate shown is exactly what is measured.

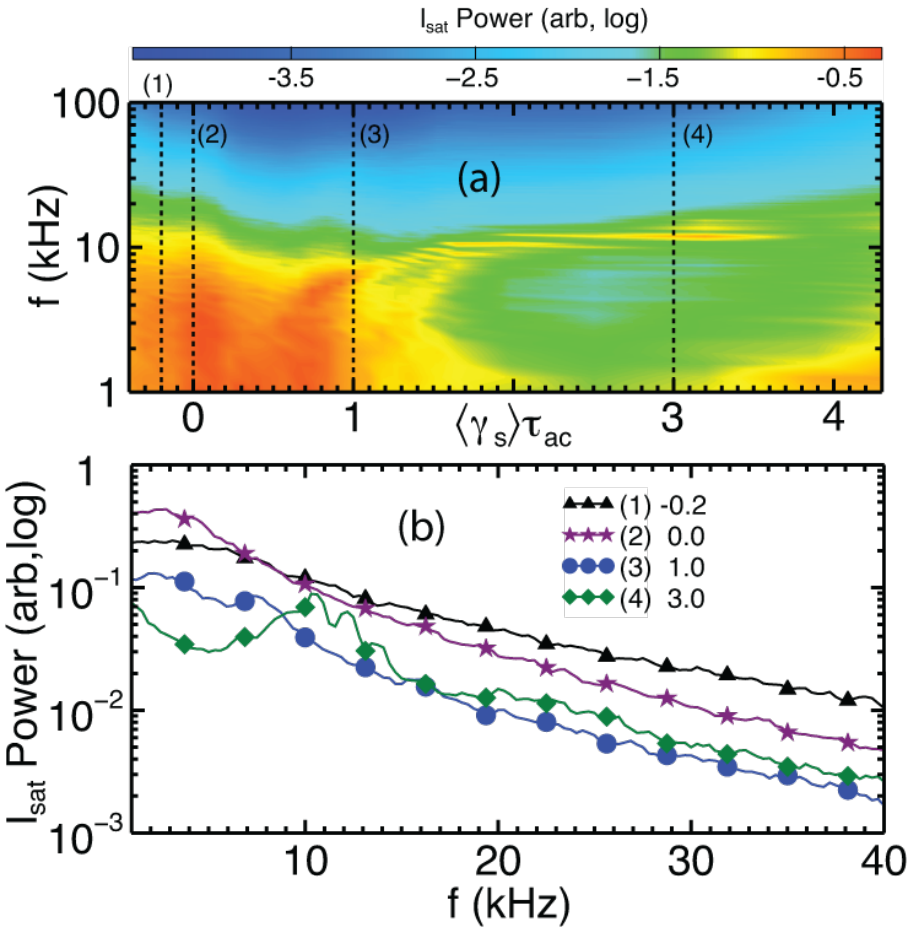

Figure 6.9: (a) Contour plot of log $I_{\rm sat}$/density fluctuation power versus shearing rate and frequency. (b) Power spectra for four different values of shearing rate.

6.4.2 Crossphase

The relative crossphase between density fluctuations and $E \times B$ or v_r fluctuations are also modified by the change in shearing rate. Crossphase is calculated using the the cross-spectrum of the two-time series quantities as in,

$$\theta = \tan^{-1} \frac{\langle Q(f,r) \rangle_{f,r}}{\langle C(f,r) \rangle_{f,r}} \tag{6.5}$$

where Q and C are the imaginary and real parts of the cross-spectrum, calculated from the product of the complex FFTs of the two time-series in question as in,

$$G(f,r) = \hat{x}^*(f,r)\hat{y}(f,r) \tag{6.6}$$

For power summed plots, the cross-spectrum is first averaged over frequencies to power-weight the crossphase signal, and then averaged radially, before the phase is determined using Equation 6.5. For contour plots, the cross-spectrum is averaged only radial points first.

Figure 6.10 shows the $\cos[\phi_{(n,vr)}]$ as a function of normalized shearing rate and frequency. Since the crossphase contributes to the particle flux as the cosine of the crossphase, the full range of possible values are -1 to 1. If the relative crossphase is near zero, the contribution to outward flux will be maximal, near 1. Crossphase on the order of 90° yields a $\cos[\phi_{(n,vr)}] \sim 0$ and thus minimal flux occurs regardless of any other quantity. Crossphase $> 90°$ yields negative power which are indicative of inward particle flux.

For frequencies $<$ 5kHz, the crossphase is near 1 and constant for almost all shearing rates. At frequencies between 5 and 10, the crossphase remains close to 1 up to a normalized shearing rate of 1, then begins to drop to values of about 0.5. Beyond 10kHz, the crossphase again remains near 1 for shearing rates less than 1, but then drops quickly and changes sign for higher shearing rates. Note also that the $\cos[\phi_{(n,vr)}]$ for shearing rates and frequencies where the coherent modes are present are in the transition region where crossphase begins to decrease substantially. Thus, even though density fluctuations tend to peak in these regions, crossphase tends to minimize its contribution to the overall flux. The line plots

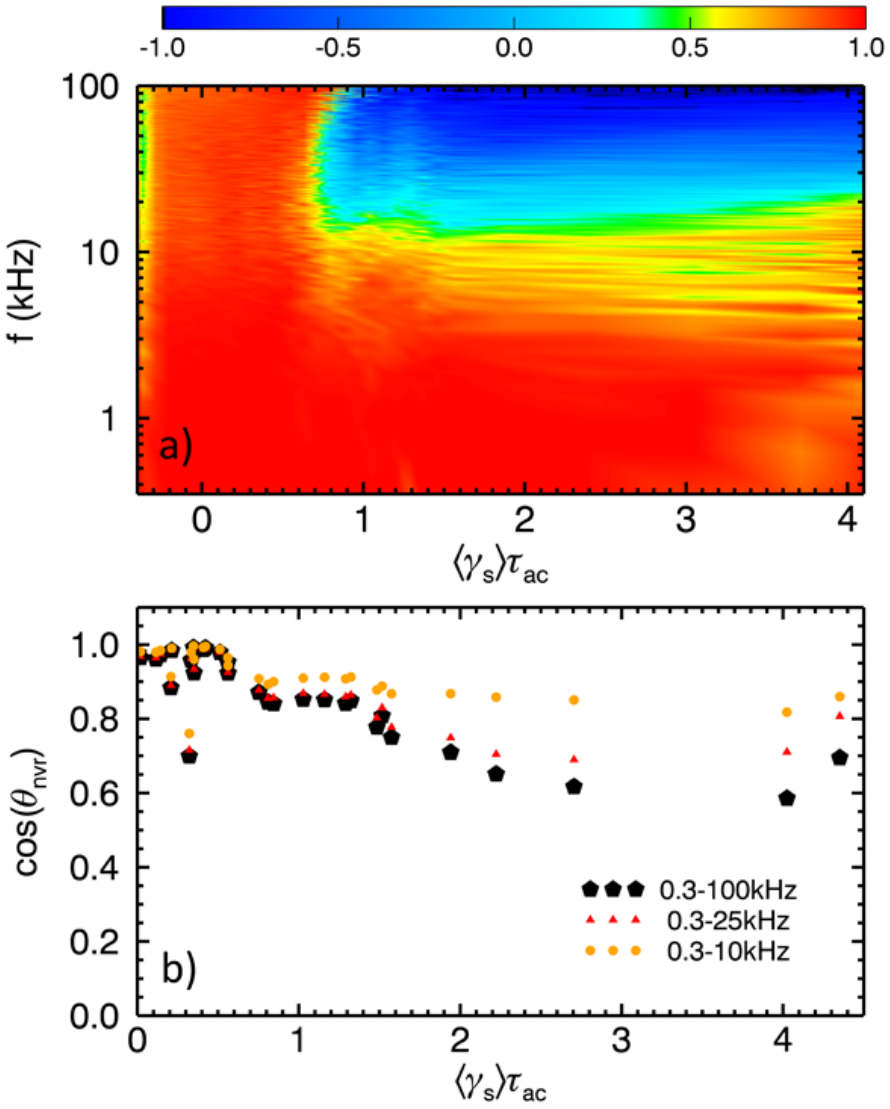

Figure 6.10: (a) Contour plot of density fluctuations versus shearing rate and frequency and (b) Line plots showing summed fluctuation power over different frequency bands as a function of sheared flow. It should be noted that the shearing rate scales are slightly different between contour and line plots. In order to properly display the contour plots, a monotonically increasing function of shear versus bias is fit to the sheared flow data. Since the line plots are scatter plots, the shearing rate shown is exactly what is measured.

of Figure 6.10(b) show how the crossphase changes very little at low frequencies, but does changes slightly when higher frequencies are incorporated.

Density fluctuation amplitude and crossphase tend to receive the most focus in transport shear suppression studies, but two other elements also contribute to the particle flux: radial velocity fluctuations and coherency.

6.4.3 Radial Velocity Fluctuations

Radial velocity fluctuations in Figure 6.11 show much less variation with shearing rate than density fluctuations, though both exhibit the sharp drop-off for frequencies $>$ 10kHz. The line plots show that fluctuation amplitude does not drop by more than 50% for even the highest shearing rates. It is also interesting to note that unlike flux and density fluctuations, the peak in radial velocity fluctuations does not appear to coincide with either the minimum in shearing rate or the minimum in average flow velocity as shown in Figure 6.12. This would appear to indicate that radial electric field fluctuations are not precisely modified by flow or sheared flow, but nevertheless exhibit suppression with shearing rate.

6.4.4 Coherence

The final component of flux, coherence, is a measure of how much correlation exists between each frequency component of the density and radial velocity fluctuations. Rather than showing general trends with shearing rate, Figure 6.13, exhibits smaller regions of higher correlation, specifically around zero shearing rate and in the regions where the coherent modes are active. In fact, the coherency clearly shows what was discussed in the mode analysis section Chapter 5: that the coherent modes observed begin at separate frequencies, but begin to coalesce and interact with increased shearing rate. The summed line plots show a very gradual decrease in coherency with shearing rate—much slower than the other quantities and has the least impact on the change in flux with sheared flow.

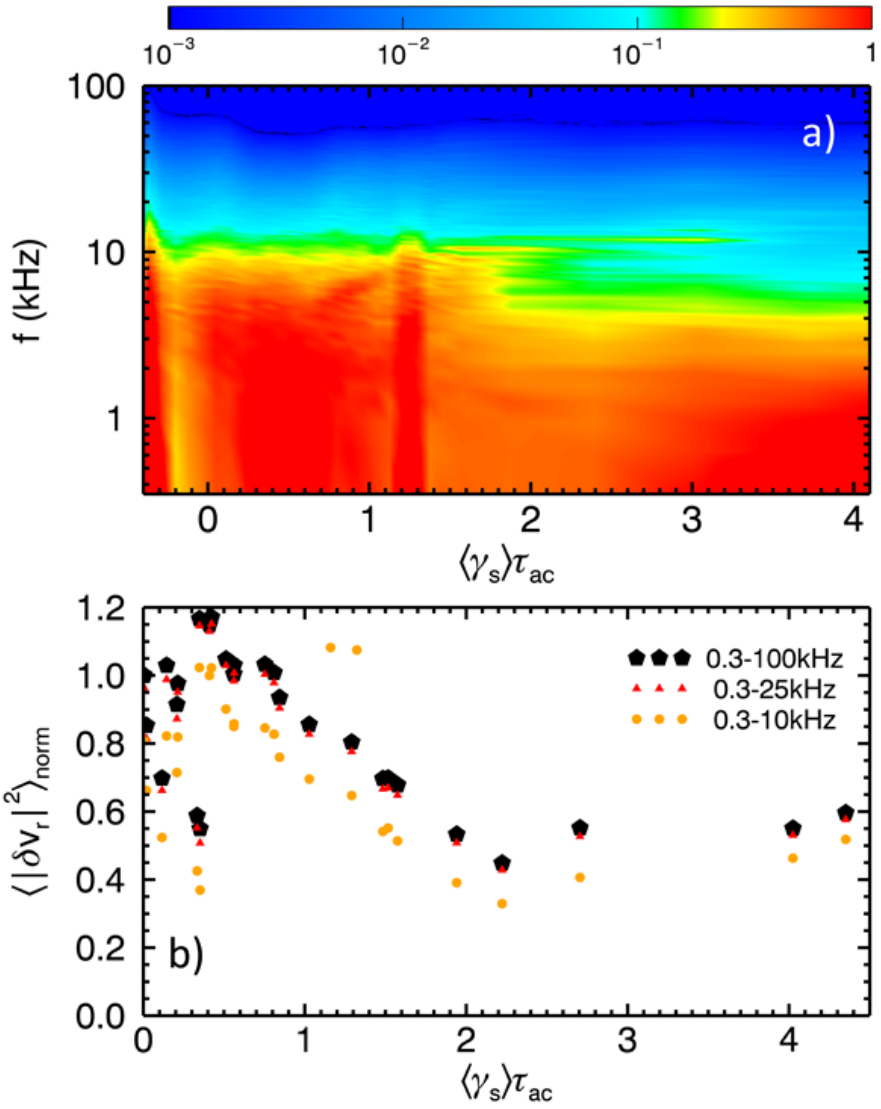

Figure 6.11: (a) Contour plot of V_r fluctuations versus shearing rate and frequency and (b) Line plots showing summed fluctuation power over different frequency bands as a function of sheared flow. It should be noted that the shearing rate scales are slightly different between contour and line plots. In order to properly display the contour plots, a monotonically increasing function of shear versus bias is fit to the sheared flow data. Since the line plots are scatter plots, the shearing rate shown is exactly what is measured.

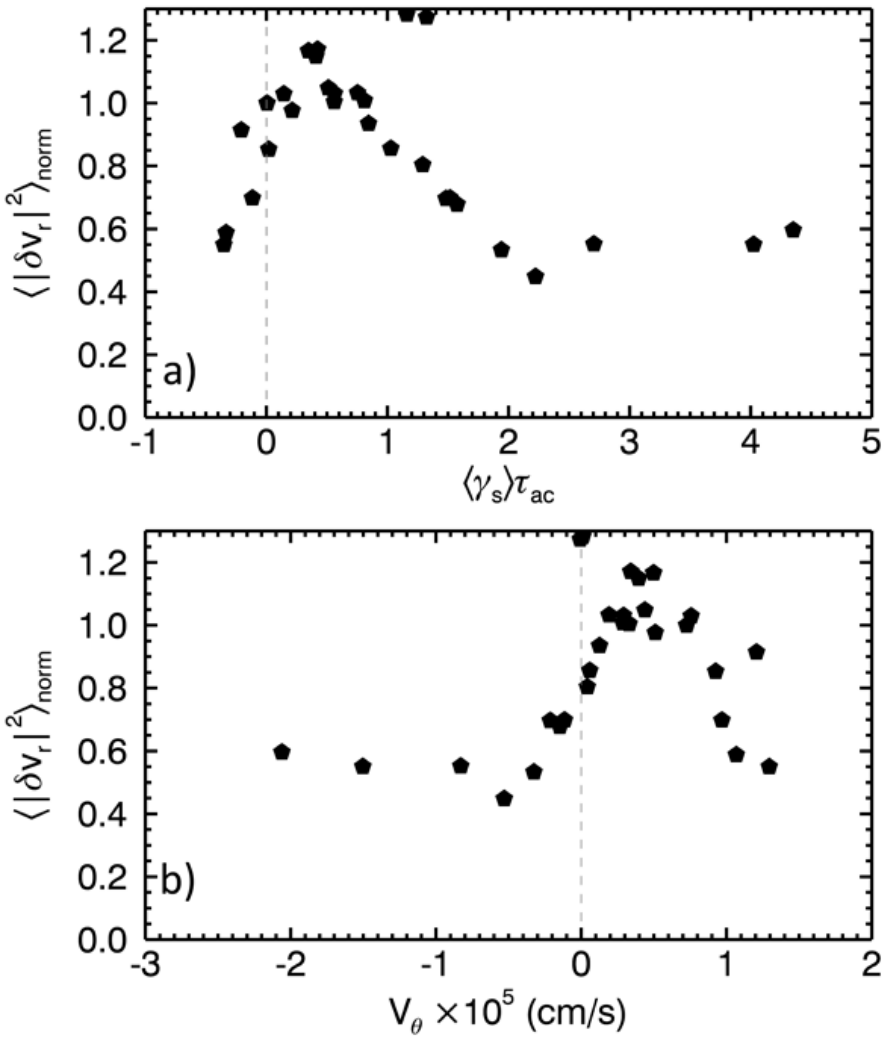

Figure 6.12: Line plots of radial velocity fluctuations as functions of (a) signed sheared flow and (b) signed mean flow indicating that the peak does not coincides with the zero of either scale.

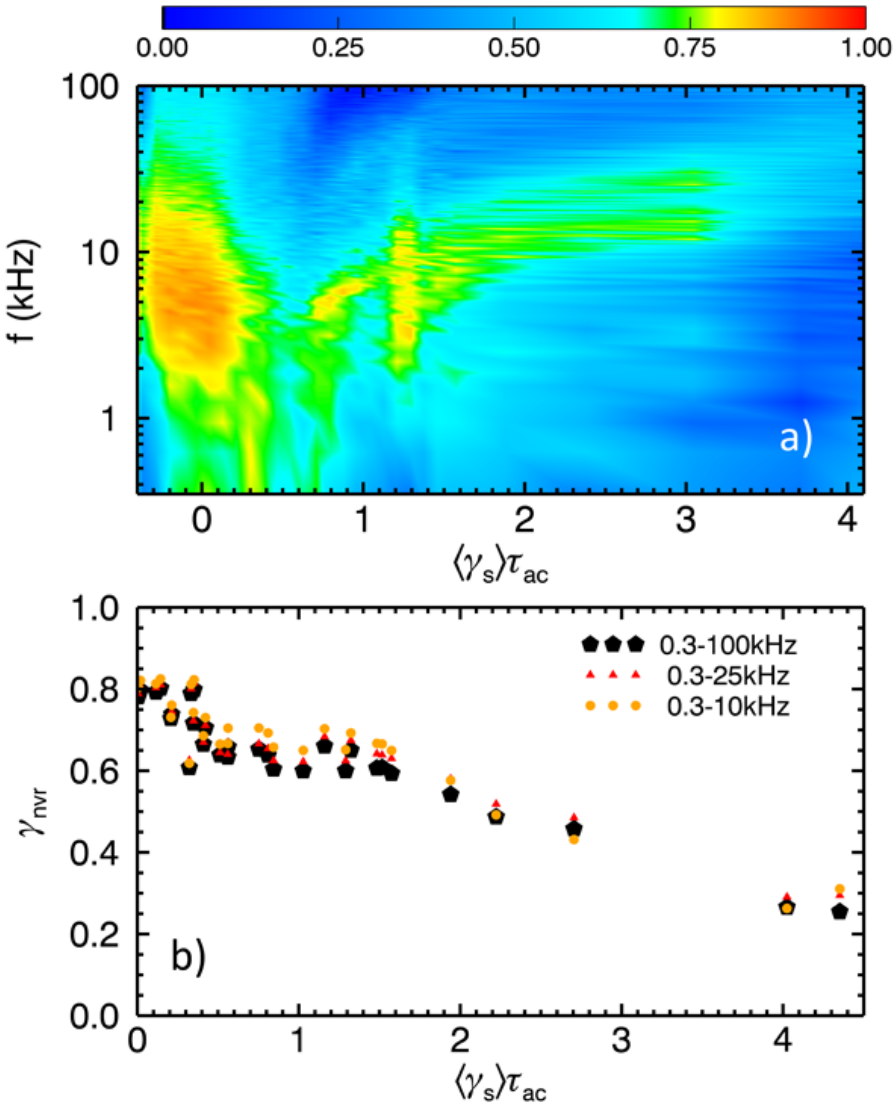

Figure 6.13: (a) Contour plot of coherency shearing rate and frequency and (b) Line plots showing summed flucutation power over different frequency bands as a function of sheared flow. It should be noted that the shearing rate scales are slightly different between contour and line plots. In order to properly display the contour plots, a monotonically increasing function of shear versus bias is fit to the sheared flow data. Since the line plots are scatter plots, the shearing rate shown is exactly what is measured.

6.5 Radial Correlation Length

Measurements of the radial correlation length were recorded as a function of shearing rate using a two-probe correlation technique as discussed in Chapter 5. A reference probe collecting I_{cmrsat} is kept stationary at a particular axial and radial location within LAPD. A second Langmuir probe situated at an axial point closer to the cathode is moved shot-to-shot in a rectangular grid around the radial location of the reference probe. The cross-field cross-correlation function of these two measurements is computed shot-to-shot for a delay time τ as $C(x, y, \tau) = \langle I_{cmrref}(x, y, t) I_{cmrmot}(x, y, t + \tau) \rangle$.

Figure 6.14(a) shows the normalized correlation function $C(x, y)/C_{cmrmax}$ for the unbiased state (flow in the IDD), a minimum shear state, and a high bias state (large EDD flow) with a reference probe located at $x = 29.5$cm, $y = 0$cm (right in the middle of the shear layer). The black curve represents the contour line where $C(x, y)/C_{cmrmax} = 0.5$. The radial correlation length Δr_c is defined here as the radial width of this black curve through the reference probe location. The variation of the correlation length versus shearing rate is shown in Figure 6.14 (normalized to the maximum radial correlation length calculated for all biases). The correlation length is found to decrease substantially with shear. A break in the trend of decreasing correlation length is observed for larger shearing rates where the correlation function appears to be dominated by a coherent mode (which also appears in the temporal power spectrum). Such a decrease in radial correlation length is consistent with the decorrelation model of shear suppression; however, since these measurements are made in the steady-state plasma, these radial correlation lengths also incorporate the steepened density gradient which itself can decrease radial correlation. In Figure 6.14(b) the ratio of the radial correlation length to the density gradient scale length is shown, indicating that this ratio remains constant with shearing rate. In order to evaluate the effect of shearing rate on radial correlation length independent of changes to the gradient scale length, the correlation length could be studied in the transient phase after the flow is turned on. This effect discussed in more detail in Chapter 8.

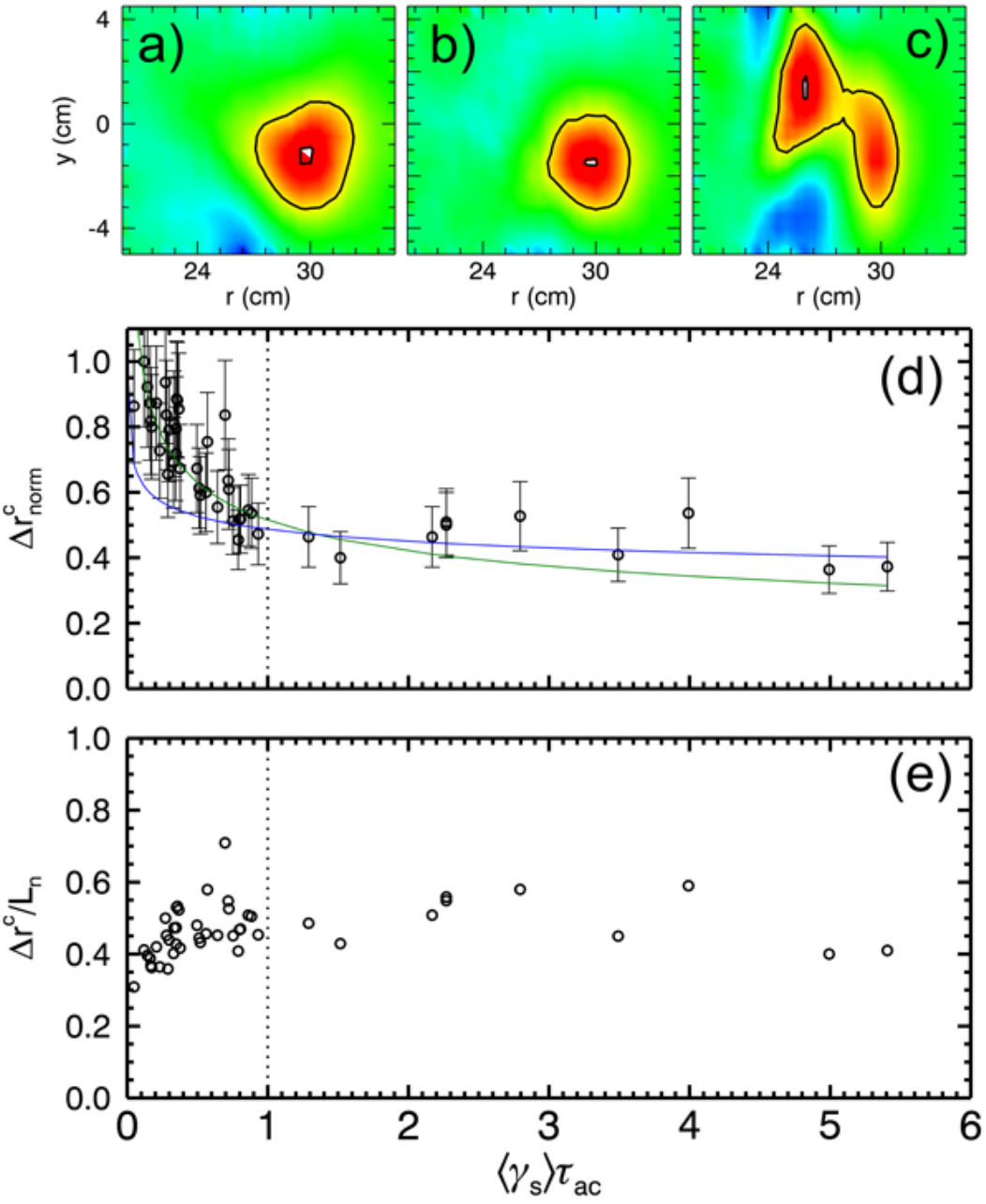

Figure 6.14: Normalized correlation functions for (a)unbiased, IDD flow state, (b)no shear state, and (c)high bias, high EDD flow state where the black curve represents a decrease of 0.5 from peak. (d)Radial correlation length normalized to maximum correlation length versus normalized shearing rate with M2 fits for weak (green) and strong (blue) shear. (e)Ratio of radial correlation length to density gradient scale length.

This chapter shows that suppression of turbulent particle flux is observed with increasing shearing rate and can be attributed mostly to a suppression of density fluctuation amplitude, but some contribution to the suppression are also shown to be due to changes in crossphase, radial velocity fluctuation amplitude and coherency. The decrease in crossphase does not come until higher shearing rates are reached and mostly only for frequencies greater than 10kHz, but this decrease does mitigate the overall particle transport that would be caused by increased density fluctuation amplitude in this region of shearing rate and frequency space due to the coherent mode. Overall, though, the decrease in flux is primarily due to a decrease in turbulent amplitude. This observation is again distinct from rotation experiments on LAPD. In those experiments, turbulent amplitude decreased little while the turbulent crossphase experienced a significant change, leading to reduced particle flux. This may also be an effect of the difference in magnetic field (400G versus 1000G). It could also stem from the difference in shearing rates; peak shearing rates on the previous experiment reached 150kHz compared to the 120kHz achieved here. Some predictions suggest that crossphase suppression becomes dominant at high shearing rates [61]. This is somewhat observed here as crossphase is clearly more suppressed at the highest biases.

The next chapter extends this quantitative analysis begun here by comparing various decorrelation models to the scaling observed in this chapter. The ability to produced sheared flow in both the weak and strong shearing regime as compared to the inverse autocorrelation time allows for comparison to models which make separate predictions for these two levels of sheared flow.

CHAPTER 7

Quantitative Scaling of turbulent quantities with sheared flow

As mentioned in Chapter 2, the mechanism for suppression of turbulence and transport by flow or flow shear is still not completely understood. Part of the problem has been a lack of detailed experimental measurements with fine variation in the flow or shearing rate. This chapter presents an attempt to provide a detailed dataset for the reduction of turbulent quantities as a function of shearing rate This chapter uses the local analysis for shear scaling and makes experimental fits based on various decorrelation models and compares these fits to the predictions made by the models.

7.1 Models of Shear Suppression

While various mechanisms for flow or flow shear suppression have been proposed, one of the earliest models developed is the shear decorrelation model. These models based on radial decorrelation of turbulent structures by sheared flow are prevalent in the theoretical literature [61–70] and provide a number of predictions concerning the quantitative scaling of turbulent quantities with shear. The basic premise underlying these models is the competition between linear or nonlinear turbulence dynamics and the tendency of sheared flows to "rip apart" or decorrelate turbulent structures; this leads to reduced fluctuation amplitude and decreased radial transport step-size. A large number of theoretical models have been developed which use this underlying principle. Variation in the predictions of these models arise from assumptions: strength of flow shear compared to turbulence timescales (strong

vs weak), the underlying instability driving the turbulence (i.e. Ion Temperature Gradient (ITG) or Resistive Pressure Gradient Driven Turbulence (RPGDT)), as well as consideration of passive versus dynamic scalars.

Two of the earliest models of shear suppression were decorrelation models developed by Biglari, Diamond, Terry [62] (hereafter BDT) and Shaing [63]. The BDT theory presents a generalized analysis of the transport of a passive scalar in a mean sheared flow in the strong-shear regime with constant turbulent drive (pressure gradient). The BDT model predicts that normalized fluctuation amplitude scales directly with shear to the -2/3 power:

$$\frac{\langle|\tilde{\xi}|^2\rangle}{\langle|\tilde{\xi}|^2\rangle_{\gamma_s=0}} \sim (\gamma_s \tau_{ac})^{-2/3} \tag{7.1}$$

where ξ can be any quantity such as density or temperature. Conversely, the Shaing model focuses on the weak shear limit and predicts a scaling of the form:

$$\frac{\langle|\tilde{\xi}|^2\rangle}{\langle|\tilde{\xi}|^2\rangle_{\gamma_s=0}} \sim 1 - \alpha(\gamma_s \tau_{ac})^2 \tag{7.2}$$

where α is a constant containing mode number information.

Zhang and Mahajan [64, 65] developed a model which included the self-consistent modification of the fluctuation spectrum and the diffusion coefficient by flow shear. This allowed the development of a model for shear suppression of turbulent amplitude which could span both the weak and strong shear regimes:

$$\left(\frac{\langle|\tilde{\xi}|^2\rangle}{\langle|\tilde{\xi}|^2\rangle_{\gamma_s=0}}\right)^{-1} \sim 1 + \alpha(\gamma_s \tau_{ac})^2 \tag{7.3}$$

The resulting model shows correspondence to the Shaing model in the weak shear regime while the BDT model can be recovered in the strong shear regime but only for the case where the diffusion coefficient is constant (independent of fluctuation amplitude).

Work by Ware and Terry [66, 67] made predictions for the effect of shear on particle transport specifically in resistive pressure-gradient driven turbulence (RGPDT). Their work predicted a decrease in flux as $\Gamma_p \sim 1 - \gamma_s^2$ in the weak shear limit. Additionally, the model predicted a decrease in the cosine of the crossphase between density and radial velocity

fluctuations of the form $1 - \gamma_s^2$. They too incorporated the modification of the pressure gradient, formulating an expression for shear suppression of radial particle diffusivity of the form:

$$\frac{D}{D_{\gamma_s=0}} \sim 1 - \beta(\gamma_s)^2 \tag{7.4}$$

where β is a constant which depends on the linear growth rate and radial mode width.

Further work by Terry, Newman and Ware [61] examined the modification of flux in the strong shear regime for a non-mode-specific turbulent system, predicting a direct scaling of $\Gamma_p \sim \gamma_s^{-4}$ overall. Here fluctuation amplitude reduction contributed one power while crossphase reduction contributed three powers of γ_s, indicating that, in the strong shear limit, crossphase modification is the dominant flux suppression mechanism rather than reduction of the fluctuation amplitude.

Kim and Diamond [68] recast the decorrelation model to include resonance absorption between the shear flow and fluctuations leading to a much weaker dependence of particle flux on shear, $\Gamma_p \sim \gamma_s^{-1}$, and even weaker dependence of the crossphase on shear: $\cos(\theta_{nv_r}) \sim \gamma_s^{-1/6}$. In this model, fluctuations decreased as $|\tilde{n}|^2 \sim \gamma_s^{-5/3}$. Additional work along these lines [69] considered a more self-consistent model for the turbulence, treating the fluctuating flows dynamically using interchange drive. This model predicted a decrease in fluctuating radial velocity amplitude as a function of shear which scales as $|\tilde{v_r}|^2 \sim \gamma_s^{-3}$ in the weak shear limit, and as $|\tilde{v_r}|^2 \sim \gamma_s^{-4}$ in the strong-shear limit.

Finally, work by Newton and Kim has utilized numerical simulations using a generic turbulence model [70] with a finite correlation time, $\tau_{ac} \geq \gamma_s^{-1}$. Their work produced scalings of $D \sim \gamma_s^{-1.75}$, $|\tilde{n}|^2 \sim \gamma_s^{-2.41}$, and $\cos(\theta_{nv_r}) \sim \gamma_s^{-0.22}$ which correspond to the strong shear regime for this dataset.

7.2 Experimental Shear Suppression Scaling

As shown in Chapter 6, radial particle flux and fluctuation amplitude are reduced as shearing rate is increased and the resulting transport changes cause observable steepening of the den-

Table 7.1: Power-law fits for $|\tilde{n}^2|$ with shear for frequencies in 350Hz to 100kHz. Model form is the particular model used in the fit, with C a constant and ν resulting best-fit exponent.

Model form	γ_s regime	ν	χ^2	χ^2/ndf	σ
$\sim 1 - C\gamma_s^\nu$	$\gamma_s\tau_{ac} < 1$	0.743	7.644	0.450	0.164
$\sim 1 - C\gamma_s^\nu$	$\gamma_s\tau_{ac} > 1$	0.218	0.337	0.037	0.118
$\sim C\gamma_s^\nu$	$\gamma_s\tau_{ac} < 1$	-0.178	25.08	1.320	0.038
$\sim C\gamma_s^\nu$	$\gamma_s\tau_{ac} > 1$	-0.513	0.254	0.028	0.328

sity gradient. Figure 7.1 shows the experimental results for measurements of density fluctuation amplitude, radial velocity fluctuation amplitude and density-radial velocity crossphase as functions of normalized shearing rates. The shearing rates achieved span two regimes: a weak-shear regime where $\gamma_s\tau_{ac} < 1$ and a strong-shear regime where $\gamma_s\tau_{ac} > 1$. The blue solid lines correspond to the best fits for the strong-shear cases while the green are the best fits for the weak-shear case. Similar plots for particle flux and diffusivity $D = \Gamma/|\nabla n|$ are shown in Figure 7.2. All data presented is averaged over the radial range $27 < r < 31$cm as indicated in Figure 6.1. Error bars of +/-20% for each quanitity are shown on the plots and used in the fits, reflecting a statistical error from the number of shots used to average the quantity ($\sigma \sim 1/\sqrt{cmrN_{shots}}$).

Some achieved parameter regimes for the shearing rate and density gradient length scales are presented in Figure 7.3. The azimuthal velocity scale length is calculated as $L_v = |\nabla \ln(v_{E\times B})|^{-1}$. This value is compared to the density gradient scale length, $L_n = |\nabla \ln n|^{-1}$ as a function of normalized shearing rate. This plot shows that for the all of the strong shear regime, and nearly half of the weak shearing regime, $L_n > L_v$. The reverse is true only for the weakest shear. In general, the velocity gradient scale length decreases much faster than the density gradient scale length with increased shearing rate magnitude and is smaller than the density gradient scale length for most of the dataset.

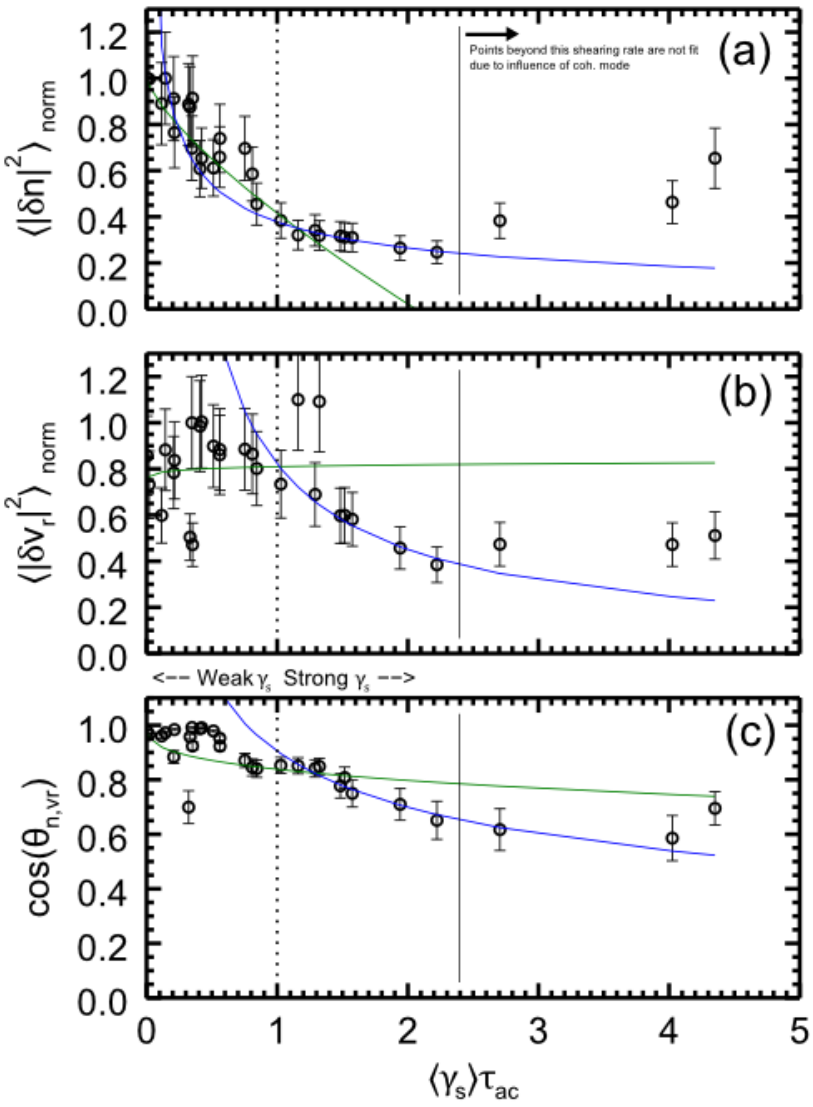

Figure 7.1: (Color online) Scaling of (a)density fluctuation amplitude, (b)radial velocity fluctuation amplitude, and (c)density-radial velocity crossphase. Density and velocity fluctuations are each normalized to the value measured at minimum shear. The green curves correspond to $1 - \gamma_s^\nu$ fits of the weak shear regime. The blue curves correspond to γ_s^ν fits.

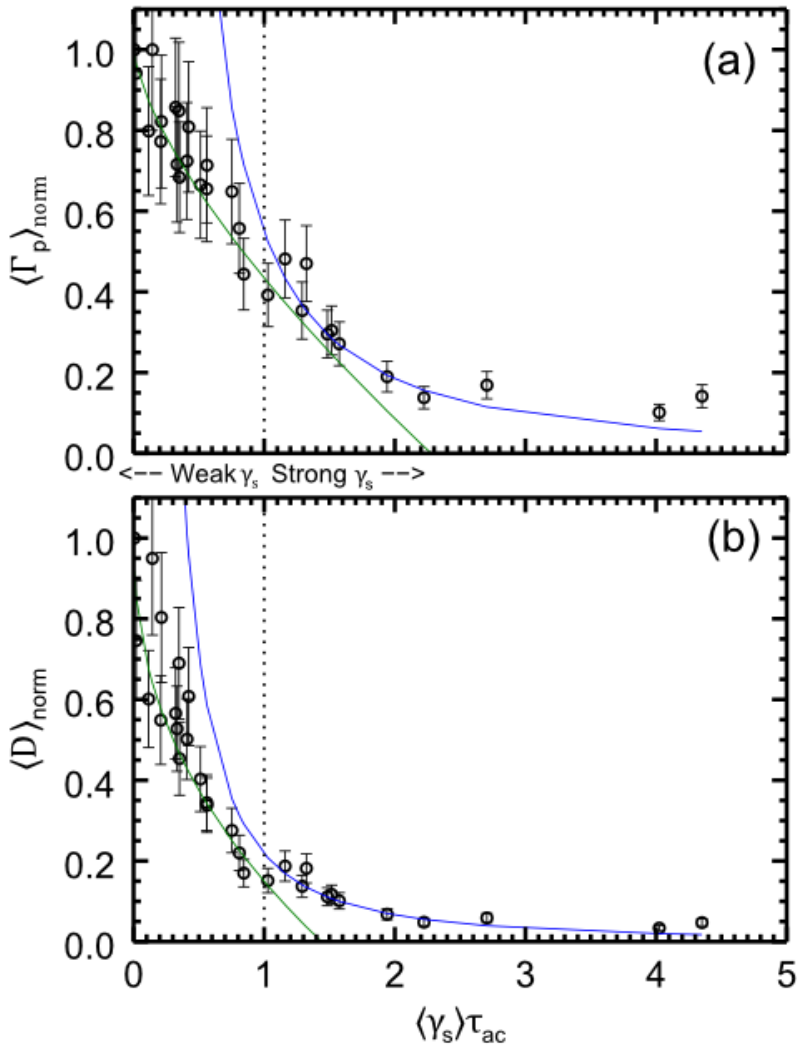

Figure 7.2: (Color online) Scaling of (a)radial particle flux and (b)diffusion coefficient each normalized to the value at minimum shear, $\Gamma_p^0 = 1.7 \times 10^{16} cm^{-2}$ and $D_0 = 36.7 m^2/s$. The green curves correspond to $1 - \gamma_s^\nu$ fits of the weak shear regime with $\nu = 0.693$ for flux and $\nu = 0.445$ for D. The blue curves correspond to γ_s^ν fits with $\nu = -1.571$ for flux and $\nu = -1.715$ for D. The last three points in each plot are not included in the fits do to potential influence of the coherent mode at high shearing rate.

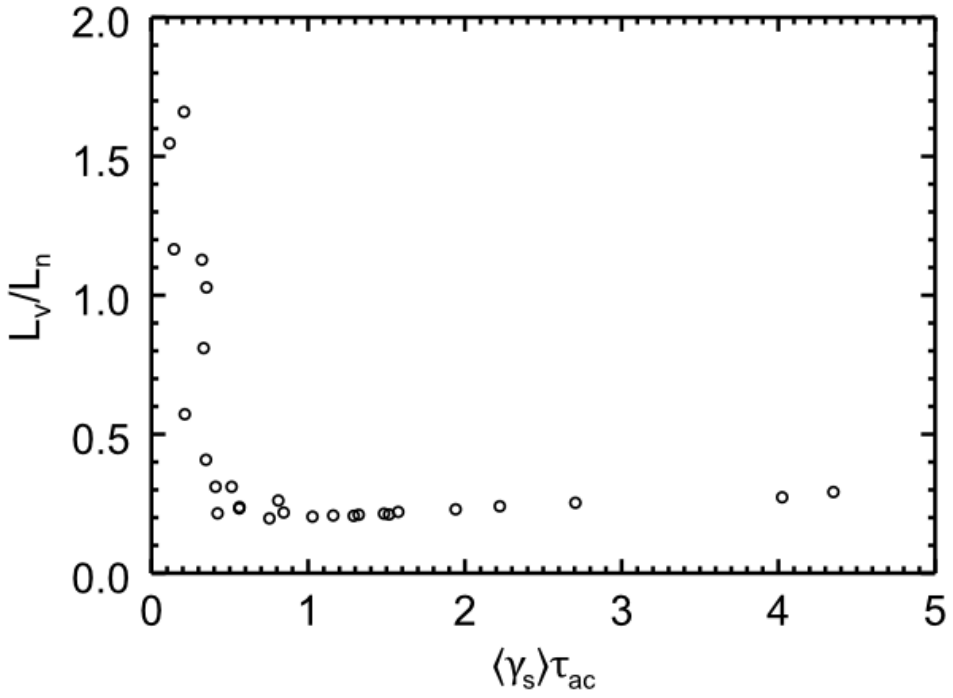

Figure 7.3: Ratio of velocity gradient length scale to density gradient length scale versus normalized shearing rate in the radial region of 27 to 31cm.

Table 7.2: Power-law fits for $|\tilde{v}_r^2|$ scaling with shear for frequencies in 350Hz to 100kHz.

Model form	γ_s regime	ν	χ^2	χ^2/ndf	σ
$\sim C\gamma_s^\nu$	$\gamma_s\tau_{ac} < 1$	0.014	15.99	0.888	0.040
$\sim C\gamma_s^\nu$	$\gamma_s\tau_{ac} > 1$	-0.866	0.392	0.056	0.360

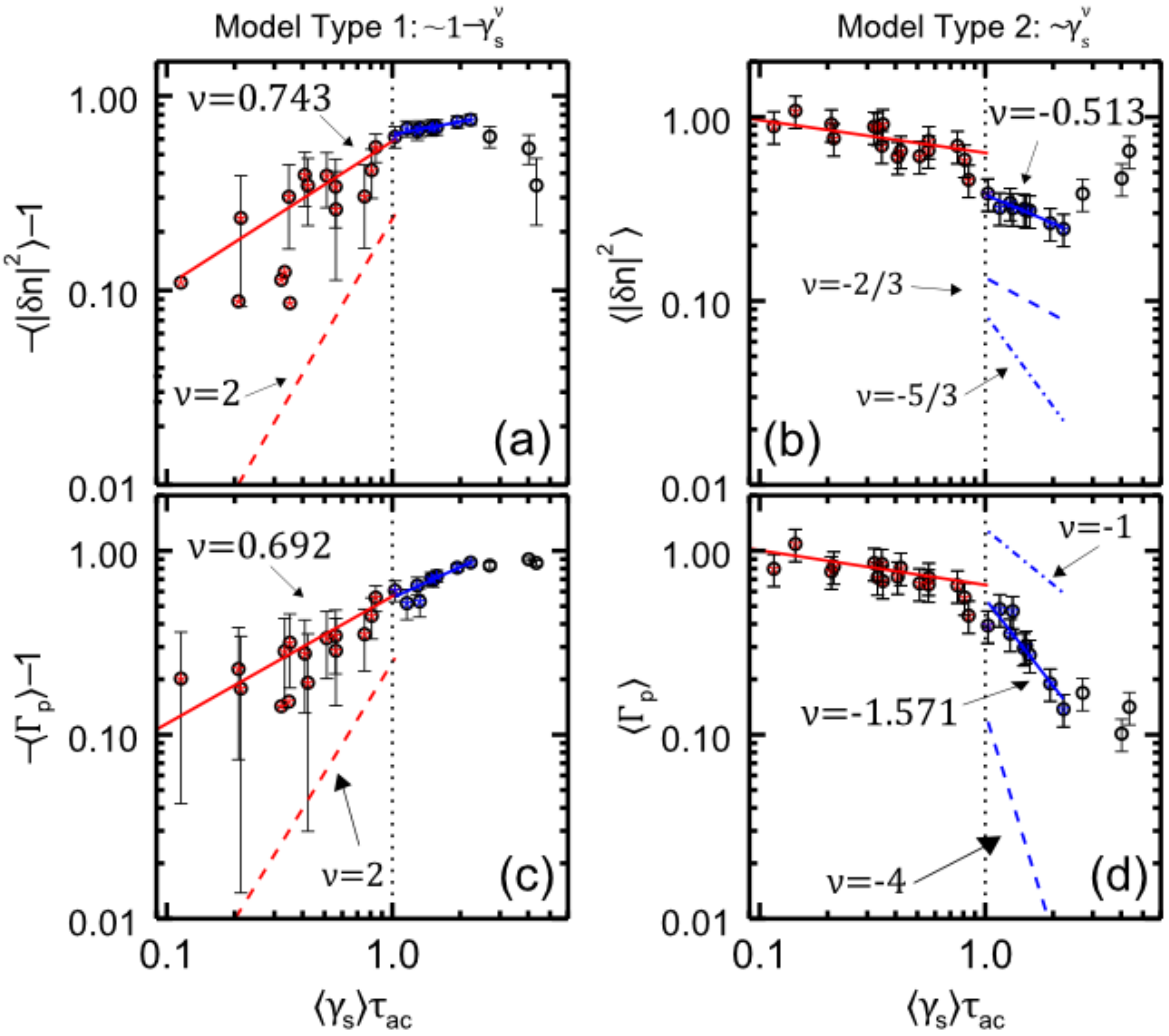

Figure 7.4: (Color online) Log-Log plot of (a-b)density fluctuation amplitude and (c-d)particle flux versus shearing rate. Weak shear fits, (a) and (c), are shown with the solid red lines and a theoretical prediction—dashed line—of $\nu = 2$ is included for comparison of slope (line is manually offset). Strong shear fits, (b) and (d), are shown with the solid blue lines and theoretical predictions are indicated with the dashed lines.

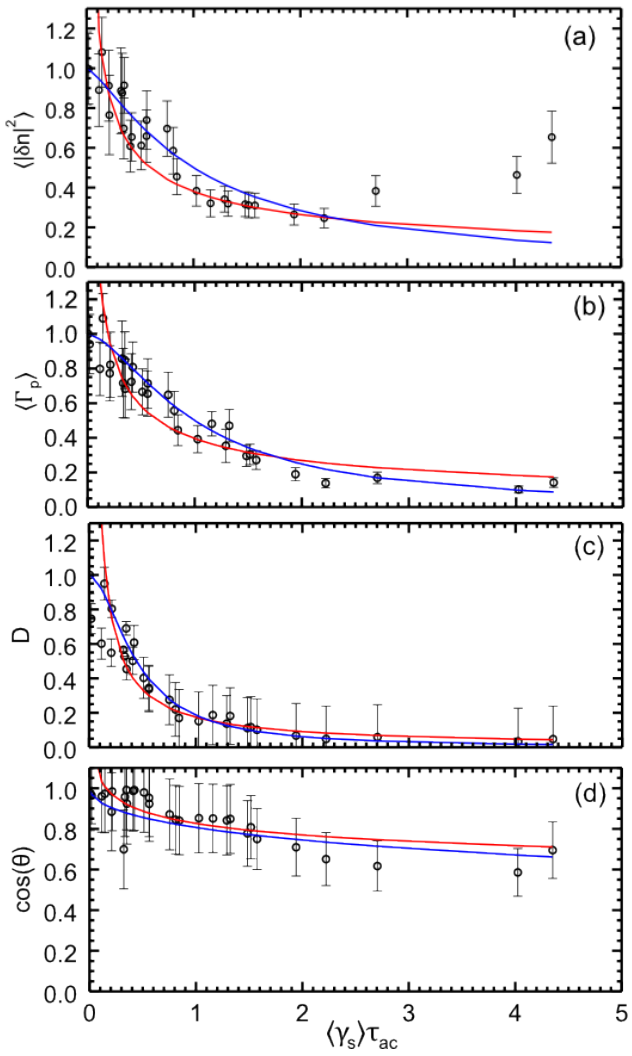

Figure 7.5: (Color online) Fits over a shear range spanning both weak and strong regimes for (a) density fluctuation amplitude, (b)particle flux, (c)diffusivity, and (d)crossphase. Red lines correspond to $\sim C\gamma_s^{\nu}$ model while the blue curves correspond to the $\sim 1/(1 + C\gamma_s^{\nu})$ model.

Table 7.3: Power-law fits for Γ_p scaling with shear for frequencies in 350Hz to 100kHz.

Model form	γ_s regime	ν	χ^2	χ^2/ndf	σ
$\sim 1 - C\gamma_s^\nu$	$\gamma_s\tau_{ac} < 1$	0.693	5.157	0.3034	0.142
$\sim 1 - C\gamma_s^\nu$	$\gamma_s\tau_{ac} > 1$	0.556	2.899	0.3221	0.010
$\sim C\gamma_s^\nu$	$\gamma_s\tau_{ac} < 1$	-0.188	29.84	1.57	0.038
$\sim C\gamma_s^\nu$	$\gamma_s\tau_{ac} > 1$	-1.571	4.013	0.446	0.327

Table 7.4: Power-law fits for $D = \Gamma_p/\nabla n$ scaling with shear for frequencies in 350Hz to 100kHz.

Model form	γ_s regime	ν	χ^2	χ^2/ndf	σ
$\sim 1 - C\gamma_s^\nu$	$\gamma_s\tau_{ac} < 1$	0.445	11.60	0.682	0.054
$\sim 1 - C\gamma_s^\nu$	$\gamma_s\tau_{ac} > 1$	0.187	3.188	0.354	0.030
$\sim C\gamma_s^\nu$	$\gamma_s\tau_{ac} < 1$	-0.300	50.43	2.65	0.040
$\sim C\gamma_s^\nu$	$\gamma_s\tau_{ac} > 1$	-1.715	4.610	0.512	0.327

Table 7.5: Power-law fits for $cos(\theta_{nv_r})$ scaling with shear for frequencies in 350Hz to 100kHz.

Model form	γ_s regime	ν	χ^2	χ^2/ndf	σ
$\sim 1 - C\gamma_s^\nu$	$\gamma_s\tau_{ac} < 1$	0.324	2.89	0.152	0.545
$\sim 1 - C\gamma_s^\nu$	$\gamma_s\tau_{ac} > 1$	1.272	0.037	0.004	1.573
$\sim C\gamma_s^\nu$	$\gamma_s\tau_{ac} < 1$	-0.022	2.49	0.131	0.040
$\sim C\gamma_s^\nu$	$\gamma_s\tau_{ac} > 1$	-0.373	0.155	0.017	0.328

The variation of the experimentally measured quantities with normalized shearing rate was fit to functions motivated by models discussed above: functions of the form $1-\gamma_s^\nu$ (hereafter M1) and of γ_s^ν (hereafter M2). For M1, the measured quantity, y, was normalized to the value at zero shear, then transformed as $-(1-y)$. Then, taking the logarithm of both sides, a linear fit was made for points in the weak shear and in the strong shear separately. The resulting slope of the fit is taken as the power ν. For M2, no transformation of the quantity y is made before taking the logarithm and fitting. For a complete comparison to the wide range of model predictions made, fits were made for density fluctuation amplitude, radial particle flux, density-radial velocity fluctuation crossphase, radial velocity (ExB) fluctuation amplitude, radial correlation length, and experimentally determined diffusivity ($\Gamma/|\nabla n|$). The best fits are summarized in Table 7.1- 7.6 for each model type and for both weak and strong shear. The χ^2 and χ^2/ndf (where ndf is the number of degrees of freedom) is also indicated in the tables as well as the one standard deviation error, σ, in the fit parameter, ν. For weak shear fits, all points less than the weak shear cutoff $\gamma_s\tau_{ac} < 1$ are used in the fit. For strong shear, all but the last three points are used. The last points appear to be strongly influenced by the presence of a coherent mode that develops in the highest shear and flow cases and is thought to be a break from the scaling observed in the strong shear regime. For quantities determined by averaging over frequency (e.g. density and velocity fluctuation amplitudes, flux and diffusivity) the frequency band used was 350Hz to 100kHz.

The log-log plots highlight the break in the trend between the weak and strong shear regimes. It should be noted that in addition to turbulent quantities showing a different trend with shear below and above a normalized shearing rate of unity, at the same time, the density gradient scale length also shows a marked change in behavior [71]. The gradient scale length decreases rapidly (increasing pressure-gradient drive) in the weak shear regime followed by saturation in the strong shear regime (constant turbulent drive with increased shear). Therefore care has to be taken in interpreting the change in the trends plotted above: it could be occurring due to a change in the shear regime but also could be due to the change in trend for the turbulence drive.

Table 7.6: Power-law fits for Δr_c scaling with shear for frequencies in 350Hz to 100kHz.

Model form	γ_s regime	ν	χ^2	χ^2/ndf	σ
$\sim C\gamma_s^\nu$	$\gamma_s\tau_{ac} < 1$	-0.290	5.8730	0.1631	0.084
$\sim C\gamma_s^\nu$	$\gamma_s\tau_{ac} > 1$	-0.113	3.7040	0.3370	0.111

Lastly, fits were made a range of shearing rate that spanned portions of both the weak and strong shear regimes; specifically, a range that included all but the lowest two shearing rate values and the three highest shearing rate values (again, dropping the last three to avoid any influence of the coherent mode). The models used are M2 and a third model based on the Zhang and Mahajan interpolated from Eqn.(7.3) which was designed to describe both weak and shear scaling (hereafter M3). Fits and χ^2 values are displayed for density fluctuation amplitude, particle flux, diffusivity, and crossphase in Table 7.7 and are shown plotted against the data in Figure 7.5.

7.2.1 Density and Velocity Fluctuations

The best fits for scaling of density fluctuation amplitude are shown in Table 7.1. For the weak shear regime, the χ^2 values suggest M1 to be a slightly better fit to the data than M2. Though M1 is not used for prediction of strong shear scaling in the literature, a fit was made to it here for completeness; values of χ^2 show M2 to be the better model for the strong shear regime.

The $\nu = -0.512$ fit for M2 in the strong shear limit is reasonably close to the BDT prediction of $-(2/3)$. However, it should be reiterated that BDT assumes a fixed turbulence drive and that in this dataset, the gradient scale length decreases substantially as shear is increased, resulting in an increase in turbulent drive. This actually implies a stronger than BDT scaling of fluctuation amplitude suppression overall. The fit scaling is much smaller than that predicted by Kim/Diamond ($\nu = -5/3$) and Newton/Kim ($\nu = -2.41$). For

Table 7.7: Power law fits for all quantities over a range that spans both weak and strong shear. The smallest two shearing rate values are excluded to improve the fitting routine and the three highest shearing rate values are excluded to avoid effects of the coherent mode.

Parameter	Model form	ν	χ^2	χ^2/ndf	σ
$\langle\|\tilde{n}^2\|\rangle$	$\sim 1/(1+C\gamma_s^\nu)$	1.229	11.07	0.461	0.143
$\langle\|\tilde{n}^2\|\rangle$	$\sim C\gamma_s^\nu$	-0.527	13.63	0.568	0.059
$\langle\Gamma_p\rangle$	$\sim 1/(1+C\gamma_s^\nu)$	1.555	21.68	0.903	0.124
$\langle\Gamma_p\rangle$	$\sim C\gamma_s^\nu$	-0.557	28.65	1.193	0.059
$\langle D\rangle$	$\sim 1/(1+C\gamma_s^\nu)$	1.174	74.84	3.12	0.047
$\langle D\rangle$	$\sim C\gamma_s^\nu$	-0.938	37.16	1.55	0.059
$cos(\theta_{nv_r})$	$\sim 1/(1+C\gamma_s^\nu)$	0.514	9.12	0.405	0.278
$cos(\theta_{nv_r})$	$\sim C\gamma_s^\nu$	-0.102	3.621	0.151	0.059

M2 weak shear, the experimental fit of $\nu = -0.116$ also suggests weaker scaling than the prediction by Kim/Diamond of $-(2/3)$.

A prediction for the scaling of radial velocity fluctuation amplitude is only made by Kim and Diamond [69] in the dynamically evolved case. Fits, listed in Table 7.2, suggest a much weaker scaling than predicted for both weak and strong shear. The weak shear fit actually shows a slight increase in fluctuation amplitude rather than a $\nu = -3$ scaling while in the strong shear regime a fit of $\nu = -0.866 << -4$ is found.

From fits over the full range of shearing rates, shown in Table 7.7, M2 appears to be a slightly better model than M3. The M2 fit, $\nu = -0.527$, is similar to the strong shear only fit, but clearly has a worse χ^2 value.

7.2.2 Flux and Diffusivity

Particle flux and diffusivity fits and χ^2 results are shown in Table 7.3 and 7.4 respectively. Like density fluctuations, M1 seems to be slightly better than M2 for fitting data in the weak shear limit based on χ^2 values. However, for strong shear, the M1 model actually has a lower χ^2 than the M2 model, though M1 is not derived in the strong shear limit in the literature. Despite the higher χ^2, the fit of $\nu = -1.571$ falls in between the extremes of predictions of $\nu = -1$ and $\nu = -4$. The weak shear fit of $\nu = -0.188$ falls far short of the Kim/Diamond M2 prediction of $\nu = -1$.

Diffusivity has lower χ^2 values for M1 with weak shear and strong shear. The only predictions for D come from Terry and Ware with a functional form like M1 and a numerical simulation result from Newton and Kim [70] for evolved turbulence with a finite correlation time. The experimental fit of $\nu = 0.445$ again falls short of the Terry/Ware predicted $\nu = 2$, though the M2 fit in the strong shear limit with $\nu = -1.715$ is extremely close to the Newton/Kim predicted value of $\nu = -1.75$. The full range results suggest M3 a slightly better fit for flux while M2 a slightly better fit for diffusivity.

7.2.3 Crossphase and Correlation Length

Fits for the scaling of cosine of the crossphase between density and radial velocity fluctuations are shown in Table 7.5. M1 is found to fit only slightly better than M2 for both weak and strong shear limits. The M2 fit in the weak limit of $\nu = -0.022$ and M2 fit in the strong limit of $\nu = -0.373$ both tend to support the prediction of mild scaling with crossphase made by Kim/Diamond with $\nu = -(1/6)$ and Newton/Kim with $\nu = -0.22$, rather then the large scaling of $\nu = -3$ made by Terry [61]. In fact, the full range fit of M2 for crossphase of $\nu = -0.102$ is in excellent agreement with the Kim/Diamond fit of $\nu = -(1/6)$ which is predicted for *both* weak and strong shear.

It should be pointed out that the variation of cross-phase with shear in this dataset is markedly different than what was observed in an earlier LAPD experiment where flow was

driven by biasing the vacuum chamber wall [39]. This previous experiment was performed at lower magnetic field and at larger bias, resulting in a stronger $E \times B$ rotation and much stronger normalized shearing rate ($\gamma_s \tau_{cmrac} \sim 20$). In that work a strong modification of cross-phase was observed (with little to no amplitude reduction).

Finally, a fit to radial correlation length is made and compared to the prediction made by BDT [62]. Neither the weak shear fit of $\nu = -0.290$ nor the strong shear of $\nu = -0.113$ is unreasonably far from the predicted value of $\nu = -1/3$ though the χ^2 values do not suggest a great fit to either model. It should again be noted that these correlation lengths are measured in the steady-state period when the density gradient scale length will have already adjusted due to the change in transport. Thus, as discussed in Chapter 6, this decrease in radial correlation length could be due to the turbulence adjusting to the new gradient scale length rather than a direct response to shear.

While the large variation in fits for six turbulent quantities makes careful model validation difficult, there are a number of conclusions that can be drawn from the analysis reported here. First the experimental results from this dataset show a distinct difference in scaling between the weak and strong shear regimes, consistent with expectations from many models. The models fit to separate regimes generally have lower or at least comparable χ^2 values than those fit to a range in shearing rate that spans both weak and strong regimes. Second, none of the three models tested were clearly better than the others based on χ^2 goodness of fit. The fits were generally not very close to predicted values though a few quantities yield fits that were very close to the theory—namely, as the strong shear density M2 fit of ν = -0.515, the strong shear M2 diffusivity fit of ν = -1.715, or the full range crossphase M2 fit of ν = -0.102. However, the goodness-of-fit for the alternative models in each of these cases were either not significantly worse, or were in fact better. Third, the data clearly supports the prediction that density fluctuation amplitude is more strongly suppressed than the crossphase and thus makes a more significant contribution to the suppression of radial transport. However it should be noted that at much stronger shear (in previous LAPD datasets), dominant modification of crossphase is observed. Finally, as indicated by the

wide range of predictions, the scaling of shear suppression may be dependent on the nature of the turbulence used in the model. Many of the suppression models discussed are mode specific such as RPGDT for the Terry/Ware models or interchange turbulence for the later Kim/Diamond models. Neither of these two models fit the LAPD results quantitatively well which suggests the need for a model based on LAPD-specific turbulent drive.

No model correctly captures the observed variation in all turbulent quantities; however some models do make predictions which are close to observations for one or two turbulent quantities. Qualitative agreement with some models is found: in particular in the fact that transport suppression is found experimentally to be due to fluctuation amplitude reduction rather than by crossphase change. The quantitative disagreement with these models could arise due to a number of issues. Models that assume a fixed turbulent drive (do not allow for changes in density gradient scale length) are unlikely to match the data. Additionally, many models assume a turbulence model which may be inappropriate (ITG or interchange drive are unlikely to be relevant to LAPD, although rotational interchange can be active). While the various models cited in this paper deal with constant sheared flow, variations in scalings may arise to due fluctuations in the shearing rate [69, 72, 73]. It is also possible that decorrelation is incorrect as the underlying physical mechanism for shear suppression. Alternative models have been proposed, including enhanced coupling to damped eigenmodes [41] (this model focuses mainly on zonal flows rather than mean flows, however) or suppression due to spectral shift [42].

This chapter wraps up the detailed analysis into the effect of flow changes on turbulence and transport in the established steady-state. The next chapter takes a brief look at how the these changes manifest in time. Specifically, the chapter presents how the flow profile changes in time (using a Mach probe measurement rather than the swept probe) as well as how density and floating potential fluctuations change with these rotation changes.

CHAPTER 8

Dynamic modifications with biasing and transport modeling

While the majority of this dissertation has centered on the steady-state evaluation of plasma parameters for various bias states, this section will focus on the dynamics of the bias turn-on and turn-off looking at how profiles and fluctuating quantities change with time and how the level of biasing modifies the rate of this change.

8.1 Bias Voltage and Current

The temporal measurement of bias voltage and current was discussed in Chapter 4. The bias current reaches an initial non-zero value very quickly within about 10μs and is likely the result of current flow directly between the cathode and the limiter edge that overlaps the cathode source. A corresponding initial voltage difference between the anode and the limiters is also reached. From these initial values, the current and the voltage difference continue to rise though much more slowly than the initial jump. Within about 250μs, the current begins to level out and then reaches its steady-state value by about 1ms after bias turn-on. This increase in current from the initial non-zero value to the steady-state value is thought to consist mostly of cross-field current that develops between the limiter-connected field lines and the anode-connected field lines. An example for a given power supply voltage of 100V (Bias 22) is shown in Figure 8.1.

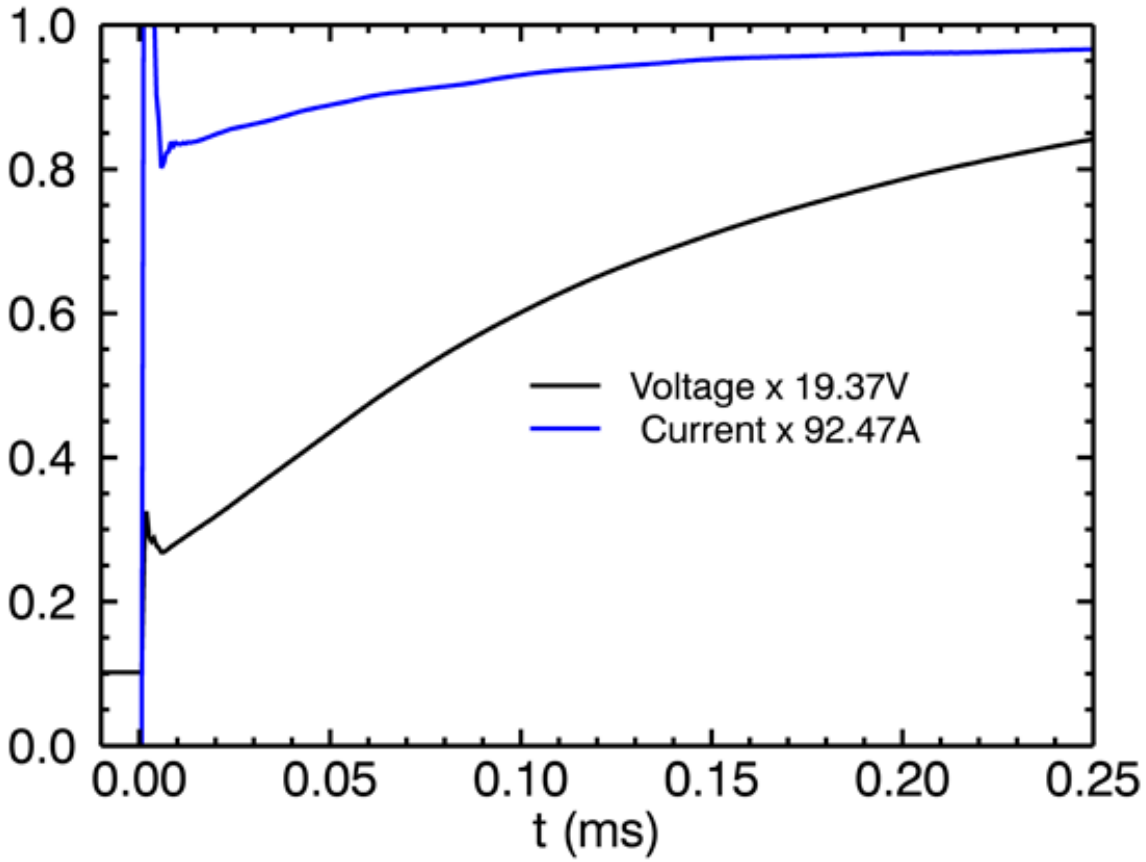

Figure 8.1: Plasma Potential profiles

8.2 Plasma Response

The change in plasma parameters (flow, shear, density, density fluctuations, floating potential fluctuations, and flux) as a function of time after bias turn-on is examined in this section. Each profile is constructed by averaging the time-series probe measurements at each radial position. The time-series probe measurements are sampled at 1.5625MHz resulting in a minimum time interval of 6.4×10^{-7}s. To provide some averaging, 40 samples are combined so that each profile shown accounts for about 0.026ms. The flow profiles with time are determined using Mach probe measurements which can be constructed from saturated current time-series measurements (unlike swept-Langmuir probe measurements which are only taken at a single point in time). The measured Mach number is converted into an angular velocity using $V_\theta = MC_s$. An unbiased temperature profile like that in Figure 5.2 is used in the calculation of the sound speed; any increases in temperature from biasing are not taken into account. Sheared flow profiles are taken as the radial gradient of these Mach probe profiles. Density is determined in the same manner as the steady-state profiles (only over the smaller time window) while density fluctuations and floating potential fluctuations are determined by calculating the root-mean-square of the mean for each 40 sample time block. The flux is determined by directly averaging over the product of mean-subtracted density and radial velocity time-series measurements, $\Gamma_p = \langle \tilde{n}\tilde{v_r} \rangle$, rather than using the cross-spectrum approach used for the steady-state profiles.

8.2.1 Mach Flow Dynamics

The change in the rotational state of the plasma as the bias current increases is shown in Figure 8.2. Four biases are shown: the first, Bias 7 (lim-ano = -5V)—Figure 8.2(a), is the bias consistent with the minimum shearing rate in the steady-state; Bias 13 (lim-ano = -0.2V)(b) has medium flow in EDD in the steady-state; Bias 22 (lim-ano = 4.7V)(c) has large EDD flow and Bias 29 (lim-ano = 8.4V)(d) has the strongest flow. Since the flow is determined using the Mach probe, there is an overall offset in magnitude of the measured flow. This can

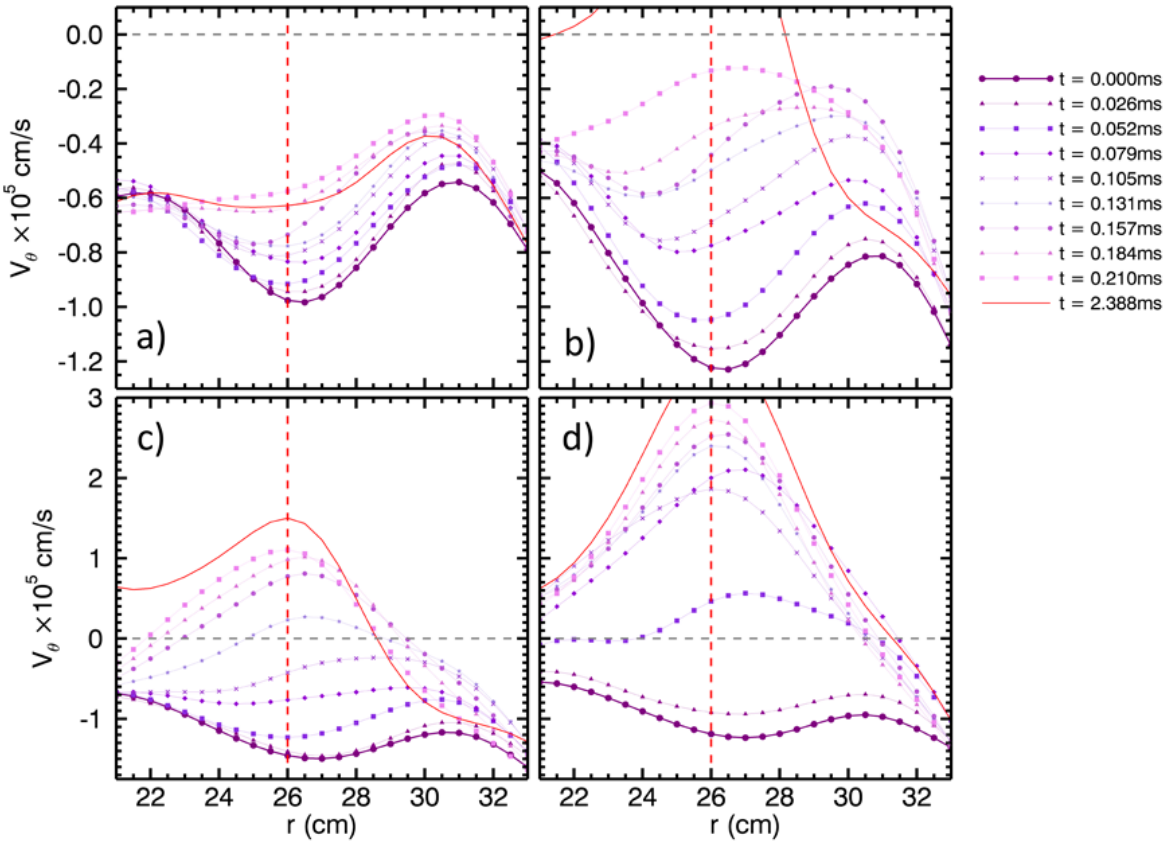

Figure 8.2: Mach Probe Flow Profiles as a function of time for four biases (a)Bias 7 (lim-ano = -5V), (b)Bias 13 (lim-ano = -0.2V), (c)Bias 22 (lim-ano = 4.7V) and (d)Bias 29 (lim-ano = 8.4V)

be seen in Figure 8.2(a); the swept-Langmuir flow measurement shows nearly a minimum amount of flow while the Mach probe measurement shows significant flow. Nevertheless, the change in flow can still be determined from the Mach probe.

All four plots in Figure 8.2 show that the flow profile near the limiter edge is changed evenly as a function of time. The dark, thick purple line with circles shows the profile at the moment the IGBT switch is triggered. Then, the flow profile change is tracked at 0.026ms intervals with a lightening purple color changing symbols as indicated in the legend. The initial flow is mostly the same for each bias (note the change in scale for plots (c) and (d)). As the bias is increased, there is clearly a larger amount of change for each time step. An example of the steady-state profile is shown by the red curves at 2.388ms.

This increased flow change is unsurprising given the role current plays in the force dynamics. The amount of cross-field current was shown to increase as bias was increased in Figure 4.19. If $J \times B$ provides the torque on the system, there will be an angular acceleration proportional to the torque given a "rotational inertia" of the plasma column.

The change in flow is most insightful when compared with changes in the other plasma parameters.

8.2.2 Density Dynamics

The four biases in Figure 8.4 show the progression of density profile change as current and flow are changed. For Bias 7 (lim-ano = -5V), referencing plot (a) of Figures 8.2 and 8.4, the flow is reduced from a moderate value in the IDD to a much smaller magnitude and with much less shear. The density profile changes very little; almost no change is seen beyond the limiter edge, and a slight decrease in density is observed just within the limiter edge. In the steady-state regime indicated by the red curve, the density within the limiter edge is shown to drop slightly more while density outside the limiter edge has actually increased, showing the effect of the increased cross-field transport.

Both Biases 13 (lim-ano = -0.2V) and 22 (lim-ano = 4.7V), (b) and (c), show a similar

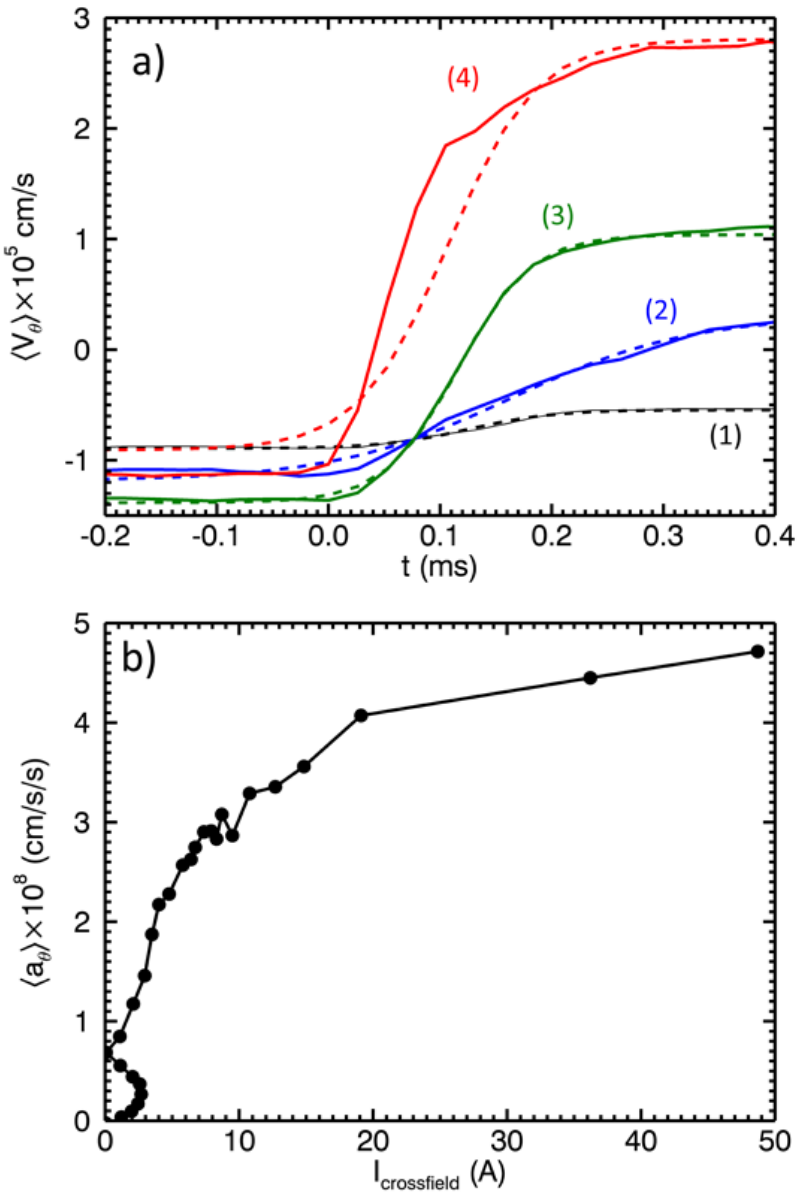

Figure 8.3: (a) Mach Probe Flow as a function of time averaged spatially over 24-28cm. (1)Black is Bias 7 (lim-ano = -5V), (2)Blue Bias 13 (lim-ano = -0.2V), (3)Green Bias 22 (lim-ano = 4.7V) and (4)Red Bias 29 (lim-ano = 8.4V) with the dotted lines in each a hyperbolic tangent fit to the data. The second plot (b) shows acceleration as calculated by the average derivative of the tanh fits as a function of the estimated cross-field current.

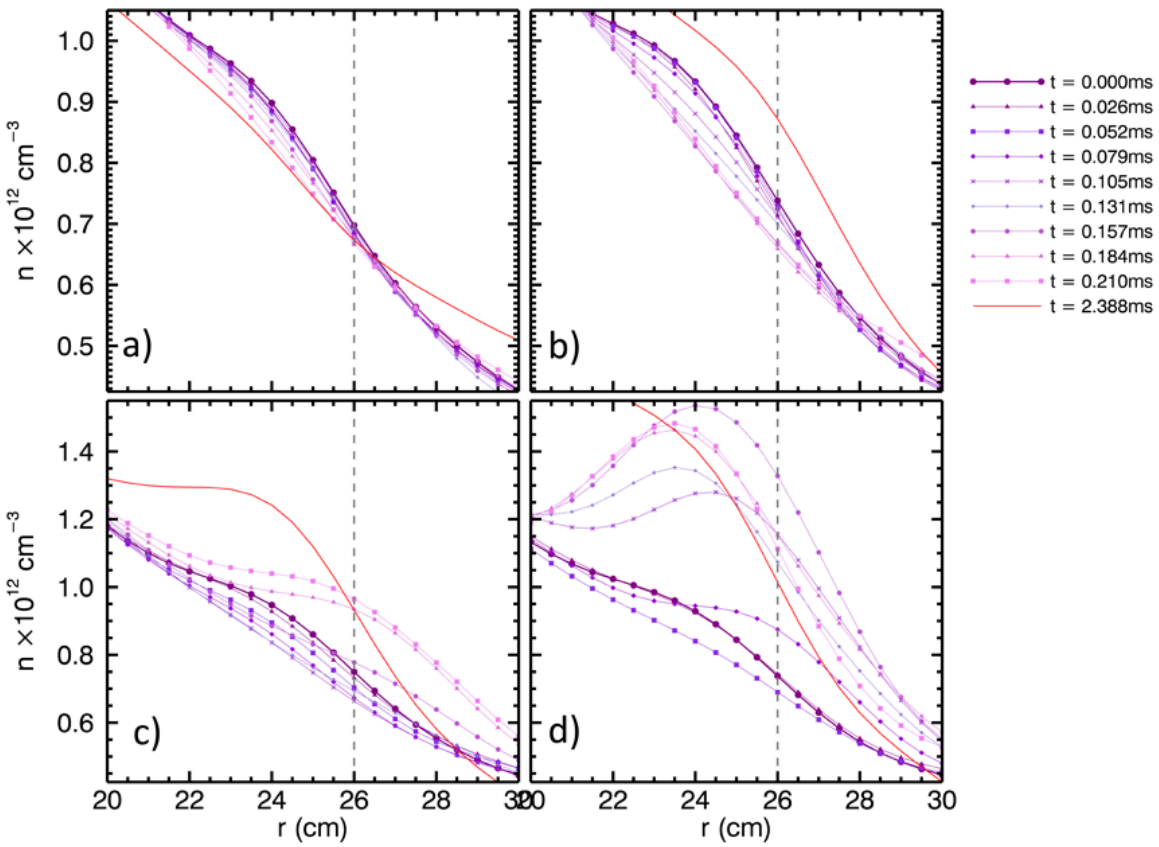

Figure 8.4: Density Profiles as a function of time for four biases (a)Bias 7 (lim-ano = -5V), (b)Bias 13 (lim-ano = -0.2V), (c)Bias 22 (lim-ano = 4.7V) and (d)Bias 29 (lim-ano = 8.4V)

initial decrease in plasma inside the limiter edge without any significant changes outside it. For Bias 13, the decrease in density continues for at least the first 200μs, but eventually shows a slightly steepened steady-state profile. Comparing these curves to the flow curves in Figure 8.2(b), it is apparent that the flow at t=0.210ms has not yet been reversed into the EDD as will eventually occur in the steady-state. In this sense, the density profiles of Bias 7 and Bias 13 for the first 200μs are very similar as the flow states for these two cases are comparable. The only difference is that the flow steadies near zero for Bias 7 while the flow continues to change for Bias 13. Bias 22 in Figure 8.4(c) then shows the effect on the density profile of flow being reversed and then driven in the EDD direction. This happens because the higher cross-field current achieved in the higher bias increases the flow faster so that nearly zero flow state in Bias 22 occurs at about 0.131ms rather than 0.210ms in Bias 7. At t=0.157ms, the flow is now mostly in the EDD and the density responds by increasing slightly beyond the limiter edge and begins to resemble the steady-state flow of Bias 13. Further increasing the flow and flow shear for t=0.184 and t=0.210ms corresponds to increased density at the limiter edge and beyond. At this point, the change in profiles would seem to be counter to what is observed in the steady-state. Here, increased flow shear appears to result in an increase in density, and not exactly a profile steepening (the profile on the edge does appear to be steepened, but this could be more the result of the increase density at the limiter edge rather than decreased transport). However, comparison of the density at t=0.210ms and the steady-state profile at t=2.388ms, shows a change that is consistent with decreased transport—that is, a steepened profile and increased core density. Since the flow profile at t=0.210ms in nearly the same as the steady-state form, the change in density profile must be due to decreased transport as no further significant flow changes take place.

Bias 29 (lim-ano = 8.4V) represents an even more accelerated version of this process. The density dip occurs by t=0.052ms and by t=0.105ms, the density profile already resembles the steady-state profile of Bias 22. Similarly, the mach flow profiles of t=0.105ms of Bias 29 and the steady-state of Bias 22 also match. While the peak flow of Bias 29 occurs beyond

the 0.210ms time block in this plot, the effect of the decreased transport can already be observed in the decreasing edge density and steepening gradient from t=0.157 to t=0.210 and eventually to the steady-state profile at t=2.388.

Taken together, these four biases demonstrate the overall dynamical process of the bias transition. While some parts of the process are clearly the result of the shear suppression observed in the steady-state data, other steps are not so clearly understood. In all four of the representative biases, the initial effect of biasing on the density profile is a slight decrease in magnitude just inside the limiter edge. The spontaneous profile has somewhat of a hump in the 24-26cm region that gets flattened out in the early steps of the bias. This leveling effect corresponds to the time block when flow is nearly zero. While this could possibly be a change due to increased transport in a zero flow/shear period, the timing makes this seem unlikely as profile changes from transport cannot respond in a matter of 50μs as occurs in Bias 29. Instead, perhaps, the change in density is due directly to a change in the flow.

After this initial density dip period, the biases that drive flow in the EDD show an increase in density particularly around the limiter edge. Again, this change is unlikely to be due to transport modification because of the short time scale. As shown in Chapter 5, the temperature appears to be increased at the limiter edge. This could result in a slight increase in density from increased ionization. Unfortunately, like swept-Langmuir flow measurements, swept temperature measurements do not yield a time series and triple-probe temperature measurements proved to be too unreliable in this gradient region to be of much use. Thus the dynamics of temperature changes here could not be compared to flow and density changes to verify this hypothesis.

After this last density increase, actual transport modifications appear to occur. The transition from the profiles of the first 200μs to the steady-state period show a steepening of the density profile and increased density within the limiter edge—and interior to the region of sheared flow. Moreover, these changes do occur on a timescale characteristic of transport modification.

8.2.3 Density/Floating Potential Fluctuations and Flux Dynamics

As in the steady-state analysis, fluctuating quantities are examined and compared to the density profile to help determine the mechanisms involved in the dynamical changes.

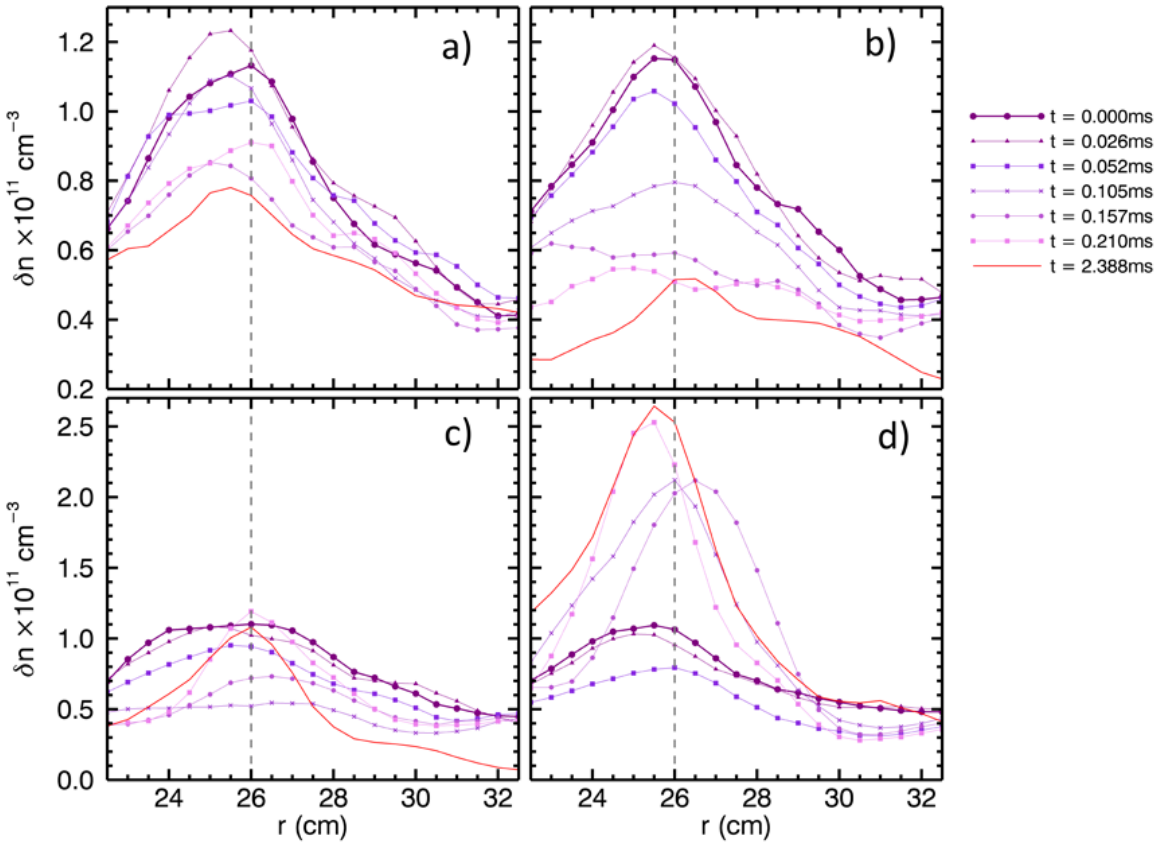

Figure 8.5: Density RMS (fluctuation) Profiles as a function of time for four biases (a)Bias 7, (b)Bias 13, (c)Bias 22 and (d)Bias 29

Figure 8.5 shows a similar set of profiles for increasing time for Biases 7, 13, 22, and 29. The most striking common feature of the four plots is the tendency for density fluctuations to drop almost immediately with the onset of bias. Biases 7 and 13 show perhaps a slight increase in fluctuations at t=0.026ms, but a significant decrease in magnitude by t=0.105ms. Eventually the steady-state profile shows the lowest level of fluctuations for these first two biases. For Bias 7, this is different than what was observed in the steady-state analysis of

Chapter 6 where fluctuations appear to peak in this bias state; however, it should be noted that these fluctuations values take into account all frequencies while the peak in Chapter 6 was really shown to occur in frequencies less than 10kHz. Biases 13, 22, and 29 are certainly consistent with the previous chapters results as the fluctuation level in the 27-31cm region decreases from Bias 7 to 13 to 22, but shows an upward tick for Bias 29.

The apparently fast drop in density fluctuations is what is most curious here, though, especially for Biases 13 and 22. The comparison of density and flow in the previous section showed a slight decrease in density gradient just inside the limiter edge, but it was thought to not be consistent with transport changes. Nevertheless, the mechanisms that cause transport changes may still exist at this point in time; the presence of sheared flow can cause a decrease in density fluctuations even if the timescale is too short for the density profile to be modified by reduced transport. The puzzling aspect of this observation is the fact that decrease in density fluctuation is concurrent with the *decrease* in shearing rate as the flow is reversed. It would appear that the mean sheared flow is not present at these points in time to cause the decrease in density fluctuations observed.

An alternative to mean sheared flow, however, could be the presence of fluctuating sheared flow. That is, there may exist radially sheared profiles at even smaller time scales than those encountered here. While this would be extremely difficult to measure directly, there is some circumstantial evidence for this effect in the form of V_f fluctuations. Figure 8.6 shows profiles of V_f RMS for increasing time and for the same four biases examined previously. Though Bias 7 does not appear to show very much change in time, Biases 13, 22, and 29 all show *increased* V_f fluctuations with time in the region outside the limiter (and nearly across the entire region for Biases 22 and 29). This increase in potential fluctuation may be connected to the changing mean flow at these times and may provide the shearing needed to modify the density fluctuations. As shown by the red curves, these peaks in V_f fluctuations eventually die away resulting in steady-state edge fluctuations that are less than the spontaneous case.

This overall effect is summarized in Figure 8.7, which shows the various plasma quantities averaged over the radial region of 27 to 31cm as a function of time from bias turn-on for

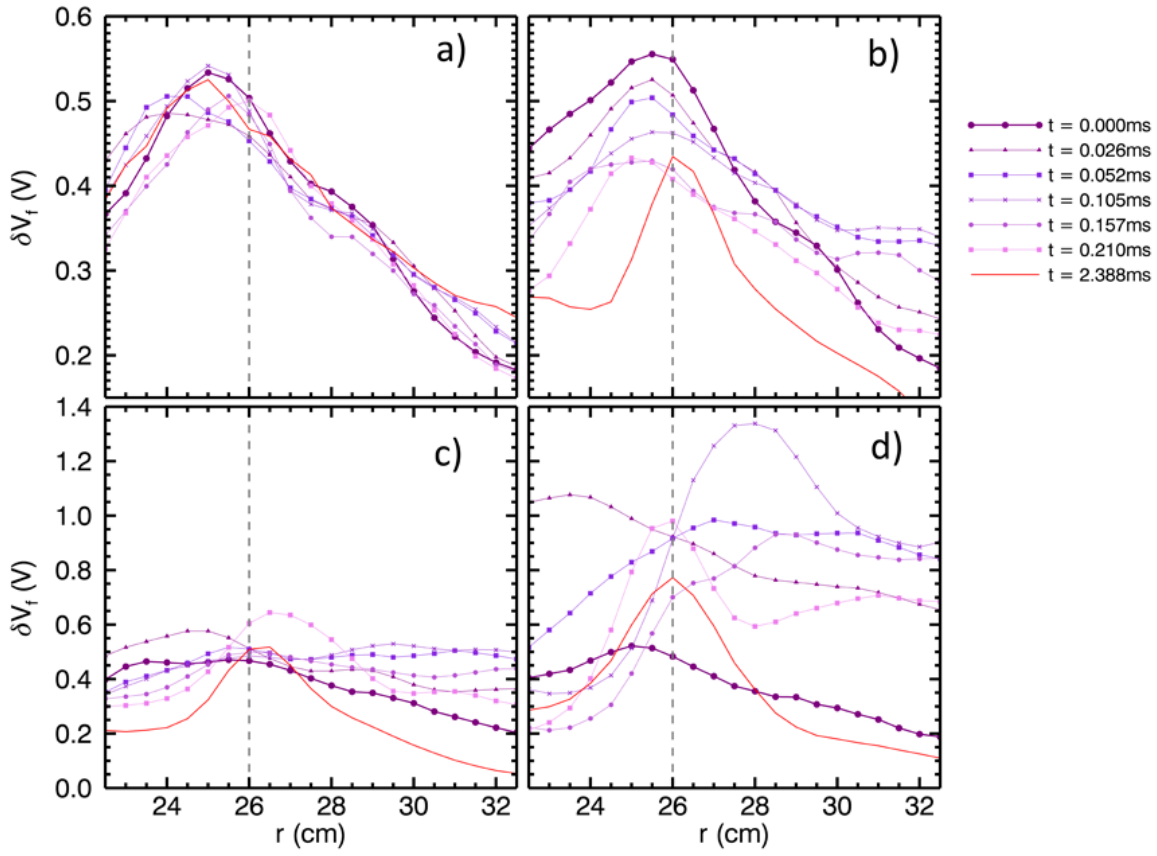

Figure 8.6: Floating potential RMS (fluctuation) Profiles as a function of time for four biases (a)Bias 7, (b)Bias 13, (c)Bias 22 and (d)Bias 29

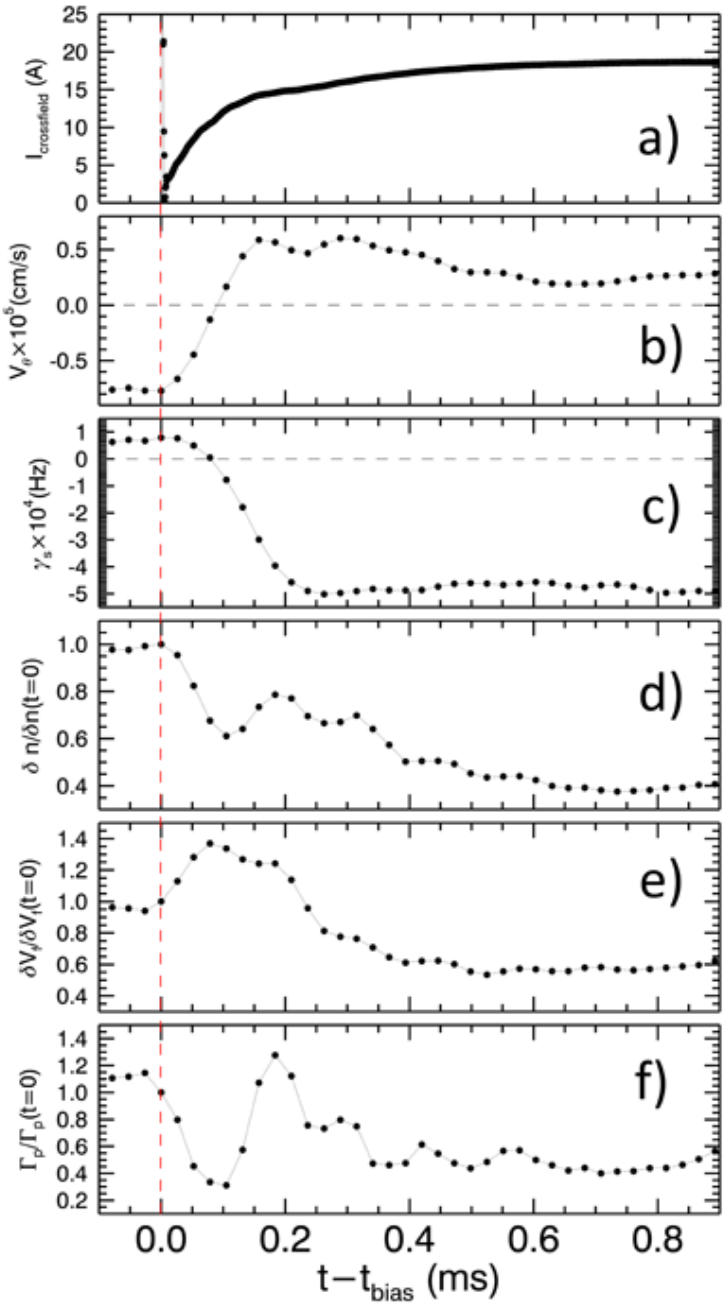

Figure 8.7: Averaged quantities in the region of 27 to 31cm for Bias 22 (a)cross-field current, (b) mach flow, (c) mach sheared flow, (d)density RMS normalized to the value at t=0, (e) v_f RMS normalized to the value at t=0, and (f) particle flux normalized to the value at t=0

Bias 22. The transition from IDD flow to EDD flow can be seen with increasing cross-field current in Figure 8.7(a) and (b). Note the drop in both density fluctuations and particle flux immediately at bias turn-on and continued decrease despite the flow and flow shear states nearing zero. The V_f fluctuations meanwhile show an initial increase at bias turn-on, but eventually drop down in value as the mean shearing rate reaches its maximum value. Also note that there is a jump in density fluctuation and particle flux around t=0.2ms, which could be the onset of the flow driven coherent mode. By the edge of the plot, at t=0.9ms, the quantities have mostly reached a steady value consistent with shear suppressed fluctuations and transport reduction.

The interplay of V_f fluctuations and overall mean shear may suggest that fluctuation and transport reduction in these bias transitions begin with a zonal-flow-like fluctuation shear suppression, but evolve into a mean sheared flow suppression. More detailed time measurements are likely needed to resolve this issue as well as comparison to transport models and simulation code.

8.3 Flow Relaxation

Lastly, the dynamics of the flows after the bias current drive is removed is considered. After bias is turned off, and thus the rotation drive shut-off, the plasma rotation begins to slow and return to the unbiased state. Examples of this slowdown is shown for four biases in Figure 8.8 As can be seen in Figure 8.9(c) and (d), the bias current changes immediately upon bias turn-off, responding within about $3\mu s$ with a large spike of negative current and transitions into a region of inductive transients. The transients taper off by about 0.1ms as indicated by the first blue dotted line in Figure 8.9(c). This flow relaxation period can be used to determine the primary damping element that slows this flow down.

From the ion force equation, a damping force proportional to the ion flow can be written as,

$$nm_i \frac{dv_\theta}{dt} = -nm_i \alpha v_\theta \tag{8.1}$$

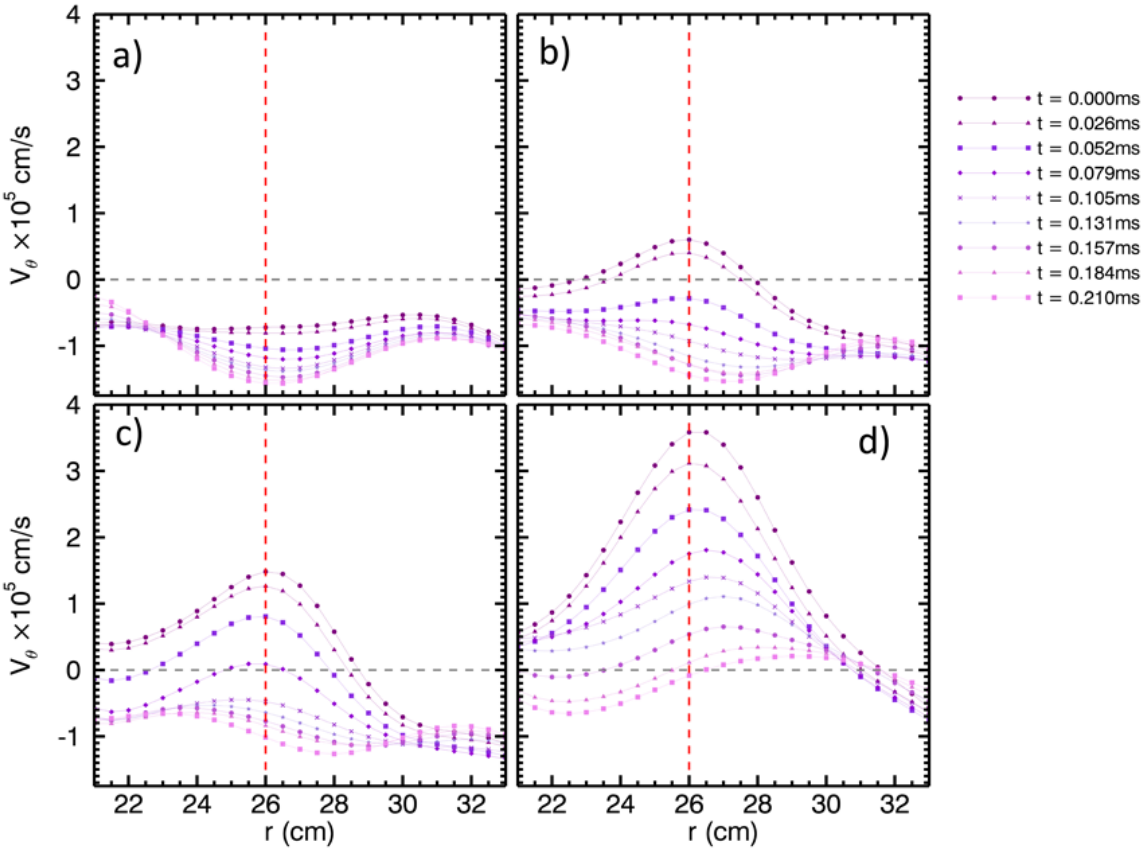

Figure 8.8: Mach Probe Flow Profiles as a function of time after bias shutoff (a)Bias 7, (b)Bias 13, (c)Bias 22 and (d)Bias 29

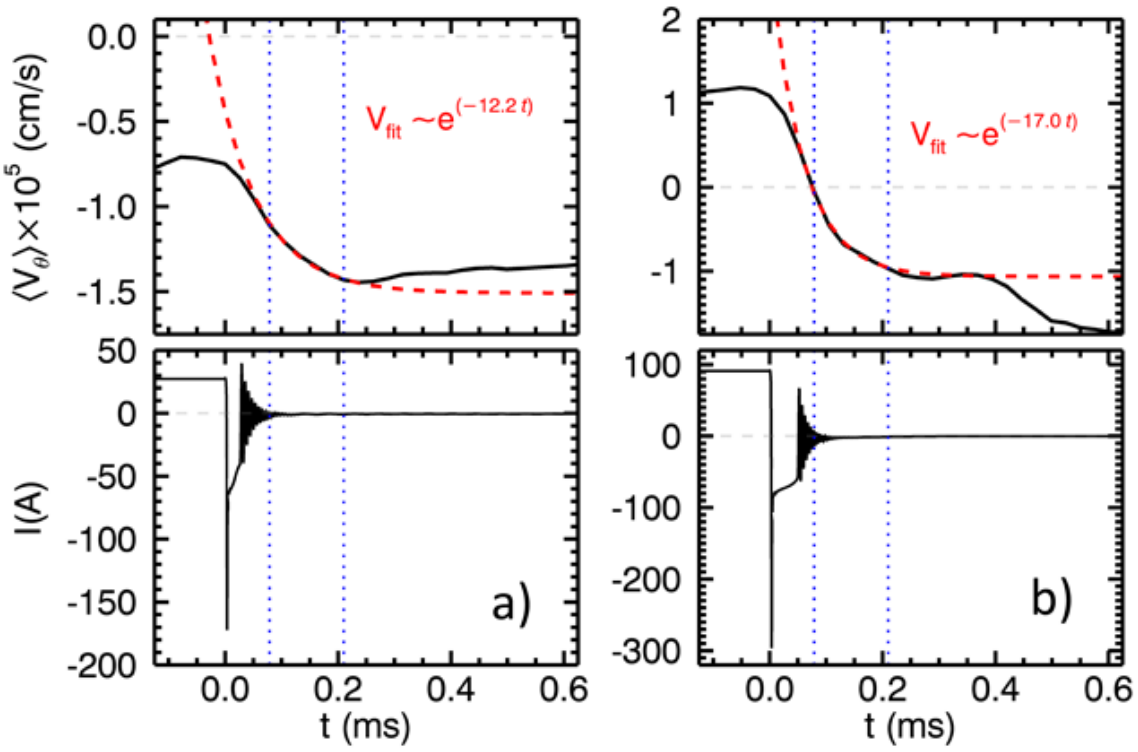

Figure 8.9: Mach Probe Flow summed over 24-28cm as function of time after bias shutoff (a)Bias 7 and (b)Bias 22 with corresponding current traces. An exponential is fit to the blue region of the flow vs time traces and the fit functional form is shown above: 12.2 for Bias 7 and 17.0 for Bias 22.

This dominant damping mechanism is assumed to be ion-neutral collisions, so α can be replaced with ν_{in} and the differential equation solved as,

$$v_\theta = v_\theta(0)e^{-\nu_{in}t} + C \tag{8.2}$$

where the C is just a constant and $v_\theta(0)$ is the initial plasma flow. Figure 8.9(a) shows the flow relaxation versus time for a low bias state (Bias 7) which corresponds to a bias state with injected current $\sim 30A$. The above model assumes no torque from the injected current so the flow time traces are fit in a region just after the transients have died away and the injected current goes to zero—a period of about $100\mu s$. Examples of exponential fits to these flows are displayed in Figure 8.9(a) and (b) for a relatively low bias in (a) and for a relatively strong bias in (b). Despite the large difference in initial flow values, the flows decrease at a consistent rate supporting the validity of the single damping mechanism model. The remaining biases with a measurable change in velocity have similar exponents with an average fit $\nu_{in} = 14.5kHz$ weighted by the chi-square of the fits. It should also be noted that the decrease in flow deviates from this exponential trend both immediately after the bias shut-off and beyond 0.2ms after shut-off. The decrease in flow begins slower than would be expected for exponential decay and the likely cause is the presence of the transient currents. Deviations with increasing time after the bias turn on are likely due to the processes which determine the spontaneous flow of the plasma and can no longer be predicted merely by damped flow.

The average damping rate of 14.5kHz is fairly close to the values calculated using Equation 4.4 which gave a range of 10.038kHz$< \nu_{in} <$12.638kHz, derived from a measured neutral pressure and assuming a constant ion temperature of 1eV. It is feasible that ion heating can occur due to biasing, which would tend to increase this collision frequency. Another possible contribution to the overall damping mechanism is the ion-ion viscosity,μ_{ii}. A viscosity term can be added to Equation 8.1 yielding,

$$\frac{dv_\theta}{dt} = -\nu_{in}v_\theta + \mu_{ii}\left(\frac{d^2}{dr^2}(v_\theta) + \frac{1}{r}\frac{d}{dr}(v_\theta) - \frac{v_\theta}{r^2}\right) \tag{8.3}$$

Though the contribution of the viscosity is much smaller than the ion-neutral collision fre-

quency because of factors of $1/r$, it could explain a small discrepancy in the measured and predicted values. If ion heating is not contributing, the measured average damping rate of 14.5kHz would suggest a neutral density of $5.94 \times 10^{12} cm^{-3}$ compared to a neutral density of $4.11 \times 10^{12} cm^{-3}$ based on neutral pressure measurements.

CHAPTER 9

Conclusions

The modification of turbulence and transport on the LAPD through a continuous variation of flow and flow shear states is investigated. The flow is set through a system of biased limiters, which form an iris-like aperture between the cathode source and main vacuum chamber, which drives rotation through the torque on injected current between the anode/cathode connected field lines and limiter connected field lines. It extends on previous rotation experiments conducted on the LAPD, which drove flow by biasing the middle section of the vacuum chamber [38, 39]; however, this newer approach allowed for a much more gradual variation of flow and flow shear as well as the ability to produce a nearly zero flow state and flow states that rotate in both azimuthal directions.

The effects of varying the rotation state of the plasma on plasma parameters and turbulent fluctuations are examined. The density profile undergoes an evolution that reflects changes in the radial confinement in the plasma and in plasma production. As plasma rotation is decreased, the density profile gradient relaxes indicating a degradation in particle confinement. As plasma rotation is increased in either azimuthal direction, the density profile gradient steepens reflecting particle confinement improvement. Changes in radial particle flux mirror these changes in confinement. Measured temperature profiles show that while core and far edge temperatures appear to be little affected by the biasing, the region at the limiter edge undergoes electron temperature heating on the order of 2-3eV. Comparison to transport models also show that the density profiles in the high flow high shear states are best matched to calculations when both radial transport is reduced and plasma production is increased in the regions of increase electron temperature. Profiles of effective source, calcu-

lated as the divergence of radial flux, also provide evidence for increased plasma production with biasing.

Highly biased, highly rotating states also show evidence for non-local transport. A local model of transport, like that which follows Fick's Law, prescribes a direction of flux that is dictated by the direction of the density gradient. However, measurements of flux in the high bias states shows flux in a radial direction opposite that suggested by the density gradient. The nature of this possible non-local mechanism is not fully investigated here, but could be related to the high plasma rotation or the development of the interacting coherent modes at the limiter edge.

Turbulent fluctuation spectra undergo changes corresponding to the flow state as well. Log-linear plots of density and floating potential frequency spectra have a much more linear scaling with frequency in plasma states with flow compared to the state with minimal flow. This suggests a change in the nature of the temporal fluctuations as flow is removed from the system. Log-linear plots of wavenumber spectra also exhibit similar changes in shape with flow state. Lorentzian pulses can be observed in time traces of the density fluctuations and are shown to match up with the associated exponential spectra. The wavenumber spectra also indicate that the propagation direction of the fluctuations changes; modes predominately propagate in the direction of rotation.

A mode analysis is also performed utilizing the ability of the biasing system to modify the gradients that provide free-energy to the instabilities. While a number of types modes can be present in the plasma, this work explored the contributions of three linear instabilities: the resistive drift-wave, the rotational interchange, and the Kelvin-Helmholtz modes. Though any definite connection of a linear mode to saturated turbulence can only be made with the help of non-linear simulation, the comparison of features of the measured spectral density with locations of gradient drives and calculations of growth rates made using a Braginskii-fluid-model eigenfunction solver can provide strong clues as to the likely modes present. The analysis suggests that rotational interchange modes are present in states with flow in either azimuthal direction, but only drift-waves are present in the zero flow states. Kelvin-

Helmholtz modes appear to be present in regions of shearing and likely make a sizable contribution to the fluctuations particularly in strongly biased states and in a region just outside the limiter edge where gradients in vorticity are shown to be highest.

A strong conclusion can be made for the driving instability of a pair of coherent modes that develop in the EDD direction flow states. These modes appear in the range of 2-8kHz of the density fluctuation spectra. As rotation velocity is increased, the modes increase in frequency and amplitude reaching frequencies up to 12kHz. The development of sidebands suggest interaction between these growing coherent modes. At the highest bias and rotation state, the modes appear to lose their linearity, creating a semi-broadband spectra. From fluctuation profiles, the modes are clearly localized to the limiter edge, which also corresponds to the region of maximum flow suggesting that they are rotational interchange driven modes. Comparison with linear calculations also show that the measured frequencies of the modes compare very well with the frequency and azimuthal mode number of the predicted fastest growing modes. These calculations indicate that the low frequency mode is pure (n=0) rotational interchange while the higher frequency mode is an n=0.5 coupled drift-interchange mode.

A localized comparison of plasma quantities and shearing rate show a strong correlation between decreased turbulent fluctuations and transport with increased flow shear. The shearing rate is normalized to the inverse autocorrelation time measured in the minimum flow shear state. The average shearing rate in the region of 27cm $< r <$ 31cm, just beyond the limiter edge, varies from 0 to 5 times this inverse autocorrelation time. The measured gradient length scale in this region is shown to evolve from 9cm in the unbiased state, to 14cm in the minimum sheared flow state to 5cm in the highest sheared flow states. Radial particle flux also decreases with shear; the components of this particle flux—density fluctuations, radial velocity fluctuations, crossphase and coherency—can be measured separately and their relative contributions to flux suppression with shear determined. These analyses showed that suppression of density fluctuations was the dominant contributer to flux decrease, a result that differs from the conclusions made in Carter *et al* [39], which indicated that suppression

of crossphase was more important.

The quantitative scaling of these quantities with shearing rate was also made in an attempt to compare with a variety of decorrelation models, which make predictions on how these parameters should scale with sheared flow. The results showed that three models based on a normalized shearing rate ($\sim C\gamma_s^\nu, \quad \sim 1-C\gamma_s^\nu, \quad \sim 1/(1+C\gamma_s^\nu)$) compared poorly to the experimental scaling. A few models were able to match fairly close to the experimental data: the density fluctuation scaling compared well to the prediction made by Biglari, Diamond and Terry [62], though the model does not take into account the changes in density gradient scale length that occur in the experiment; predictions of the scaling of crossphase made by Kim and Diamond [69] also come very close to the experimental values.

Finally, a brief examination into the dynamics of the biasing experiment is made. Comparison of the profiles of Mach probe measured flow show that rotational acceleration increases with higher injected cross-field current. The density fluctuations are also shown to decrease initially with bias turn-on despite mean flow and shearing rates that near zero as the flow reverse direction. This decrease corresponds with an initial increase in floating potential fluctuations that persists only while the flow is in transition. It is speculated that fast flow fluctuations during the plasma spin up may provide a mechanism to suppress density fluctuations initially before the mean sheared flow eventually takes over. Lastly, the spin down of the plasma is monitored after bias turn-off. The decrease in flow occurs exponentially at a rate that is consistent with the ion-neutral collision frequency of the plasma.

While this work endeavored to examine a broad range of phenomena related to the changing rotation state of LAPD, a significant number of avenues remain to be explored. First and foremost though, limiter biasing experiments of the type presented here should be continued. As mentioned at various points throughout the dissertation, these results actually differed significantly from previous biasing experiments conducted on LAPD which were conducted using chamber wall biasing rather than with limiters, but also at a much smaller field and mostly higher values of flow and flow shear. The limiter biasing experiments should be expanded into varying magnetic fields to determine the effect of gyroradius on transport

changes. Other machine variables such as pressure can be modified as well to determine the effect of changes in ion-neutral damping. Better electron temperature measurements, as well as direct ion temperature measurements should be made to explore the nature of the heating by biasing.

Other avenues of research should also be pursued. An analysis of the momentum balance of the system and its possible connection to spontaneous flow should be made. As indicated, the LAPD plasma undergoes rotation without any obvious outside force. This spontaneous flow can be the result of currents to boundaries that are not being taken into account or due to turbulent driven currents generated by gradients in the Reynolds Stress. The ability to null out the rotation of the plasma provides a unique opportunity help determine the origins of this spontaneous flow.

Though not reported in this dissertation, changes in intermittency were observed in the dataset as a function of rotation state. The nature of intermittent fluctuations and transport can be investigated further using the biasing setup.

Also, while the mode analysis could make reasonable conjectures as to the instabilities dominant in the system, a full non-linear simulation is necessary to complete the analysis. Work in this vein is already started by Brett Friedman using full non-linear Braginskii fluid code called BOUT++ [50].

Lastly, a more comprehensive analysis of the biasing dynamics should be attempted. This should can be accomplished in connection with the development of a viable Lanthanum Hexaboride emissive probe that can measure changes in plasma potential at a much finer timescale than can be achieved with swept Langmuir probes. The effect of fluctuating flows on density power and particle flux should be examined in connection with the study of zonal flow turbulence modification and compared to the steady-state results made in this dissertation.

APPENDIX A

LAPD Transport Model

A model for the production of plasma and particle loss on the LAPD was developed by J. Maggs. A full description of the model is given in [38]; this appendix serves to summarize the components of the model, describe slight modifications to the original model, and layout the parameters used for the model comparison to experimental data in Chapter 5.

The model simulates the production of plasma starting with a beam of electrons from the cathode source impinging on a volume of neutral gas. The source term then consists of an ionization term from beam electrons, $R_b n_b n_0$, and an ionization term from thermal electrons from the produced plasma, $R_p n_e n_0$. n_b, n_e and n_0 are the beam, plasma and neutral densities respectively. The ionization rates per electron beam, R_b and R_p are functions of the ionization cross-section, which depends on the beam energy and the electron temperature respectively, and the beam or thermal velocity. As [38] notes, these cross-sections can be found in published data.

The neutral density is assumed to be spatially constant, but have a temporal dependence. The neutral density is determined using the equation of state for a gas, $p_0 = n_0 k T_0$, where $T_0 = 300\text{K}$ and the pressure is determined from the calibrated ion gauge measurement. A recorded pressure of 2.3×10^{-5} Torr is calibrated to helium pressure by diving through by the factor 0.18, yielding a helium pressure of 1.28×10^{-4} Torr. Thus an initial neutral density of $4.8 \times 10^{12}\text{cm}^{-3}$ is utilized in the model.

The beam energy and density are dependent on the discharge current of the anode-

cathode circuit and is modeled for this dataset as,

$$I_{dis} = \frac{1}{2}\left(1 + \tanh\left(\frac{t_{ind} - 0.01}{0.002}\right)\right) \tag{A.1}$$

where t_{ind} is the time step index. The radial extent of the source, representing the cathode region modified by the insertion of the limiters is modeled as,

$$S(r) = \frac{1}{2}\left(1 - \tanh\left(\frac{(r - r_e)}{L_b}\right)\right) \tag{A.2}$$

where r is radius and $L_b = 0.5$cm is the length scale of the source gradient. The limiter edge, r_e, for this case is, of course, 26cm.

The plasma production due to thermal electrons is dependent on the temperature of the electrons. The electron temperature profile is set to the unbiased temperature profile given by Figure 5.2. Unlike the beam source term which increases in time with the discharge current, the electron temperature profile is initially at its full value, although this component of the plasma source does not have as much of an impact until the plasma density itself grows large enough.

The source terms are balanced by both an axial loss term and a radial loss term. The axial or end loss term, n/τ_L, is modified by the end loss rate, τ_L, which in principle can be determined experimentally (or heuristically as in Chapter 3), but in this modeling scheme is allowed to be manually set in order to match the profile. The model was slightly modified in order to allow for two different end loss rates for field lines inside the limiter edge and field lines outside the limiter edge. For this dataset, an end loss rate for $r < 26$cm was set to $250s^{-1}$ and $500s^{-1}$ for $r > 26$cm. These values gave the best match to the unbiased experimental density profile as shown in Figure 5.3(a) and were held constant during the simulated biasing.

The full radial loss term incorporates particle flux due to both frictional forces and thermal forces; however, only the friction force is used here and the resulting diffusion coefficient is assumed to be Bohm, $D_B = T_e/16B$.

The source and sink balance equation is solved at each time step using a tri-diagonal method again detailed in [38]. After enough time steps are taken for the plasma to reach

a steady-state, the "bias turn-on" is simulated by changing either or both the electron temperature profile or the radial diffusion coefficient. The calculated density begins to respond to the changed plasma production rate and/or changed plasma sink accordingly, eventually reaching a new steady state. As shown in Figure 5.3(b) and (c), the combination of a temperature profile change to a peaked profile with a maximum temperature of 6eV and a decrease in diffusion coefficient from 1 to 0.2 times Bohm was needed to match the high bias experimental density profile. In this case the change in transport was set to be the same throughout the entire radial extend of the plasma, but the model can be adjusted to include different transport levels at different radial locations (as would be suggested by the experimental diffusion coefficient or particle flux measurements.)

In addition to changes in plasma density, the temporal change in neutral density is recorded. For these calculations, the neutral density was shown to decrease by about 20% for the plasma discharge and showed very little change during the biased segment of time.

APPENDIX B

Comparison of Mach Flow and Swept Measurements

The primary diagnostics for measuring flow on the LAPD are the Mach probe and the swept Langmuir probe. Both techniques have their assets and their drawbacks and are discussed in this section.

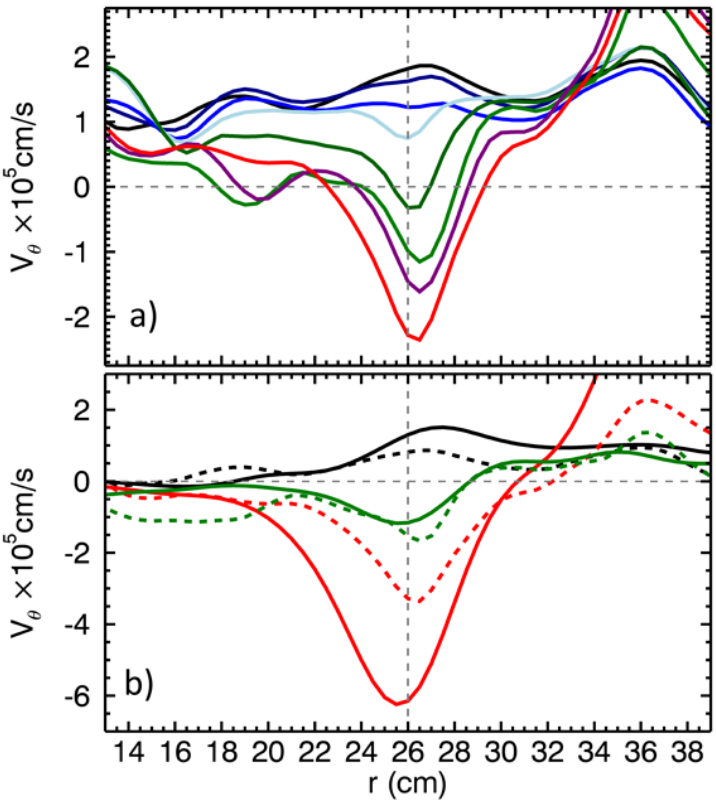

Figure B.1: (a)Mach probe measured azimuthal velocity profiles ranging from the unbiased state (blue) to the strongest bias (red). (b) A comparison between Mach probe measured flows (dashed lines) and swept Langmuir probe measured flows (solid lines).

The main advantages of the Mach probe measurements are that it 1)can fairly easily be analyzed and 2)can provide a time series measurement. However, the measurement can be susceptible to an overall offset; this can occur when the faces of the Mach probe are not the same area and thus there is always a difference in relative I_{sat} values even at zero flow because the different faces collect slightly different amounts of current. This can be alleviated somewhat making a measurement with the Mach probe facing in one direction, then flipping it over and taking the same measurement. This allows the opposite faces to sample the same region of plasma so that any area difference can be offset somewhat by calibration factors. Nevertheless, offsets tend to remain. As discussed in Chapter 3, the Mach probe is also affected by diamagnetic flow due to measurements in a density or temperature gradient. Chapter 3 discussed a theoretically approach for extracting actual $E \times B$ flow information for a Mach probe signal in a gradient region, but the errors in the procedure can compound quickly and overwhelm the actual signal.

The swept probe measurement on the other hand generally offers a very robust measurement of the swept plasma potential (and thus swept electric field/radial velocity) compared to the Mach probe. The drawback is that the measurement must be made over a longer time period compared to the sampling rate meaning a time series of plasma potential is not easily achieved. Moreover, the analysis of the IV curves can be time consuming especially for measurements in the edge when fitting regions must often be manually determined.

The top plot(a) in Figure B.1 shows a scan of Mach probe profiles as a function of increasing bias. The shape of the profiles is roughly the same as the swept probe measured velocity shown in Figure 4.16. The difference is that the scans are offset in the IDD direction by about 1×10^5cm/s and the range of flow values from peak to peak is smaller; the Mach flow values span $\sim 4.5 \times 10^5$cm/s while the swept probe flow values span $\sim 7 \times 10^5$cm/s.

This difference can be clearly seen in Figure B.1(b) which shows the first and last bias swept profiles in solid black and red and the Mach probe profiles in dashed black and red. An intermediate bias is shown in green for both. The Mach probe profiles have been decreased by 1×10^5cm/s in order to better match the swept values in the core region.

The relative similarity of these two techniques shows that flow measurements of this dissertation are generally well made. Also, while the flow magnitudes may be off, the time series measurements of the Mach probe can still be quite useful in determining general changes in the flow profiles and that even the value of this changing flow may only be off by about a factor of 2. Also, the comparison shows that a shearing rate measurement extracted from both profiles is fairly similar and again may only differ by a factor of 2.

Until a much better flow measurement can be made (such as with an emissive Langmuir probe which can measure time series of plasma potential directly), using both a Mach probe and a swept-probe to compliment one another is advised.

APPENDIX C

Two-Point Correlation Analysis

The two-point correlation analysis is a statistical technique for extracting spatial wavenumber quantities from a local measurement. The technique is especially useful in situations where high temporal resolution is available, but not necessarily high spatial resolution. Using two simultaneous fluctuation measurements—either saturated current or floating potential—separated a relatively small distance, d, apart, an "'instantaneous"' or local wavelength can be determined from the relative crossphase between the two measurements as demonstrated in Figure C.1. For these experiments, the two saturated current measurements are taken on a single probe tip separated by d= 3.23mm as in Figure C.2.

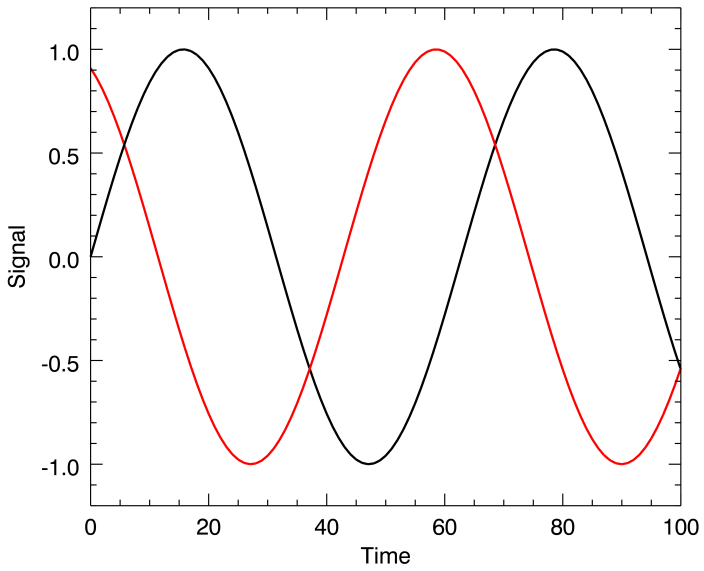

Figure C.1: Pictoral representation of instantaneous wavelength.

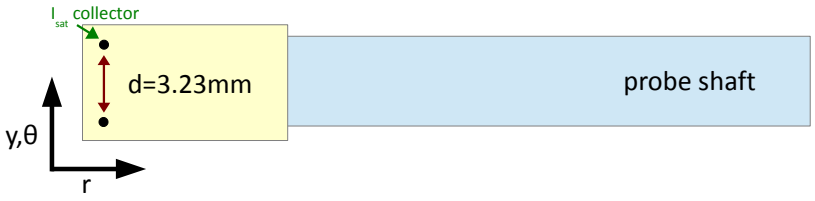

Figure C.2: Diagram of probe setup for two-point correlation measurement.

Following the derivation of the two-point correlation method from Beall 1982, we start by defining the cross-spectrum between the fluctuation measurements,

$$H^{(j)}(d,f) = \Phi^{(j)}(I_1,f)\Phi^{(j)}(I_2,f) = C^{(j)}(f) + iQ^{(j)}(f) \tag{C.1}$$

where $\Phi^{(j)}(I_n,f)$ is the FFT for each shot, j, of the upper and lower saturated current probe tip.

$$\theta^{(j)}(f) = \tan^{-1}\left(\frac{Q^{(j)}(f)}{C^{(j)}(f)}\right) \tag{C.2}$$

$$K^{(j)}(f) = \frac{\theta^{(j)}}{d} \tag{C.3}$$

Similar to a Nyquist frequency, the ranges of wavenumbers accessible by this technique in order to exclude $2\pi n$ indeterminices, are

$$\frac{-\pi}{d} > K > \frac{\pi}{d} \tag{C.4}$$

which for $d = 3.22mm = 0.322cm$ gives a wavenumber range of $-9.75cm^{-1} > K > 9.75cm^{-1}$. Wavelengths as small as 0.644cm are thus measurable with this probe. With the set of wavenumbers as a function of frequency for each shot, $K^{(j)}(f)$, a temporal fluctuation amplitude from the FFT is histogrammed to a wavenumber and frequency bin represented in the to build a local spectral density function of frequency and local wavenumber as,

$$S_l(K,f) = \frac{1}{M}\sum_{j=1}^{M} I_{0,\Delta K}(K - K^{(j)}(f))(\frac{1}{2}[S_1^{(j)}(f) + S_2^{(j)}(f)]) \tag{C.5}$$

where $S_n^{(j)}(f)$ is the fluctuation power for the upper and lower saturated current measurements and M is the total number of shots. The indicator function, $I_{0,\Delta K}$, represents the histogramming process that selects the fluctuation amplitude for the local wavenumber, $K(f)$, in the range $K + \Delta K$ for each frequency, f. For this calculation, a ΔK of $0.01 cm^{-1}$ is used while the frequencies used are discrete and determined from the number of samples used in the Fast Fourier Transform as,

$$\Delta f = \frac{1}{t_n \Delta t} = \frac{1}{5000(6.4 \times 10^{-7} s)} = 312.5 Hz \tag{C.6}$$

APPENDIX D

Probe Electronics

D.1 Voltage Isolation Circuit

Division: 10 ($900k\Omega/90k\Omega$) using Precision Thin Film Dividers (Caddock 1776-C68) **Bandwidth:** up to 1MHz **Isolation:** LF411 Op-Amp + BUF640 Buffer

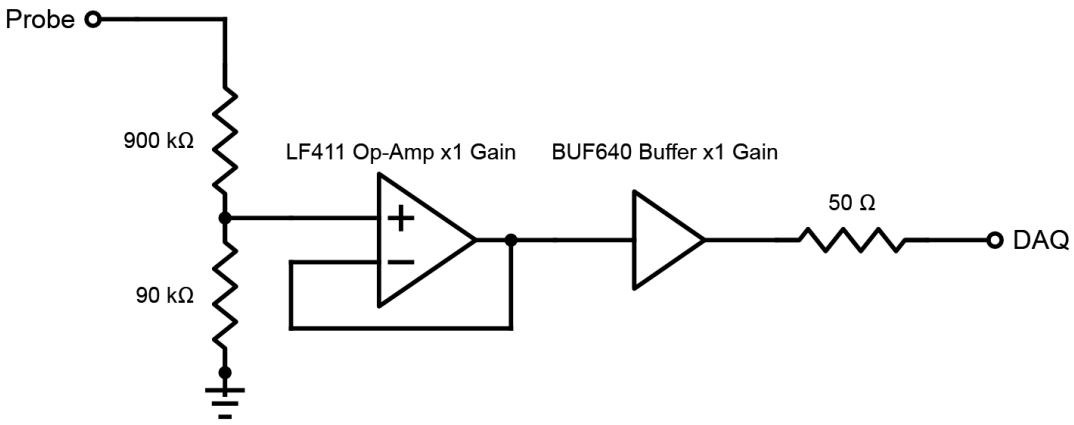

Figure D.1: LF411+BUF640 Div 10 Voltage Isolation Circuit

D.2 Ion Saturation Current Collection with Isolation

Tektronix-Sony 100MHz Optical Isolators

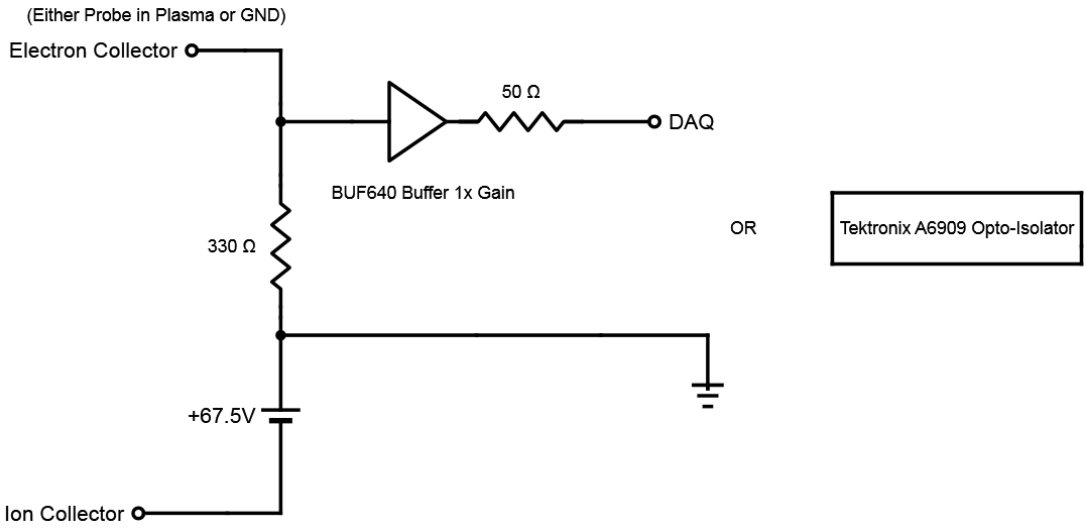

Figure D.2: Saturated Current collection circuit with Isolation

APPENDIX E

To Plasma

O Plasma!, will you reveal your ways to me

From saturated currents into plasma density?

Your flows I yearn to ponder, their direction and their shear,

Howre youre turbulently driven is not so very clear.

I build my probes with care, grinding down ceramic tube;

I mount the tips on shafts, then rub them down with lube.

On motor driven tracks, into the plasma core,

Ill scan your vacuum landscape to see whats there to store.

Your cathode burns quite brightly, primaries stream along

To knocking off electrons from the orbits they belong.

The cables pulse with power, the coils electrify,

The field will then confine you into gyroradii.

Your fluctuations travel azimuthally around,

Yet the search for what they are will undoubtedly confound,

As gradients can birth them, as well as shearing flow,

Can interfere and dampen or non-linearly grow.

Ill correlate your signals; Ill calculate your mean.

Ill stare blankly at the data with no clue to what Ive seen.

My probes will always penetrate the depths of mystery,

But the answers to my queries are found only spectrally;

The frequencies suggest which physics may be right,

Yet only in the phase regime will theory come to light.

And so my bluish beauty, so ephemeral and slight.

I see you for a millisecond 'fore youre gone from sight.

But Ive taken all my data, as much as any could,

And shall repeat my searching 'til youre completely understood.

Bibliography

[1] F. Wagner, G. Becker, K. Behringer, D. Campbell, A. Eberhagen, W. Engelhardt, G. Fussmann, O. Gehre, J. Gernhardt, G. v.Gierke, G. Haas, M. Huang, F. Karger, M. Keilhacker, O. Kluber, M. Kornherr, K. Lackner, G. Lisitano, G. Lister, H. Mayer, D. Meisel, E. Muller, H. Murmann, H. Niedermeyer, W. Poschenrieder, H. Rapp, H. Rohr, F. Schneider, G. Siller, E. Speth, A. Stabler, K.H.Steuer, G. Venus, O. Vollmer, and Z. Yu, Phys. Rev. Lett. **49**, 1408 (1982).

[2] F. Wagner, Plas. Phys. Control Fusion **49**, B1 (2007).

[3] K. Burrell, T. Carlstrom, E. Doyle, D. Finkenthal, P.Gohil, R. Groebner, D. Hillis, J. Kim, H. Matsumoto, R. Moyer, T. Osborne, C. Rettig, W. Peebles, T. Rhodes, H. St.John, R. Stambaugh, M. Wade, and J. Watkins, Plas. Phys. Control Fusion **34**, 1859 (1992).

[4] V. Erckmann, F. Wagner, J. Baldzuhn, R. Brakel, R. Burhenn, U. Gasparino, P. Grigull, H. Hartfuss, J. Hoffmann, R. Jaenicke, H. Nedermeyer, W. Ohlendorf, A. Rudyj, A. Weller, S. Bogdanov, B. Bomba, A. Borschegovsky, G. Cattanei, A. Dodhy, D. Dorst, A. Elsner, M. Endler, T. Geist, L. Giannone, H. Hacker, O. Heinrich, G. Herre, D. Hildebrandt, V. Hiznyak, V. Il'in, W. Kasparek, F. Karger, M. Kick, S. Kubo, A. Kuftin, V. Kurbatov, A. Lazaros, S. Malygin, V. Malygin, K. McCormick, G. Muller, V. Orlov, P. Pech, H. Ringler, I. Roi, F. Sardei, S. Sattler, F. Schneider, U. Schneider, P. Schuller, G. Siller, U. Stroth, M. Tutter, E. Unger, H. Wolff, E. Wursching, and S. Zopfel, Phys. Rev. Lett. **70**, 2086 (1993).

[5] O. Sakai, Y. Yasaka, and R. Itatani, Phys. Rev. Lett. **70**, 26 (1993).

[6] K. Steinmetz, J.-M. Noterdaeme, F. Wagner, F. Wesner, J. Baumler, B. Becker, H. Bosch, M. Brambilla, F. Braun, H. Brocken, A. Eberhagen, R. Fritsch, G. Fussmann, O. Gehre, J. Gernhardt, G. Gierke, E. Glock, O. Gruber, G. Haas, J. Hofmann,

F. Hofmeister, A. Izvozchikov, G. Janeschitz, F. Karger, M. Keilhacker, O. Kluber, M. Kornherr, K. Lackner, G. Lisitano, E. van Mark, F. Mast, H. Mayer, K. McCormick, D. Meisel, V. Mertens, E. Muller, H. Murmann, H. Neidermeyer, W. Poschenrieder, S. Puri, H. Rapp, H. Rohr, F. Ryter, K.-H. Schmitter, F. Schneider, C. Setzensack, G. Siller, P. Smeulders, F. Soldner, E. Speth, K.-H. Steuer, O. Vollmer, H. Wedler, , and D. Zasche, Phys. Rev. Lett. **58**, 124 (1987).

[7] J. Lohr, B. Stallard, R. Prater, R. Snider, K. Burrell, R. Groebner, D. Hill, K. Matsuda, C. Moeller, T. Petrie, H. S. John, and T. Taylor, Phys. Rev. Lett. **60**, 2630 (1988).

[8] K. Hoshino, T. Yamamoto, H. Kawashima, N. Suzuki, Y. Uesugi, M. Mori, H. Aikawa, S. Kasai, T. Kawakami, T. Matsuda, Y. Miura, K. Odajima, H. Ogawa, T. Ogawa, H. Ohtsuka, T. Shoji, H. Tamai, T. Yamauchi, T. Kondo, I. Nakazawa, C. Neufeld, and H. Maeda, Phys. Rev. Lett. **63**, 770 (1989).

[9] T. Osborne, N. Brooks, K. Burrell, T. Carlstrom, R. Groebner, W. Howl, A. Kellman, L. Lao, T. Taylor, D. Hill, N.Ohyabu, and M. Perry, Nucl. Fusion **30**, 2023 (1990).

[10] K. Burrell, Phys. Plasmas **4**, 1499 (1997).

[11] R. Groebner, K. Burrell, and R. Seraydarian, Phys. Rev. Lett. **64**, 3015 (1990).

[12] K. Ida, S. Hidekuma, Y. Miura, T. Fujita, M. Mori, K. Hoshino, N. Suzuki, T. Yamauchi, and the JFT2-M Group, Phys. Rev. Lett. **65**, 1364 (1990).

[13] R. Taylor, B. James, S. Jin, L. Keller, P. Lee, N. L. Jr., G. Morales, L. Oren, H. Park, W. Peebles, S. Talmadge, and C. Yu, 9th IAEA Conf. on Plasma Physics and Controlled Nuclear Fusion, Baltimore **Vol. III**, 251 (1982).

[14] G. Fidel'man, Sov. J. Plasma Phys. **11**, 376 (1985).

[15] R. Taylor and L. Oren, Phys. Rev. Lett. **42**, 446 (1979).

[16] P. Phillips, A. Wootton, W. Rowan, C. Ritz, T. Rhodes, R. Bengtson, W. Hodge, R. Durst, S. McCool, B. Richards, K. Gentle, D. Brower, W. Peebles, N. L. Jr., P. Schoch, J. Forster, R. Hickok, and T. Evans, J. Nucl. Mater. **145-147**, 807 (1987).

[17] R. Taylor, M. Brown, B. Fried, H. Grote, J. Liberati, G. Morales, P. Pribyl, D. Darrow, and M. Ono, Phys. Rev. Lett. **63**, 2365 (1989).

[18] R. Moyer, K. Burrell, T. Carlstrom, S. Coda, R. Conn, E. Doyle, P. Gohil, R. Groebner, J.Kim, R. Lehmer, W. Peebles, M. Porkolab, C. Rettig, T. Rhodes, R. Seraydarian, R. Stockdale, D. Thomas, G. Tynan, and J. Walkins, Phys. Plasmas **2**, 2397 (1995).

[19] J. Hugill, Nucl. Fusion **23**, 331 (1983).

[20] P. Liewer, Nucl. Fusion **25**, 543 (1985).

[21] W. Rowan, C. Klepper, C. Ritz, R. Bengston, K. Gentle, P. Phillips, T. Rhodes, B. Richards, and A. Wootton, Nucl. Fusion **27**, 1105 (1987).

[22] A. Wootton, B. Carreras, H. Matsumoto, K. McGuire, W. Peebles, C. P. Ritz, P. Terry, and S. Zweben, Phys. Fluid B **2**, 12 (1990).

[23] S. Zweben, J. Boedo, O. Grulke, C. Hidalgo, B. LaBombard, R. Maqueda, P. Scarin, and J. Terry, Plas. Phys. Control Fusion **49**, S1 (2007).

[24] G. Tynan, L. Schmitz, R. Conn, R. Doerner, and R. Lehmer, Phys. Rev. Lett. **68**, 3032 (1992).

[25] R. Weynants, G. V. Oost, G. Bertschinger, J. Boedo, P. Brys, T. Delvigne, K. Dippel, F. Durodie, H. Euringer, K. Finken, D. Gray, J. Hey, D. Hillis, J. Hogan, L. Konan, R. Leners, A. Messian, A. Pospieszczyck, U. Samm, R. Schorn, B. Schweer, G. Telesca, R. Vannieuwenhove, and P. Vandenplas, Nucl. Fusion **32**, 837 (1992).

[26] R. Weynants and G. V. Oost, Plasma Phys. Control Fusion **35**, B177 (1993).

[27] R. Weynants, S. Jachmich, and G. V. Oost, Plasma Phys. Control Fusion **40**, 635 (1998).

[28] S. Jachmich, G. V. Oost, R. Weynants, and J. Boedo, Plasma Phys. Control Fusion **40**, 1105 (1998).

[29] J. Boedo, D. Gray, S. Jachmich, R. Conn, G. Terry, G. Tynan, G. V. Oost, R. Weynants, and T. Team, Nucl. Fusion **40**, 7 (2000).

[30] J. Boedo, D. Gray, P. Terry, S. Jachmich, G. Tynan, R. Conn, and T.-. Team, Nucl. Fusion **42**, 117 (2002).

[31] G. V. Oost, J. Adamek, V. Antoni, P. Balan, J. Boedo, P. Devynck, I. Duran, L. Eliseev, J. Gunn, M. Hron, C. Ionita, S. Jachmich, G. Kirnev, E. Martines, A. Melnikov, R. Schrittwieser, C. Silva, J. Stockel, M. Tendler, C. Varandas, M. V. Schoor, V. Vershkov, and R. Weynants, Plas. Phys. Control Fusion **48**, 621 (2003).

[32] P. Peleman, Y. Xu, M. Spolaore, J. Brotankova, P. Devynck, J. Stockel, G. V. Oost, and C. Boucher, J. Nucl. Fusion Mat. **363-365**, 638 (2007).

[33] J. Cabral, C. Varandas, M. Alonso, P. Belo, R. Canario, H. Fernandes, R. Gomes, A. Malaquias, P. Malinov, F. serra, F. Silva, and A. Soares, Plas. Phys. Control Fusion **40**, 1001 (1998).

[34] C. Silva, H. Figueiredo, I. Nedzelskiy, B. Goncalves, and C. Varandas, Plas. Phys. Control Fusion **48**, 727 (2006).

[35] D.Craig, A. Almagri, J. Anderson, J. Chapman, C. Chiang, N. Crocker, D. D. Hartog, G. Fiksel, S. Prager, J. Sarff, and M. Stoneking, Phys. Rev. Lett. **79**, 10 (1997).

[36] V. Antoni, E. Martines, D. Desideri, L. Fattorini, G. Serianni, M. Spolaore, L. Tramontin, and N. Vianello, Plas. Phys. Control Fusion **42**, 83 (2000).

[37] G. Kirnev, V. Budaev, M. Dremin, E. Gerasimov, S. Grashin, L. Khimchenko, S. Krilov, Y. D. Pavlov, D. Shelukhin, S. Soldatov, N. Timchenko, G. V. Oost, and V. Vershkov, Plas. Phys. Control Fusion **45**, 337 (2003).

[38] J. Maggs, T. Carter, and R. Taylor, Phys. Plasmas **14**, 052507 (2007).

[39] T. Carter and J. Maggs, Phys. Plasmas **16**, 012304 (2009).

[40] P. Diamond, S.-I. Itoh, K. Itoh, and T. Hahm, Plasma Phys. Control Fusion **47**, R35 (2005).

[41] P. Terry and R. Gatto, Phys. Plasmas **13**, 062309 (2006).

[42] G. Staebler, R. Waltz, J. Kinsey, and W. Solomon, Proceedings of the 24th Fusion Energy Conference **International Atomic Energy Agency**, Vienna, 2012 (2012).

[43] M. Shi, D. Pace, G. Morales, J. Maggs, and T. Carter, Phys. Plasmas **16**, 062306 (2009).

[44] J. Maggs and G. Morales, Phys. Rev. Lett. **107**, 185003 (2011).

[45] J. Maggs and G. Morales, Phys. Rev. E **86**, 015401(R) (2012).

[46] J. Huba, *NRL Plasma Formulary* (Office of Naval Research, 2011).

[47] F. Chen, *Introduction to Plasma Physics and Controlled Fusion*, 2nd ed. (Plenum Press, 1984).

[48] J. Maggs and G. Morales, Geo. Res. Lett. **23**, 633 (1996).

[49] P. Popovich, M. Umansky, T. Carter, and B. Friedman, Phys. Plasmas **17**, 102107 (2010).

[50] B. Friedman, T. Carter, D. S. M.V. Umansky, and B. Dudson, Phys. Plasmas **19**, 102307 (2012).

[51] D. Jassby, Phys. Fluids **15**, 9 (1972).

[52] W. Gekelman, H. Pfister, Z. Lucky, J. Bamber, D. Leneman, and J. Maggs, Rev. Sci. Instrum. **62**, 2875 (1991).

[53] A. Burke, J. Maggs, and G. Morales, Phys. Plasmas **7**, 544 (2000).

[54] D. Pace, M. Shi, J. Maggs, G. Morales, and T. Carter, Phys. Plasmas **15**, 122304 (2008).

[55] I. H. Hutchinson, Phys. of Plas. **15**, 123503 (2008).

[56] E. Powers, Nucl. Fusion **14**, 749 (1974).

[57] W. Horton, J. Perez, T. Carter, and R. Bengtson, Phys. Plasmas **12**, 022303 (2004).

[58] G. Hornung, B. Nold, J. Maggs, G. Morales, M. Ramisch, and U. Stroth, Phys. Plasmas **18**, 082203 (2011).

[59] J. Penano, G. Morales, and J. Maggs, Phys. Plasmas **7**, 144 (2000).

[60] J. Perez, W. Horton, R. Bengtson, and T. Carter, Phys. Plasmas **13**, 055701 (2006).

[61] P. Terry, D. Newman, and A. Ware, Phys. Rev. Lett. **87**, 18 (2001).

[62] H. Biglari, P. Diamond, and P. W. Terry, Phys. Fluids B. **2**, 1 (1990).

[63] K. Shaing, E. Crume, and W. Houlberg, Phys. Fluids B **2**, 6 (1990).

[64] Y. Zhang and S. Mahajan, Phys. Fluids B **4**, 1385 (1992).

[65] Y. Zhang and S. Mahajan, Phys. Fluids B **5**, 7 (1993).

[66] A. Ware, P. Terry, P. Diamond, and B. Carreras, Plasma Phys. Control Fusion **38**, 1343 (1996).

[67] A. Ware, P. Terry, B. Carreras, and P. Diamond, Phys. Plasmas **5**, 173 (1998).

[68] E.-J. Kim and P. Diamond, Phys. Rev. Lett. **90**, 7 (2003).

[69] E.-J. Kim, P. Diamond, and T. Hahm, Phys. Plasmas **11**, 10 (2004).

[70] A. Newton and E.-J. Kim, Phys. Plasmas **18**, 052305 (2011).

[71] D. Schaffner, T. Carter, G. Rossi, D. Guice, J. Maggs, S. Vincena, and B. Friedman, Phys. Rev. Lett. **109**, 135002 (2012).

[72] M. Leconte, P. Beyer, S. Benkadda, and X.Garbet, Phys. Plasmas , 112301 (2006).

[73] A. Newton and E.-J. Kim, Phys. Plasmas **14**, 122306 (2007).